Thermomechanical state of the southern Central Andes: implications for active deformation patterns in the transition from flat to steep subduction

---

Lic. Constanza Rodriguez Piceda

Kumulative Dissertation
zur Erlangung des akademischen Grades
"doctor rerum naturalium"
(Dr. rer. nat.)
in der Wissenschaftsdisziplin Geophysik

eingereicht an der
Mathematisch-Naturwissenschaftlichen Fakultät
Institut für Geowissenschaften
der Universität Potsdam
und
Sektion 4.5 Sedimentbeckenanalyse
Deutsches GeoforschungZentrum Potsdam

Ort und Tag der Disputation: Potsdam, 29.04.2022

Hauptbetreuer*in:	Prof. Manfred R. Strecker, PhD
Betreuer*innen:	Prof. Dr. Magdalena Scheck-Wenderoth
Gutachter*innen:	Prof. Manfred R. Strecker, PhD Prof. Dr. Magdalena Scheck-Wenderoth Prof. Dr. Carla Braitenberg

https://doi.org/10.25932/publishup-54927
https://nbn-resolving.org/urn:nbn:de:kobv:517-opus4-549275

Abstract

The Andes are a ~7000 km long N-S trending mountain range developed along the South American western continental margin. Driven by the subduction of the oceanic Nazca plate beneath the continental South American plate, the formation of the northern and central parts of the orogen is a type case for a non-collisional orogeny. In the southern Central Andes (SCA, 29°S-39°S), the oceanic plate changes the subduction angle between 33°S and 35°S from almost horizontal (< 5° dip) in the north to a steeper angle (~30° dip) in the south. This sector of the Andes also displays remarkable along- and across- strike variations of the tectonic deformation patterns. These include a systematic decrease of topographic elevation, of crustal shortening and foreland and orogenic width, as well as an alternation of the foreland deformation style between thick-skinned and thin-skinned recorded along- and across the strike of the subduction zone. Moreover, the SCA are a very seismically active region. The continental plate is characterized by a relatively shallow seismicity (< 30 km depth) which is mainly focussed at the transition from the orogen to the lowland areas of the foreland and the forearc; in contrast, deeper seismicity occurs below the interiors of the northern foreland. Additionally, frequent seismicity is also recorded in the shallow parts of the oceanic plate and in a sector of the flat slab segment between 31°S and 33°S. The observed spatial heterogeneity in tectonic and seismic deformation in the SCA has been attributed to multiple causes, including variations in sediment thickness, the presence of inherited structures and changes in the subduction angle of the oceanic slab. However, there is no study that inquired the relationship between the long-term rheological configuration of the SCA and the spatial deformation patterns. Moreover, the effects of the density and thickness configuration of the continental plate and of variations in the slab dip angle in the rheological state of the lithosphere have been not thoroughly investigated yet. Since rheology depends on composition, pressure and temperature, a detailed characterization of the compositional, structural and thermal fields of the lithosphere is needed. Therefore, by using multiple geophysical approaches and data sources, I constructed the following 3D models of the SCA lithosphere: (i) a seismically-constrained structural and density model that was tested against the gravity field; (ii) a thermal model integrating the conversion of mantle shear-wave velocities to temperature with steady-state conductive calculations in the uppermost lithosphere (< 50 km depth), validated by temperature and heat-flow measurements; and (iii) a rheological model of the long-term lithospheric strength using as input the previously-generated models.

The results of this dissertation indicate that the present-day thermal and rheological fields of the SCA are controlled by different mechanisms at different depths. At shallow depths (< 50 km), the thermomechanical field is modulated by the heterogeneous composition of the continental lithosphere. The overprint of the oceanic slab is detectable where the oceanic plate is shallow (< 85 km depth) and the radiogenic crust is thin, resulting in overall lower temperatures and higher strength compared to regions where the slab is steep and the radiogenic crust is thick. At depths > 50 km, largest temperatures variations occur where the descending slab is detected, which implies that the deep thermal field is mainly affected by the slab dip geometry.

The outcomes of this thesis suggests that long-term thermomechanical state of the lithosphere influences the spatial distribution of seismic deformation. Most of the seismicity within the continental plate occurs above the modelled transition from brittle to ductile conditions. Additionally, there is a spatial correlation between the location of these events and the transition from the mechanically strong domains of the forearc and foreland to the weak domain of the orogen. In contrast, seismicity within the oceanic plate is also detected where long-term ductile conditions are expected. I therefore analysed the possible influence of additional mechanisms triggering these earthquakes, including the compaction of sediments in the subduction interface and dehydration reactions in the slab. To that aim, I carried out a qualitative analysis of the state of hydration in the mantle using the ratio between compressional- and shear-wave velocity (v_p/v_s ratio) from a previous seismic tomography. The results from this analysis indicate that the majority of the seismicity spatially correlates with hydrated areas of the slab and overlying continental mantle, with the exception of the cluster within the flat slab segment. In this region, earthquakes are likely triggered by flexural processes where the slab changes from a flat to a steep subduction angle.

First-order variations in the observed tectonic patterns also seem to be influenced by the thermomechanical configuration of the lithosphere. The mechanically strong domains of the forearc and foreland, due to their resistance to deformation, display smaller amounts of shortening than the relatively weak orogenic domain. In addition, the structural and thermomechanical characteristics modelled in this dissertation confirm previous analyses from geodynamic models pointing to the control of the observed heterogeneities in the orogen and foreland deformation style. These characteristics include the lithospheric and crustal thickness, the presence of weak sediments and the variations in gravitational potential energy.

Specific conditions occur in the cold and strong northern foreland, which is characterized by active seismicity and thick-skinned structures, although the modelled crustal strength exceeds the typical values of externally-applied tectonic stresses. The additional mechanisms that could explain the strain localization in a region that should resist deformation are: (i) increased tectonic forces coming from the steepening of the slab and (ii) enhanced weakening along inherited structures from pre-Andean deformation events. Finally, the thermomechanical conditions of this sector of the foreland could be a key factor influencing the preservation of the flat subduction angle at these latitudes of the SCA.

Zusammenfassung

Die Anden sind eine ~7000 km lange N-S-verlaufende Hochgebirgskette, die entlang des westlichen südamerikanischen Kontinentalrandes entstanden ist. Aufgrund der Subduktion der ozeanischen Nazca-Platte unter die kontinentale südamerikanische Platte ist die Bildung des nördlichen und zentralen Teils des Gebirges typisch für eine nicht-kollisionale Orogenese. In den südlichen Zentralanden (SZA, 29-39° S) verändert sich der Subduktionswinkel der ozeanischen Platte zwischen 33 ° S und 35 ° S von fast horizontal (< 5° Einfallen) im Norden zu einem steileren Winkel (~ 30 ° Einfallen) im Süden. Begleitet wird dieser Trend von systematischen, Süd-gerichteten Abnahmen der topographischen Erhebung, der Krusteneinengung und der Vorland- und Orogenbreite, sowie von Variationen im Deformationsstil des Vorlandes, wo die Einengung des Deckgebirges in unterschiedlichem Maße von einer entsprechenden Deformation des Grundgebirges begleitet wird. . Darüber hinaus sind die SZA eine seismisch sehr aktive Region. Die Kontinentalplatte zeichnet sich durch eine relativ flache Seismizität (< 30 km Tiefe) aus, die sich hauptsächlich auf die Übergänge vom Orogen zu den Vorlandbereichen konzentriert; im Gegensatz dazu tritt tiefere Seismizität in den zentralen Bereichen des nördlichen Vorlandes auf. Darüber hinaus ist häufig auftretende Seismizität auch in den flachen Teilen der ozeanischen Platte und im Plattensegment mit flach einfallender Subduktion zwischen 31 ° S und 33 ° S festzustellen. Die beobachtete räumliche Heterogenität der tektonischen und seismischen Deformation in den SZA wurde auf mehrere Ursachen zurückgeführt, darunter Schwankungen der Sedimentmächtigkeit, das Vorhandensein vererbter Strukturen und Veränderungen des Subduktionswinkels der ozeanischen Platte. Es gibt jedoch bislang keine Studie, die den Zusammenhang zwischen der langfristigen rheologischen Konfiguration der SZA und den räumlichen Deformationsmustern untersucht hat. Darüber hinaus wurden die Auswirkungen der Dichte- und Mächtigkeitsvariationen in der kontinentalen Oberplatte und der verschiedenen Subduktionswinkel auf den rheologischen Zustand der Lithosphäre noch nicht grundlegend untersucht. Da die Rheologie von der Gesteinsart, dem Druck und der Temperatur abhängt, ist eine detaillierte Charakterisierung der Zusammensetzung, Struktur und des thermischen Feldes der Lithosphäre erforderlich. Daher habe ich unter Verwendung kombinierter Modellierungsansätze und geophysikalischer Daten die folgenden 3D Modelle für die Lithosphäre der SZA konstruiert: (i) ein auf seismischen Daten basierendes Struktur- und Dichtemodell, das anhand des beobachteten Schwerefeldes validiert wurde; (ii) ein thermisches Modell, das die Umwandlung von Mantelscherwellengeschwindigkeiten in Temperaturen mit Berechnungen des konduktiven Wärmetransports für stationäre Bedingungen in der obersten

Lithosphäre (<50 km Tiefe) integriert und durch Temperatur- und Wärmeflussmessungen validiert wurde; und (iii) ein rheologisches Modell der langfristig bedingten Lithosphärenfestigkeit, das auf den zuvor erzeugten Modellen gründet.

Die Ergebnisse dieser Dissertation zeigen, dass die thermischen und rheologischen Bedingungen in den heutigen SZA durch verschiedene Mechanismen in unterschiedlichen Tiefen gesteuert werden. In flachen Tiefen (< 50 km) wird das thermomechanische Feld durch die heterogene Zusammensetzung der kontinentalen Lithosphäre differenziert. Eine Überprägung durch die ozeanische Platte ist dort nachweisbar, wo die ozeanische Platte flach (< 85 km tief) und die radiogene Kruste dünn ist, was insgesamt zu niedrigeren Temperaturen und einer höheren Festigkeit im Vergleich zu Bereichen führt, in denen die Platte steil einfällt und die radiogene Kruste dick ist. In Tiefen > 50 km treten die größten Temperaturschwankungen dort auf, wo die subduzierten Platte nachgewiesen wurde, was bedeutet, dass das tiefe thermische Feld den Subduktionswinkel gesteuert wird.

Die Ergebnisse dieser Doktorarbeit legen nahe, dass der langfristige thermomechanische Zustand der Lithosphäre die räumliche Verteilung rezenter Seismizität beeinflusst. Der größte Anteil innerhalb der Kontinentalplatte registrierter Erdbebentätigkeit tritt oberhalb des modellierten Übergangs von spröden zu duktilen Bedingungen auf. Außerdem besteht eine räumliche Korrelation zwischen Erdbebenclustern und den Übergängen von den mechanisch rigideren Vorlandbereichen (Forearc und Foreland) zum mechanisch schwächeren Orogen. Demgegenüber wird vermehrte Seismizität innerhalb der ozeanischen Platte auch dort nachgewiesen, wo entsprechend der Modellierung langfristig duktile Bedingungen erwartet werden. Ich habe daher den möglichen Einfluss zusätzlicher Mechanismen untersucht, die ein Auslösen dieser Erdbeben begünstigen könnten, darunter die Kompaktion von Sedimenten an der Subduktionsgrenzfläche und Dehydrationsreaktionen innerhalb der Platte. Dazu habe ich eine qualitative Analyse des Hydratationszustandes des Mantels unter Verwendung des Verhältnisses zwischen Kompressions- und Scherwellengeschwindigkeit (Vp/Vs-Verhältnis aus einemseismischen Tomographiemodell) durchgeführt. Die Ergebnisse dieser Analyse zeigen, dass der Großteil der Seismizität räumlich mit hydratisierten Bereichen in der subduzierten Platte und im darüber liegenden kontinentalen Mantel korreliert, mit Ausnahme eines Erdbebenclusters, das innerhalb des flachen Plattensegments auftritt. In diesem Bereich wechselt die subduzierte Platte von einem flachen in einen steilen Subduktionswinkel und Erdbeben werden wahrscheinlich durch Biegevorgänge in der Platte ausgelöst.

Auch die wichtigsten Variationen in den beobachteten tektonischen Mustern scheinen durch die thermomechanische Konfiguration der Lithosphäre beeinflusst zu sein. Die mechanisch starken Bereiche von Forearc und Foreland zeigen aufgrund ihrer Verformungsbeständigkeit geringere Verkürzungsraten als der relativ schwache Bereich des Orogens. Darüber hinaus bestätigen die in dieser Dissertation modellierten strukturellen und thermomechanischen Eigenschaften der Lithosphäre auch frühere Analysen geodynamischer Simulationen, denen zufolge der Deformationsstil im Orogen- und Vorlandbereich jeweils von Variationen in der Lithosphären- und Krustendicke, im Vorhandensein schwacher Sedimente und in der gravitativen potentiellen Energie kontrolliert wird.

Eine Sonderstellung nimmt der nordöstliche Vorlandbereich der SZA ein, wo eine verstärkte Seismizität und eine das Deck-und Grundgebirge erfassende Deformation zu beobachten sind, obwohl die modellierte Krustenfestigkeit dort Werte übersteigt, die für die in diesem Gebiet anzunehmenden tektonischen Spannungen typisch wären. . Mechanismen zur Lokalisierung verstärkter Deformation in einem Gebiet beitragen können, das nach den vorliegenden Modellen einer tektonischen Verformung widerstehen sollte, sind: (i) erhöhte tektonische Kräfte durch ein steileres Abtauchen der Platte und (ii) Schwächezonen in der Kruste, die auf prä-andine Deformationsereignisse zurückgehen. Schließlich könnten die thermomechanischen Bedingungen in diesem Teil des Vorlands ein Schlüsselfaktor für die Erhaltung des flachen Subduktionswinkels in diesen Breiten der SZA sein.

Declaration of author contributions

In this cumulative dissertation, Chapters 3, 4, 5 and 6 consist of published or accepted-for-review studies, in which Constanza Rodriguez Piceda is first author. The numbering of figures, table and equations, together with the orthography were adjusted to the style of the thesis. The supplementary materials for this publications are included in the appendixes and the related bibliography is presented at the end of the dissertation.

Chapter 3 is based on ' *Lithospheric density structure of the Southern Central Andes constrained by 3D data-integrative gravity modelling*, International Journal of Earth Sciences, 110, 2333–2359, https://doi.org/10.1007/s00531-020-01962-1, 2021' co-authored by Constanza Rodriguez Piceda, Magdalena Scheck-Wenderoth, Maria Laura Gómez Dacal, Judith Bott, Claudia Prezzi and Manfred Strecker. CRP and MSW designed the study. CRP carried out the gravity-modelling study and prepared the manuscript under the supervision of MSW, MS, MLGD and JB. All co-authors contributed to the reviewing and editing of the paper.

Chapter 4 is based on '*Controls of the lithospheric thermal field of an ocean-continent subduction zone: the southern Central Andes*' submitted to Lithosphere and co-authored by Constanza Rodriguez Piceda, Magdalena Scheck-Wenderoth, Judith Bott, Maria Laura Gómez Dacal, Mauro Cacace, Michael Pons, Claudia Prezzi and Manfred Strecker. CRP, MSW and MC designed the study. CRP carried out the thermal modelling workflow, interpreted the results and prepared the manuscript under the supervision of MSW and MS. JB, MLGD, MC, MP and CP participated in the interpretation of the results. All co-authors contributed to the reviewing and editing of the manuscript.

Chapter 5 is based on '*Long-term lithospheric strength and intraplate seismicity in the southern Central Andes*' submitted to Geophysics, Geochemistry, Geosystems and co-authored by Constanza Rodriguez Piceda, Magdalena Scheck-Wenderoth, Mauro Cacace, Judith Bott and Manfred Strecker. CRP and MSW designed the study. CRP carried out the rheological modelling workflow, processed the seismic catalogue, interpreted the results and prepared the manuscript under the supervision of MSW and MS. MC and JB participated in the interpretation of the results. All co-authors contributed to the reviewing and editing of the manuscript.

Chapter 6 is based on '*The role of mantle hydration and flexure on slab seismicity in the southern Central Andes*' submitted to Nature Communications and co-authored by Constanza Rodriguez Piceda, Yagian Gao, Mauro Cacace, Magdalena Scheck-Wenderoth, Judith Bott, Manfred Strecker and Frederik Tilmann. CRP and MC devised the main conceptual ideas and proof outline of this work. CRP wrote the manuscript with support of all co-authors. YG conducted the seismic tomography imaging. CRP carried out the rheological model and the processing of the seismic catalogues. MSW and MS supervised the study. All the authors contributed to the interpretation of results and the editing of the manuscript.

Table of Contents

List of Figures

List of Tables

List of symbols and abbreviations

Symbol	Property	Unit
α	Thermal expansion coefficient	K^{-1}
α_s	Subduction angle of the oceanic plate	°
σ_D	Peierls critical stress	Pa
$\Delta\sigma_b$	Byerlee's Law strength	Pa
$\Delta\sigma_D$	Dorn's law strength	Pa
$\Delta\sigma_d$	Dislocation creep yield strength	Pa
$\dot{\varepsilon}$	Strain rate	s^{-1}
λ	Bulk thermal conductivity	$W\ m^{-1}\ K^{-1}$
μ	Shear modulus	Pa
μ_f	Internal friction coefficient	-
η_{eff}	Effective viscosity	Pa s
ρ	Density	Kgm^{-3}
ρ_b	Bulk density	kgm^{-3}
ρ_f	Fluid density	kgm^{-3}
ω	Wave frequency	Hz
ϕ	Internal friction angle	°
a	Wave frequency exponent	-
A_D	Dorn's law strain rate	s^{-1}
A_p	Dislocation creep pre-exponential factor	$Pa^{-n}s^{-1}$
C_p	Specific heat capacity	$Jkg^{-1}K^{-1}$
f	Sensitivity factor	Km/% or °C/%
f_f	Byerlee's friction coefficient	-
f_p	Pore fluid factor	-
G	Gravitational acceleration	ms^{-2}
H or Q_p	Activation energy	$Jmol^{-1}$
H_L	Mechanical thickness	m

h_i	Thickness of lithospheric unit	m
h_{ns}	Thickness of the non-subducting section of the oceanic plate	m
IS_C	Crustal integrated strength	Pa
IS_L	Lithospheric integrated strength	Pa
k	Thermal diffusivity	m^2 s^{-1}
K	Compressibility	Pa^{-1}
M_W	Moment magnitude	-
$Mg\#$	Magnesium number	-
n	Frequency exponent	-
P	Pressure	Pa
q	Heat flow	Wm^2
Q	Anelasticity attenuation	-
Q_D	Dorn activation energy	Jmol^{-1}
Q_s	Quality factor of S-wave velocity	-
R	Universal gas constant	JK^{-1}mol^{-1}
S	Radiogenic heat production	Wm^{-3}
t	Age of oceanic plate	t
T	Temperature	°C or K
T_e	Elastic thickness	m
V	Activation volume	m^3
v	Solid velocity	ms^{-1}
v_p	P-wave velocity	ms^{-1}
v_s	S-wave velocity	ms^{-1}
v_p/v_s	P-wave/S-wave ratio	-
X	Rock composition	-
z	Depth below topography	m

Abbreviation	**Explanation**
AFTB	Aconcagua fold-thrust belt
BAF	Low back-arc and foreland areas
BDT	Brittle-ductile transition
bmsl	Below mean sea level
CB	Cuyo basin
CC	Coastal cordillera
CD	Central Depression
CN	Cold nose
Cp	Clinopyroxene
Cpto	clinopyroxenite
EAB	Extra-Andean basins
ESP	Eastern Sierras Pampeanas
FC	Frontal Cordillera
FS	Flat slab domain
GPE	Gravitational potential energy
JFR	Juan Fernandez Ridge
LAB	Lithospheric-asthenospheric boundary
Lherz	lherzolite
LRFTB	La Ramada fold-thrust belt
MFTB	Malargüe fold-thrust-belt
NB	Neuquén basin
OB	Ophiolitic belt
Ol	Olivine
Opx	Orthopyroxene
P	Payenia volcanic province

PrC	Precordillera
SCA	southern Central Andes
Sp	spinel
SS	Steep slab domain
TrB	Triassic basins
TZ	Transition zone domain
VFL	Valle Fértil lineament
Webst	Websterite
WSP	Western Sierras Pampeanas
XFe	Iron content

Chapter 1: Introduction

1.1 Motivation and principal scientific questions

Subduction zones are non-collisional, convergent margins where the largest part of Earth's material is recycled into the lower mantle (Christensen & Hofmann, 1994; Hofmann, 1997). They are main drivers of plate motion, mountain-building processes, and the domains where the most important generation of continental crust occurs (Bebout et al., 2018; Stern, 2002). These processes are the source of seismic, tsunami and volcanic hazards with devastating effects on the population (e.g. Chlieh et al., 2011; Gregori & Christiansen, 2018; Lara et al., 2021). Therefore, a profound understanding of the dynamics of subduction zones and its impact on deformation and crustal genesis is of utter importance.

At subduction margins, the overriding plate can be subjected to either extensional or compressional tectonic regimes (Jarrard, 1986). The Andes, a ~7000-km-long, N-S trending mountain range developed along the western margin of South America, represent the type area for a compressional orogen evolving above a subduction zone (Jordan et al., 1983; Fig. 1.1). Tectonic shortening within this orogen is associated with the westward motion of the continental South-American plate toward the trench of the eastward-subducting oceanic Nazca Plate, which is slowly retreating (Faccenna et al., 2017). However, the orogen displays significant variations of tectonic styles, amount of crustal shortening, and orogenic width along and across the strike of the subduction zone, which cannot be explained solely by the plate-convergence velocity (Cristallini & Ramos, 2000; Giambiagi et al., 2015; Kley & Monaldi, 1998; Lossada et al., 2018; Mescua et al., 2014).

1.1.1 The tectonic segmentation of the Andes

The causative mechanisms behind the segmentation of the Andean orogen has been a matter of long-standing debate (e.g., Barrionuevo et al., 2021; Faccenna et al., 2017; Gutscher, 2018; Ibarra et al., 2019, 2019; Jordan et al., 1983; Kley et al., 1999; Kley & Monaldi, 2002; Liu, 2020; Manea et al., 2012; Martinod et al., 2020; Oncken et al., 2006; Ramos & Folguera, 2009; Sobolev et al., 2006; Sobolev & Babeyko, 2005). End-member models have stressed the importance of slab-related processes, including the angle of subduction of the oceanic plate (i.e., past episodes of flat- or steep-subduction) or different modes of coupling at the subduction interface (Gutscher, 2018; Horton, 2018; Martinod et al., 2020; Ramos & Folguera, 2009; Sobolev & Babeyko, 2005). In other studies it has been argued that deformation in the upper plate is controlled by the characteristics of the overriding plate, including composition, thickness, temperature, climate, and inherited structures from previous deformational phases (Allmendinger et al., 1983; Barrionuevo et al., 2021; Ibarra et al., 2019, 2021; Kley et al., 1999; Kley & Monaldi, 2002; Lamb & Davis, 2003; Liu, 2020; Manea et al., 2012; Pearson et al., 2013; Ramos et al., 2002; Sobolev & Babeyko, 2005). The similarity shared between these hypotheses is that that the localization of deformation is caused by a variation in the strength of the lithosphere (i.e., the amount of stress that the lithosphere is able to withstand without experiencing permanent deformation), which is driven by the complex interaction between the involved plates. Therefore, the study of this interaction and how it conditions the rheological state of the lithosphere is pivotal for the understanding of the segmentation of deformation in the Andean mountain belt at long(geological) timescales, involving millions of years.

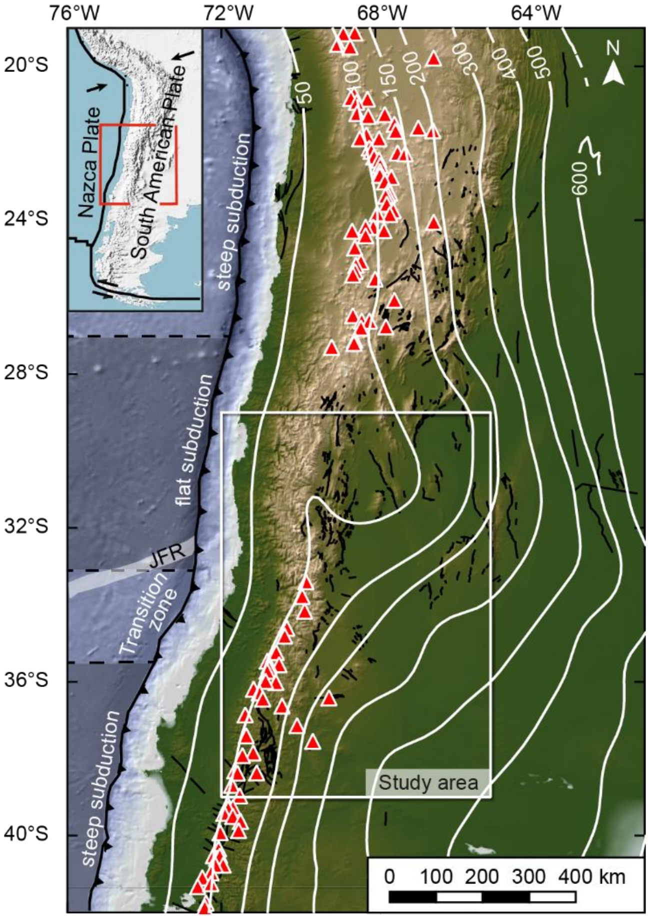

Figure 1. 1: Topography and bathymetry of the Central Andes based on the ETOPO1 global relief model (Amante & Eakins, 2009), showing the extent of the subduction segments with different subduction angles. The boundaries between the subduction segments in the oceanic domain are indicated with black dashed lines. The Juan Fernandez

Ridge (JFR) is marked by a white transparent layer. The depth contours (km below sea level) of the subducting slab from Slab2 (Hayes et al., 2018) are shown as white lines. The white rectangle denotes the extent of the southern Central Andes modelled in this study. Red triangles denote the location of active volcanic edifices. Black lines depict active hazardous faults (Costa et al., 2020)

1.1.2. Strength and deformation in a subduction orogen

There is broad agreement that the existence of strength heterogeneities conditions lithospheric deformation in response to tectonic stresses at long timescales. In this context a mechanically weak lithosphere is prone to greater amounts of shortening under the same stress field in comparison to a mechanically stronger one (Davy & Cobbold, 1991; Karner et al., 2004; McKenzie & Priestley, 2008; Ranalli, 1997; Sloan et al., 2011; Vauchez et al., 1998; Willett et al., 1993). If the lithosphere is thickened enough, the increased gravitational potential energy (GPE) can prevent the crust to keep deforming, inducing a propagation of the deformation front to foreland areas with lower GPE (Mareschal & Jaupart, 2011; Stüwe, 2007). These concepts have been recently revisited for the case of the Andes in the framework of the StRATEGy project (Barrionuevo et al., 2021; Ibarra et al., 2019a, 2021; Liu, 2020; Meeßen, 2019). One part of these studies has focused on the control of the strength of the overriding plate with respect to foreland deformation (Liu, 2020; Meeßen, 2019). For instance, Liu (2020) analysed, by means of geodynamic modelling, the factors that induce the development of a certain structural style in the foreland. These factors include the strength ratio between orogen and foreland, the thickness of sediments, crust and lithosphere, and the GPE of the orogen. The resulting deformation patterns can range from the formation of a thin-skinned fold-and-thrust belt, which involves the deformation of the sedimentary cover (Fig. 1.2a), to a thick-skinned broken-foreland where the crystalline crust is also deformed (Fig. 1.2d; Dahlen, 1990; Davis et al., 1983; Jordan et al., 1983). Between these two end-members, intermediate expressions of foreland-deformation patterns are ‘thick-skinned dominated’ (Fig. 1.2b) and ‘mixed thick- and thin- skinned’ types (Liu (2020; Fig. 1.2c).

In a second line of studies within the StRATEGy project, work has focused on the link between orogenic deformation and long-term strength. By applying geodynamic models, Barrionuevo et al. (2021) explored the implications of lower crustal composition on the onset of different deformation modes (pure-shear vs. simple-shear) in the orogen between 33°S and 36°S. In the pure-shear mode, upper and lower crustal deformation is vertically aligned, contrary to the simple-shear mode, where the locus of upper crustal shortening is horizontally displaced with respect to lower-crustal shortening (Fig. 1.2e-f). These authors suggested that a more felsic lower crust would facilitate pure-shear deformation, while a more mafic and thus stronger crust would induce simple-shear deformation. Additionally, they argued that the depth configuration of the lithosphere-asthenosphere boundary (LAB) affects the vergence of the orogenic wedge. An asymmetric configuration of the LAB (i.e., shallow LAB beneath the orogen contrasting with a deeper LAB beneath the forearc and foreland areas) would promote west-dipping detachments and eastward propagation of faulting, as proposed by recent kinematic models of the SCA (Armijo et al., 2010; Riesner et al., 2018).

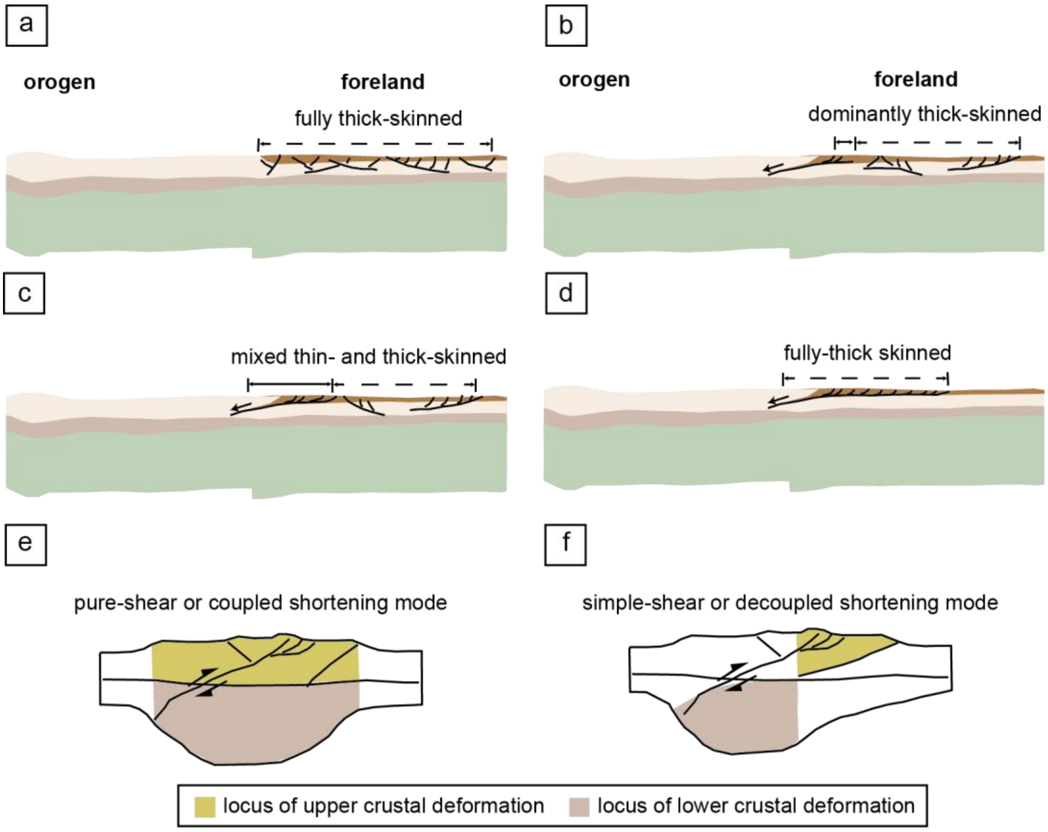

Figure 1.2: Long-term deformation patterns of the Andean orogen and its foreland (modified from Liu, 2020). Foreland deformation styles: (a) fully thick-skinned, (b) dominantly thick-skinned, (c) mixed thin- and thick-skinned, and (d) fully thick-skinned. Orogenic deformation modes: (a) pure-shear or coupled; (b) simple-shear or decoupled.

In addition to playing an essential role at geological timescales, long-term rheology is thought to be equally important for the occurrence of seismogenic processes. For instance, it has been proposed that the depth at which rocks transition from a preferentially brittle to a preferentially ductile mode of deformation in the lithosphere ('brittle-ductile transition' or BDT, Goetze & Evans, 1979) provides a conservative estimate of the down-dip extent of the seismogenic zone (e.g., Scholz, 1988; Sibson, 1982). Moreover, compilations of crustal seismicity in different regions show that cold and/or mafic crustal sectors are characterized by deep-seated seismicity, which supports the notion of a rheological control that is inherited from paleotectonic processes (Anikiev et al., 2020; Craig & Jackson, 2021; Jackson et al., 2008; Maggi et al., 2000; Spooner et al., 2020). However, subsequent reports of seismicity below the BDT, prompted other authors to argue that there is no straightforward relationship with long-term strength and that other causative mechanisms should come into play, including the presence of fluids or grain-size reduction around shear zones (Prieto et al., 2017; Thielmann et al., 2015; Thielmann, 2018).

These disagreements between studies suggest that lithospheric strength is not uniform but site-specific and, thus, each region should be investigated separately. Since rheology depends on temperature and lithology of the rock units (Evans & Kohlstedt, 1995; Ranalli & Murphy, 1987), the assessment of the strength configuration of a certain area also requires first-order descriptions on the composition, thickness, and thermal configuration of the lithosphere. Moreover, these configurations can be compared to the predictions of geodynamic models (Barrionuevo et al., 2021; Liu, 2020) in order to determine the degree to which long-term deformation is controlled by long-term strength in a certain region.

1.1.3. The case of the southern Central Andes

The southern Central Andes (29°S–39°S, Fig. 1.1) represent a suitable natural experimental setup to investigate the thermomechanical state of the lithosphere, the relationship between the subducting and overriding plates, as well as its influence regarding deformational styles for several reasons. The region displays major along-strike variations in terms of topographic elevation, amount of crustal shortening and thickening, orogenic width, foreland deformation style, and seismicity distribution (e.g. Alvarado et al., 2005, 2009; Cristallini & Ramos, 2000; Giambiagi et al., 2015; Kley & Monaldi, 2002; Lossada et al., 2018; Mescua et al., 2014; Ramos & Folguera, 2009). In addition, the oceanic Nazca slab changes its dip angle at 33°S– 35°S from the Chilean-Pampean flat-slab zone (< 5° dip, 27°S–33°S) in the north to a steeper sector south of 35°S (~30° dip).

The causes for the peculiar tectonic setting and the preservation of the flat-subduction scenario in the SCA have been a matter of controversy. The onset of flat subduction at ~19 Ma is supposed to coincide with the southward migration of an aseismic ridge (Juan Fernández Ridge, Fig.1.1). This led some authors to postulate that the flattening of the slab was caused by the positive buoyancy of this plateau-like oceanic domain (Gutscher et al., 2000; Kay & Mpodozis, 2002; Yáñez et al., 2001). This hypothesis, however, was questioned by other authors who argued that the positive buoyancy of the plateau is not sufficient to maintain flat subduction (Espurt et al., 2008; van Hunen et al., 2004). More recently, Schellart & Strak (2021) proposed that, in case of a long-lived subduction scenario, an oceanic plateau could even lead to the steepening of the slab over time. These authors argued that this might be due to the subduction of the bathymetric anomaly, which decreases the rate of subduction and subsequently reduces the suction forces that sustain the subhorizontal dip angle, ultimately leading the slab to steepen. A number of alternative mechanisms regarding the role of plateau subduction was proposed, all involving inhibition of slab roll-back and consequent flattening. These mechanisms comprise either a fast trench-ward motion of the overriding plate (e.g., van Dinther et al., 2010; van Hunen et al., 2000; Wolf & Huismans, 2019) or stagnation of the slab in the mantle-transition zone coupled with an increase of the suction forces in the mantle wedge during episodes of long-lived subduction (Schellart & Strak, 2021). An additional factor that could trigger and/or preserve the sub-horizontal angle of the slab is the presence of a strong overriding plate (Hu et al., 2016; Manea et al., 2012; Rodríguez-González et al., 2012; Schellart & Strak, 2021; Sharples et al., 2014). Therefore, the detailed rheological characterization of the SCA is also essential to discern whether it may potentially influence the subduction angle.

A number of studies have provided different constraints on the compositional, thickness and thermal characteristics of different regions of the SCA. For instance, seismic and gravity data from different sources have been used to characterize the thickness and lithology of the units that compose several subregions of the Pampean flat-slab segment (e.g., from CHARGE, SIEMBRA, ESP seismic experiments; Alvarado et al., 2005, 2009; Álvarez et al., 2012; Ammirati et al., 2015, 2016, 2018; Heit et al., 2008; Ibarra et al., 2019b; Marot et al., 2014; McGlashan et al., 2008; Meeßen et al., 2018; Perarnau et al., 2012; Pérez Luján et al., 2015; Porter et al., 2012). In contrast to the flat-slab region, a small number of investigations to the south of 33°, have concentrated on the thickness of the crystalline crust (Gilbert et al., 2006; Heit et al., 2008). However, research focused on the large-scale compositional heterogeneities in the crust of the steep-slab region are rather scarce (Deshayes, 2008; Marot et al., 2014; Tassara et al., 2006).

With regard to the thermal field, a small number of constraints are derived from borehole temperature measurements and surface heat-flow data (Collo et al., 2018; Hamza & Muñoz, 1996; Uyeda & Watanabe, 1982). Despite these developments, to date there is no study that integrates these local-scale investigations into consistent density, structural, thermal, and rheological models of the SCA lithosphere. Likewise, none of these studies have evaluated the effect of variations in lithology and the subduction angle of the slab in the rheological configuration and with respect to the characteristics of the thermal field. These types of studies have proven useful to better understand the regional variations of deformation in different tectonic settings (e.g. Anikiev et al., 2020; Gholamrezaie et al., 2021; Ibarra et al., 2019b, 2021; Spooner et al., 2020). The main conclusions drawn by these studies show that crustal heterogeneities exert a strong influence on the localization of seismic-scale deformation.

In light of this ongoing discussion, the main goal of this dissertation is to evaluate the present-day lithospheric configuration of the SCA in terms of thickness, composition, temperature, and strength, and relate these characteristics to active deformation patterns. Accordingly, the three specific research questions providing the basis for this study are:

(i) Which are the lithological, structural, and thermo-mechanical characteristics of the lithosphere in the SCA?

(ii) How does the thermomechanical state of the lithosphere vary in response to the crustal heterogeneities of the overriding plate and with respect to the dip angle of the subducting slab?

(iii) How does the long-term thermo-mechanical configuration of the SCA relate to tectonic and seismic deformation patterns?

To answer these principal research questions, I generated a 3D structural and density model of the present-day lithosphere in the SCA by integrating geological and geophysical data, including seismic, seismological, petrological and gravity data. In a following step, I computed the thermal field of the lithosphere and tested the results against thermal observations. Subsequently, I calculated the strength of the lithosphere to discuss the controlling factors of the thermomechanical field. In addition, these results were then compared with seismic catalogues and neotectonic structures to address possible causative relationships between the long-term thermomechanical state of the lithosphere and observed deformation patterns. I furthermore discussed the possible effect of the long-term strength of the overriding plate in the preservation of the flat-subduction setting in the north of the study area. Finally, I investigated the possible mechanisms that may control the localization of seismicity within the subducting plate.

1.2. Structure and workflow of the analysis

This dissertation follows a stepwise procedure, i.e. each model was used as a basis for the development of the models that where built in the subsequent steps. The workflow includes: (i) the construction of a 3D data-driven gravity model describing the density and thickness variations of the main lithospheric units (hereafter: ‘structural model’); (ii) the calculation of the 3D lithospheric thermal field; (iii) the computation of the 3D lithospheric strength configuration; (iv) a qualitative analysis of the state of hydration in the mantle using the ratio between compressional- and shear-wave velocity (v_p/v_s ratio) from previous seismic tomography; and (v) the discussion of the causative mechanisms of tectonic and seismic deformation from the modelled structural and thermomechanical fields. A summary of the first-order structural features and the main tectono-magmatic events of the SCA is provided in **Chapter 2**.

Chapter 3, which has been published in Rodriguez Piceda et al. (2021), describes the procedure of building the structural model. Different data, including seismic, seismological, and petrological data were integrated into this model. Both forward and inverse gravity approaches were applied to further constrain the lithospheric density structure of the investigated region.

Chapter 4 describes the workflow of how to derive the thermal configuration of the SCA. Shear-wave velocities from a seismic tomography experiment were used to derive the temperatures in the mantle below 50 km depth. In the uppermost lithosphere (< 50 km depth), the structural model of Chapter 3 formed the base to compute the conductive thermal field using a Finite Element Method under the assumption of steady-state conditions. In an attempt to quantify the validity of this last assumption in the SCA, a simulation that accounts for the additional effects of advection of cold temperatures due to the motion of the subducting slab on the present-day thermal field was carried out. Moreover, the modelling results were calibrated making use of borehole-temperature data and surface heat-flow measurements.

In **Chapter 5**, I used the structural and thermal configurations from chapters 3 and 4, respectively, together with the parametrization of mechanical properties, to compute the yield strength and effective viscosity of the lithosphere. These results were then compared to a compiled catalogue of seismicity, with the aim to derive causative relationships between the strength heterogeneities and the spatial distribution of seismic deformation.

In **Chapter 6**, I evaluated the possible controlling mechanisms of seismicity within the Nazca slab, including fluid-mediated processes (i.e. dehydration reactions of hydrous minerals and compaction of sediments). To gain information on the variations of fluid-content in the slab and the ambient mantle, I used the v_p/v_s ratio from seismic tomography. In this context, regions of high v_p/v_s ratios are interpreted as areas of hydrated mantle and/or zones of partial melting, where seismicity is likely to occur due to compaction effects and dehydration reactions. In regions with dry mantle and seismicity, I analyzed the effect of flexural stresses within the slab with respect to the occurrence of seismicity.

Chapter 7 discusses how the results from the previous chapters contribute to answering the principal research questions posed at the start of this thesis and that guide me in this study. Overall, this chapter aims at providing a comprehensive analysis of the role of the structural and thermomechanical fields of the lithosphere together with slab-dip geometry on the expression of active deformation processes, including seismicity distribution and tectonic patterns. Furthermore, I provide an outlook for future work in this area.

Finally, **Chapter 8** summarizes the most important results of this dissertation.

Chapter 2: Geological setting

In a west- to east-oriented transect the southern Central Andes (SCA) comprise the forearc, the magmatic arc, the back-arc, and the foreland. Each of these domains can be subdivided into different morphotectonic provinces based on their Mesozoic-Cenozoic tectonic evolution (Fig. 2.1, Forsythe, 1982; Hervé et al., 1988; Jordan et al., 1983; Mpodozis & Ramos, 1990):

(i) The **forearc** comprises the Coastal Cordillera and the Central Depression;

(ii) The **magmatic arc** is represented by the western part of the Principal Cordillera;

(iii) The **back-arc**, includes the fold-and-thrust belts of Eastern Principal Cordillera, the thick-skinned structures of the Frontal Cordillera, and the Payenia volcanic province. A number of these morphotectonic provinces exhibits a mixed style of deformation. For instance, the Principal Cordillera includes fully thick-, fully thin-, and mixed thick- and thin-skinned structures that have been identified in the Malargüe, Aconcagua, and La Ramada fold-and thrust belts, respectively. Conversely, the Precordillera is characterized by a fully thick- skinned structure in the northern and central parts that transitions into a fully thick-skinned structure south of 32°S and east of 68.5°W;

(iv) The **foreland** comprises the thick-skinned structures of the Sierras Pampeanas basement uplifts, the San Rafael Block, and a series of foreland basins, the largest of which are the Cuyo and the Neuquén basins.

2.1. Paleozoic and Mesozoic evolution

The early tectonic history of the SCA during the Neoproterozoic and Paleozoic is characterized by a series of shortening events mostly related to the amalgamation of terranes to the proto-margin of Gondwana (e.g., Astini et al., 1995; Escayola et al., 2011; Ramos et al., 1986; Ramos et al., 2010; Rapalini, 2005). Four major pre-Andean orogenic events have been recognized: (1) the late Neoproterozoic to early Cambrian Pampean orogeny; (2) the early Ordovician Famatinian orogeny; (3) the middle-late Ordovician Ocloyic orogeny; (4) the late Devonian-early Carboniferous Chanic orogeny, and (4) the early Permian San Rafael orogeny (Astini & Dávila, 2004; Bahlburg & Hervé, 1997; Casquet et al., 2018; Charrier et al., 2015; Heredia et al., 2018; Ramos et al., 1986; Ramos, 2018; Schwartz et al., 2008).

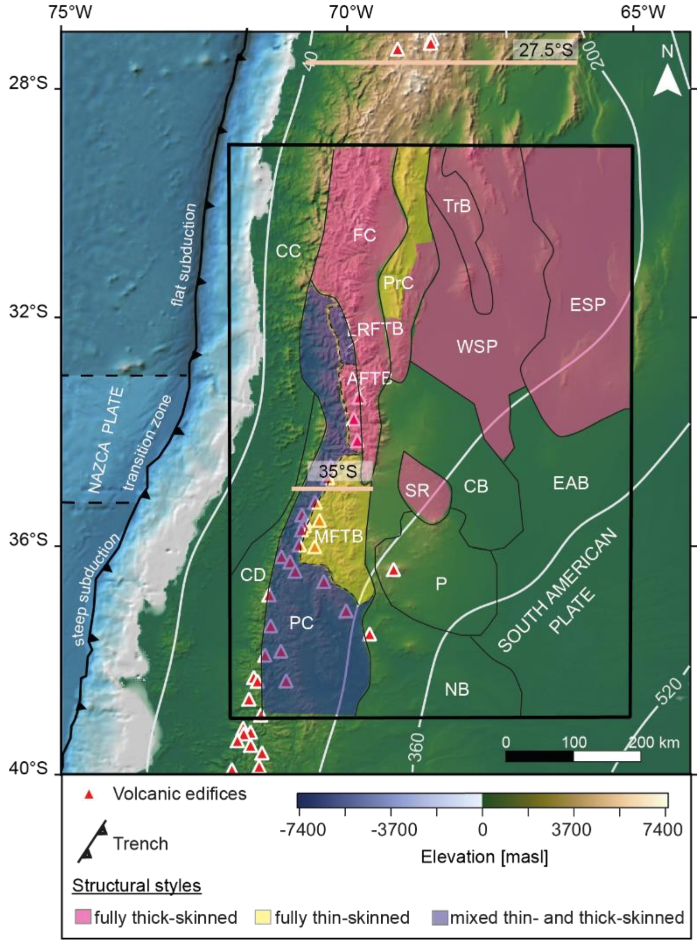

Figure 2.1: Topographic elevation and bathymetric depths of the study area extracted from the ETOPO 1 global relief model (Amante & Eakins, 2009), showing the main morphotectonic provinces of the southern Central Andes, color-coding corresponding to structural style: CB: Cuyo basin, CC: Coastal Cordillera, CD: Central Depression, EAB: Extra-Andean basins, ESP: Eastern Sierras Pampeanas, NB: Neuquén basin; P: Payenia, PC: Principal Cordillera (LRFTB= La Ramada fold-thrust belt, AFTB: Aconcagua fold-thrust belt, MFTB: Malargüe fold-thust-belt), FC: Frontal Cordillera, PrC: Precordillera, TrB: Triassic basins, WSP: Western Sierras Pampeanas. The dashed black lines in the oceanic part denote the boundaries between the subduction segments. The white lines depict the depth contours of the top of the slab from the Slab2 subduction-zone geometry model (Hayes et al., 2018). The pink lines mark the location of the profiles in Figure 2.2.

Geological records of the Pampean orogeny (Aceñolaza & Toselli, 1976) were reported in the Sierras Pampeanas (e.g., Rapela et al., 1998). Numerous hypotheses have been proposed to explain the origin of this deformation event, yet the most widely accepted model involves the collision of three terranes: the Arequipa, Pampia and Antofalla terranes (Escayola et al., 2011; Ramos, 2008, 2010). Subsequently, the Famatinian orogenic cycle (Aceñolaza & Toselli, 1976) affected mainly the area commonly referred to as the Western Sierras Pampeanas; this part of the orogen has been related to the formation of a magmatic arc at the western margin of Gondwana (Ramos et al., 2010). The Ocloyic orogeny (e.g., Astini, 2003)) was associated with the collision of the Cuyania exotic terrane (Ramos, 2010), and evidence of this orogeny can be found in the western Sierras Pampeanas (Astini & Dávila, 2004). In the late Devonian-early

Carboniferous, the collision of the Chilenia exotic terrane is thought to have been responsible for the Chanic deformation event (Ramos et al., 1986). Rock assemblages attesting to this orogeny are known from the Frontal Cordillera and the southern part of the Precordillera (Giambiagi et al., 2011; 2014). Finally, the San Rafael orogeny (Azcuy & Caminos, 1987) represents the last Palaeozoic compressional event, which is related to renewed subduction under the Gondwanan margin, which resulted in the uplift of the San Rafael Block (Bahlburg & Hervé, 1997).

In contrast to the contractional episodes which characterized the SCA during the Paleozoic, the Mesozoic was dominated by extensional tectonism, which has been linked to the break-up of Gondwana (e.g., Charrier, 1979; Legarreta & Gulisano, 1989; Legarreta & Uliana, 1999). In the late Permian-early Triassic, the acidic magmatic rocks of the Choiyoi Group were formed during this extensional regime (e.g., Kleiman & Japas, 2009; López-Gamundí, 2006; Sato et al., 2015). The extension continued during the late Triassic and early Jurassic, leading to the formation of Cuyo and Neuquén rift basins (Legarreta & Gulisano, 1989; Uliana et al., 1989). Rift-related sedimentation in both basins lasted until the early Cretaceous, with continental provenance in the Cuyo Basin and both marine and continental sources in the Neuquén Basin (Ávila et al., 2006; Barredo, 2012; Howell et al., 2005; Vergani et al., 1995). Subsequently, these depocentres developed into foreland basins during the Andean orogeny (e.g., Fuentes & Horton, 2020; Howell et al., 2005; Vergani et al., 1995).

2.2. Andean evolution

The subduction of the Nazca plate under the South-American plate has been active since at least the Jurassic (Maloney et al., 2013; for a review see Horton, 2018; Ramos, 2018; Ramos & Kay, 2006). However, the first episode of Andean compressional deformation is thought to have occurred in the late Cretaceous to Paleocene (Fennell et al., 2015; Martínez et al., 2016). This phase is related to the partial basin inversion of the Coastal and Frontal Cordilleras, the Central Depression, and the Neuquén Basin, and it is documented by magmatic intrusions, synorogenic volcano-sedimentary deposits and angular disconformities between the early Cenozoic geological units found in the Principal and Frontal cordilleras (Horton, 2018a; Martínez et al., 2016, 2018). The late Oligocene-early Miocene was characterized by extension and crustal thinning, leading to the formation of intra-arc basins in the Principal Cordillera (e.g., Charrier et al., 2015; Jordan et al., 2001; Winocur et al., 2015). Subsequently, shortening resumed in the late Oligocene (~22 Ma; Charrier et al., 2015; Godoy et al., 1999), which is evidenced by the syntectonic sediments in the Principal and Frontal cordilleras and in the foreland (Fock, 2005; Giambiagi et al., 2001; Riesner et al., 2018). In the early Miocene, the compressional regime continued with the deformation of the Frontal Cordillera (Martínez et al., 2017; Winocur et al., 2015), the western part of the Precordillera (Allmendinger et al., 1990; Jordan et al., 1983), and the eastern part of Principal Cordillera (Giambiagi et al., 2001, 2003; Giambiagi et al., 2015; Giambiagi & Ramos, 2002). The middle-late Miocene (15–9 Ma) represents the major compressional event in the Precordillera (Allmendinger & Judge, 2014; Jordan et al., 2001) and the Principal Cordillera (Giambiagi et al., 2001, 2003; 2015; Giambiagi & Ramos, 2002). Additionally, further uplift of the Frontal Cordillera occurred (Giambiagi et al., 2003; Irigoyen et al., 2000). Subsequently, deformation migrated to the east. Between 28°S and 32°S, this deformation front affected the eastern part of the Precordillera and the Sierras Pampeanas since 10–5 Ma (Jordan et al., 1983; Strecker et al., 1989). Between 32°S and 36°S, shortening occurred in the eastern Frontal Cordillera and in the western part of the Cuyo Basin at ~4 Ma (Giambiagi et al., 2003; Irigoyen et al., 2000).

In summary, the Cenozoic Andean tectonic cycle is dominated by compressional phases, where the main deformation front migrated from west to east and from north to south. This is documented by the evolution of the shortening rate in the different morphotectonic provinces between 45 Ma and 0 Ma (Fig. 2.2, Giambiagi, *pers. comm.*, 2021; Kley & Monaldi, 1998). In addition, there is a decrease of shortening, from the flat- to the steep-slab segment (Fig 2.2).

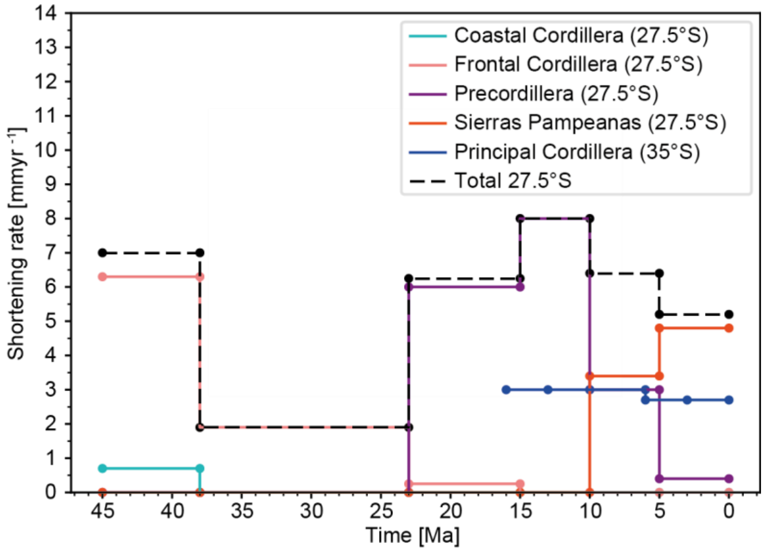

Figure 2. 2: Shortening-rate evolution for the different main morphotectonic provinces at two exemplary cross sections of the flat (27.5°S) and steep (35°S) subduction segments (Giambiagi, *pers. comm., 2021*). Locations of the profiles are shown in Figure 2.1.

2.3. Magmatic-arc evolution

The magmatic regime related to the subduction zone in the SCA alternated between periods of activity and periods of relative quiescence, driven by changes in the geodynamic conditions through time (e.g., Hildreth & Moorbath, 1988; Iannelli et al., 2020; Jones et al., 2016; Litvak et al., 2018; Oliveros et al., 2018; Ramos et al., 2014; Ramos & Kay, 2006; Scheuber et al., 1994). Early magmatism occurred in the western Sierras Pampeanas associated to the instauration of a continental arc during the Ordovician Famatinian orogeny (Bahlburg et al., 2009). A gap in magmatic activity occurred during the Devonian (Bahlburg et al., 2009; Bahlburg & Hervé, 1997). From the late Palaeozoic until the late Cretaceous, the subduction margin was subjected to extension, leading to the formation of the Chilean Coastal Batholith (Hervé et al., 1988; Parada et al., 1999) and related volcanoclastic deposits in the Coastal Cordillera (Oliveros et al., 2010, 2018). In the early Miocene-Pliocene, the magmatic arc was located on the western slope of the present-day Principal Cordillera, and migrated subsequently to its current location along the border between Argentina and Chile (Fig.1.1; e.g. Jones, 2014; Kay et al., 2005; Stern & Skewes, 1995). Retro-arc volcanic activity also developed in the early Pleistocene and continued until the present day in the Payenia volcanic province, presumably as a consequence of a slab-steepening episode (Kay et al., 2006a-b; Kay & Copeland, 2006; Ramos & Folguera, 2009). A gap in the magmatic activity since the Miocene has existed above the flat-slab segment between 27°S and 33°S (Jones et al., 2016; Kay & Mpodozis, 2002; Poma et al., 2017; Ramos et al., 2002).

In the flat subduction segment, late Oligocene-early Miocene extension was characterized by volcanism with basaltic to andesitic composition (Kay & Mpodozis, 2002; Litvak et al., 2007). In the early Miocene (~18 Ma), the magmatic arc migrated to the east into the Precordillera and Sierras Pampeanas and is interpreted to have been related to the incipient shallowing of the oceanic slab (Kay, 1991; Kay & Mpodozis, 2002). Magmatic activity ceased at 8–5 Ma in the Principal Cordillera and at 2–5 Ma in the Precordillera and Sierras Pampeanas, indicating that the flattening of the slab had been fully achieved by then (Jones et al., 2016; Ramos et al., 2002).

Chapter 3: Lithospheric density structure of the southern Central Andes constrained by 3D data-integrative gravity modelling

3.1 Abstract

The southern Central Andes (SCA) (between 27°S and 40°S) are bordered to the west by the convergent margin between the continental South American Plate and the oceanic Nazca Plate. The subduction angle along this margin is variable, as is the deformation of the upper plate. Between 33°S and 35°S, the subduction angle of the Nazca plate increases from sub-horizontal (<5°) in the north to relatively steep (~30°) in the south. The SCA contain inherited lithological and structural heterogeneities within the crust that have been reactivated and overprinted since the onset of subduction and associated Cenozoic deformation within the Andean orogen. The distribution of the deformation within the SCA has often been attributed to the variations in the subduction angle and the reactivation of these inherited heterogeneities. However, the possible influence that the thickness and composition of the continental crust have had on both short-term and long-term deformation of the SCA is yet to be thoroughly investigated. For our investigations we have derived density distributions and thicknesses for various layers that make up the lithosphere and evaluated their relationships with tectonic events that occurred over the history of the Andean orogeny and, in particular, investigated the short and long term nature of the present-day deformation processes. We established a 3D model of lithosphere beneath the orogen and its foreland (29°S–39°S) that is consistent with currently available geological and geophysical data, including the gravity data. The modelled crustal configuration and density distribution reveal spatial relationships with different tectonic domains: the crystalline crust in the orogen (the magmatic arc and the main orogenic wedge) is thicker (~55 km) and less dense (~2900 kgm^{-3}) than in the forearc (~35 km, ~2975 kgm^{-3}) and foreland (~30 km, ~3000 kgm^{-3}). Crustal thickening in the orogen probably occurred as a result of stacking of low-density domains, while density and thickness variations beneath the forearc and foreland most likely reflect differences in the tectonic evolution of each area following crustal accretion. No clear spatial relationship exists between the density distribution within the lithosphere and previously-proposed boundaries of crustal terranes accreted during the early Paleozoic. Areas with ongoing deformation show a spatial correlation with those areas that have the highest topographic gradients and where there are abrupt changes in the average crustal-density contrast. This suggests that the short-term deformation within the interior of the Andean orogen

and its foreland is fundamentally influenced by the crustal composition and the relative thickness of different crustal layers. A thicker, denser and potentially stronger lithosphere beneath the northern part of the SCA foreland is interpreted to have favoured a strong coupling between the Nazca and South American plates, facilitating the development of a sub-horizontal slab.

3.2 Introduction

The southern Central Andes (SCA) between approximately 27°S and 40°S formed as a result of subduction of the oceanic Nazca Plate beneath the continental South American Plate. This area is an ideal natural laboratory in which to study orogenic processes since it is the type area for orogeny on a non-collisional, oceanic-continental convergent margin. One remarkable feature of the region is the along-strike variation in the subduction angle of the oceanic plate, which changes between 33°S and 34.5°S from sub-horizontal (<5°) in the north to relatively steep (~30°) in the south (Fig. 3.1a; e.g. Cahill & Isacks, 1992). The Andean orogen has a slightly curved shape that is convex towards the east, with major structures having a general N-S trend to the north of 33°S and a NNE-SSW trend to the south (Arriagada et al., 2013). This distinct change in structural trend is known as the Maipo Orocline (Farías et al., 2008).

The continental crust of the Andean orogen (i.e. the magmatic arc and the main orogenic wedge) has been affected by both thick- and thin-skinned styles of deformation (Jordan et al., 1983). There are also systematic reductions from north to south in the amounts of crustal shortening and thickening, the topographic elevation, and the orogenic width (Cristallini & Ramos, 2000; Giambiagi et al., 2015; Kley & Monaldi, 1998; Lossada et al., 2018; Mescua et al., 2016). This configuration is the result of a multi-stage, tectono-magmatic evolution that has included both contractional and extensional cycles, lasting from the Neoproterozoic to the present day. While the crustal structure at shallow depths is relatively well documented, a number of unknowns remain regarding the characteristics and configuration of the deep crust and lithospheric mantle. Furthermore, the extent to which inherited variations in the composition and geometry of different layers in the upper plate may have influenced the location and style of the deformation remains poorly understood.

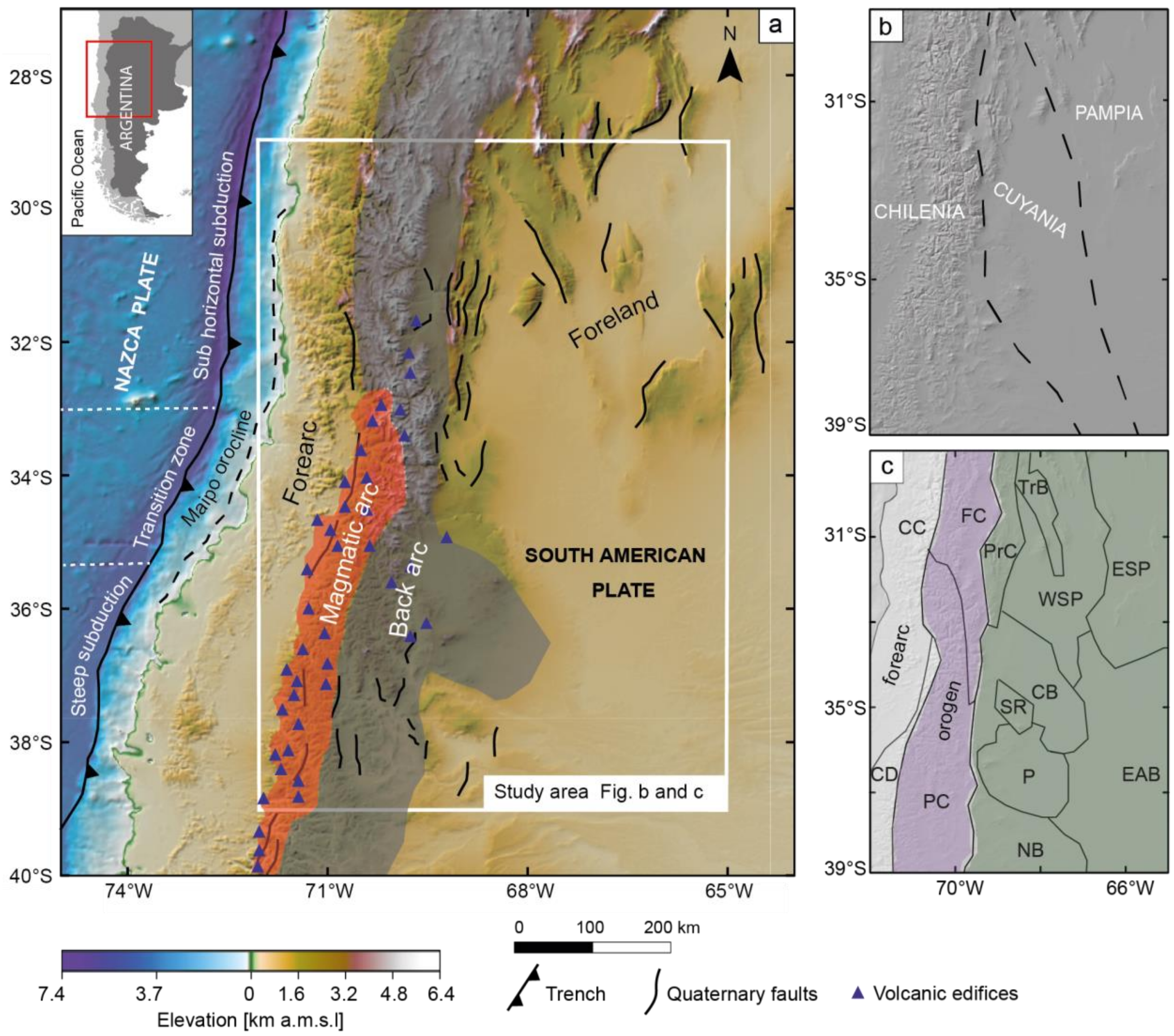

Figure 3.1: (a) Topographic elevation and bathymetric depths of the study area extracted from the ETOPO 1 global relief model (Amante & Eakins, 2009), showing three subduction segments with increasing subduction angles from north to south. The extent of the forearc, the magmatic arc (red-shaded), the back-arc (grey-shaded) and the foreland are also depicted. The white rectangle shows the extent of the study area. The model covers a region measuring 700 km x 1000 km. Thick black lines indicate the main Quaternary tectonic faults (Sagripanti et al., 2017). The dashed black line shows the extent of the Maipo Orocline. On the right hand are shaded relief of the study area overlain with: (b) proposed sutures between terranes accreted to Gondwana during the Palaeozoic, modified from Ramos et al. (2010), and (c) morphotectonic domains with constituting morphotectonic provinces considered in this study: (i) forearc as white shaded area (CC: Coastal Cordillera; CD: Central Depression), (ii) orogen as purple shaded area (PC: Principal Cordillera, FC: Frontal Cordillera) and (iii) low-elevation back-arc and foreland regions as green shaded area (CB: Cuyo basin;; EAB: Extra-Andean basins; ESP: Eastern Sierras Pampeanas;; NB: Neuquén basin; P: Payenia; PrC: Precordillera; TrB: Triassic basins; WSP: Western Sierras Pampeanas)

Seismic data from a number of different sources have been used to constrain the first-order discontinuities and seismic properties of the South American lithosphere, focusing primarily on the sub-horizontal slab region (e.g. from CHARGE, SIEMBRA, ESP seismic experiments; Alvarado et al., 2005; Ammirati et al., 2013, 2018). These investigations were mainly used to generate data with which to construct 2D cross sections or establish 3D models of sub-regions of the SCA. Their results have placed the Moho at an average depth of ~70 km below mean sea level (bmsl) in the orogen and at depths ranging between 35 and 55 km bmsl in the foreland, with the depth decreasing eastwards (Alvarado et al., 2005, 2009; Ammirati et al., 2015, 2016, 2018; Heit et al., 2008; McGlashan et al., 2008; Perarnau et al., 2012; Pérez Luján et al., 2015; Porter et al., 2012). West to east variations in the velocities of P and S waves have also been identified in the sub-horizontal slab region, with a relatively low-velocity zone beneath the orogen (between 69°W and 70°W) and the easternmost part of the foreland (between 65°W and 67°W), and a high-velocity zone in the back-arc and the westernmost part of the foreland (i.e. between ~67°W and 69°W; e.g. Ammirati et al., 2015, 2016, 2018; Marot et al., 2014; Ward et al., 2013). Most of these researchers have interpreted each of these velocity zones to reflect crustal terranes with different compositions that were accreted to the Gondwana margin during the early Paleozoic (e.g. Ramos et al., 2010). The most widely accepted of the various paleogeographic reconstructions addressing the nature of these terranes has been the Pampia-Cuyania-Chilenia model, which is based largely on surface and near-surface geological observations (e.g. Ramos et al., 1986; Ramos, 2010; Ramos et al., 2010). This model indicates the existence of two major terrane boundaries within the area that are thought to have had a direct impact on its tectonic evolution during the Cenozoic and consequently on its present-day characteristics (Fig. 3.1b).

In contrast to the sub-horizontal slab region, a small number of geophysical investigations to the south of 33°S have focused on the thickness of the crystalline crust (Gilbert et al., 2006; Heit et al., 2008). The results of these investigations suggest an eastward reduction in the Moho depth, from 50 km bmsl in the orogen to 40 km bmsl in the foreland. With regard to the crustal composition, possible large-scale lithological heterogeneities in the steep-slab region have yet to be investigated. Such investigations could furnish information on the extent of the crustal terranes that have been inferred to make up the overriding plate (e.g. Ramos et al., 2010). If these terranes do indeed exist and no significant overprint of their petrological compositions occurred subsequent to their accretion, compositional variations similar to those inferred for the sub-horizontal slab region leading also to variations in seismic velocity and density would also be expected. In view of these complexities and the remaining open questions, the generation of a 3D, lithospheric scale, data-integrative and gravity constrained structural model of the SCA was considered likely to provide further insights into the deep lithospheric configuration beneath the Andean orogen. Models addressing this issue and aiming to decipher relevant lithospheric characteristics have been established for regions further north within the Central Andes (e.g. Ibarra et al., 2019; Meeßen et al., 2018; Prezzi et al., 2009), and for the oceanic

Nazca Plate (Tassara, 2006; Tassara & Echaurren, 2012). Despite these developments, a major gap remains in our understanding of the SCA.

We have therefore generated a 3D model of the lithosphere beneath the SCA and their foreland (29°S-39°S and 65°-72°W, Fig. 3.1a) by integrating geological and geophysical observations. This model describes the density and thickness variation of the main lithospheric layers. The modelled densities were derived from lithologic data and seismic velocities (e.g. Mescua et al., 2016; Schaeffer & Lebedev, 2013). The main crustal interfaces (the Moho, top of the crystalline crust, and the base of the oceanic Nazca plate) are mostly based on gravity-independent data interpreted during earlier studies (e.g. Assumpção et al., 2013; Heine, 2007). To further constrain the intracrustal structure, however, we relied on gravity forward and inversion techniques. We also assessed the sensitivity of the derived intracrustal structure to different density configurations in specific lithospheric units.

We discuss below the resulting thickness and density configurations for the crystalline crust in terms of their relationships with the spatial configuration of proposed tectonic domains and with respect to published models of accreted crustal terranes (Ramos et al., 2010). In our analysis, we first attempt to assess the extent to which the main discontinuities and compositional variations within the lithosphere relate to the tectonic events that have occurred in the region throughout its orogenic history. We also discuss the influence that the upper-plate lithospheric structure has on the localization of short-term surface deformation, and on the subduction angle of the Nazca Plate.

3.3. Geologic setting

From west to east, the SCA comprise the forearc, the magmatic arc, the back-arc and the foreland. Each of these morphotectonic provinces can be subdivided into different areas according to their Mesozoic-Cenozoic tectonic evolution (Fig. 3.1a; Jordan et al., 1983; Mpodozis & Ramos, 1990). The forearc includes the Coastal Cordillera and the Central Depression; the magmatic arc is represented by the Eastern Principal Cordillera; the back-arc comprises the N-S oriented fold and-thrust belts of Western Principal Cordillera, the thick-skinned structure of Frontal Cordillera, and the Payenia volcanic province; the foreland includes the Precordillera; the Sierras Pampeanas basement uplifts, the San Rafael block and the Cuyo and Neuquén basins (Fig. 3.1c). In this study, the magmatic arc and the main orogenic wedge (Principal Cordillera and Frontal Cordillera) are referred as 'Andean orogen' (Fig. 3.1c).

The present-day configuration of the SCA results from a number of tectonic events that have occurred from the Neoproterozoic to the present day. Early stages in the tectonic evolution of the study area (Fig. 3.1) involved tectonic shortening and the accretion of crustal terranes to the proto-margin of Gondwana (e.g. Astini et al., 1995; Escayola et al., 2011; Ramos et al., 1986; Ramos et al., 1996, 2010; Rapalini, 2005) During the late Neoproterozoic to early Cambrian, the Pampean orogeny affected the eastern part of the study area between 27°S and 33°S, the area that is now known as the Sierras Pampeanas (e.g. Rapela et al., 1998). A further four subsequent major orogenies have been identified during the Paleozoic, these being (1) the early Ordovician Famatinian orogeny, (2) the middle-late Ordovician Ocloyic orogeny, (3) the late Devonian-early Carboniferous Chanic orogeny, and (4) the early Permian San Rafael orogeny (for reviews of these orogenies see Heredia et al., 2018; Ramos, 2018; Rapela et al., 1998). The Famatinian orogeny resulted in the establishment of a magmatic arc along the western margin of Gondwana, vestiges of which still exist today in the central-western part of the Sierras Pampeanas (Ramos et al., 2010). The Ocloyic and Chanic orogenies have traditionally been associated with the accretion of the Cuyania and Chilenia exotic terranes, respectively (for reviews of these orogenies see Giambiagi et al., 2015; Ramos et al., 2010). The San Rafael orogeny has been interpreted as representing a renewed onset of the subduction processes that generated a broad orogenic belt and crustal thickening along the western margin of the study area (e.g. Azcuy & Caminos, 1987; Japas & Kleiman, 2004; Llambias & Sato, 1990).

In contrast to the compressional mountain building associated with these orogenies, the late Permian to early Jurassic was characterized by horizontal crustal extension associated with the break-up of Gondwana (e.g. Llambias et al., 1993). The Choiyoi volcanics were active during this time along most of South America's western margin, continuing until the early Triassic (e.g. Ramos & Kay, 1991). This magmatic episode was characterized by rhyolitic lavas and ignimbrites and volcaniclastic deposits (e.g. Kleiman & Japas, 2009; López-Gamundí, 2006; Spalletti & Limarino, 2017). Regional horizontal crustal extension led to the formation of the Cuyo basin and other coeval basins during the Early to middle Triassic, followed by the tectonic subsidence of the Neuquén Basin between Late Triassic and Early Jurassic (e.g. Uliana et al., 1989).

Subduction has been active along the Chile margin since at least the Jurassic, continuing to the present (Maloney et al., 2013 and references therein), while deformation and uplift of the

SCA has been recorded since the Late Cretaceous (Boyce et al., 2020; Fennell et al., 2018). A major contractional phase occurred from the Miocene through the Quaternary (e.g. Giambiagi et al., 2003; Giambiagi & Ramos, 2002; Horton, 2018; Jordan et al., 1997; Sagripanti et al., 2017). From the Early Miocene to the Pliocene the deformation migrated eastwards, forming the broken foreland of the Sierras Pampeanas (Jordan & Allmendinger, 1986; Ramos et al., 2002; Sobel & Strecker, 2003). The areal extent of this ongoing deformation episode coincides spatially with the sub-horizontal subduction segment of the Nazca Plate (Jordan et al., 1983), although such broken-foreland tectonism has also occurred in the thin-skinned sub-Andean foreland fold-and-thrust belt of the Santa Bárbara System (23°30’S–26°S, e.g. Mon & Salfity, 1995). The Santa Bárbara system is still tectonically active and records the ongoing compressional inversion of Cretaceous normal faults (e.g. Arnous et al., 2020; Kley & Monaldi, 1998; Mon & Salfity, 1995). Finally, during the Late Miocene-Pliocene, the San Rafael block (e.g. Folguera & Zárate, 2009; Japas & Kleiman, 2004) and the Coastal Cordillera (Encinas et al., 2006) were subjected to horizontal crustal shortening.

Magmatic activity during the Mio-Pliocene between latitudes 33°S and 35°S was concentrated along the western slopes of the Principal Cordillera, but subsequently migrated to its current location along the border between Argentina and Chile (Fig. 3.1a, Stern & Skewes, 1995). However, subsequent volcanism (Pliocene to Quaternary) also occurred in the present-day magmatic arc of the Principal Cordillera and in the retro-arc area of the Payenia volcanic province (Folguera et al., 2009; Llambías et al., 2010; Stern, 2004), while the area between 27°S and 33°S has remained devoid of volcanic activity (Kay et al., 2006a).

3.4 Methods

The workflow in this study involved two main steps: (1) data integration to set up an initial structural and density model (Section 3.4.1), and (2) gravity modelling that combined forward and inversion techniques (Section 3.4.2). We first integrated geological and geophysical observations in order to derive the initial geometry and densities of the main lithospheric units of the SCA and their foreland. The interfaces between the modelled lithospheric units intend to represent abrupt variations in density in the lithosphere, delimiting bodies with homogenous physical properties. To further constrain our model we tested the effect of its geometrical configuration on the gravity field. The differences between observed and predicted gravity fields reflect variations in the density or thickness that were ignored in the initial model. Since the density of the crystalline crust was considered to be homogeneous in the initial model despite indications of local variations in the physical properties (density, seismic velocity), we assumed that any major differences between observed and predicted gravity fields were indicative of density heterogeneities within the crystalline crust and therefore used them to obtain the horizontal density variations within this layer. For this purpose, the crust was split into two horizontal layers of different densities and the variations in the depth of the discontinuity between the two layers computed.

3.4.1 Set up of the initial model

The initial lithospheric model considered four major density interfaces: the ground-air/ground-water interfaces based on topography/bathymetry, the top of the crystalline crust (i.e. the base of the sediments), the Moho, and the base of the oceanic plate. To establish these interfaces we compiled different datasets and interpolated them to a regular grid with a 25 km resolution, using the convergent interpolation algorithm of the Petrel software (Schlumberger, 2011). The model covered an area measuring 700 km x 1100 km (white rectangle in Fig. 3.1), extending to a depth of 200 km.

Figure 3.2 shows the spatial distribution of the input data used to establish the initial 3D model, while Table 3.1 provides information on resolution and source. We used the ETOPO1 global relief model (Amante & Eakins, 2009) for the topography and bathymetry. The sub-surface structures were defined by integrating information from a number of seismically constrained models, including the South American crustal thickness from the model by Assumpção et al. (2013), the sediment thickness from the CRUST1 crustal model (Laske et al., 2013), and the Slab2 subduction zone geometry model (Hayes et al., 2018). We also included data from seismic reflection and refraction profiles across the Chilean margin (Araneda et al., 2003; Contreras-Reyes et al., 2008, 2014, 2015; Flueh et al., 1998; von Huene et al., 1997; Krawczyk et al., 2006; Moscoso et al., 2011; Sick et al., 2006), sediment-isopach maps from the ICONS intracontinental basin database (6 arc minute resolution, Heine, 2007), and two oceanic sediment compilations: one along the axis of the southern part of the trench (0.05 degree resolution; Völker et al., 2013) and the other on a global-scale with 0.5 degree resolution (GlobSed, Straume et al., 2019).

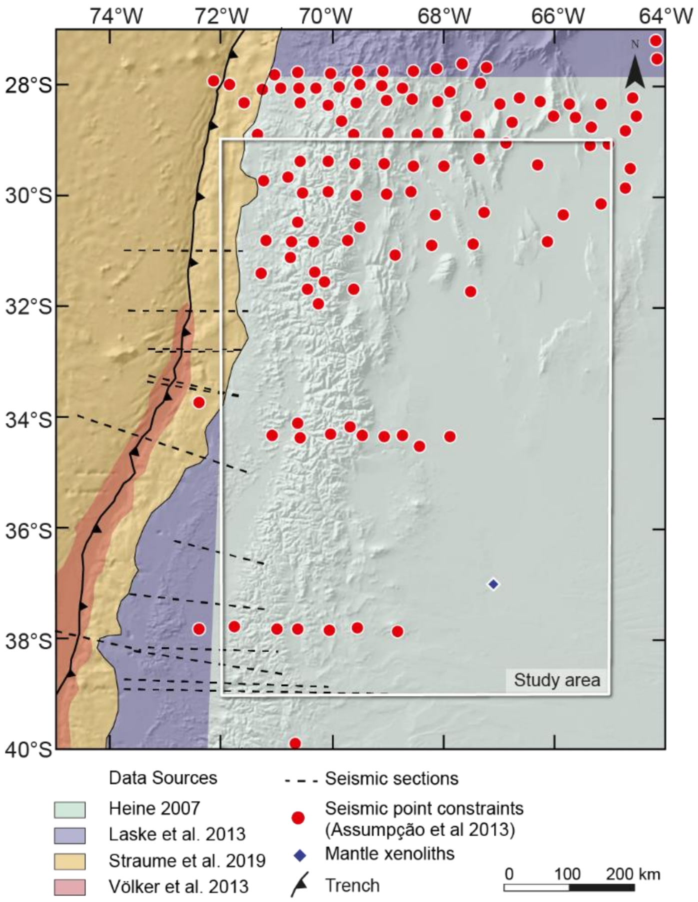

Figure 3.2: Distribution of input data. Sediment thickness derived from: the ICONS intracontinental basin database (Heine, 2007); the CRUST1seismically-constrained global model (Laske et al., 2013); the GlobSed global oceanic sediment thickness model (Straume et al., 2019) and a seismically-constrained model of the sediment thickness along the southern part of the trench axis by Völker et al. (2013). Black dashed lines indicate the location of 2D sections from seismic experiments used to constrain the top of the oceanic crystalline crust, the depth of the continental Moho and the subduction interface close to the trench (Araneda et al., 2003; Contreras-Reyes et al., 2008, 2014, 2015; Flueh et al., 1998; von Huene et al., 1997; Krawczyk et al., 2006; Moscoso et al., 2011; Sick et al., 2006). Red circles indicate the data point constraints selected from seismic profiles that were used in the crustal thickness model of Assumpção et al. (2013) which was utilized to derive the depth of the continental Moho. The blue diamond shows the sample location for the mantle xenoliths (Conceição et al., 2005; Jalowitzki et al., 2010). The black rectangle shows the extent of the study area. The thin black line indicates the South-American coastline

The uppermost layer for the oceanic part of the model is the seawater; its thickness was derived by subtracting the bathymetric depths obtained from the ETOPO1 model (Amante & Eakins, 2009) from the mean sea level. The uppermost layer for the continental part of the model is the sedimentary layer; the sediment thickness was obtained from the ICONS (Heine, 2007) and CRUST1 (Laske et al., 2013) data sets. The sediment thickness for the oceanic part of the model obtained from Völker et al. (2013) and GlobSed (Straume et al., 2019) and was cross-checked against available seismic profiles. The thickness of the continental crystalline crust was obtained from the model by Assumpção et al. (2013), with seismic profiles used for additional constraints close to the trench.

The thickness of the subducting section of the oceanic plate (h_s) was obtained from the Slab2 model (Hayes et al., 2018). The thickness of the non-subducting section (h_{ns}) was approximated by the thickness of the thermal boundary layer, as defined by the characteristic thermal diffusion distance (e.g. Turcotte & Schubert, 2002):

$$h_{ns} = 2.32\sqrt{kt} \qquad (3.1)$$

where k is the thermal diffusivity of the oceanic plate, which in this case we assigned a constant value of 8e-7 m^2s^{-1} (Hasterok, 2013), and t is the age of the oceanic plate obtained from a global model by Müller et al. (2008). The oceanic plate was subsequently subdivided into three units. The upper two units correspond to the basaltic and eclogitic layers of the oceanic crystalline crust, with the transformation from basalt to eclogite occurring at a depth of about 35 km bmsl (Faccenda & Dal Zilio , 2017). The lower unit represents the mantle component of the oceanic slab. For the oceanic crustal layers we assumed a constant thickness of 7 km, which is consistent with local estimates based on seismic data (e.g. von Huene et al., 1997). The thickness of the mantle component of the slab was computed by subtracting the 7 km from the total thickness of the oceanic plate (h_s and h_{ns} for the subducting and non-subducting sections of the oceanic plate, respectively). To calculate the true vertical thickness of each individual layer (h_v) we took into account the subduction angle α_s extracted from the SLAB2 model (Hayes et al. 2018) using the following equation:

$$h_v = \mathrm{h}/\cos a_s \qquad (3.2)$$

The depths to the model interfaces were computed by downward stacking of the modelled layer thicknesses. Depths to the top of the crystalline crust for both continental and the oceanic areas were obtained by adding the thicknesses of continental or oceanic sediments, respectively, to the topographic elevation or bathymetric depth. The depth to the Moho was calculated by adding the thickness of the crystalline crust to the top of the crystalline crust.

The depth of the interface between the subducting oceanic plate and the upper plate (subduction interface) was defined by interpolating the depth to the top of the oceanic crystalline crust with the depth to the top of the slab from the Slab2 model. Seismic section interpretations were used (where available) to sort out any inconsistencies between different data sources. The depth of the oceanic Moho was computed by adding the true vertical thickness of the oceanic crust (h_v) to the depth of the subduction interface. To obtain the depth to the base of the oceanic plate we added the thickness of the mantle component of the slab to the depth of the oceanic Moho.

Table 3. 1: Summary of input data used to constrain the initial 3D density and structural model of the SCA and their forelands

Unit		**Data set**	**Original spatial resolution**	**Density [kgm^{-3}]**
Water		ETOPO1[a]	1 arc minute	1030
Oceanic sediments		GlobSed[b]	0.5°	2300
		southern central axis[c]	0.05°	
Continental sediments		ICONS[d]	0.1°	2400[f]
		CRUST1[e]	1°	
Continental Crust		Moho depth from Assumpção et al. (2013) and seismic profiles[g]	0.5°	2800[h]
Oceanic plate	Crust - Basalt	SLAB2[i], thermal boundary layer[j] and seismic profiles[g]	0.5°	2900[k]
	Crust - Eclogite			3200[l]
	Mantle			3360[m]
Continental Lithospheric mantle – sublithospheric mantle		SL2013sv (S-wave velocity anomalies)[n]	Horizontal: 0.5° Vertical: 25 km	3D distribution (3298-3398) [o]

[a] Global relief model of Amante & Eakins (2009). [b] Global oceanic sediment thickness map of Straume et al. (2019). [c] Sediment thickness map of Völker et al. (2013). [d] Intracontinental basin dataset of Heine (2007). [e] sediment thickness from Laske et al. (2013). [f] Average density of intracontinental basins in the SCA region (Mescua et al., 2016 and references therein; Sigismondi, 2012). [g] Moho extracted from 2D seismic refraction and reflection data (Araneda et al., 2003; Contreras-Reyes et al., 2008, 2014, 2015; Flueh et al., 1998; von Huene et al., 1997; Krawczyk et al., 2006; Moscoso et al., 2011; Sick et al., 2006). [h] Average density of the basement (Mescua et al., 2016); [i] Thickness and subduction angle from (Hayes et al., 2018). [j] Thickness of the slab based on Equation 2. [k] Densities of oceanic crust between 0 and 35 km bmsl for a composition of 40% fresh anhydrous basalts/gabbros and 60% fully hydrated basalts (Stern, 2002) . [l] Density of the oceanic crust deeper than 35 km bmsl, corresponding to eclogite (Faccenda & Dal Zilio, 2017; Hacker et al., 2003). [m] Density of the mantle material in the oceanic plate of peridotitic composition (Hacker et al., 2003). [n] Tomographic model from Schaeffer & Lebedev (2013); [o] Velocity to density conversion using the approach of Goes et al. (2000), as implemented by Meeßen (2017).

Once the main lithospheric interfaces had been defined we assigned constant densities to each of the units in the initial model, except for the lithospheric mantle. Table 3.1 summarizes the model layers and their assigned densities. The continental sediments were modelled with a density of 2400 kgm^{-3} as this has previously been estimated to be the mean density of the sediments in the Neuquén and Cuyo basins (Fig. 3.1c; Mescua et al., 2016 and references therein; Sigismondi, 2012). The initial density assigned to the continental crystalline crust was 2800 kgm^{-3}, which is equivalent to a felsic composition (Christensen & Mooney, 1995). It also reflects the average composition of the exposed basement rocks (in the Cuyania and Chilenia crustal terranes and the Choiyoi magmatic province; see references in Mescua et al. (2016).

For the oceanic plate we assigned a density of 2900 kgm^{-3} to the basaltic crustal layer, which is typical for a crust that has experienced hydrothermal alteration by seawater circulation (Stern, 2002). The eclogitic crustal layer was assumed to have a density of 3200 kgm^{-3} (Faccenda & Dal Zilio, 2017; Hacker et al., 2003). For the lower unit of the slab we assigned a density of 3360 kgm^{-3}, which corresponds to a peridotitic mantle (Hacker et al., 2003).

The thermal field and its effect on the density distribution within the mantle can be assessed through the analysis of S-wave velocities due to their sensitivity to temperature. We computed mantle densities using the SL2013sv global upper mantle tomographic model (0.5° resolution; Schaeffer & Lebedev, 2013). This model is based on the inversion of surface and S waveforms for depths between 25 km and 700 km bmsl At shallow depths (<75 km bmsl) the modelled velocities reflect both crustal and mantle components as a result of sampling over a depth range of 50 km. We therefore only used velocities from depths >75 km bmsl.

The S-wave velocities from the SL2013sv model were converted into densities using the Python VelocityConversion tool (Meeßen, 2017; Appendix A.1), following a modified approach developed by Goes et al. (2000). In order to compute mantle densities this method required a mantle composition, which we derived from the petrology and geochemistry of mantle xenoliths found in the Agua Poca volcanic area (Conceição et al., 2005; Jalowitzki et al., 2010; Fig. 3.2). These xenoliths consist mainly of anhydrous spinel lherzolite, with minor quantities of harzburgite and banded pyroxenite (Bertotto et al., 2013). A summary of the relevant petrological and geochemical analyses is provided in the Appendix A.2. The final step involved interpolation of the obtained mantle density distribution over a 3D grid (voxel) and subsequent integration of this distribution into the initial model.

3.4.2 Gravity modelling

We used gravity modelling to derive additional constraints on the lithospheric structure of the study area. This involved checking the gravity field calculated from the model (referred to below as the ‘calculated gravity’) against the measured gravity (referred to below as the ‘observed gravity’). For our study, we compared the calculated gravity to the gravity disturbance (observed gravity) from the EIGEN 6-C4 global gravity model (Förste et al., 2014;

Ince et al., 2019) at a fixed elevation of 6 km above the datum, which had a horizontal resolution of 10 km (Fig. 3.3). EIGEN 6-C4 model integrates data from both terrestrial and satellite sources, and although some of the short wave-length response that a full terrestrial data set would possess main remain unresolved, it was considered appropriate for the scale of the modelling.

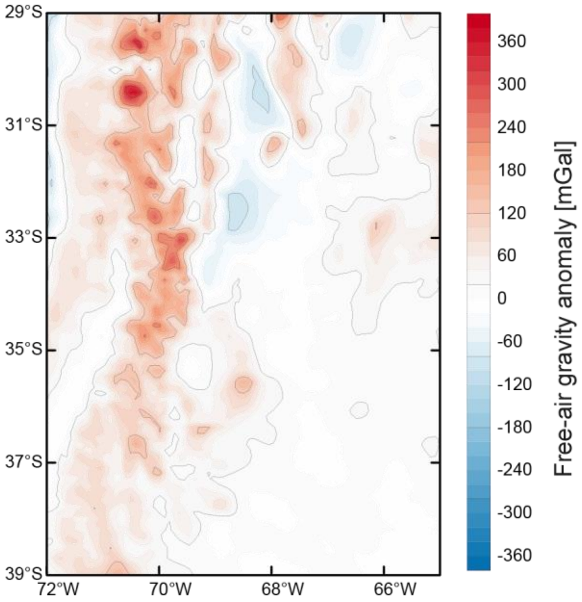

Figure 3.3: Gravity disturbance from the EIGEN 6-C4 global gravity field model ('Observed gravity'; Förste et al., 2014; Ince et al., 2019) at 6 km above the datum used for the gravity modelling of our study. The positive values corresponds spatially to the topographic highs (e.g. in the orogen, the Payenia volcanic province and the Sierras Pampeanas) and the negative values in the northern part of the study region, with the oceanic domain and the foreland basins

One of the methods used to compare calculated gravity with observed gravity relies on forward modelling. This method involves iteratively modifying the free parameters (i.e. the density or geometry of the layers) of an initial model until the calculated gravity matches the observed gravity. In order to forward model the gravity disturbance associated with our initial model we used the IGMAS+ software (Götze & Lahmeyer, 1988; Schmidt et al., 2010), which is an interactive tool for processing and integrating gravity data. The input surfaces are interfaces between different units, each with its own constant density. The software triangulates between previously-defined parallel vertical sections (working sections) and the input interfaces, thus generating polyhedra that represent the three-dimensional units of the model. The algorithm then calculates the volumetric contribution of each of the units to total the gravity (the calculated gravity), by transforming the volume integral of each polyhedron to a surface integral (Götze, 1984; Götze & Lahmeyer, 1988). The IGMAS+ software allows density variations to be introduced within the various units by integrating gridded data (voxels) with the voxelization tool, which in our case was used to integrate the density values in the mantle derived from seismic velocities. The final calculated gravity is then the sum of the different contributions from the homogeneous units and the voxels. The IGMAS+ software can also be used to compute the difference between the observed gravity and the calculated gravity (gravity residual), so that the two fields can be automatically compared. The user can iteratively modify the geometry or the density of the modelled units and recompute the calculated gravity, and thus the residual gravity, after each modification.

For our research, the initial model was subdivided into 69 working sections running from west to east, with a spacing of 25 km equivalent to the horizontal resolution of the model. To avoid any edge effects we used an enlarged version of the initial model by extending the interfaces by 300 km in the N-S direction and by 500 km E-W. The voxelization tool was used to take into account any density variations within the mantle, using the previously described voxel grid. The gravity field was continued upwards to 6 km above the datum, thus allowing comparisons to be made between the calculated gravity and the observed gravity.

Because different lithospheric density models can yield similar calculated gravity fields, we aimed to minimize the number of parameters to be modified by comparing the geometries and densities of different layers with those in the previously described data sets. Since most of the parameters were substantially constrained by gravity-independent observations, we considered the residual between the observed gravity and the calculated gravity to be due to density variations within the unit for which the least information is available, i.e., the continental crystalline crust. To derive a density discontinuity within this layer we inverted the gravity residual obtained from the forward modelling. For this purpose, the continental crystalline crust was assumed to consist of two layers with different average densities: an upper crystalline crust of 2800 kgm^{-3} and a lower crystalline crust of 3100 kgm^{-3}. These values were based on the results obtained by Ammirati et al. (2015) in the sub-horizontal slab area of the SCA. These authors converted the P-wave velocities at different depths in a regional model into densities, using the empirical relationship between P-wave velocity and density reported by Brocher, (2005). Inverse modelling of the gravity residual was carried out using the "Fatiando a Terra" Python tool (Uieda et al., 2013) and an approach similar to that followed by Meeßen et al. (2018). A schematic diagram of the gravity inversion procedure is provided in Figure 3.4. The algorithm sets initial density perturbations (seeds) at the base of a prism mesh and propagates them until the residual gravity reaches a prescribed minimum threshold. In this study, we fixed the initial seed distribution at 500 m above the Moho and the density perturbations within the continental crystalline crust were introduced by thickening the lower crustal unit after each propagation step. The thickness was increased by 500 m between each step. In order to avoid non-unique solutions, the seeds were only allow to grow upwards and were constrained to the continental crystalline crust. The resulting interface separating the upper and lower continental crystalline crustal units was subsequently integrated into the initial lithospheric configuration, to derive the final model.

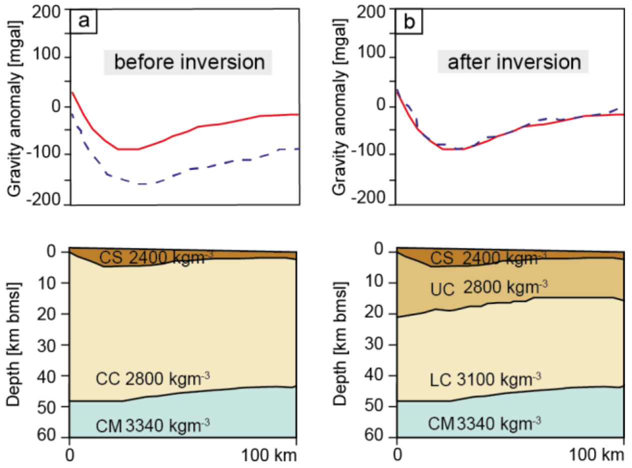

Figure 3.4: Schematic plots illustrating the use of gravity inversion to determine the thickness of the lower crust. Exemplary cross-sections showing the thickness of the main crustal layers down to 60 km bmsl (a) before and (b) after inversion of the initial model gravity residual. CS = continental sediments, CC = continental crust, UC= upper continental crystalline crust, LC = lower continental crystalline crust, CM = continental mantle. The observed and calculated gravity responses throughout the cross sections are shown in solid red and dashed blue lines, respectively

3.5 Results

3.5.1 Initial structural model

The main characteristics of the initial 3D structural model derived from the integration of different data sets are illustrated in Figure 3.5. Figure 3.5a shows a 3D representation of the initial model, together with the topographic elevation and the bathymetric depths extracted from the ETOPO1 model (Amante & Eakins, 2009). The highest topographic elevation (~4.8 km amsl) occurs in the central-northern part of the SCA. The elevation of the orogen then decreases southward down to ~2 km amsl. The highest topographies in the eastern back-arc and the foreland occur in the Precordillera, the Payenia volcanic province and the Sierras Pampeanas, where elevations range between ~2 and ~3.5 km amsl, with maximum elevations in the

Precordillera and western Sierras Pampeanas. The forearc and most of the foreland have a maximum elevation of ~1.5 km amsl The oceanic domain has a maximum depth of 4.5 km bmsl, close to the trench.

Figure 3.5b shows the depth to the top of the crystalline crust, which increases beneath the Neuquén and Cuyo basins to 4.5 and 5 km bmsl, respectively. The maximum sediment thickness reaches ~5 km in the main depocentres of both of these basins (Fig. 3.5c), these being the Dorso de los Chihuidos in the Neuquén basin and the Santa Clara-Tupungato depression in the Cuyo basin. There is also an abrupt increase in the depth to the top of the crystalline crust from the orogen at 32°S to the Cuyo Basin at 33°S. Other basins in the foreland are of minor extent and the depths to the top of the crystalline crust do not exceed 3 km bmsl; the sediment thickness in these areas is between 2 and 3 km. In the oceanic domain, the depth to the top of the crystalline crust increases towards the trench to ~4.5 km bmsl and the sediment thickness reduces to less than 500 m.

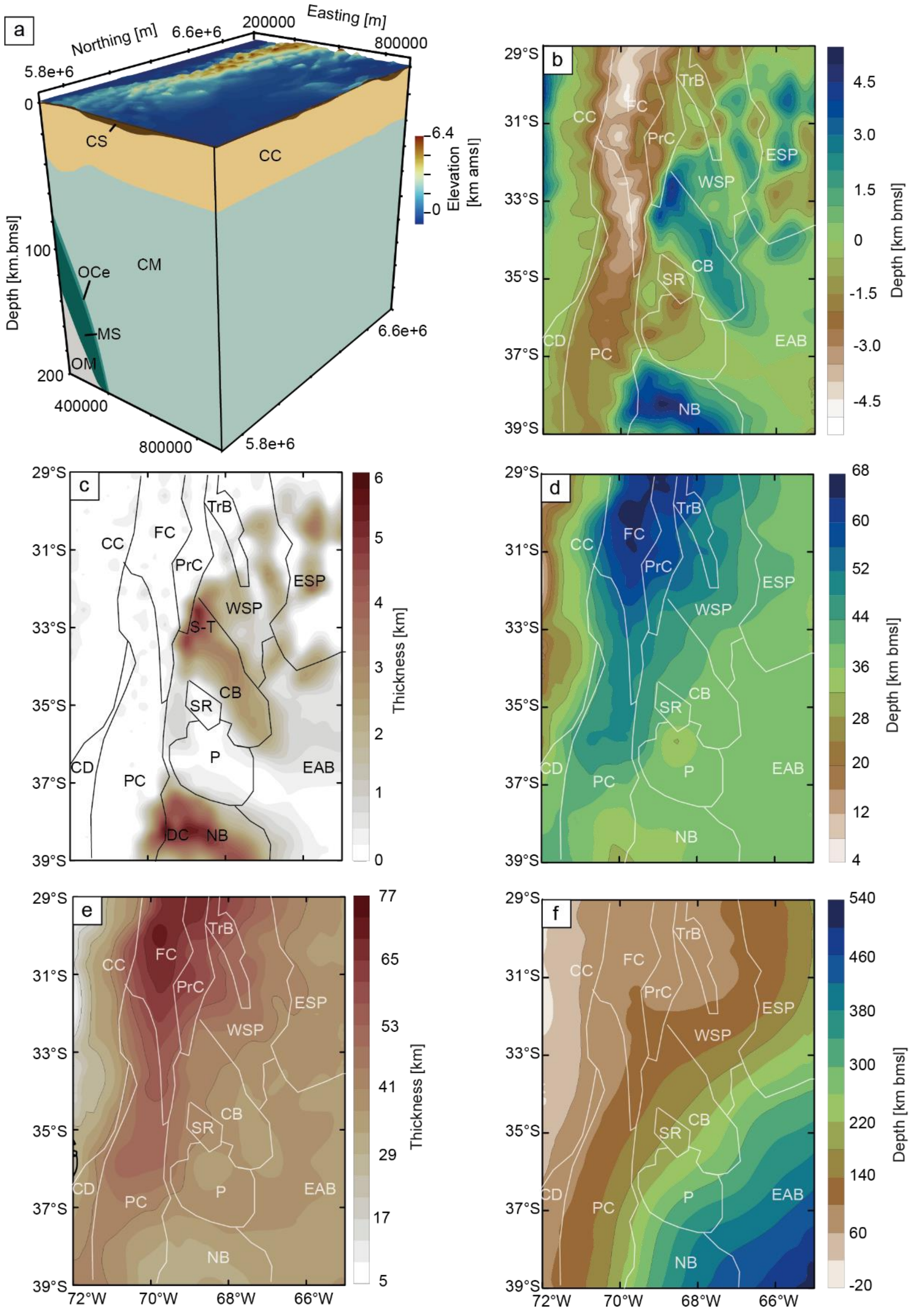

Figure 3.5: Set up of initial model. (a) 3D representation of the initial model. Abbreviations used for the main lithospheric layers are: CS: continental sediments, CC: continental crust, CM: continental mantle, OCe: eclogitic oceanic crust, MS: mantle slab and OM: oceanic mantle. (b) Depth to the top of the crystalline crust obtained from the difference between the topographic elevation and sediment thickness. (c) Thickness of oceanic and continental sediments obtained from the thickness maps compilations in the ICONS database (Heine, 2007), the GlobSed model (Straume et al., 2019) and the seismically constrained CRUST1 model (Laske et al., 2013); SC-T: Santa Clara- Tupungato depocentre in the Cuyo Basin, DC: Dorso de los Chihuidos depocentre in the Neuquén basin. (d) Depth to the Moho from Model A (Assumpção et al., 2013) with additional seismic constraints (e.g. von Huene et al., 1997). (e) Thickness of the crystalline crust obtained from the difference between the depth to the top of the crystalline crust and the depth to the Moho. (f) Depth of the interface between the subducting oceanic plate and

the upper plate coinciding with the depth to the top oceanic crystalline crust to the west of the trench and with the depth to the top surface of the subduction zone model Slab2 (Hayes et al., 2018) to the east of the trench with additional seismic constraints (von Huene et al., 1997). The location of seismic profiles used to derive (d) and (f) are shown in Figure 3.3. Boundaries of the main morphotectonic provinces are also marked: for abbreviations see Figure 3.1c

The depth to the Moho is shown in Figure 3.5d. A strong E-W variation is evident in the northern part of the study area where the Moho is less than 10 km bmsl in the oceanic domain but reaches approximately 68 km bmsl within the orogen; it is about 38 km bmsl in the eastern part of the foreland. In contrast, variations in the Moho depth are less pronounced in the central and southern parts of the study area. In the central part of the area a shallow Moho (~30 km bmsl) has been documented in the forearc region (71°S–72°S) and a deeper Moho (~50 km bmsl) within the orogen. The Moho in the southern part of the area is generally shallow (~30-35 km bmsl) in the Payenia volcanic province and along the western margin of the Neuquén basin, and deeper (~42–48 km bmsl) in the Andean orogen. The foreland in the rest of the study area has a more or less constant Moho depth of ~38 km bmsl

Figure 3.5e illustrates the thickness of the crystalline crust, obtained by subtracting the depth to the top of the crystalline crust (Fig. 3.5b) from the Moho depth (Fig. 3.5d). The thickness of the crystalline crust shows similar trends to those described above for the depth of the Moho. In the northern part of the study area we identified a marked variation in thickness, with a thin (~7-10 km) crystalline crust in the oceanic domain, becoming thicker (up to ~70 km) beneath the orogen and then thinner again (between ~35 and 40 km) towards the eastern foreland. The thickness variations are less pronounced in the central part of the study area, where the thickness of the crystalline crust is between ~20 km and ~40 km beneath the forearc and foreland and ~50 km beneath the orogen. In the southern part of the study area the greatest thickness for the crystalline crust (~50 km) occurs beneath the orogen and the least thickness (~20 km) beneath the Neuquén Basin. In the rest of the foreland the thickness of the crystalline crust ranges between ~30 km and ~40 km.

Figure 3.5f shows the depth to the top of the oceanic crust, which is also the top of the subducting oceanic plate. The oceanic plate dips towards the east, with the subduction angle varying from north to south. In the northern part of the study area (29°S –33°S) the slab subducts sub-horizontally beneath the orogen and part of the eastern Sierras Pampeanas, and then steepens further to the east. The subhorizontal subduction segment lies at depths of between 90 and 95 km bmsl. The width of the subhorizontal segment narrows progressively southward from 33°S to 35°S, after which the entire slab has a steeper dip. The change in subduction angle follows the westward migration of the trench from north to south (Fig. 3.1). The general depth of the subducting slab reaches ~300 km bmsl in the north-eastern part of the study area and ~500 km bmsl in the south-eastern part.

3.5.2 Density distribution within the mantle

The density distribution within the mantle is dependent on both its temperature and its composition; we first assessed the influence of temperature. Figures 3.6a and 3.6b show the temperature distribution at 100 km and 200 km bmsl, respectively, obtained by converting S-wave velocities from the SL2013sv tomographic model (Schaeffer & Lebedev, 2013). At 100 km bmsl (Fig. 3.6a) there is a small regional trend of increasing temperatures from north to south, ranging from ~1000°C in the northernmost part of the study area to ~1050°C in the southernmost part. The tomography also indicates a low-temperature zone (~850°C) in the western part of the study area between 33°S and 35°S that reaches a minimum beneath the orogen. The temperature follows a similar distribution at 200 km bmsl but differs in the absolute values, which range from ~1200°C in the north to ~1300°C in the south (Fig. 3.6b). A low-temperature zone (~1000°C) is again present in the west at roughly the same location as in 100 km depth distribution.

Figure 3.6c illustrates the distribution of vertically averaged density within the mantle (between 75 and 200 km bmsl), obtained by converting the SL2013sv S-wave velocities. The values range from 3340 kgm^{-3} in the north-western and southern parts of the study area to 3360 kgm^{-3} in the centre (0.5% variation). There is a northeast-southwest trend in relatively high values (~3356 kgm^{-3}), which is similar to the trend observed in the temperature distributions. It is interesting to note that this low temperature and high density feature coincides spatially with the area in which the subduction angle of the oceanic slab changes from sub-horizontal in the north to a steeper gradient in the south (Fig. 3.5f); it also corresponds with the areal extent of the Maipo Orocline (Fig. 3.1a). However, this low temperature and high density feature does not extend beyond south of 38°S, where the dip of the slab is also steep but the mantle has the lowest densities in the study area. These low densities occur beneath an area of thin crust in the vicinity of the Neuquén Basin (Fig. 3.5e).

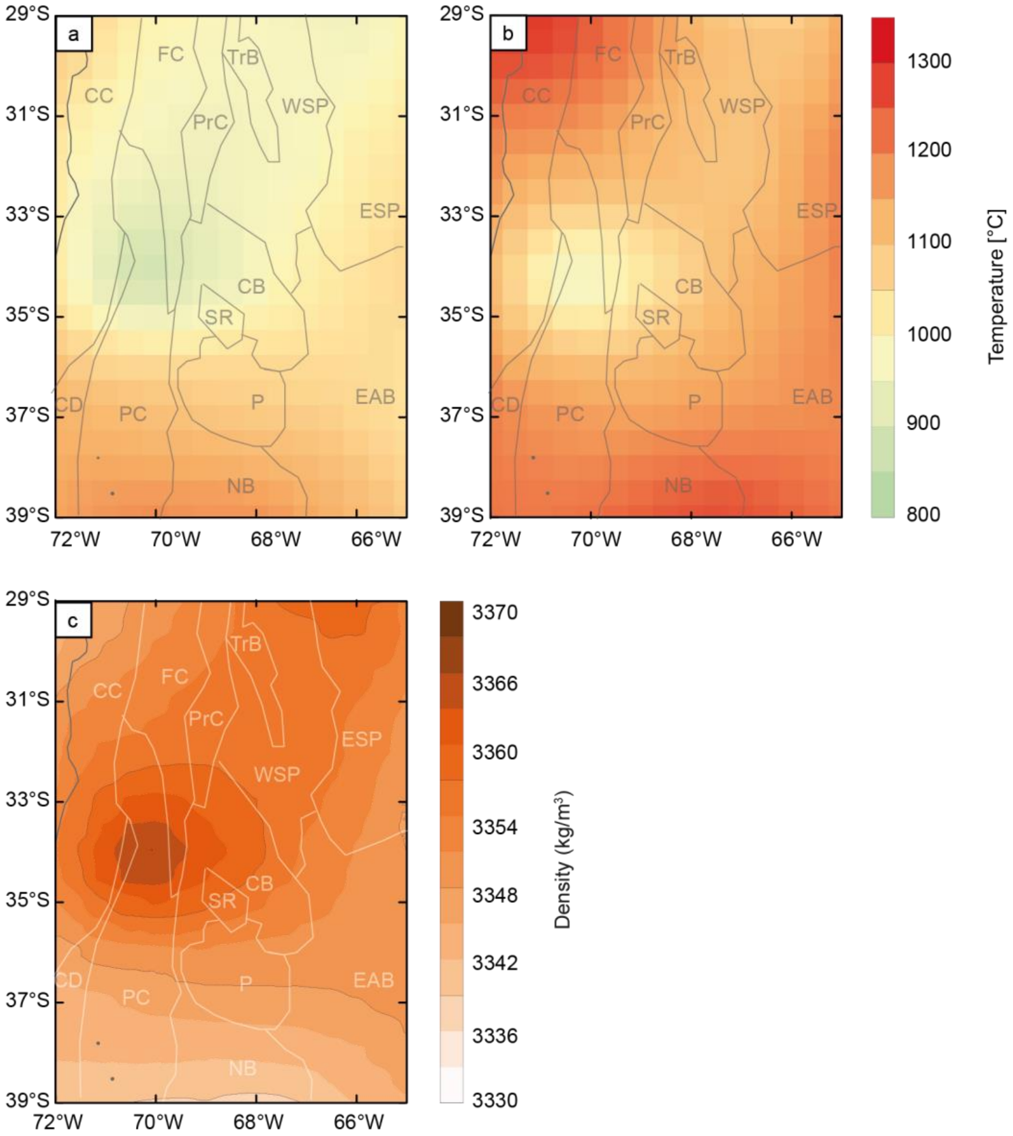

Figure 3.6: Results from the conversion of shear-wave velocities of the SL2013tomographic model (Schaeffer & Lebedev, 2013) to temperatures and densities in the mantle. Temperature distribution shown for the depths of: (a) 100 km and (b) 200 km (base of the model), (c) Average mantle density, calculated pointwise vertically over a depth range of 75 km to 200 km from the 3D voxel grid. Boundaries of the main morphotectonic provinces are also marked: for abbreviations see Figure 3.1c

3.5.3 Forward gravity modelling

The gravity and gravity residual calculated from the initial configuration with the densities presented in Table 3.1 are shown in Figures 3.7a and 3.7b, respectively. Figure 3.7c is a histogram of gravity residuals. The calculated gravity indicates positive values of up to 360 mGal between 70 and 72°W (Fig. 3.7a). To the east the Precordillera, the Triassic basins and parts of the Sierras Pampeanas all exhibit a negative anomaly down to -180 mGal. In contrast, the Payenia province and the easternmost Sierras Pampeanas are characterized by a positive anomaly of up to 180 mGal. The calculated gravity exhibits a number of discrepancies with respect to the observed gravity field. Firstly, there is a long-wavelength positive residual ranging from 80 to 240 mGal in the northern part of the study area, which indicates a substantial mass deficit in the model (Fig. 3.7b). Secondly, there is an isolated positive, short-wave-length residual at ~30.5°S-70.5°W that correlates spatially with the Elquí-Limari batholith (Nasi et al., 2010). Thirdly, negative residuals (up to -280 mGal) are common on the western part of the study area within the oceanic domain and within the south-central parts of the forearc and the orogen (69.5°W-72°W). The back-arc area of the Payenia volcanic province also exhibits negative residuals of about -80 mGal. These features indicate a mass excess in the initial model. In the remaining parts of the study area, the gravity residual ranges between -30 and 30 mGal, suggesting that the initial model yields a good approximation of the observed gravity in those areas.

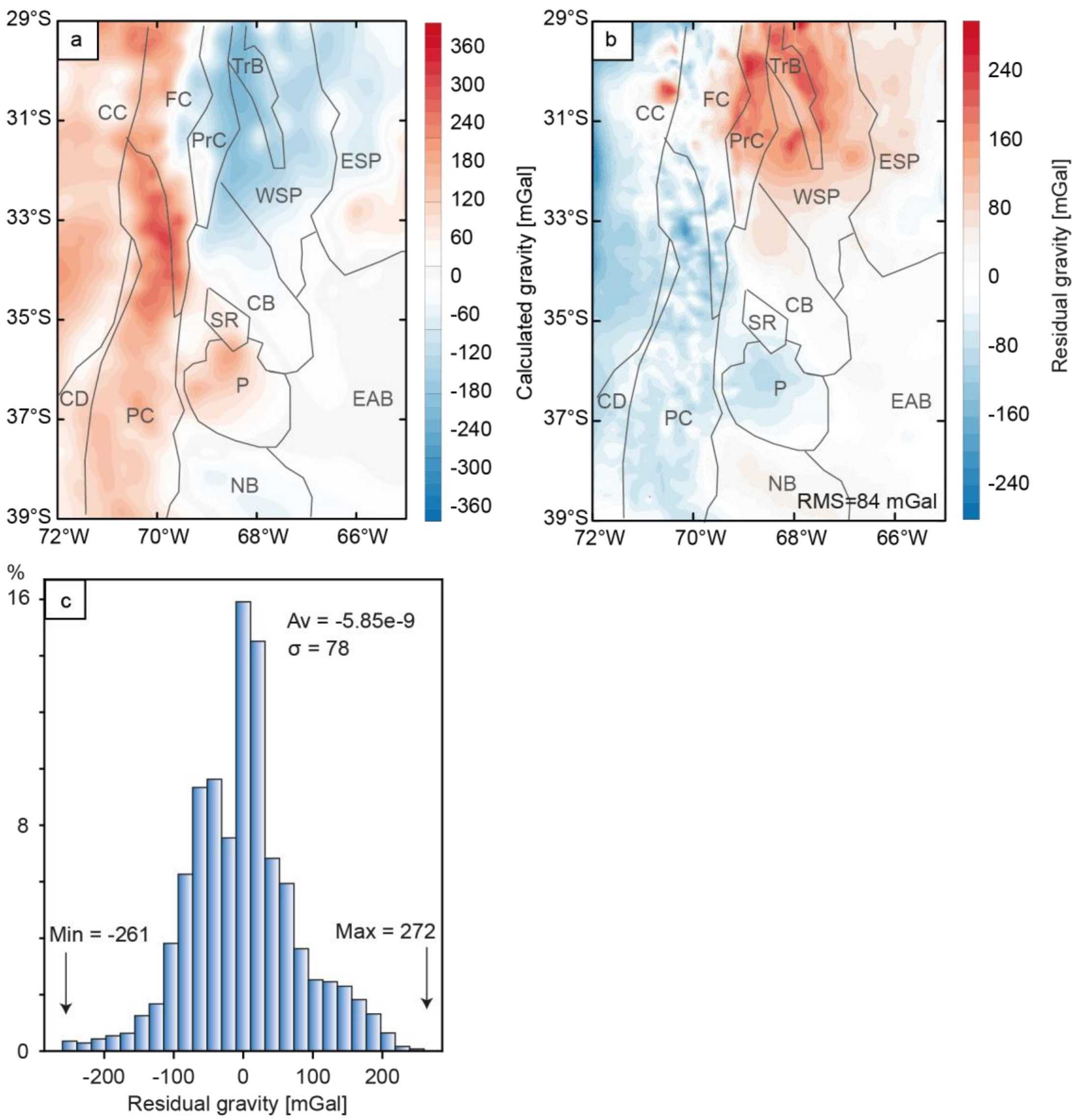

Figure 3.7: (a) Calculated gravity and (b) gravity residual –as the difference between the observed gravity and the calculated gravity- from the initial model. Positive residuals indicate a mass excess in the model, while negative residuals indicate a mass deficit. (c) Histogram and statistics (average, standard deviation σ, minimum and maximum values) for the gravity residual from the initial model. All values are expressed in mGal. Boundaries of the main morphotectonic provinces are also marked in (a) and (b): for abbreviations see Figure 3.1c

3.5.4 Inverse modelling

We computed the depth to the top of the lower continental crust (Fig. 3.8a) by inverting the gravity residual of the initial model and assuming that any changes to the density configuration required for the calculated gravity to match the observed gravity would occur within the crystalline crust. The modelled depth of the intracrustal discontinuity (separating an upper crust, with a density of 2800 kgm^{-3}, from a lower crust with a density of 3100 kgm^{-3}) increases to ~40 km bmsl beneath the orogen (69.5°W–71°W). In contrast, beneath the forearc (71°W–72°W), the back-arc area of the Precordillera, the northern part of the foreland (the

Sierras Pampeanas), and the Neuquén basin, the depth to this intracrustal density discontinuity decreases down to 5 km bmsl

Figure 3.8b shows the thickness of the lower continental crystalline crust layer, obtained by subtracting the depth to the top of the lower continental crystalline crust from the Moho depth. The modelled lower crystalline crust in the northern part of the study area is relatively thick, ranging between 30 and 50 km beneath the Precordillera and the western Sierras Pampeanas, and parts of the northern forearc and the Neuquén basin also have a thick lower crystalline crust (~25 km). In contrast, a thin lower crystalline crust was modelled for the south-central part of the orogen (~17 km), the volcanic province of Payenia (~15 km), and the oceanic domain (~5 km). In the remaining foreland area the lower crystalline crust has a thickness of between ~20 and 25 km.

Through the integrated forward and inverse modelling we derive the final model. The residual gravity trends of this final model is shown in Figure 3.8c–d. The final model accurately reproduces the observed gravity disturbance over most of the study area (RMSE=20 mGal). Nevertheless, short-wave-length (<20 km) residuals remain in the north-central part of the orogen, possibly due to intracrustal heterogeneities at a scale that the model is unable to resolve.

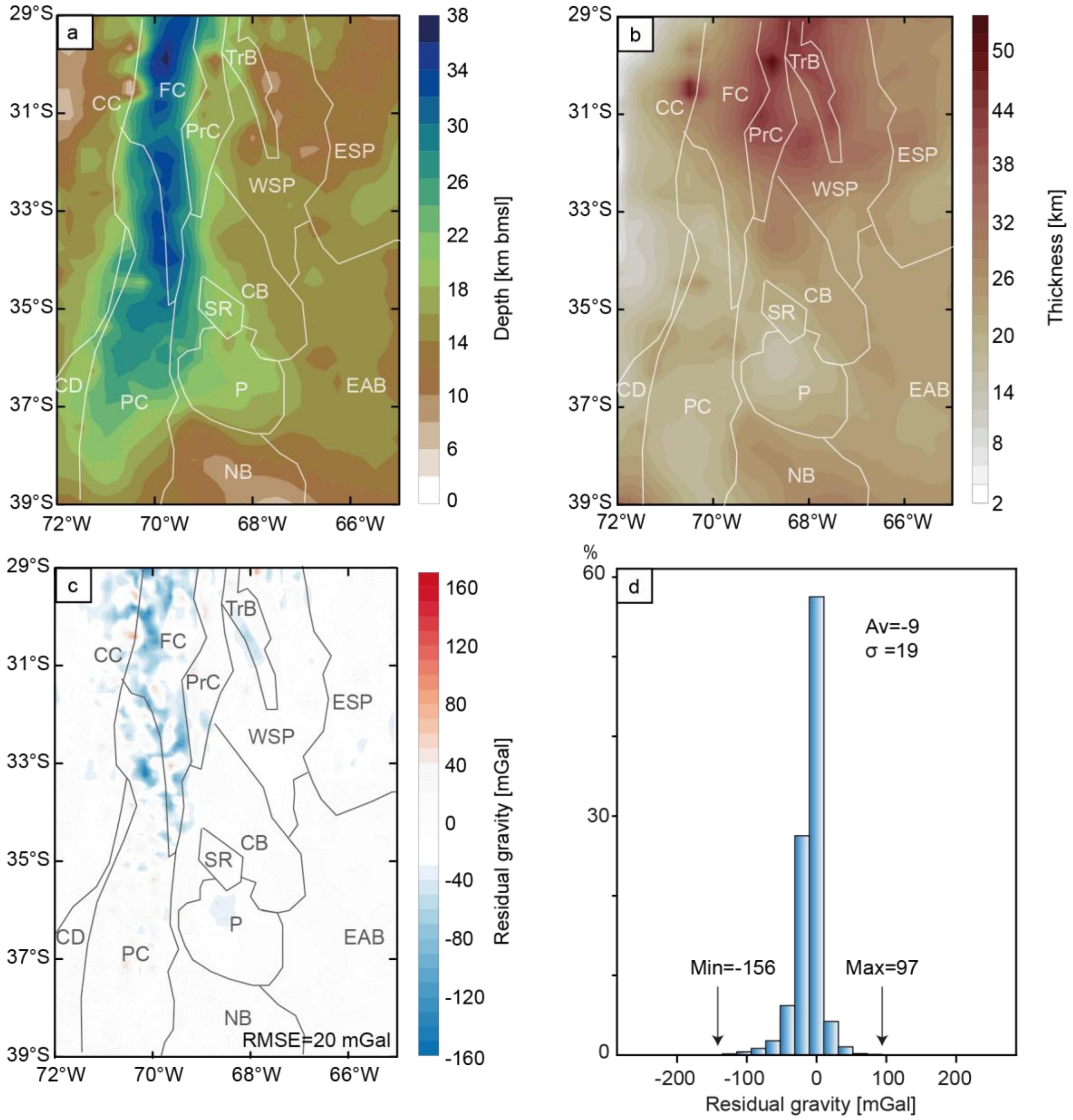

Figure 3.8: (a) Depth to the top of the continental lower crystalline crust computed from the inversion of the gravity residual of the initial model. (b) Thickness of the continental lower crystalline crust calculated by adding the depth to the top of the lower continental crystalline crust to the depth to the Moho. (c) Gravity residual following inversion, derived from the final model. (d) Histogram statistics (average, standard deviation σ, minimum and maximum values) for the gravity residual from the final model. All values are expressed in mGal. Root mean square error (RMSE) = 20 mGal. Boundaries of the main morphotectonic provinces are also marked in (a-c): for abbreviations see Figure 3.1c

We also computed the density distribution for the entire continental crystalline crust by averaging the densities of the upper and lower layers, taking into account the spatial variations in their thicknesses. Figure 3.9 presents the resulting average-density distribution, overlain with the boundaries of the morphotectonic provinces (as in Fig. 3.1c). Areas with high average densities (>3000 kgm^{-3}) in the continental crystalline crust correlate spatially with the north-central part of the back-arc Precordillera fold-and-thrust belt, the basement uplifts of the western Sierras Pampeanas, the north-eastern Sierras Pampeanas, and the foreland basins of

Cuyo and Neuquén. In contrast, areas with lower average crystalline crustal densities (~2900 kgm^{-3}) correlate with the oceanic domain, the Principal Cordillera, the Frontal Cordillera, the southern part of the Precordillera, and the Payenia volcanic province. Intermediate average crustal densities (between 2950 and 3000 kgm^{-3}) occur in the narrow part of the southern Coastal Cordillera, the fore-arc basin of the Central Depression, and the remaining foreland areas (the south-eastern Sierras Pampeanas, the San Rafael Block and the sedimentary basins away from Andes).

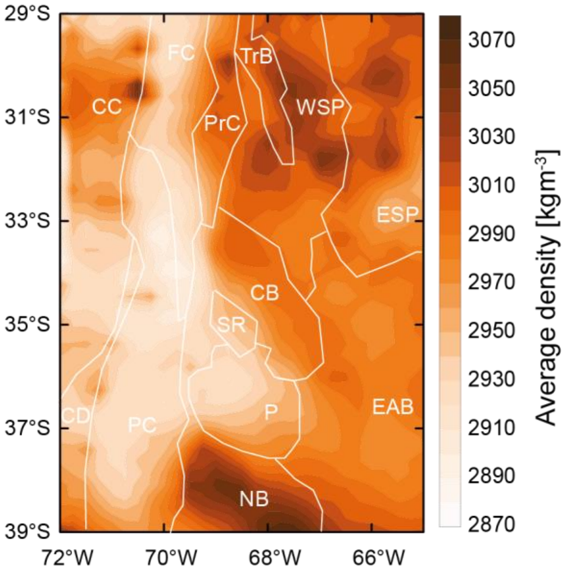

Figure 3.9: Average crustal density of the total (upper and lower) crystalline crust as derived from the final model. Boundaries of the main morphotectonic provinces are also marked: for abbreviations see Figure 3.1c

Figures 3.10a and 3.10b depict the gradient of (i) topographic elevation, and (ii) average crustal density, also showing those crustal seismic events with a moment magnitude of 4 or more (International Seismological Centre, 2021) and the geodetically derived orientations of contractional and extensional strain rates (Drewes & Sánchez, 2017). Although the geodetically derived data covers our entire study area, only those sites with the highest horizontal strain rates (>5e-8 y^{-1}) are shown. A clear spatial correlation is evident between high horizontal strain rates (Drewes & Sánchez, 2017) and the steepest topographic gradients in the study area (Fig. 3.10a). A spatial correlation is also observed between the horizontal strain rate and areas with abrupt variations in the average crustal density (Fig. 3.10b). Most of the large magnitude (≥4) seismic events also occur in areas with marked variations in the average crustal density.

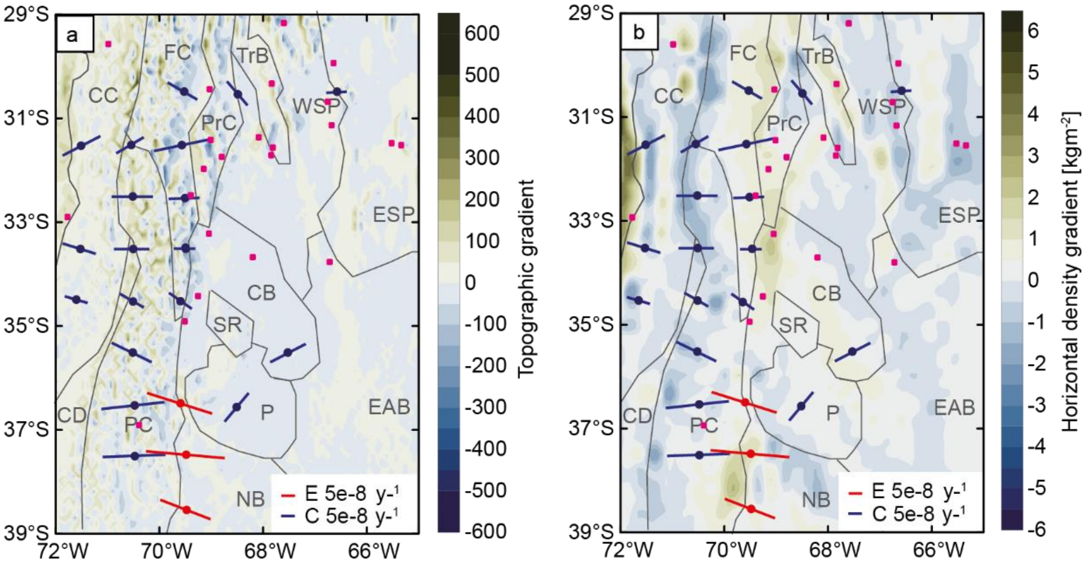

Figure 3. 10: Gradient of (a) topography and (b) average crustal density overlain with: seismic events of moment magnitude ≥4 (small magenta squares; International Seismological Centre, 2021) and geodetically derived orientations of contractional and extensional strain rate (Drewes and Sanchez 2017). The lengths of the red and blue lines indicate the magnitude of the maximum horizontal strain rate. Only the sites with the highest maximum horizontal strain rate (> 5e-8 y^{-1}) are shown. Blue lines indicate compression. Red lines indicate extension. Boundaries of the main morphotectonic provinces are also marked: for abbreviations see Figure 3.1c

3.6 Sensitivity analysis

The chosen densities for the final model are between specific error ranges (e.g. Christensen & Mooney, 1995). We therefore analysed the sensitivity of the gravity field to different density configurations for the continental sediments, the continental crystalline crust, and the mantle. We first established alternative configurations to those of the initial model by imposing a density perturbation on the continental sediments, the continental crystalline crust, and the mantle, one at a time. As a second step in the sensitivity analysis, we carried out a gravity inversion (as in Chapter 3.5.4) for each configuration to compute the individual effect of each density perturbation on the resulting thickness of the lower crystalline crust. We also calculated the residual gravity following the inversion for each alternative configuration, in order to determine the most robust configuration, i.e. the configuration that most closely matched the observed gravity field. Since the gravity field is dependent on the density, depth, and mass of the rock units (e.g. Turcotte & Schubert, 2002), this type of analysis allows the effect that density perturbations have on the resulting lower crustal thickness to be quantified. We were thus able to determine whether or not the gravity residuals did indeed represent intracrustal heterogeneities or whether they simply resulted from an erroneous attribution of densities to the other lithospheric units.

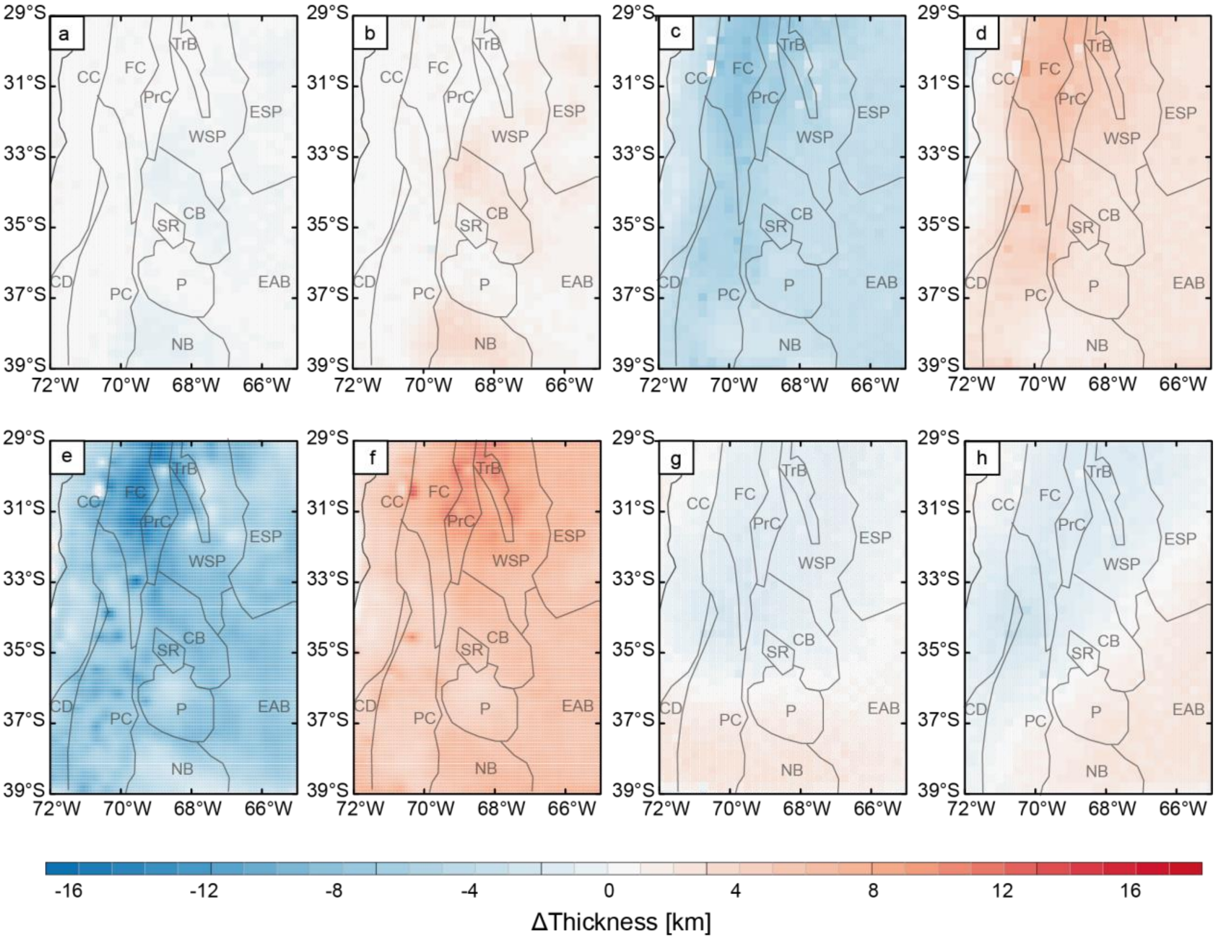

Figure 3.11: Variation of the thickness of the continental lower crystalline crust with respect to the final model induced by varying the density in selected modelled units: (a) continental sediments = 2300 kgm^{-3} ;(b) continental sediments = 2600 kgm^{-3}; (c) continental upper crystalline crust = 2750 kgm^{-3}; (d) continental upper crystalline crust = 2850 kgm^{-3}; (e) continental lower crystalline crust = 3000 kgm^{-3}; (f) continental lower crystalline crust = 3200 kgm^{-3}; (g) homogeneous mantle = 3360 kgm^{-3}; (h) density distribution within the mantle obtained through conversion of S wave velocities from the SEMUM2 tomographic model (French et al., 2013). Positive values indicate a thinner lower crust than in the final model. Boundaries of the main morphotectonic provinces are also marked: for abbreviations see Figure 3.1c

Firstly, for the continental sediments we selected densities of 2300 and 2600 kgm^{-3}, based on the maximum and minimum densities encountered for the Cuyo and the Neuquén basins (Mescua et al., 2016). For a density of 2300 kgm^{-3} the thickness of the lower continental crystalline crust increases by up to 1.5 km (Fig. 3.11a) compared to the final model. In contrast, for a sediment density of 2600 kgm^{-3} the lower continental crystalline crustal unit is up to about 3 km thinner than in the final model (Fig. 3.11b). These variations occur mainly beneath the Neuquén and Cuyo basins (Fig. 3.11a-b). For both of these densities, the inversion enabled us to match the observed gravity field within a RMSE of 21 mGal (Fig. 3.12a-b). Nevertheless, negative residuals (<-30 mGal) remained along the north-western border of the study area, possibly indicating the presence of intracrustal heterogeneities that cannot be resolved at the scale of the model.

Secondly, another important predefined feature in the modelling process was the density of the continental crystalline crust. We investigated the effect of varying the density of the upper layer by ±50 kgm^{-3} (1.7%). Modelling the lowest density in that range for the upper continental crust yielded resulted in a maximum increase of 9 km in the thickness of the lower continental crystalline crust in the northern part of the orogen (Fig. 3.11c). In contrast, there was a reduction in thickness of the lower continental crystalline crust of 1.5 km in the oceanic domain (Fig. 3.11c). Modelling the highest density in the range for the upper continental crust reduced the thickness of the lower continental crystalline crust to 8 km, as opposed to an increase in thickness of the same layer of 1.5 km in the oceanic domain (Fig. 3.11d). The models with reduced or increased upper continental crustal densities were able to accurately reproduce the gravity field following inversion, with RMSEs of 19 mGal and 22 mGal, respectively (Fig. 3.12c-d). However, residual anomalies in the northern part of the study area were predominantly >30 mGal, indicating that the alternative models are not able to accurately reproduce the observed gravity in this part of the study area (Fig. 3.12c-d).

Thirdly, we investigated the effects of varying the density of the lower continental crystalline crust by ±100 kgm^{-3}. Reducing the density of this lower crystalline unit resulted in an increase in its thickness of up to 17 km in the northern part of the orogen (Fig. 3.11e). In contrast, increasing the density by the same amount resulted in a lower crust that was up to 12.5 km thinner (Fig. 3.11f). With regard to the gravity residuals of these last two configurations, the inversion yielded a less accurate match with the observed gravity than the final model and the other alternatives described above in this section (RMSE = 33 mGal for the less dense lower continental crystalline crust and 25 mGal for the denser lower unit; Fig. 3.12e-f). The final model (Chapter 3.5.4) was therefore preferred over these alternative configurations.

The fourth step in the sensitivity analysis involved investigating the effect of varying the density distribution in the mantle. We first considered a constant mantle density of 3360 kgm^{-3}. Following inversion, the lower crust was up to 3.5 km thicker along the western part of the study area than in the final model (Fig. 3.11g). This area has the largest density differences between the preferred model and the model with a constant mantle density. In addition, the resulting lower crust was up to 2 km thinner in the southern part of the study area. With regard to the gravity residuals, the inversion yielded an accurate match with the observed gravity field

(RMSE=21 mGal; Fig. 3.12g), but negative residuals (<-30 mGal) remained in the north-western part of the study area.

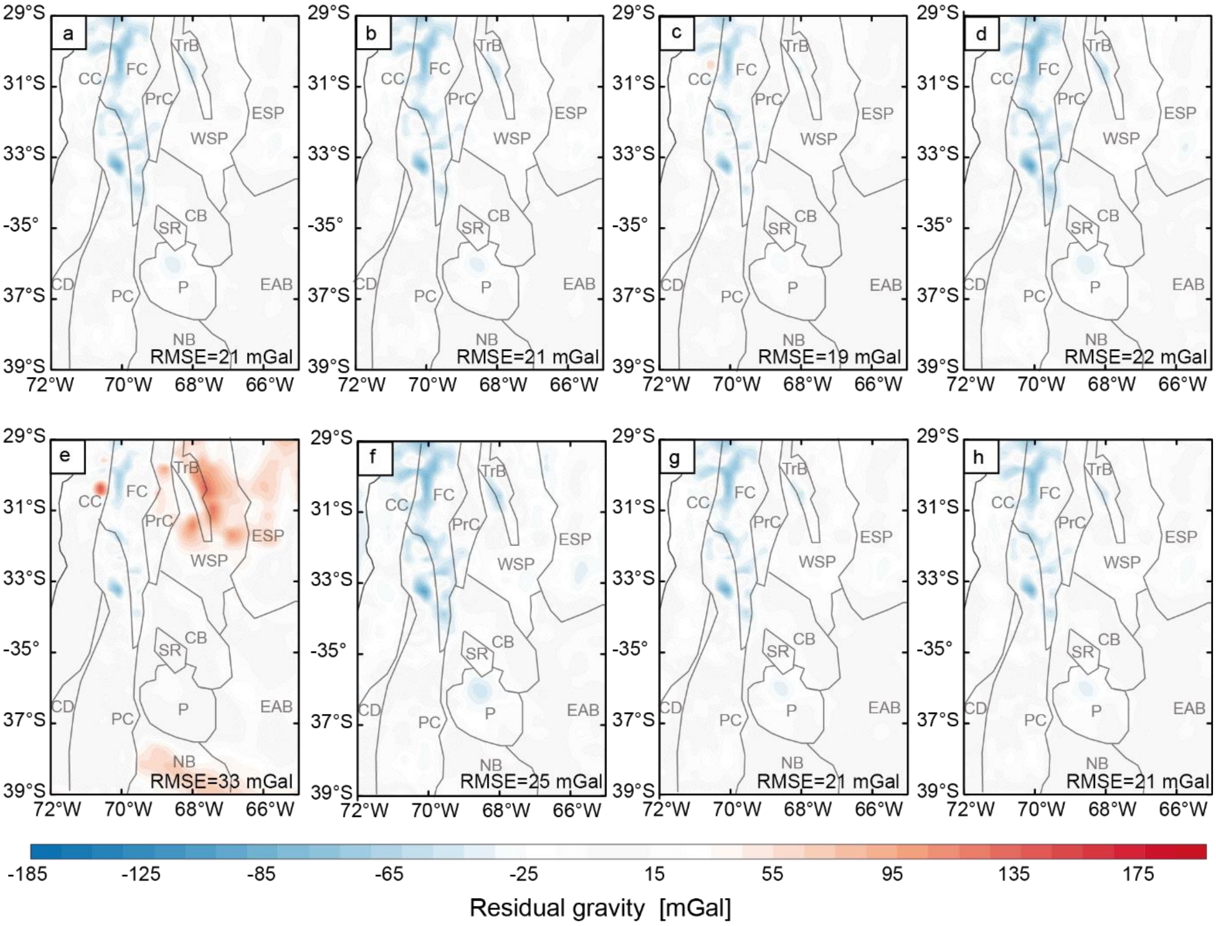

Figure 3.12: Gravity residual (difference between observed and calculated gravity) from models with density variations in selected modelled units after inversion: (a) continental sediments = 2300 kgm^{-3}; (b) continental sediments = 2600 kgm^{-3}; (c) continental upper crystalline crust = 2750 kgm^{-3}; (d) continental upper crystalline crust = 2850 kgm^{-3}; (e) continental lower crystalline crust = 3000 kgm^{-3}; (f) continental lower crystalline crust = 3200 kgm^{-3}; (g) homogeneous mantle = 3360 kgm^{-3}; (h) density distribution within the mantle obtained through conversion of S wave velocities from the SEMum2 tomographic model (French et al., 2013). RMSE (root mean square) in mGal. Boundaries of the main morphotectonic provinces are also marked: for abbreviations see Figure 3.1c

Finally, we modified the mantle density configuration by considering a different tomographic model than the SL2013sv tomography model used for the final configuration, in which S wave velocities were converted to densities (French et al., 2013). This model has a coarser horizontal resolution (2°) than the SL2013sv tomography (0.5° resolution), but it can be used to investigate the effect that the mantle density has on the gravity field, and therefore also on the resulting intracrustal structure. The resulting lower crust was up to 2 km thicker in the western part of the study area and up to 1 km thinner in the southern part (Fig. 3.11h). This alternative configuration also yielded an accurate match with the observed gravity, with similar values to those in the final model (RMSE = 21 mGal; Fig. 3.12h).

Table 3.2: Summary of results from sensitivity analysis. ΔThkLC: induced variation in the thickness of the lower crust. The alternative tomographic model used for the sensitivity analysis of the mantle density distribution was the SEMum2 model (French et al., 2013). The factor f is calculated by dividing the relative density variation by the absolute value of the ΔThkLC and measures how uncertainties in the parametrization affect the derived intracrustal structure

Density parameter	**Imposed density (ρ) variation [kgm^{-3}]**	**Relative density variation [%]**	**Maximum ΔThkLC [km]**	**f [km/%]**
Mantle	constant **ρ** = 3360	0.6	-3.5	5.80
	SEMUM2	0.5	2	4.00
Sediments	2300 (-100)	4.1	-1.5	0.37
	2600 (+200)	8.2	3	0.37
Upper continental crystalline crust	2750 (-50)	1.79	-9	4.75
	2850 (+50)	1.79	8	5.03
Lower continental crystalline crust	3000 (-100)	3.23	-17	5.26
	3200 (+100)	3.23	12.5	3.87

Table 3.2 summarizes the results of the sensitivity analysis for different densities in the various units. In order to compare the different outcomes we calculated a factor f by dividing the induced variations in lower continental crustal thickness by the percentage that parameters were altered by to induce these variations. This factor measures how the lower continental crustal thickness changes in response to variations in the predefined densities of the modelled units. This approach, indicates that the intracrustal structure is more sensitive to density perturbations in the mantle (f = 5.8 km/%) than to those in the crystalline crust (f = ~5.3 km/%). The areas in which the largest variations in thickness occur generally have a thick crust, e.g. beneath the northern part of the orogen and the adjacent foreland (Fig. 3.11e-f). This would imply that perturbations in the average crustal density are relatively small (<18 kgm^{-3}) compared to the average density for the entire crustal column. The major trends in the resulting density distribution would therefore persist, even in scenarios with different upper and lower crustal densities. In contrast, the densities of the sediments do not have any significant effect on the thickness of the lower crust, or therefore on the resulting crustal density distribution (f = 0.37 km/%).

On the basis of these effects resulting from variations in the input data, we conclude that the main spatial trends in the depth to the top of the lower crust would persist despite changes to the input data, within the range of natural variability.

3.7. Discussion

Our results indicate that the crystalline crust in the orogen is thick (Fig. 3.5e, 40 to 70 km) and has a low density (Fig. 3.9, ~2900 kgm^{-3}), which suggests a felsic composition. Although data on the crustal composition beneath the SCA is scarce, seismic surveys to the north of 36°S have indicated low seismic velocities beneath the orogen compared to beneath the adjacent foreland (e.g. Ammirati et al., 2016; Marot et al., 2014; Ward et al., 2013). Our model agrees with these observations in that the average density of the crystalline crust beneath the orogen is lower than beneath most of the foreland (Fig. 3.9, ~3000 kgm^{-3}), which suggests compositional differences between the two areas.

The mechanisms that produced an overall less dense crust beneath the orogen are likely to have been related to plutonic additions with felsic to intermediate compositions, associated with the various Andean-type magmatic arcs that were first established along the western margin of the study area at 580 Ma and that are currently represented by the Cenozoic Andean volcanic chain (e.g. Kay et al., 2006; Stern & Skewes, 1995). Mescua et al. (2016) have also suggested that the upper levels of the crystalline crust in the orogenic interior have relatively low densities. This area of low crustal densities correlates spatially with the vestiges of the extensive extensional Choiyoi magmatic province (Fig. 3.13a; Mescua et al., 2016; Spalletti & Limarino, 2017), which was responsible for the extrusion of felsic magmas and the intrusion of granitic material during the Late Permian-Triassic (e.g. Cristallini & Ramos, 2000; Giambiagi & Ramos, 2002; Llambias & Sato, 1990; Mpodozis & Ramos, 1990, Kay et al., 1994; Ramos et al., 2002). Other driving mechanisms associated with the Cenozoic Andean orogeny could also have been responsible for the lower average densities in the crust beneath the orogen. These may have involved the stacking of upper-crustal rocks by thrusting (e.g. Ramos et al., 2002) and/or the underthrusting of cratonic material, possibly introduced from the east and bringing less dense material into the deep crust (Armijo et al., 2015). This last mechanism is, however, deemed less likely to have occurred in the SCA since there is no geophysical evidence for westward-directed thrusting of the cratonic material beneath the Andes between 29°S and 39°S (e.g. Alvarado et al., 2005, 2009; Ammirati et al., 2015, 2016, 2018; Heit et al., 2008;

McGlashan et al., 2008; Perarnau et al., 2012; Pérez Luján et al., 2015; Porter et al., 2012). The low average crustal density beneath the orogen may be characteristic of ocean-continent subduction scenarios, as has previously been suggested in other gravity modelling studies of the Central Andes(e.g. Ibarra et al., 2019; Tassara et al., 2006). In contrast, collisional orogens on continent-continent margins usually possess a dense mafic lower crust, as observed in the Urals, the Himalayas, and the European Alps (e.g. Kumar et al., 2019; Spooner et al., 2019; Stadtlander et al., 1999).

To the east of the Andean orogen, the remainings of the back-arc and foreland exhibit marked variations in the thickness (Fig. 3.5e) and average density (Fig. 3.9) of the crystalline crust. Three distinctive domains stand out: (1) a northern domain (29°S–34.5°S) with a thick crust (40–60 km) and high densities (~3000–3050 kgm^{-3}); (2) a southern domain (37°S–39°S) with a thinner crust (~20 km) and high densities (~3050 kgm^{-3}); and (3) a central domain (34.5°S–37°S) with intermediate crustal thicknesses (35–45 km) and low to intermediate densities (~2900-2950 kgm^{-3}).

The high average crustal densities in the northern part of the foreland (including most of the Sierras Pampeanas) and the north-central sector of the Precordillera (29°S–34.5°S) suggest a mafic crustal composition adjacent to the orogen. This is compatible with the results from a number of field investigations that have concluded that the basement rocks are mainly gabbros and leuco-gabbros (e.g. Pérez Luján et al., 2015; Ramos, 2010; Vujovich & Kay, 1998). Our results suggest that the middle and lower crustal levels also have mafic compositions. The higher crustal densities in this part of the foreland compared to the orogen interior could be associated with partial eclogitization of the lower crust, as has been previously suggested on the basis of geophysical studies, in particular in view of the increase in v_p and the v_p/v_s ratio beneath the foreland(e.g. Alvarado et al., 2007, 2009; Ammirati et al., 2013, 2015, 2018; Gilbert et al., 2006; Marot et al., 2014). The factors causing partial eclogitization in the lower crust remain unclear (e.g. Ammirati et al., 2015), although some studies suggest that this process could be facilitated by small amounts of water released from the sub-horizontal section of the subducted oceanic crust (Leech, 2001; Yang et al., 2008).

In the eastern part of our study area, high crustal densities (3000–3100 kgm^{-3}; Fig. 3.9) predominate in parts of the Sierras Pampeanas. Isostatic processes and the overall higher density crust in this morphotectonic province could explain why the elevation is relatively low in this particular area (Allmendinger et al., 1990; Bellahsen et al., 2016), despite its large crustal thickness (~50–60 km, Fig. 3.5e). However, the style of deformation, which involves isolated reverse-fault bounded uplifts of crystalline blocks, may also provide an explanation for the lack of crustal stacking and topographic growth. It has been proposed on the basis of the surface geology that the eastern Sierras Pampeanas are underlain by a felsic crust (e.g., Ramos et al., 2010 and references therein). However, our own results suggest that, apart from the shallower crustal layers, the average crustal composition in this part of the Sierras Pampeanas is likely to be mafic. Nevertheless, mafic rocks are not the only materials in the lower crust that can attain densities above 3000 kgm^{-3}. For example, according to Hacker et al. (2011), rocks with high proportions of felsic components such as pelites and wackestones can attain high densities when metamorphosed under extreme P/T conditions (such as 1050°C at 3 GPa). These authors referred to the addition of such highly metamorphosed sediments to the base of the crust as ‘crustal relamination’. Possible lithologies with this potential are those of the metasedimentary rocks belonging to the Puncoviscana Formation of north-western Argentina (Turner, 1960), as proposed by Meeßen et al. (2018). These rocks have been interpreted to have been deposited in the Puncoviscana ocean along the western Gondwana margin between 540 to 524 Ma (Escayola et al., 2011). Although outcrops of the Puncoviscana Formation are only found to the north of 27°S (e.g. Turner, 1960), it has been proposed that correlative sedimentary rocks extended further south (Escayola et al., 2011). Indirect evidence for the existence of these sedimentary rocks within our study area may possibly exist in the Ordovician igneous rocks of the Sierras Pampeanas (Alasino et al., 2016; Ducea et al., 2015; Otamendi et al., 2009). The results of petrological and isotopic analyses suggest that the main petrogenetic processes operating at that time involved metasedimentary materials. Nevertheless, no unambiguous evidence has been found to confirm that these metasedimentary rocks did indeed originated in the passive-margin basins of Gondwana. The corroboration of such a hypothesis would require isotopic evidence from rocks that are equivalent to the Puncoviscana Formation; unfortunately, no such data is currently available from within the study area.

In contrast to most of the Sierras Pampeanas, the south-eastern part of the Sierras Pampeanas has a low average crustal density (2960 kgm^{-3}, Fig. 3.9). This is in agreement with the seismic results and outcrop observations from the area, which indicate that the underlying crystalline crust has a felsic composition (e.g. Alvarado et al., 2009; Ammirati et al., 2018; Perarnau et al., 2012). These felsic rocks may have originated from the intense magmatic activity that shaped the eastern calc-alkaline magmatic belt of the Pampean orogen during Neoproterozoic-Cambrian times (Ramos et al., 2010 and reference therein).

The crystalline crust in the southern part of the foreland (37°S–39°S, which correlates spatially with the Neuquén basin) is thin (~20 km, Fig. 3.5e) and has a high average density (~3050 kgm^{-3}, Fig. 3.9). This area is likely to have been affected by magmatism associated with the Choiyoi extensional event (Fig. 3.13a), leading to crustal thinning and underplating of mafic material during basin initiation (Kay et al., 1989; Llambias et al., 1993), as has been interpreted for the magmatic Kenya Rift (KRISP Working Party, 1991). These past processes could account for the present-day crustal configuration of the Neuquén basin. Despite the Neuquén and Cuyo basins having similar sediment thicknesses, our model suggests a substantial difference in the configuration of the crystalline crust beneath these basins (Fig. 3.5c). In contrast to the thin, dense crust beneath the Neuquén basin, the crust beneath the Cuyo basin is relatively thick (50–40 km, Fig. 3.5e) and less dense (~2950–3000 kgm^{-3}, Fig. 3.9). The modelled difference in the configuration of the crystalline crust could relate to differences in the main process that drove the evolution of the two basins, even though the evolution of these depocentres was in both cases initiated by rifting and thermal subsidence. This was followed by partial compressional reversal of the normal faults and flexural subsidence due to the load of the adjacent Andean orogen (e.g., Barredo, 2012; Giambiagi et al., 2008). The thin, dense crystalline crust beneath the Neuquén basin may indicate that the main processes involved in the generation of accommodation space were the earlier rifting processes, rather than the subsequent flexure in response to shortening and thrust-stack loading during the Andean orogeny. In contrast, the relatively thick and light crystalline crust beneath the Cuyo basin may indicate that the flexural processes had a larger influence on the generation of basin subsidence than the previous extensional processes.

There is a distinct area of low average crustal density (~2900 kgm^{-3}, Fig. 3.9) evident within the central part of the back-arc region adjacent to the orogen (34.5°S–37°S) that corresponds to the Payenia volcanic province. The low crustal densities compared to surrounding areas are likely to be related to the felsic effusive products from the Choiyoi volcanics (Fig. 3.13a). The density distribution may also have been affected by regional magmatic and thermal processes, since intraplate volcanism has been active in the region for the last 20 Ma (Folguera et al., 2006; Kay et al., 2006; Llambias et al., 2010).

Our results for the area to the west of the SCA suggest that the crystalline crust beneath the forearc comprises two domains: a northern domain of high average density (~ 3000 kgm^{-3}; Fig. 3.9) and a southern domain of slightly lower average density (2950 kgm^{-3}, Fig. 3.9). The presence of intermediate to mafic rocks from Jurassic-Cretaceous magmatism (Parada et al.,

2007) could explain the high crustal densities in the northern domain. These crustal densities are also in agreement with the results from regional geophysical investigations where P-wave crustal velocities of up to 6.5 kms^{-1} have been interpreted to indicate crystalline crustal rocks (Contreras-Reyes et al., 2014, 2015). In the southern part of the forearc, the spatial extent of the relatively low modelled crustal densities correlates well with the distribution of exposed late Paleozoic andesitic and medium-grade metamorphic rocks (Herve et al., 2013; Muñoz et al., 2000), and it is consistent with the P-wave velocities of ≤6 kms^{-1} modelled for the entire crustal column of the area (Contreras-Reyes et al., 2008; Krawczyk et al., 2006). Toward the oceanic domain, the reduction in average crustal density modelled along the entire fore-arc may relate to eroded or highly tectonized volcanics (Contreras-Reyes et al., 2014, 2015).

On a regional scale, there is a rough spatial correlation between the modelled crustal density distribution (Fig. 3.9) and average S-wave velocities derived from ambient-noise tomography of the Central Andes (Fig. 3.13b; Ward et al., 2013). Areas of lower crustal densities generally have lower seismic velocities, while areas with higher crustal densities crust have higher velocities. However, this pattern does not apply to the Payenia volcanic province. A careful interpretation of the seismic velocities beneath this area is therefore required, specially in view of the fact that the small number of seismic recording stations in the area means that they are only able to provide limited coverage and relatively few seismic records, which compromises the reliability of the seismic results (see Figure 1 of Ward et al., 2013).

Our study has revealed that the orogen, the southern part of the forearc, the Payenia volcanic province, and the southern part of the Sierras Pampeanas are areas with low crustal densities and seismic velocities, which suggests that they may all be underlain by crust of mainly felsic composition. In contrast, zones with high densities and seismic velocities are likely to have a more mafic crust, as is the case for the northern part of forearc and most of the foreland. The low crustal density and low seismic velocity areas are therefore likely to have higher concentrations of radiogenic elements than their mafic counterparts (e.g. Vilà et al., 2010) and these felsic areas may therefore contribute significantly to the heat budget of the lithosphere, making it hotter and therefore probably weaker and more susceptible to deformation processes. In contrast, a more mafic crust is likely to be cooler and to be able to withstand higher stress levels before reaching the P-T window for brittle or viscous deformation (e.g. Burov, 2007).

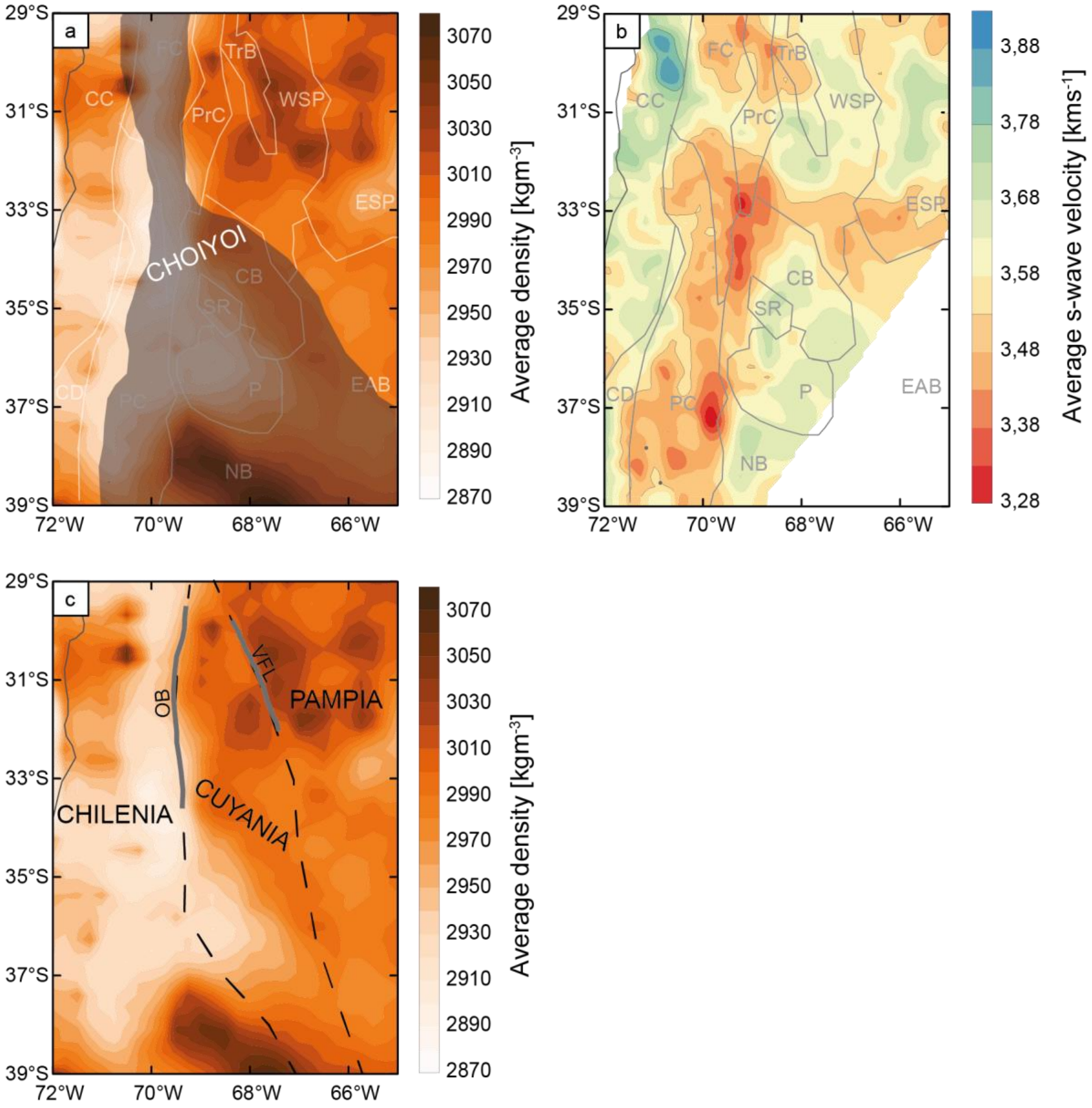

Figure 3.13: (a) crystalline crustal density distribution and morphotectonic units overlain with the extent of the Permo-Triassic Choiyoi magmatic rocks (modified from Mescua et al., 2016; Spalletti & Limarino, 2017). (b) Average shear-wave velocity from ambient noise tomography in the Central Andes (Ward et al., 2013) overlain with morphotectonic units boundaries. The white areas are areas with no data coverage (e.g. oceanic domain, Neuquén basin, Extra-Andean basins). (c) Crystalline crustal density distribution overlain with proposed lines of suture between different terranes accreted to Gondwana during the Palaeozoic (modified from Ramos et al., 2010). Thick grey lines show the extent of the ophiolitic belt to the west (OB) and the Valle Fértil Lineament to the east (VFL). For abbreviations of morphotectonic province names, see Figure 3.1c

Our results show that compositional variations in the overriding plate, such as those we derived in our study, need to be taken into account when investigating the rheological behaviour of the lithosphere and associated deformation patterns in tectonically active areas adjacent to a convergent plate margin. In this context, our analysis has shown that the geodetically derived distribution of high horizontal strain rates and high-magnitude seismic events correlates with areas that have high topographic gradients (Fig. 10a) and marked variations in gravity-constrained average crustal densities (Fig. 10b). This suggests that short-term (i.e. earthquake-related) deformation is likely to be localized in these areas. These spatial correlations are probably related to an increase in gravitational potential energy (GPE) due to the high topographic gradients and abrupt variations in crustal density. Part of the increased GPE would be transferred into the elastic strain field, ultimately facilitating seismogenic processes (Barrows & Barrows, 2010; Barrows & Langer, 1981).

Another question regarding density contrasts and deformation processes is whether the relationship between deep-seated density contrasts and strain distributions also applies to the long-term deformation features of the SCA. The spatial correlations between elevation, crustal thickness and long-term deformation in a sector of the Central Andes north of the area of our study (21°S-29°S) have been extensively discussed by Ibarra et al. (2019) in terms of variations in lithospheric strength and GPE. They argued that the high elevation and large crustal thickness of the orogen results in high a GPE that prevents internal deformation within the orogen, and that the deformation front is therefore propagated to areas with lower GPE, i.e. cold, strong areas such as the foreland. The first-order characteristics of the lithosphere in the sector of the Central Andes investigated by Ibarra et al. (2019) are similar to those in our study area, with felsic compositions, high elevations, and a thick crust beneath the orogenic part of the area and with more mafic compositions, lower elevations, and a thinner crust beneath the northern part of the foreland and the Neuquén basin. This suggests that similar mechanisms to those proposed for the Central Andes between 21° and 29°S are likely to have been active in the SCA, and that pre-strained areas with different densities and rheological characteristics may focus deformation under changing geodynamic boundary conditions. This has also been suggested, for example, for the early tectonic evolution of the Eastern Cordillera of Argentina north of latitude 26°, and for regions farther to the west that are now part of the Andean Plateau (the Puna; Montero-López et al., 2020). The thicker, more rigid basement of the Puna region was less affected by the initial Paleogene Andean deformation processes, while the sedimentary rocks exposed in the Cordillera Oriental experienced pervasive deformation. The zone between these these two morphotectonic provinces and the areas of early uplift and deformation coincides with the north-south oriented Ordovician Eastern Puna Eruptive Belt (Bahlburg, 1990; Bahlburg & Hervé, 1997), where basement heterogeneities such as metamorphic fabrics and shear zones were preferentially reactivated during Andean mountain building (Hongn et al., 2010; Hongn & Riller, 2007; Montero-López et al., 2020). However, additional rheological and structural studies focusing on the localization of strain over geological time-scales will be required to further test the possibility that these principles also apply to the SCA and other mountain belts.

Geodynamic numerical modelling of convergent non-collisional margins has suggested that the strength of the overriding plate influences the angle of subduction of the oceanic plate (e.g. Manea et al., 2012; Sharples et al., 2014). Upper plates in a subduction system that are thick, mechanically strong, and moving towards the trench therefore favour subhorizontal subduction due to their strong plate coupling (Sharples et al., 2014). This could be the case for the northern part of the SCA (27°S–33°S), where a gently dipping slab has been identified beneath the thick, dense and potentially strong foreland of the South American Plate. In view of these considerations, the configuration of the overriding plate could indeed contribute to the maintenance of a shallow subduction angle in the northern part of the SCA.

We also investigated the thermal field and composition of the lithospheric mantle. Temperatures and densities converted from S-wave velocities show a heterogeneous distribution, with a northeast-southwest low temperature and high density trend at all depths (Fig. 3.6a-c). We interpret these lower temperatures and higher densities as being due to sampling of the slab, which is situated farther east in the northern part of the foreland and farther west in the central part of the foreland because of the N-S variation in the subduction angle (Fig. 3.5f). It remains unclear, however, why this anomaly is not visible in the southern sector of the foreland.

Finally, our results clearly indicate that the density distributions in the crystalline crust and the lithospheric mantle are clearly not spatially correlated with terrane boundaries inferred mainly from surface observations, such as those of the Chilenia-Cuyania-Pampia terranes (Fig. 3.13c; Ramos et al., 2010 and references therein). Although we observe heterogeneities in the average crustal densities, the boundaries between the different density domains do not generally coincide with those proposed for shallow crustal depths. The only exception to this observation is to the north of the Cuyania Terrane (29°S–33°S), where a sharp transition between areas of different crustal density coincides with the proposed terrane boundaries. These horizontal density contrasts correlate spatially with the loci of major reverse faults such as that responsible for the Valle Fértil Lineament in the east (e.g. Ramos et al., 1986), and with an ophiolitic belt in the west (Haller & Ramos, 1984), interpreted as the Cuyania-Pampia and Cuyania-Chilenia boundaries, respectively (Fig. 3.13c). The near-surface expression of these features terminates at about 33 or 34°S (Álvarez et al., 2012; Boedo et al., 2016) and their southward continuation remains poorly constrained. If, however, these boundaries continue farther south, the individual crustal compositions of each terrane are likely to have been overprinted by tectonic processes that occurred subsequent to their accretion to Gondwana. An alternative scenario is that the crustal heterogeneities of each terrane stem from tectonic processes that occurred prior to their accretion to Gondwana. In line with this latter interpretation, previous investigations (Ramos et al., 1998) have argued that the crustal composition of the Cuyania terrane is heterogeneous on the basis of differences in basement composition between the Precordillera and the westernmost Sierras Pampeanas, which would have to be older than the proposed terrane collision during the Middle to Late Ordovician. It is therefore also plausible that other pre-collisional crustal heterogeneities might extend farther south. Nevertheless, from the relationship between crustal density domains and tectonic events that occurred after the terrane accretion discussed above, we favour the hypothesis that the crustal heterogeneities developed after terrane accretion. Indeed, continuous crustal domains sutured in deformation phases that occurred prior to the Andean orogeny appear to act as coherent assemblages. A possible explanation for this observation is that the dominant process controlling the present-day configuration of the SCA lithosphere is the subduction of oceanic crust at the convergent margin. Nevertheless, further investigations are required before a robust conclusion can be reached, including for instance, high resolution seismological experiments to constrain P- and S-wave velocity variations within the crust and the use of additional constraints from gravity gradients. Such detailed studies would help to clearly define the terrane boundaries, if present.

3.8 Conclusions

By integrating different geological and geophysical datasets, including seismic, gravity, and petrological data, we have derived a 3D structural and density model describing the first-order characteristics of the lithosphere beneath the southern Central Andes (SCA), their forearc and their foreland. Our findings suggest that:

1. The crystalline crust is thicker (~55 km) and less dense (~2900 kgm^{-3}) beneath the orogen (magmatic arc and main orogenic wedge) than beneath the forearc (~35 km, ~2975 kgm^{-3}) and foreland (~30 km, ~3000 kgm^{-3}). The foreland comprises three principal crustal domains: (1) a thick, dense northern domain (40–60 km, ~3000–3050 kgm^{-3}); (2) a thin, dense southern domain (~20 km, ~3050 kgm^{-3}); and (3) a central domain with intermediate crustal thickness (35-45 km) and low to intermediate crustal densities (~2900–2950 kgm^{-3}). These variations are likely to reflect differences in the long-term tectono-magmatic evolution of each domain.

2. The average-density configuration within the crystalline crust correlates spatially with the location of major seismic events and the present-day horizontal surface strain-rates. The highest horizontal surface strain rates occur in the areas with the highest topographic gradients within the orogen, and across regions with abrupt variations in crustal density. This suggests that crustal compositions and associated rheological variations exert an important influence on short-term deformation patterns.
3. North of 33°S the thick crust of the orogen and the thick and potentially strong crust of the foreland may enhance the coupling between the subducting and overriding plates, which could facilitate the establishment of a sub-horizontal subduction setting.
4. There is generally no spatial relationship evident between the boundaries proposed for the Pampia-Cuyania-Chilenia terrane model and boundaries based on either the lithospheric density distribution or the surface-deformation patterns. If these boundaries were originally present, they must have been subsequently obliterated by tectono-magmatic processes following the accretion of these terranes to the margin of Gondwana. These results also suggest that in the SCA the terrane provenance has little influence on present-day deformation.
5. The northeast-southwest trending low-temperature, high-density feature modelled for the lithospheric mantle reflects the perturbation of the thermal field by the cool subducting slab of the Nazca Plate.

Chapter 4: Controls of the lithospheric thermal field of an ocean-continent subduction zone: the southern Central Andes

4.1 Abstract

In an ocean-continent subduction zone, the assessment of the lithospheric thermal state is essential to determine the controls of the deformation within the upper plate and the dip angle of the subducting lithosphere. In this study, we evaluate the degree of influence of both the configuration of the upper plate and variations of the subduction angle on the lithospheric thermal field of the southern Central Andes (29°–39°S). Here, the subduction angle increases from subhorizontal (5°) north of 33°S, to steep (~30°) in the south. We derived the 3D temperature and heat flow distribution of the lithosphere in the southern Central Andes considering conversion of S-wave tomography to temperatures together with steady-state conductive modelling. We found that the orogen is overall warmer than the forearc and the foreland, and that the lithosphere of the northern part of the foreland appears colder than its southern counterpart. Sedimentary blanketing and the thickness of the radiogenic crust exert the main control on the shallow thermal field (< 50 km depth). Specific conditions are present where the oceanic slab is relatively shallow (< 85 km depth) and the radiogenic crust is thin, This configuration results in relatively colder temperatures compared to regions where the radiogenic crust is thick and the slab is steep. At depths >50 km, the temperatures of the overriding plate are mainly controlled by the mantle heat input and the subduction angle. The thermal field of the upper plate likely preserves the flat subduction angle and influences the spatial distribution of shortening.

4.2 Introduction

Temperature exerts a first-order control on the rheology of the lithosphere, affecting the depth of the brittle-ductile transition zone and the occurrence of thermally activated creep processes (Mareschal & Jaupart, 2013; Turcotte & Schubert, 2002). In an active ocean-continent convergent plate-boundary system, the assessment of the temperature distribution within the lithosphere is crucial for understanding the mechanisms controlling subduction geometry (e.g., slab dip and subduction-zone curvature) and the localization of deformation within the upper plate, including the vergence of thrust belts (Allmendinger & Gubbels, 1996; Barrionuevo et al., 2021; Ibarra et al., 2021; Kley et al., 1999; Kusznir & Park, 1984; Liu, 2020).

Estimating the thermal state of the system is challenging, however, as it requires deciphering the complex and continuous interplay between different heat-transport mechanisms (conduction and convection) and heat sources. These across-scales phenomena include heat conduction, advection of the oceanic plate that steadily supplies colder material, variations of thermal properties within the plates (radiogenic heat production and thermal conductivity), frictional heating along the subduction interface, latent heat due to mineralogical phase transformations within the oceanic plate, and adiabatic heating in the asthenosphere (for a review, see Goes et al., 2020; Peacock, 2020).

Many modelling studies (Boonma et al., 2019; Čížková & Bina, 2013; van Keken et al., 2019) have considered the temperature distribution of the lithosphere as the main driver of the dynamics of a subduction system. These studies adopted a simplified configuration of the upper plate in terms of its thickness and rock composition (van Keken et al., 2019). However, the continental lithosphere is the product of a complex tectonic and magmatic history, involving terrane amalgamation, trench erosion, crustal thickening during subduction and collision, and extensional overprinting either during the final stages of orogeny or from deep-seated processes in the mantle (Rudnick & Gao, 2003; Taylor, 1967). To address these considerations, other modelling studies have effectively shown how the present-day thermal field varies with respect to thickness and compositional heterogeneities within the lithosphere (Freymark et al., 2017; Kaban et al., 2014; Scheck-Wenderoth et al., 2014; Sippel et al., 2017; Spooner et al., 2020; Tesauro et al., 2009) and how these variations ultimately affect the long-term rheology of the lithospheric plate (Anikiev et al., 2020; Ibarra et al., 2021; Ibarra & Prezzi, 2019; Tesauro et al., 2009).

The southern Central Andes (SCA, 27°S–40°S, Fig. 4.1) are a suitable region for studying the effect of both a heterogeneous configuration of the upper plate and differences in subduction geometry on the lithospheric thermal field in an ocean-continent convergent plate-boundary system for several reasons. Bordering the convergent margin between the oceanic Nazca Plate and the continental South American Plate, the SCA encompass several morphotectonic provinces across the strike of the subduction zone, each characterized by a distinct pre-Cenozoic geological history and lithospheric configuration. These differences are rooted in complex tectonic and magmatic episodes of shortening and extension that span from the Neoproterozoic to the Quaternary (Astini et al., 1995; Azcuy & Caminos, 1987; Giambiagi et al., 2003; Jordan et al., 1983; Kay et al., 2006; Llambias et al., 1993; Llambias & Sato, 1990; Mpodozis & Kay, 1990; Ramos et al., 1996). Major pulses of Andean deformation are thought to have occurred during the Late Cretaceous and Miocene (Boyce et al., 2020; Fennell et al., 2015), when the style of deformation was significantly influenced not only by the characteristics of the subducting plate (Kley & Monaldi, 2002; Oncken et al., 2006; Yáñez & Cembrano, 2004), but also by the reactivation of inherited tectonic heterogeneities, which influenced Cenozoic phases of erosion, sedimentation, and geomorphic evolution (del Papa et al., 2013). The SCA are subdivided into four first-order morphotectonic provinces: the forearc, the magmatic arc, the back-arc, and the foreland (Fig. 4.1; Allmendinger et al., 1997; Isacks, 1988; Jordan et al., 1983). These extensive regions are in turn subdivided into morphotectonic provinces that are characterized by distinct structural and geomorphic features. For the purposes of this study, we have defined as the Andean orogen only the magmatic arc and backarc provinces that constitute the orogenic wedge, and thus not included the fold-and-thrust belt of the Precordillera and the Payenia volcanic province. The main features of the foreland are the reverse-fault bounded basement uplifts of the Sierras Pampeanas and the Neuquén and Cuyo basins (Fig. 4.1).

A distinct feature of the SCA is the variation in the subduction angle along the strike of the subduction zone, transitioning between 33°S and 34.5°S from subhorizontal (<5°) in the north (Chilean-Pampean flat-slab area; Ramos et al., 2002) to relatively steep (~30°) in the south (Fig. 4.1; e.g., Barazangi & Isacks, 1976; Cahill & Isacks, 1992). Even though the present-day subduction regime has been active since at least Early Jurassic (Maloney et al., 2013 and references therein), the flattening of the slab north of 33°S presumably began at ~19 Ma (Jones et al., 2014, 2015, 2016), finally achieving its subhorizontal configuration at ~7–6 Ma (for a review see Kay et al., 2006a; Kay & Mpodozis, 2002; Ramos et al., 2002). It has been proposed that this flattening event is responsible for the absence of present-day magmatism between 27°–33°S (Fig. 4.1) (Kay et al., 2006a; Kay & Mpodozis, 2002). Several causal mechanisms have been suggested for triggering flat subduction at these latitudes, including: (i) buoyancy of the slab due to the subduction of an aseismic ridge (Gutscher, 2002; Kay & Mpodozis, 2002; Yáñez et al., 2001); (ii) fast trenchward motion of the overriding plate that inhibits slab rollback and drives the trench to retreat (van Hunen et al., 2000); and (iii) enhanced coupling between the oceanic and continental plates due to the greater strength of the continental plate (Hu et al., 2016; Manea et al., 2012; Rodriguez Piceda et al., 2021; Sharples et al., 2014).

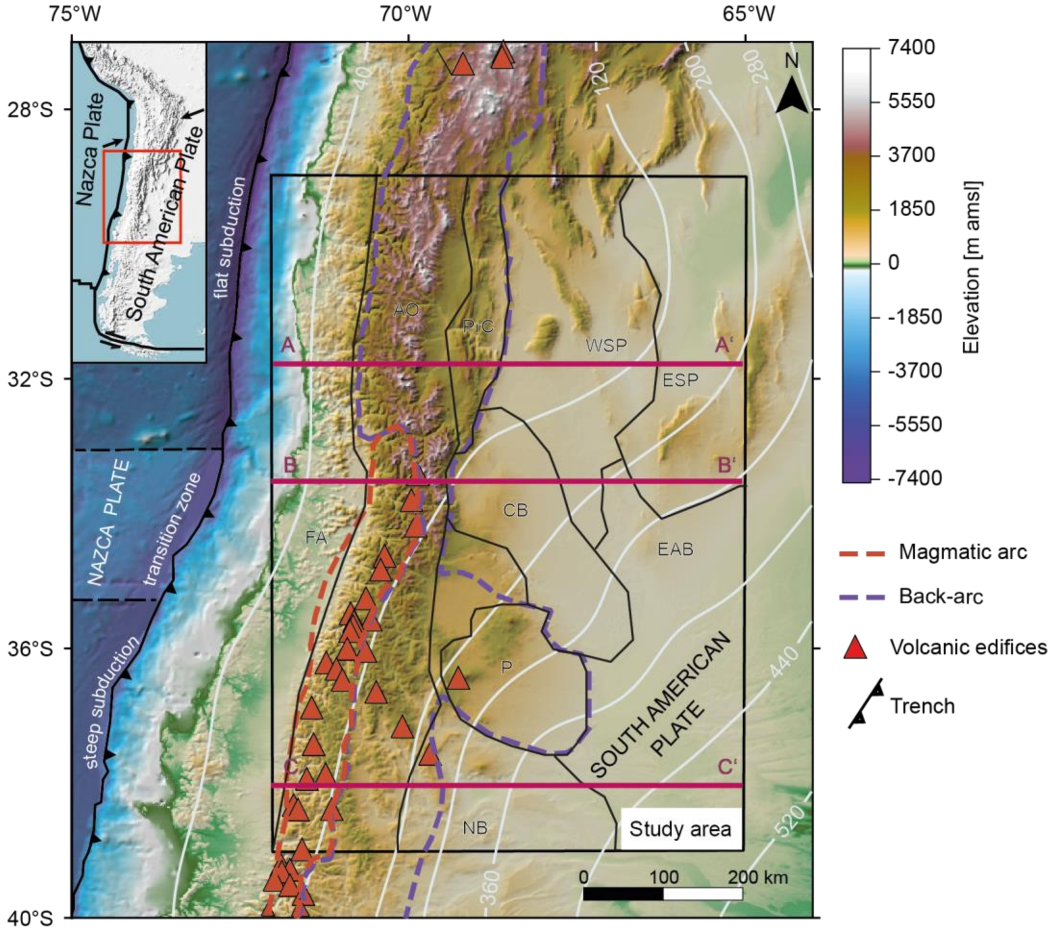

Figure 4.1: Topography and bathymetry of the region based on the ETOPO1 global relief model (Amante & Eakins, 2009), showing the extent of the subduction segments with steepening subduction angles from north to south. The boundaries between the subduction segments are indicated with black dashed lines. The depth contours (km below sea level) of the top of the slab from SLAB2 (Hayes et al., 2018) are shown in white lines. The black rectangle denotes the extent of the area modeled in this study. The boundaries between the main morphotectonic provinces are shown in black lines. Red triangles show the location of active volcanic edifices. The purple dashed lines enclose the back-arc domain, and the red dashed lines the magmatic arc. The magenta lines show the location of the cross-sections in Figure 4.13. Abbreviations of main tectonic provinces: AO = Andean orogen, CB = Cuyo Basin, ESP = Eastern Sierras Pampeanas, EAB = extra-Andean basins, FA= forearc, NB = Neuquén Basin, P = Payenia volcanic province, Prc = Precordillera, WSP = Western Sierras Pampeanas.

In the SCA, surface heat flow, shallow subsurface temperatures, and magmatic activity vary significantly across the subduction system, which generally has been attributed to the geometry of the subducting Nazca plate (Hamza et al., 2005; Hamza & Muñoz, 1996; van Hunen et al., 2000, 2002, 2004; Marot et al., 2014; Uyeda & Watanabe, 1982; Wagner et al., 2005, 2006; Ward et al., 2013). Early studies (Hamza et al., 2005, 2008; Hamza & Muñoz, 1996; Uyeda & Watanabe, 1982), based on lower surface heat-flow values (20–70 mWm^{-2}; 50–120 mWm^{-2}), suggested that the flat-slab segment is colder than its steeper counterparts, a hypothesis which was also supported by geodynamic numerical modelling (van Hunen et al., 2000, 2002, 2004) and seismic tomography (Marot et al., 2014; Wagner et al., 2006; Wagner et al., 2005; Ward et al., 2013). According to the latter studies, low v_P/v_S ratios (P-wave/S-wave velocity <1.75) characterize the flat-slab segment in the northern part of the SCA, in contrast to the higher v_P/v_S ratios encountered to the south, which are within the range typically found for most subduction zones (Manea et al., 2017). The thermal contrast between the two differently dipping segments in the SCA is commonly linked to variations in the extent of the mantle wedge and arc magmatism, both of which are drastically reduced in the flat-slab segment (Gutscher et al., 2000; Henry & Pollack, 1988; Kay et al., 2006a ; Manea et al., 2017; Manea & Manea, 2011; Prezzi et al., 2014). All previous studies therefore seem to suggest that the forearc is an area with low surface heat flow in response to the subduction of cold oceanic crust at shallow depths.

These interpretations have recently been challenged by local-scale studies which indicate that part of the thermal variations in the lithosphere of the SCA are not related to the effect of the subducting plate (Astort et al., 2019; Collo et al., 2018; Ibarra & Prezzi, 2019; Sánchez et al., 2018, 2019; Sigismondi, 2012). For example, Sánchez et al., (2018, 2019) provided evidence for a significant difference in surface heat flow between the orogen (85–95 mWm^{-2}) and the foreland (~45–60 mWm^{-2}) at the latitudes of the flat-slab region and proposed structural and/or compositional variations within the crust and different heat-flow input at the base of the lithosphere as possible reasons for this phenomenon. However, none of these hypotheses have yet been validated by a detailed study of the configuration of the lithosphere in terms of its geometry and composition.

In light of the open questions, we aim to test in this contribution how mantle thermal anomalies and first-order structural and lithological heterogeneities in the overriding plate across and along strike of the subduction system affect the thermal field of the SCA. In order to do so, we followed a data-based modelling approach. Seismic velocities (Assumpção et al., 2013) were converted to temperatures to obtain the deep thermal field in the mantle and across the subduction interface. In the model domains shallower than 50 km, where no mantle shear-wave velocity data are available for conversion to temperatures, we calculated the steady-state conductive thermal field. To test the assumption of thermal equilibrium, we analyzed the effects of time-dependent processes related to subduction dynamics by carrying out a transient analysis for the portion of the model domain with lack of constraints from seismic data. Steady-state conductive temperatures in the shallow model domain were computed based on an existing 3D structural and density model of the SCA (Rodriguez Piceda et al., 2021), which is consistent with available geological and geophysical data. We assigned thermal properties according to the lithological characteristics of the sedimentary cover rocks, the crystalline crust, continental lithospheric mantle and oceanic plate, which allowed us to evaluate the control of the lithospheric structure on the resulting temperature distribution. The validity of the inferred thermal structure was assessed by comparison with temperature and surface heat flow measurements available for the studied area and a detailed sensitivity analysis of the model. One main challenge of this approach is related to the sparse coverage of thermal measurements in certain parts of the model. To sort this problem, our results were qualitatively compared with other proxies of the thermal state of the area with larger spatial coverage, including seismic attenuation and elastic thickness patterns. As a result, we have obtained a 3D thermal model of the SCA and adjacent foreland regions that describes the relative temperature variations between the geological units of different composition and lateral and depth extents. Finally, this model allows us to make a qualitative analysis of the thermal feedback mechanisms between these different geological units.

4.2.1 Lithospheric configuration of the southern Central Andes

The main thickness and density variations of the layers constituting the SCA lithosphere were recently described in a 3D lithospheric-scale, density and structural model of the SCA (Rodriguez Piceda et al., 2021). This model was constrained by an array of geological and geophysical data, including seismic reflection and refraction profiles, seismic tomography, sediment-isopach maps, and gravimetric observations (Assumpção et al., 2013; Hayes et al., 2018; Heine, 2007; Ince et al., 2019; Mescua et al., 2016; see references in Rodriguez Piceda et al., 2021). The original model covers a region of 700 km by 1100 km with a horizontal resolution of 25 km and a depth of 200 km below mean sea level (bmsl), comprising the forearc, the Andean orogen, and the foreland regions. The vertical resolution varies as a function of the thickness of the corresponding layers, which were mainly defined on the basis of density contrasts. These layers comprise, from top to bottom: (1) water; (2) marine sediments; (3) continental sediments; (4) upper continental crystalline crust; (5) lower continental crystalline crust; (6) continental lithospheric mantle; (7) shallow oceanic crust; (8) deep oceanic crust; (9) oceanic lithospheric mantle; and (10) oceanic sub-lithospheric mantle. Figure 4.2 illustrates the main structural features of the 3D model (see Rodriguez Piceda et al. (2021) for more details)

Overall, maximum sedimentary thickness occurs in the Cuyo and Neuquén basins (Fig. 4.2a). The Andean orogen has thicker crystalline crust (55 km) than the forearc (~35 km) and the foreland (~30 km) (Fig. 4.2b). The remaining parts of the back-arc and the foreland can be subdivided into three crustal domains: (i) a thick northern domain (40–60 km); (ii) a thin southern domain (~20 km); and (iii) a central domain with intermediate crustal thickness (35–45 km). The areas with the greatest upper crustal thickness comprise the orogen (20–40 km) and the Payenia volcanic province (20 km). In contrast, in the Neuquén Basin the upper crustal thickness thins up to 5 km (Fig. 4.2c). The greatest lower crustal thickness (~30–45 km) exists in the northern part of the back-arc and foreland regions of the Precordillera and Sierras Pampeanas (Fig. 4.2d).

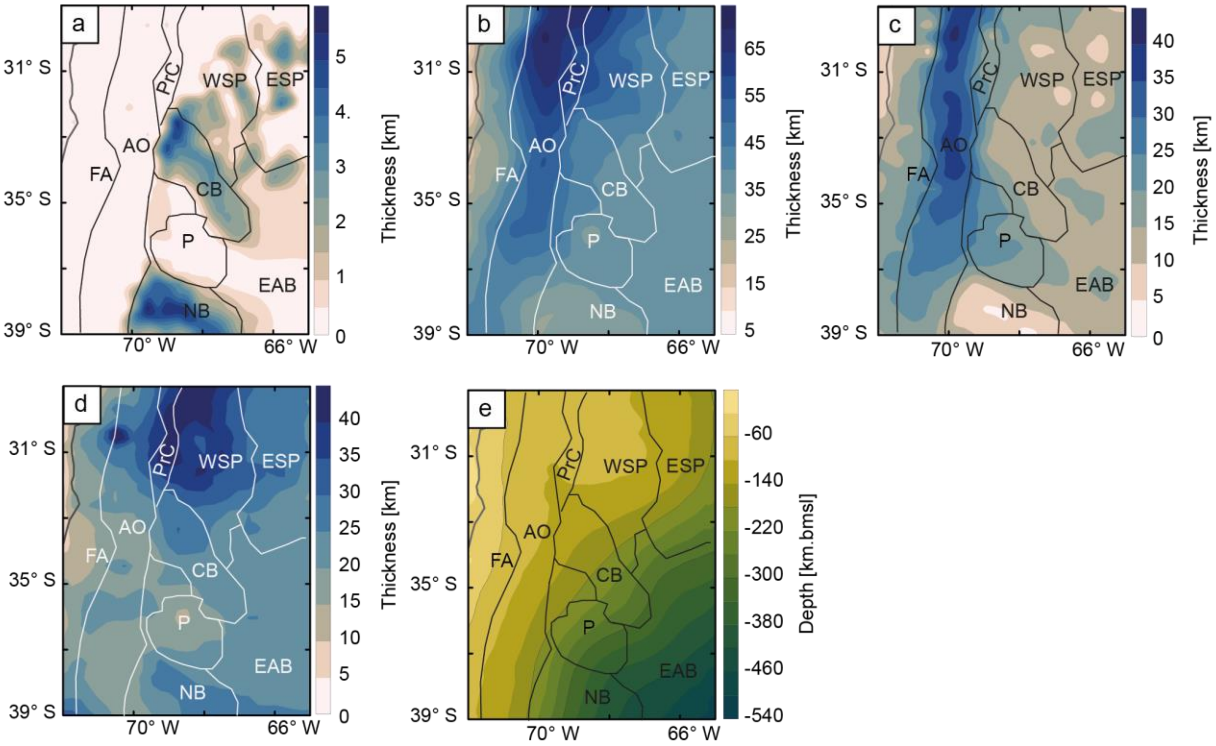

Figure 4.2: Main structural features of the studied lithosphere from the model of Rodriguez Piceda et al. (2021): thickness of (a) marine and continental sediments; (b) continental crystalline crust; (c) felsic upper continental crystalline crust; (d) mafic lower continental crystalline crust; (e) depth to the subduction interface, coinciding with the top to the oceanic crystalline crust west of the trench and with the top surface of the slab east of the trench.

4.3 Modelling approach

The general workflow followed in this study is illustrated in Figure 4.3a. Figure 4.3b shows the 3D model box, where different thermal modelling approaches and corresponding thermal boundary conditions were applied. To predict the present-day thermal configuration of the SCA and discuss its controlling factors, we subdivided the model volume into two domains: a deep domain between a depth of 50 and 200 km bmsl, where temperatures were converted from S-wave seismic velocities (here referred to as 'v_s-to-T conversion'); and, a shallow domain, including the crust and uppermost mantle down to a depth of ~50 km bmsl, where the steady-state conductive thermal field was calculated using as input the 3D structural and density model of the area (Rodriguez Piceda et al., 2021). The reasons for this subdivision are: the v_s-to-T conversion being developed for application to mantle rocks and the limited quality of mantle velocity data for depths shallower than 50 km.

4.3.1 Calculation of temperatures in the deep domain

To estimate mantle temperatures between 50 km and 200 km, we used the results of the S-wave mantle tomography of Assumpção et al. (2013). This tomographic model is an updated version of the S-wave tomography of Feng et al. (2007) for the South American region, where the velocity structure of the upper mantle was constrained through the joint inversion of S and Rayleigh waveforms and fundamental mode group velocities of Rayleigh waves. The original data set is restricted to depths between 50 km and 400 km, with a horizontal resolution of approximately 25 km (Feng et al., 2007). Our choice on the tomography of Assumpção et al. (2013) rather than other global tomographic models covering the study area (Schaeffer & Lebedev, 2013) stems from the fact that this model has a more refined lateral and vertical resolution, and offers a better spatial correlation between high-velocity features and the track of the slab (Hayes et al., 2018; Fig. B.1 in Appendix).

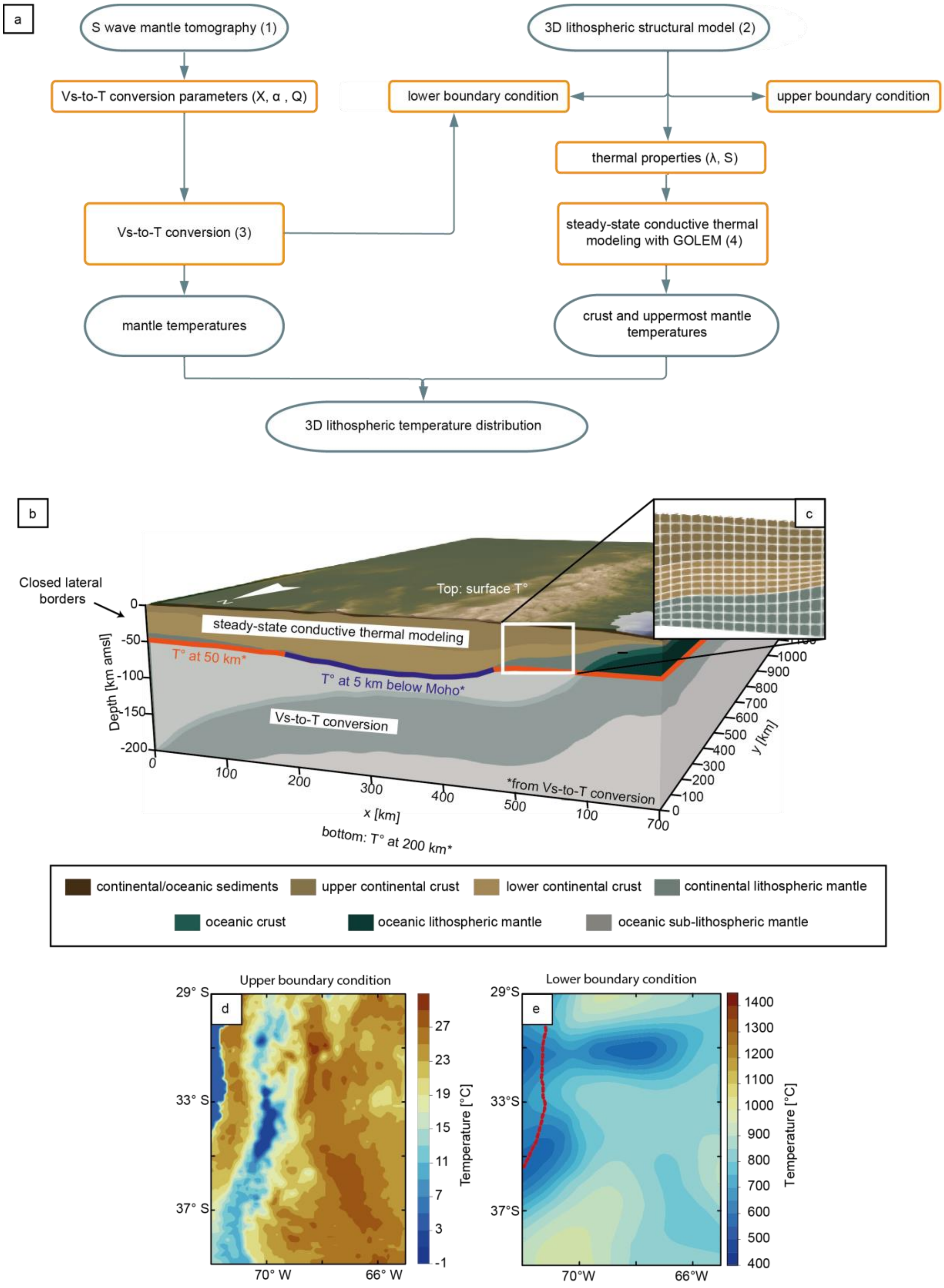

Figure 4.3: (a) General workflow followed in this study to estimate temperatures in the SCA lithosphere. (b) 3D model box indicating the lithospheric domains where the conversion of seismic velocities (grey-shaded area) and the steady-state conductive modelling (non grey-shaded area) were applied. The type of thermal boundary conditions considered for the conductive steady-state modelling are also shown. (c) close-up of Finite Element mesh used for the steady-state conductive thermal modelling. (d) Upper and (e) lower boundary conditions applied to the conductive steady-state model. (1) Rodriguez Piceda et al. (2021); (2) Assumpção et al. (2013); (3) Goes et al. (2000); Meeßen (2017),; (4) Cacace & Jacquey (2017); Jacquey & Cacace (2017). λ = thermal conductivity, S = radiogenic heat production; X = mantle composition, α = thermal expansion coefficient, Q = anelasticity.

To compute temperatures from S-wave velocities, we used the python tool VelocityConversion (Meeßen, 2017) which is a modified version of the original approach by Goes et al. (2000). The method by Goes et al. (2000) is based on laboratory measurements of mantle mineral properties and considers anharmonicity and anelasticity of seismic waves. The equation that relates v_s in a rock with a given composition X under a temperature T and a pressure P condition is written as follows:

$$v_S(P,T,X,\omega) = \sqrt{\frac{\mu(P,T,X)}{\rho(P,T,X)}} - \big(1 - \varepsilon(\omega,T,a)\big), (4.1)$$

where ω is the wave frequency, μ is the shear modulus, ρ is the density, a the wave frequency exponent, and ε the attenuation term. ε is defined as:

$$\varepsilon(\omega,T,a) = \frac{2}{Q(\omega,T)tan\left(\frac{\pi a}{2}\right)}, (4.2)$$

with Q being the attenuation due to anelasticity, described as:

$$Q(\omega,T) = A\omega^a exp\left[\frac{a(H+P.V)}{RT}\right], (4.3)$$

where A and R are the anelastic and universal gas constants, respectively; H is the activation energy and V is the activation volume.

From equation 4.1, it is clear that the computation of mantle temperatures requires to define the mantle composition X described in terms of its main mineral phases (olivine, orthopyroxene, clinopyroxene, and spinel/garnet) and iron content (Goes et al., 2000). For each mineral phase, temperature and pressure (up to 6 GPa), the density ρ and the elastic modulus M (shear modulus μ and/or compressibility K) from their values at the reference state (P_0, T_0) are calculated as:

$$\rho(P,T) = \rho(P_0,T_0)\left[1 - \alpha(T - T_0) + \frac{P-P_0}{K}\right] (4.4)$$

and

$$M(P,T) = M(P_0,T_0) + (T - T_0)\frac{\partial M}{\partial T} + (P - P_0)\frac{\partial M}{\partial P} \ (4.5)$$

where α is the thermal expansion coefficient.

The implementation by Meeßen (2017) calculates the v_s and the corresponding density at each depth in the seismic tomography for temperatures between 300 and 3000 K in steps of 1 K. For the density computation, lithostatic pressure is computed relying on the AK135 seismic model (Kennett et al., 1995). At each grid point, the algorithm compares the computed v_s with those from the tomographic model, by performing a look- up method over the table and choosing the two closest values to the velocity from the tomography. Then, the temperatures and corresponding densities are linearly interpolated to obtain the final values.

For this study, we chose different mantle compositions (spinel or garnet), listed in Table 4.1, according to the respective stable aluminum phase at depth (Wyllie, 1981). For shallow depths (50–80 km), a mantle composition corresponding to a spinel lherzolite was assigned, based on mantle xenoliths found in the Payenia volcanic province (Conceição et al., 2005; Jalowitzki et al., 2010). Between 80 km and 200 km, the stable composition was assumed to correspond to garnet lherzolite (Maaløe & Aoki, 1977). Mineral properties α, $\rho(P_0,T_0)$, $M(P_0,T_0)$, $\partial M/\partial T$ and $\partial M/\partial P$ were taken Cammarano et al. (2003) and Goes et al. (2000). The thermal expansion coefficient α was assumed constant for each mineral phase. The frequency exponent a and anelasticity parameters A, H and V were taken from Sobolev et al. (1996) (Table 4.2).

Table 4.1: Mantle composition used for the conversion of v_s to temperatures (Goes et al., 2000; Meeßen, 2017). Ol = olivine; Opx = orthopyroxene; Cpx = clinopyroxene; Sp = spinel; Gnt = garnet. The sum of mineral fractions is equal to 1. Xfe = iron content in molar fraction. Xfe is calculated as (1-Mg#)/100, where Mg# is the magnesium number.

Mantle unit	**Lithology**	**Ol**	**Opx**	**Cpx**	**Sp**	**Gnt**	**Xfe**
50-80 km	Spinel lherzolite [1]	0.60	0.17	0.19	0.04	-	0.10
80-200 km	Garnet lherzolite[2]	0.63	0.30	0.02	-	0.05	0.08

[1] Conceição et al. (2005); Jalowitzki et al. (2010); [2] Maaløe & Aoki (1977)

Table 4.2: Anelasticity parameters used for the conversion of v_s to temperatures (Sobolev et al., 1996)

Anelastic constant, A	0.48
Activation energy, H [J mol^{-1}]	5e5
Activation volume, V [m^{3}mol^{-1}]	2e-5
Frequency exponent, a	0.15

The temperature configuration derived from the v_S-to-T conversion in the parameter space of v_S and depth is shown in Figure 4.4, which also depicts three 1-D v_S profiles representative of the orogen at the latitudes of the flat slab, the steep slab, and the transition zone. In general, temperature increases with increasing depth and decreasing velocity. The largest temperature variations occur for depths shallower than 100 km and high v_S (>4.6 km s^{-1}), which is characteristic of the flat-slab domain.

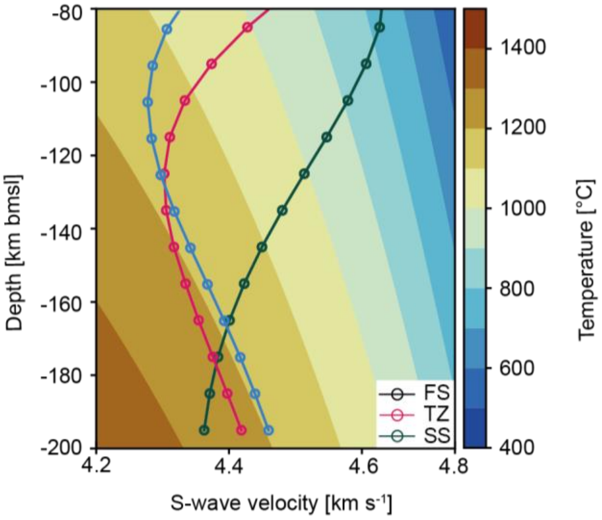

Figure 4.4: Mantle-temperature distribution as a function of v_S and depth (obtained using VelocityConversion; Meeßen, 2017) overlain by 1-D v_S profiles of the seismic tomography of (Assumpção et al., 2013). FS = flat-slab domain; TZ = transition domain; SS = steep-slab domain

4.3.1.1 Sensitivity of the vs-to-T conversion

Quantifying uncertainties in the v_S-to-T conversion is difficult due to the combined effects of uncertainties related to the conversion parameters (i.e. anelasticity model, mantle composition, An et al., 2015). An additional source of uncertainty is the S-wave tomography, as a 0.1% perturbation in v_S, for example, can translate into temperature variations of 50°–250°C. Previous studies (An et al., 2015; Goes et al., 2000) assumed a temperature uncertainty of 150°C in the v_S-to-T conversion at Moho depths, but recognized larger uncertainties at greater depths. We therefore reexamined the uncertainty of the conversion method of Goes et al. (2000) by testing the model sensitivity with respect to mantle composition X, thermal expansion coefficient α and attenuation Q. Regarding the conversion method, although several approaches exist (Deschamps et al., 2002; Priestley & Mckenzie, 2006; Steinberger & Calderwood, 2006; Stixrude & Lithgow-Bertelloni, 2005), we only tested the method of Priestley & Mckenzie

(2006) as implemented by Meeßen (2020) (Model PM). In a first step, we set up a model ('reference model' hereafter) based on the following parametrization: (i) mantle composition X corresponding to a garnet lherzolite (Table 4.1); (ii) constant expansion coefficient α and (iii) anelasticity Q by Sobolev et al. (1996) (Table 4.2). In a second stage, we tested alternative models by varying one parameter at a time: (i) mantle composition (spinel model), (ii) thermal expansion coefficient (α model) and (iii) attenuation (Q2 Model). In all cases, the conversion was limited to the depth interval of 50–200 km, as thought to be representative of the lithospheric mantle. A detailed description of the setup of these alternative models is provided in the Appendix B.2. In Chapter 4.4.1 we discuss in greater details the results from the same sensitivity analysis as applied to the tomography of Assumpção et al. (2013), while in section 4.1.2 we open a discussion on the implications of this sensitivity analysis on the modeled deep thermal field.

4.3.2 Calculation of temperatures in the shallow domain

To estimate temperatures in the shallow domain (that is in the crust and the mantle above 50 km), we used the geometry of the lithospheric layers of the 3D model as described in Section 4.2.1 (Rodriguez Piceda et al., 2021) as input to solve for the steady state heat conduction equation (Fig. 4.2). Under steady-state conditions, this equation reads as follows:

$$div(\lambda \nabla T) = -S \text{ (4.6),}$$

where T is the temperature (K), λ is the bulk thermal conductivity ($Wm^{-1}K^{-1}$), and S is the radiogenic heat production (Wm^{-3}). Equation 4.6 describes the conservation of internal energy under the assumption of thermal equilibrium. This last assumption might be over-restrictive especially for young slabs, where the additional effects from thermal advection from the advancing megathrust might be relevant. We discuss the influence of deviations from thermal equilibrium due to advection of the cold subducting plate in Section 4.5.1.1.

Temperatures were calculated with the finite element code GOLEM (Cacace & Jacquey, 2017; Jacquey & Cacace, 2017). For the thermal computation, three modifications were made to the original 3D configuration. First, the water layer was removed, thus treating the topography/bathymetry as the top of the model (cf. Fig. 4.1). Second, the horizontal resolution was increased from 25 km in the original structural model to 5 km and, third, the layers were vertically refined by a factor of 3 to 32 in order to ensure that (i) each layer has at least three finite elements and (ii) most of the model domain is represented by a cubic finite element to ensure faster numerical convergence (Fig. 4.3c). These modifications ensured to properly solve the temperatures in each node of the mesh without significantly increasing computational time.

Each unit of the 3D lithospheric model was populated with constant thermal properties (Fig. 4.3a; bulk conductivity λ and radiogenic heat production S) according to its main lithology (Appendix B.3). The characteristic lithologies, in turn, were selected based on the comparison between gravity-constrained densities (Rodriguez Piceda et al., 2021) and mean P-wave velocities (Araneda et al., 2003; Contreras-Reyes et al., 2008; Marot et al., 2014; Pesicek et al., 2012; Scarfì & Barberi, 2019), combined with rock-property compilations (Brocher, 2005; Christensen & Mooney, 1995) and other seismic properties (Alvarado et al., 2007; 2009; Ammirati et al., 2013, 2015, 2018; Gilbert et al., 2006; Wagner et al., 2005). A range of thermal properties (Čermák & Rybach, 1982; Hasterok & Chapman, 2011; He et al., 2008; Vilà et al., 2010; Xu et al., 2004) related to the chosen lithology for each layer was additionally tested until the best fit was achieved with a compilation of borehole temperatures mainly limited to the foreland basins (Collo et al., 2018). Table 4.3 summarizes the chosen values for each layer of the final (best fitting) model. A sensitivity analysis of the model results to the tested range of the thermal properties indicate that the modeled temperatures are most sensitive to variations in the thermal conductivity of the upper continental crystalline crust and the mantle (Appendix B.4).

To close equation 4.6, Dirichlet boundary conditions (i.e., fixed temperatures) were assigned along the top and base of the model. The upper thermal boundary condition was set at the topography/bathymetry (Fig. 4.3b), with temperatures extracted from the ERA-5 land database (Copernicus Climate Change Service (C3S), 2019; Fig. 4.3d, Appendix B.5). The lower boundary condition was set at the depth of the upper bound of the v_s-to-T conversion: a constant depth of 50 km bmsl for areas where the Moho is shallower than 50 km bmsl and at a surface 5 km deeper than the Moho where this interface is deeper than the abovementioned threshold (Fig. 4.3b). The temperature distribution at this boundary was derived from the v_s-to-T conversion (Fig. 4.3e; Assumpção et al., 2013); Section 4.3.1).

Table 4. 3: Lithology and thermal properties assigned to the units of the 3D structural model {Citation}. λ = bulk thermal conductivity; S = radiogenic heat production.

Layers		**λ [$Wm^{-1}K^{-1}$]**	**S [μWm^{-3}]**	**Lithology**
Continental/oceanic sediments		2.00[1]	1.00[2]	siliciclastic
Upper continental crystalline crust		3.40[1]	2.00[2]	dioritoid
Lower continental crystalline crust		2.50[1]	0.40[3]	mafic granulite
Oceanic plate	Shallow crust	1.80[1]	0.35[2]	basalt
	Deep crust	2.87[5]	0.25[2]	eclogite
Continental and Oceanic lithospheric mantle		2.24[4]	0.01[2]	moderately depleted lherzolite

[1] Čermák & Rybach (1982); [2] Vilà et al. (2010); [3] Hasterok & Chapman (2011); [4] Xu et al. (2004); [5] He et al. (2008)

4.4 Results

4.4.1 Thermal field of the deep domain

From the conversion of S-wave velocities taken from the tomography of Assumpção et al. (2013), we obtained the lower boundary condition of the steady-state conductive model (Fig. 4.4.5a) and the mantle-temperature distribution for the ~50–200 km depth interval (Figs. 5b–d). Across the lower boundary condition, temperatures range between 600°C and 1000°C. Two domains with temperatures of <700°C are identified: (i) a cold nose (CN) between 70°W and 72°W, beneath the forearc in the central and northern portion of the study area and (ii) a domain farther to the east where the slab flattens (FS) between 29.5°S and 32.5°S. The CN extends eastward above the transition zone and the steep-slab segment and is significantly attenuated above the flat-slab segment (Fig. 4.5a). With increasing depth (>75 km bmsl), this thermal feature is no longer visible, while the cold FS domain extends vertically over the entire mantle column of the overriding plate (Figs. 4.5a–c). At 80 km bmsl, temperature increases to the SW, with maximum values (~1100°C) located between 37°S–39°S and 70°W–72°W (Fig. 4.5b). At 125 km bmsl, temperatures follow a similar pattern as at 80 km depth, but differ in absolute value, with the cold FS domain reaching temperatures between 850°C and 900°C (Fig..4.5c). Towards the marine domain and to the south of the study area, temperatures increase up to 1300°C. At the base of the model (200 km bmsl), temperature ranges between ~1200°C and

~1350°C, with the lowest temperatures correlating spatially with the track of the slab (Hayes et al., 2018; Fig. 4.5d).

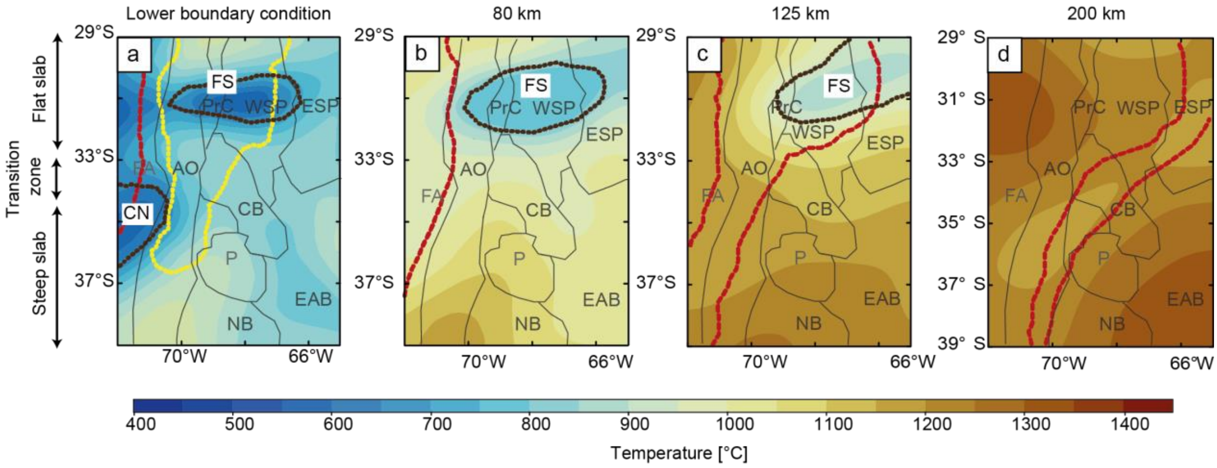

Figure 4.5: Temperature distribution obtained from the v_s-to-T conversion using the tomography of Assumpção et al. (2013) at depths of: (a) 50 km bmsl and at 5 km below the Moho in the interior of the area limited by the yellow line (lower boundary condition of the steady-state model); (b) 80 km bmsl; (c) 125 km bmsl; and (d) 200 km bmsl black lines in a–c indicate the extent of the cold mantle areas: CN = cold nose, FS = flat slab. Red lines denote the top and the bottom of the slab (Hayes et al., 2018).

We evaluated the effect of uncertainties in the parametrization of the v_S-to-T conversion applied to the seismic tomography of Assumpção et al. (2013) by comparing the model described above with alternative model scenarios (for details, see Appendix B.2). Figure 4.6 shows these alternative models in terms of the residual temperature at the lower thermal boundary condition of the steady-state model and at depths of 80, 125 and 200 km. The S-wave velocity distributions (Assumpção et al., 2013) at those depths are also depicted.

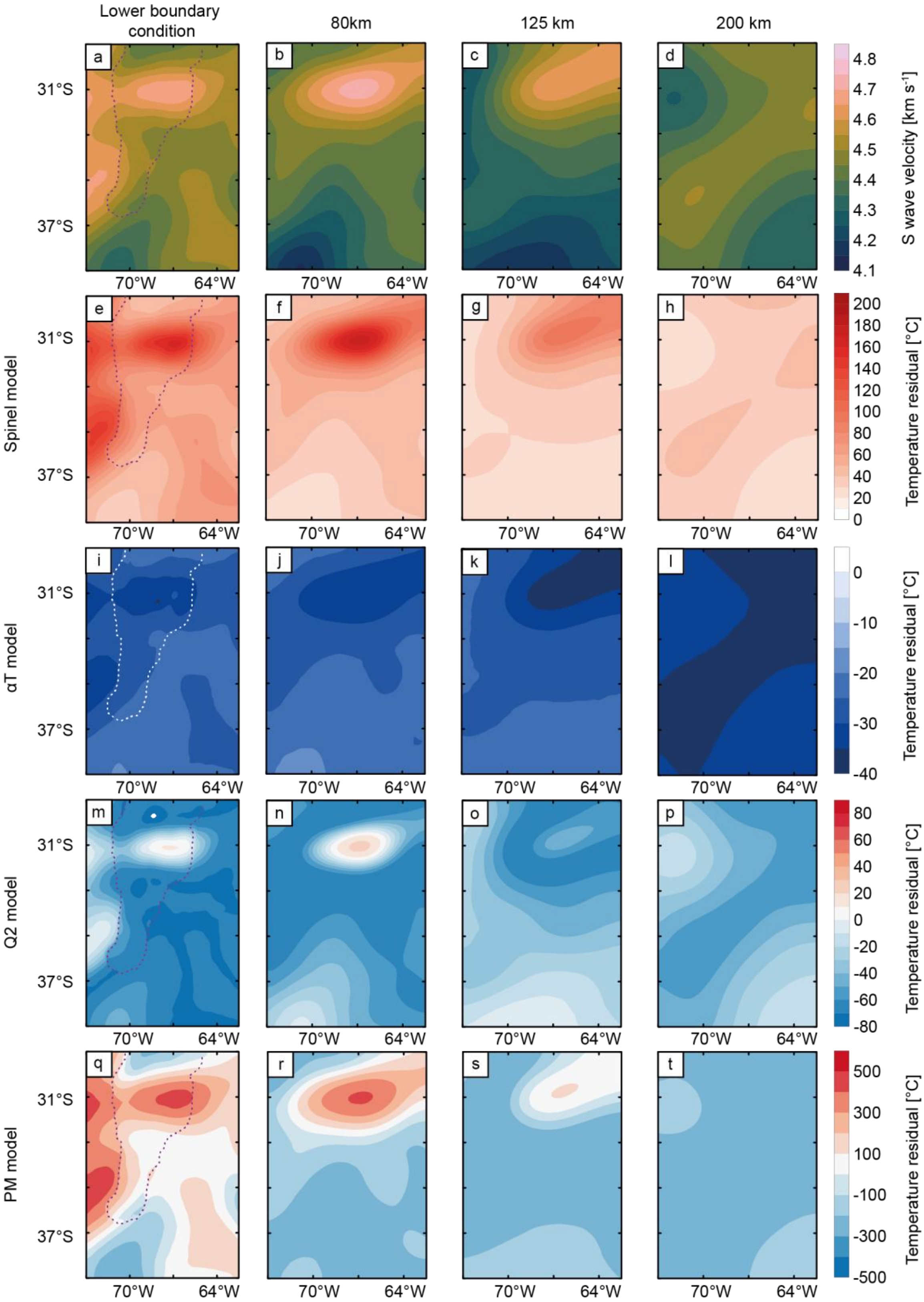

Figure 4.6: Results from sensitivity analysis of the v_s-to-T conversion (Appendix B.2). Slices at depths of the lower boundary condition of the steady state model, 80, 125 and 200 km bmsl (below mean sea level) showing the distribution of: (a-d) S-wave velocity from the seismic tomography of Assumpção et al. (2013) ; (e-t) Temperature residual (difference between the temperature fields of the reference model and each alternative configuration). (e-h) spinel model: with mantle composition of spinel lherzolite (Conceição et al., 2005; Jalowitzki et al., 2010); (i-l) αT model: with temperature-dependent thermal expansion coefficient (Cammarano et al., 2003; Goes et al., 2000; Saxena & Shen, 1992); (m-p): Q2 model: with anelasticity parameters from Berckhemer et al., (1982); (q-

t) PM model: with v_s-to-T conversion following (Priestley & Mckenzie, 2006). The dotted line in Figs. a, e, i, m and q marks the 45 km depth contour of the Moho.

Among the alternative models using the conversion method of (Goes et al. (2000), variation in mantle composition exert the strongest effect on the resulting temperature at shallow depths and where v_s is > 4.5–4.6 km s^{-1} (up to 200°C difference between the reference and the spinel models, Figs. 4.6e–f). In our study region, v_s of such high magnitudes characterizes the forearc and the flat-slab segment in the northern part of the foreland (Fig. 4.6a). Temperature residuals decrease with increasing depth, where lateral variations of v_s are less distinct. The conversion method of Priestley & Mckenzie (2006) yields the largest temperature differences among all the alternative models, predicting up to ± 400°C difference for areas with high (>4.5 km s^{-1}) and low (<4.5 km s^{-1}) v_s, respectively (Figs. 4.6q-r).

4.4.2 Thermal field of the shallow domain

From the steady-state conductive approach, we computed the thermal field of the crust and uppermost mantle to the depth of the lower boundary condition. Figure 4.7 shows the temperature distribution at depths of 2, 5, 10, 20, 25, 30, 35, 40, 45 km bmsl and of the Moho. At 2 km bmsl, temperatures range between 15°C and 165°C (Fig. 4.7a). As expected, the warmest areas are those with the highest topography (4–6 km height; cf. Fig. 4.1) and the largest upper crustal thickness (30–40 km, cf. Fig. 4.2c), which correspond to the central and northern segments of the Andean orogen. In addition, the forearc is characterized by an overall lower temperature than the orogen (40°–80°C), but by a more pronounced lateral gradient with values increasing toward the Andes. The foreland and low-elevation back-arc regions are characterized by a wide temperature range (60°–115°C), with warmer temperatures in the Precordillera, the Payenia volcanic province, and the Cuyo and Neuquén basins. Down to 25 km bmsl, the spatial trends of temperature distribution are similar to those observed at shallow depths, but with different absolute values (Figs. 4.7b–e).

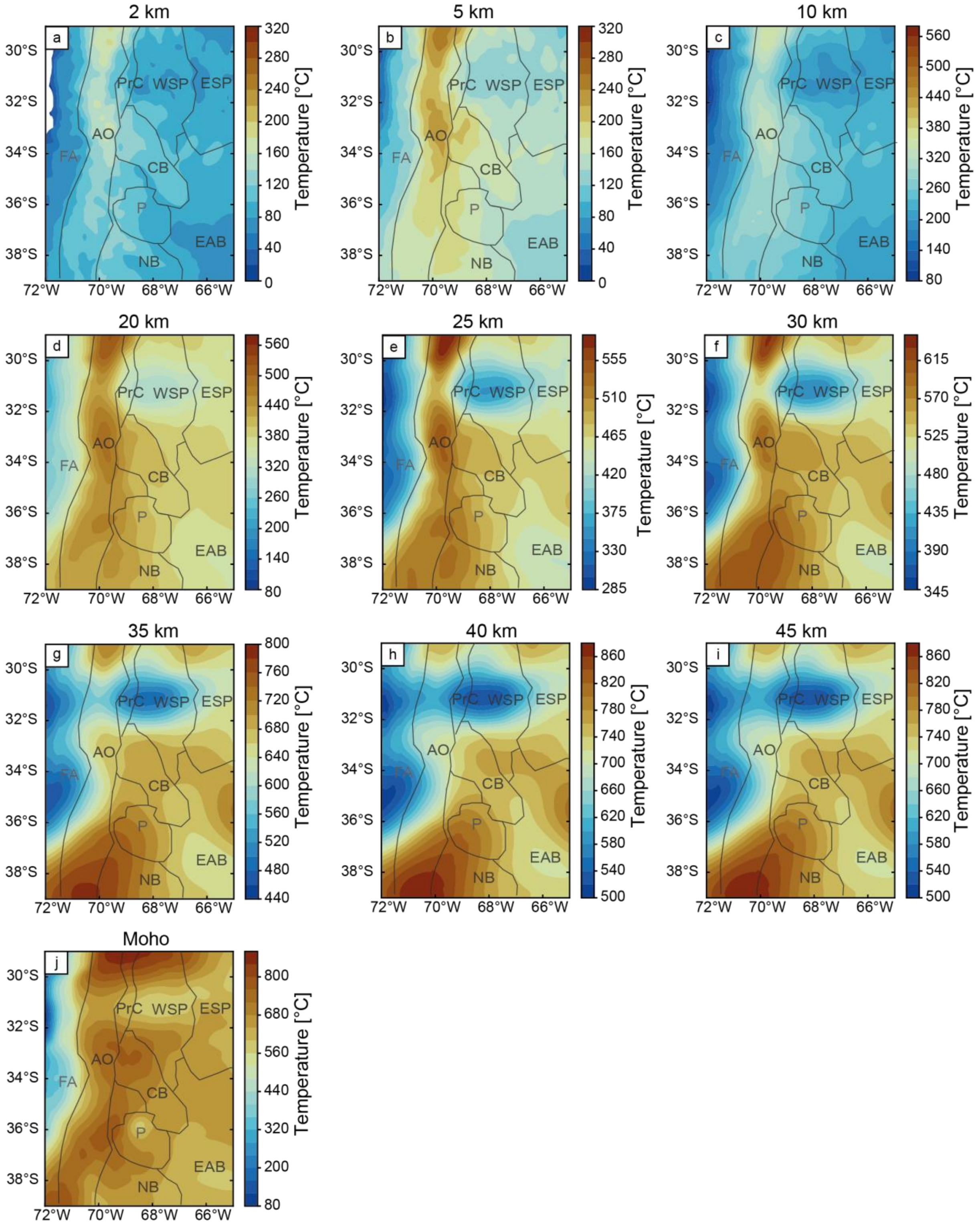

Figure 4.7: Modeled temperature distribution below sea level at different depths: (a) 2 km, (b) 5 km, (c) 10 km, (d) 20 km, (e) 25 km, (f) 30 km, (g) 35 km, (h) 40 km, (i) 45 km, and (j) Moho. Boundaries of the main morphotectonic provinces are also marked with black lines; for abbreviations see Fig. 4.1

The thermal contrast between the warm orogen and the relatively cold forearc, back-arc, and foreland regions is more pronounced with increasing depth (e.g., ~110°C at 10 km bmsl and

~200°C at 20 km bmsl.; Figs. 4.7c–d). From 20 km bmsl downward, the temperature distribution partially resembles that of the lower boundary condition (cf. Fig. 4.5a). Lowest temperatures at these depths correlate spatially with the areas where the mantle is the coldest (CN and FS areas, Fig. 4.5a). Here, the temperature minimum also correlates with a thick (~40 km, cf. Fig. 4.2b) continental crystalline crust, where the lower crust is also thickened (>30 km, cf. Fig. 4.2d).

From the modeled thermal field, we computed the surface heat flow (Appendix B.4), which varies laterally from minima of ~45–70 mWm^{-2} in the oceanic domain, most of the forearc, and foreland to maxima across the orogen (80–100 mWm^{-2}; Fig. 4.8). We observe a remarkable spatial correlation between the surface heat-flow distribution and continental crustal features. Whereas high heat flow corresponds to areas with thick upper continental crystalline crust (>25 km; e.g., within the orogen and the Payenia volcanic province; cf. Fig. 4.2c), low heat flow characterizes the deep sedimentary basins (~>3 km; e.g., the Neuquén Basin; cf. Fig. 4.2a) and/or thick lower continental crystalline crust (>25 km; e.g., most of the Sierras Pampeanas; cf. Fig. 4.2d).

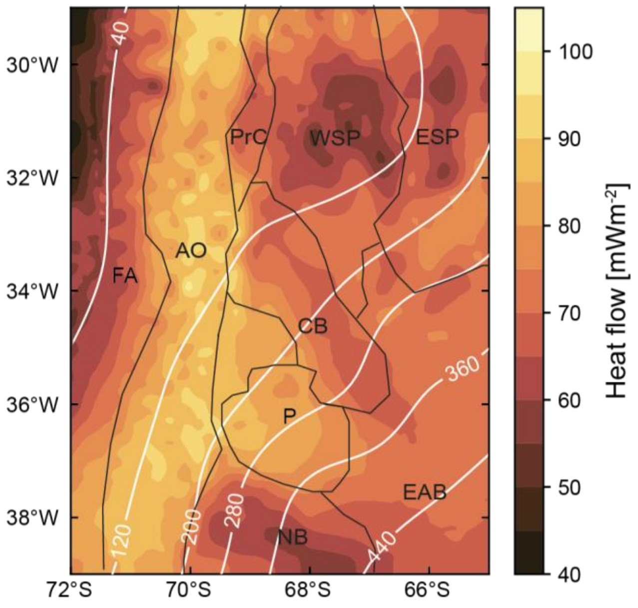

Figure 4.8: Modeled surface heat flow. Depth contours (km) of the top of the oceanic crust from SLAB2 (Hayes et al., 2018) are shown in white lines. Boundaries of the main morphotectonic provinces are also marked with black lines; for abbreviations see Fig. 4.1

4.4.3 Model validation

As a first step in the validation process, we compared modeled temperature values with the published borehole measurements of Collo et al. (2018), located mainly in the central and northern foreland (Fig. 4.9a). The residual temperature (i.e., the difference between modeled and measured values) is shown in Fig. 4.9b. Figure 4.9c illustrates measured and modeled temperatures v_S. depth, and Figure 4.9d shows the residual temperature v_S. depth. In general, we obtain a good fit of approximately ±20°C between the borehole data and the modeled temperatures, with the exception of few outliers (Fig. 4.9c).

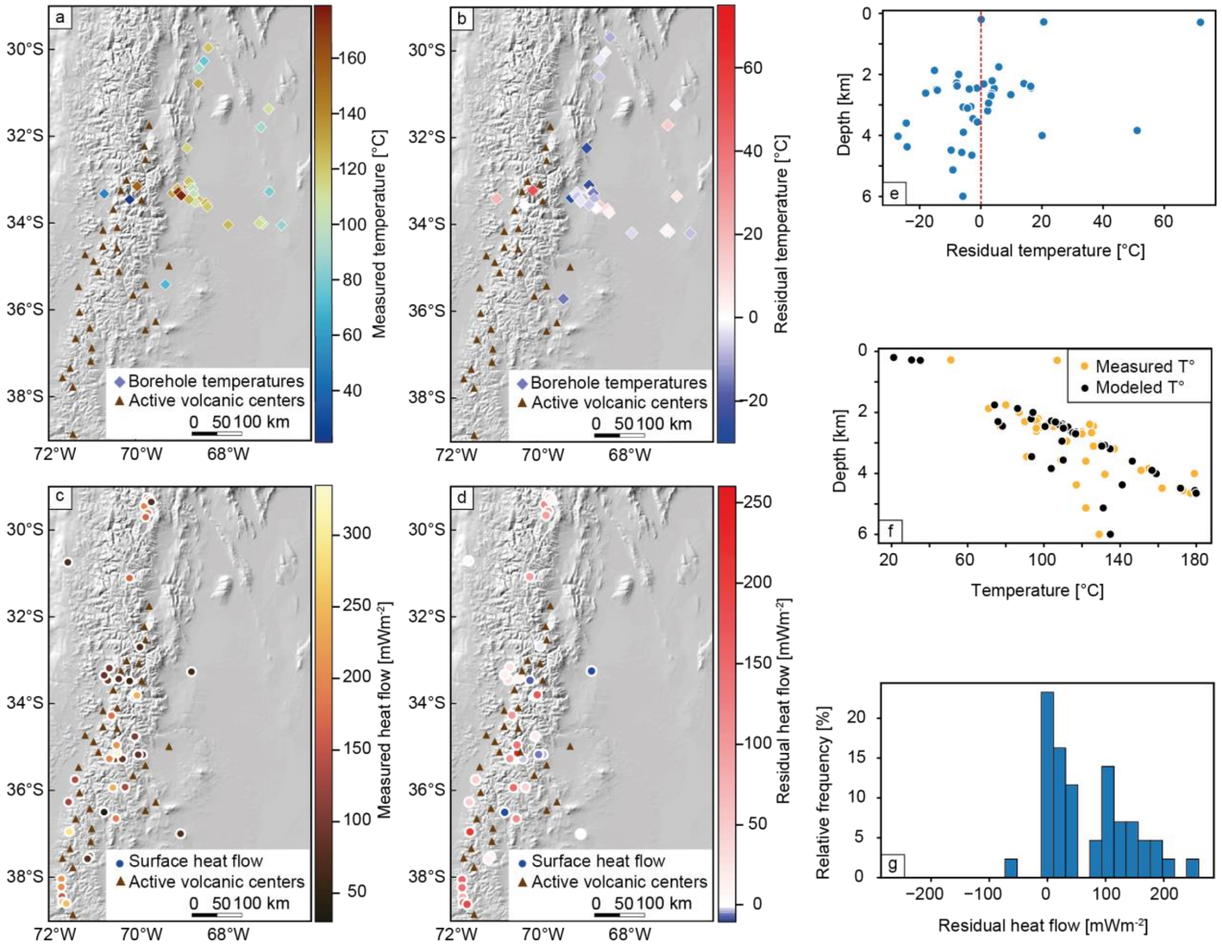

Figure 4.9: Shaded-relief image of the study area with superposed location of: (a) borehole temperatures (diamonds, Collo et al., 2018), (b) residual temperature, (c) observed surface heat flow (circles, Hamza & Muñoz, 1996; Uyeda & Watanabe, 1982); and (d) residual surface heat flow. Residual values are obtained from the subtraction between observed and modeled values. Triangles in (a-d) show the location of active volcanic centers. (c) Comparison between measured (orange) and modeled (black) temperatures vs. depth. (d) Residual temperature vs. depth. (e) Histogram of residual heat flow.

Albeit limited in coverage, in a second step we used available compilations of surface heat-flow values within the SCA (Hamza & Muñoz, 1996; Lucazeau, 2019; Uyeda & Watanabe, 1982) to validate our thermal model. These measurements are located mainly along the orogenic axis and show a large variation in their magnitudes (up to 250 mWm^{-2}), even between close measurements (Fig. 4.9a). Figure 4.9b depicts the residual surface heat flow, i.e., the difference between the predicted and the measured surface heat flow, at the location of the measurements. Figure 4.9e is a histogram of residuals of surface heat flow. In general, the model underestimates the surface heat flow with respect to the measured values, with only ~25% of the predictions matching the observations (Fig. 4.9e). Due to its purely conductive nature, the model does not reproduce the extremely high heat flow (>150 mWm^{-2}) reported for some volcanic areas in the axial sectors of the orogen. Additionally, due to its resolution, the model is not able to reproduce the observed variations in heat-flow magnitudes between adjacent measurements, which likely correlate to local features not considered in our regional study (Fig. 4.9b).

4.5 Discussion

4.5.1 Model robustness and sensitivity analysis

4.5.1.1 Steady-state assumption in the shallow lithosphere domain

One main assumption in the calculation of the shallow temperature field was to consider that the lithosphere is in steady state. However, thermal equilibrium in the overriding plate can be disturbed by the advection of the cold subducting plate (e.g., Holt & Condit, 2021; Leng & Mao, 2015). Therefore, a more appropriate modelling strategy would be to additionally account for these processes. The caveat here is that performing such an analysis requires a detailed knowledge of the past temperature distribution in order to properly initialize the system. Unfortunately, we lack such constraints in the SCA. Given these considerations, we relied in our study on the assumption of steady-state conduction, where the results are less affected by the choice of the initial temperature condition, but are mainly determined by the imposed boundary conditions (based on available observables in our study) and the model parameterization. Nonetheless, in an attempt to quantify the validity of this approximation for the SCA, we also computed a simulation that accounts for the additional effects of advection of cold temperatures due to the motion of the subducting slab on the present-day thermal field of the shallow domain. To that end, we first computed the resulting thermal field from the advection of a cold thermal front along the subduction interface (i.e., top of the oceanic crust). In a following step, we imposed this thermal evolution as the lower boundary condition on the 3D configuration of the overriding plate, and ran a transient simulation with a duration of 7 Ma, which represents the past period during which the subduction geometry remained unchanged (Jordan et al., 1983; Ramos et al., 2002). A detailed description is provided in the Appendix B.7. The comparison between the initial and final time steps at representative depth slices (10 and 40 km bmsl) indicates that the largest temperature difference (up to 450°C) is registered in a narrow band within the forearc close to the subduction interface (Fig. 4.10). Such a difference is due to the advection of the cold thermal front along this interface. In the remaining areas, temperatures at 7 Ma are up to 10°C higher than the initial time step due to diffusion within the thick radiogenic crust in the orogen. In view of these results, we consider the assumption of thermal equilibrium as an adequate approximation for the thermal calculations of the shallow domain of the overriding plate in the SCA.

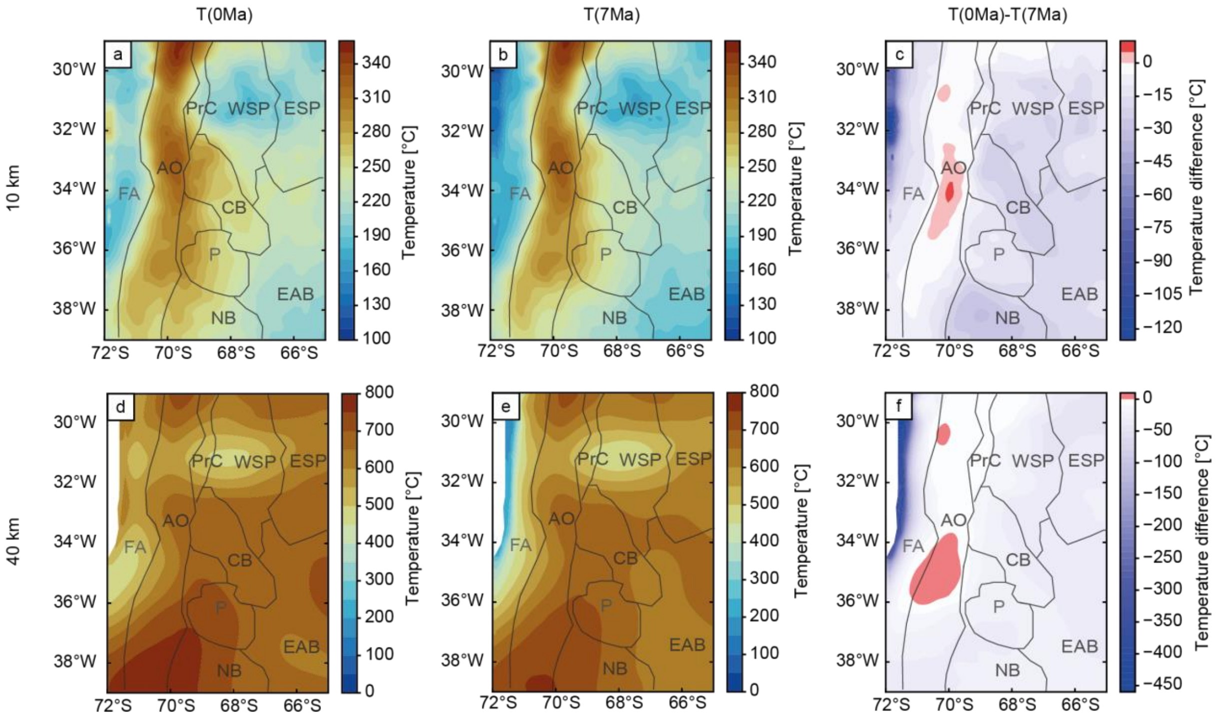

Figure 4.10: Transient temperature distribution in the overriding plate at depths of 10 and 40 km (a, b, and c), as induced by the advection at the subduction interface at 0 Ma and 7 Ma time steps. (c) and (f) show the temperature difference between (b) and (a), and (e) and (d), respectively. Boundaries of the main morphotectonic provinces are also marked with black lines. For abbreviations see Fig. 4.1.

4.5.1.2 Implications of the methodological uncertainties and limitations on the lithospheric thermal field

The model results depend on the parametrization of physical properties and boundary conditions. One source of uncertainty is the vs-to-T conversion. Sensitivity analysis of the vs-to-conversion shows that within the tested alternative models, using the conversion method of Priestley & Mckenzie (2006) and changing the mantle composition based on Goes et al. (2000) yield the largest temperature differences with respect to the reference model (Fig. 4.6). In contrast, variations in the thermal expansion coefficient α and attenuation Q has a negligible effect on the inverted thermal field. Since the conversion method of Priestley & McKenzie (2006) is associated with large uncertainties (250°–360°C) for temperatures <900°C (An et al., 2015; Priestley & McKenzie, 2013), we limit our discussion to computed temperature variations due to considered variations in the mantle composition based on the approach by Goes et al. (2000)

The temperature difference between the reference and alternative models is only significant in a limited portion of the shallow mantle (<100 km) characterized by high v_S (>4.6 km s^{-1}), as is the case for the flat-slab segment and the forearc (Fig. 4.6). Moreover, the regional thermal pattern in the mantle (i.e., the thermal contrast between the flat- and steep-slab segments) is a robust feature common to all model configurations despite variations in mantle composition. To quantify the sensitivity of the shallow thermal field to imposed variations in the mantle composition, we carried out an additional model for which we imposed as a lower boundary condition the resulting temperature distribution obtained from the conversion considering a garnet lherzolite mineral composition (Table 4.1). Temperature maps showing the difference between the two models are provided in the Appendix B.9 (Fig. B.10). Although the model with the alternative lower boundary condition predicts temperatures that are up to 80°C higher than the reference model described in Chapter 4.4, the regional thermal heterogeneity remains unchanged, with contrasts between the forearc, orogen, and foreland, and between the flat- and steep-slab segments. From these observations, we can conclude that the modeled trends in temperature variations are within the same order of magnitudes, though still within its range of uncertainty, even when considering an alternative parametrization other than the preferred vs-to-T conversion model.

Another limitation of the v_S-to-T conversion is related to the thermal structure within the slab. Although the oceanic plate displays higher v_S and lower temperatures with respect to the surrounding mantle (e.g. Fig. 4.5; Fig. B.1 in Appendix), the model thermal gradient within the plate is not as large as the one predicted by other analytical or numerical approximations of the thermal structures of subduction zones (England, 2018; van Keken et al., 2019). The strong lateral contrasts of v_s are smoothed due to the resolution of the seismic tomography. This results in lower v_s and therefore higher temperatures than the predictions of these theoretical thermal models. On the contrary, v_s and resulting temperature anomalies within the continental mantle are of larger wavelength than those of the slab, thus they can be captured by the longer wavelength surface waves of the seismic tomography. Therefore, our discussion was limited to the thermal heterogeneities of the overriding plate and subduction interface.

Additional methodological uncertainties relate to the limited resolution, coverage, and lateral differentiation of the lithospheric units in the 3D structural model, as well as to imposed thermal properties. Although there is an inherent non-uniqueness in the way thermal properties influence the results, the range over which these properties can vary is limited (see Appendix B.4). In addition to testing the effect of end-member property values, the use of a wide variety of independent lithology-constraining data sets, including borehole temperatures, seismic tomography, seismic reflection and refraction data, and gravity anomalies, helped reduce the range of property variability. Future improvement of the definition of higher-order temperature contrasts relies on more densely spaced seismic experiments focused on the deep crustal structure of the SCA and more extensive temperature measurements to cross-check the modelling results. First-order thermal effects proved to be robust even for tested variations in imposed properties.

4.5.2 Controlling factors of the lithospheric thermal field

Our results indicate that the shallow thermal field of the lithosphere (<50 km) is largely controlled by the configuration of the continental crust, with temperatures varying according to the thickness of the sedimentary rocks and crystalline crust. Close to the surface (<5 km), thick sedimentary basins (main depocenters of the Cuyo and Neuquén basins) exhibit temperatures up to ~40°C higher than at the basin margins. This is the effect of thermal blanketing produced by the low-conductive sedimentary layers (Lucazeau & Le Douaran, 1985; Scheck-Wenderoth et al., 2014; Sippel et al., 2017; Wangen, 1994). In contrast, the presence of more thermally conductive crystalline rocks leads to a more efficient heat transport where sedimentary cover rocks are absent and to colder shallow temperature at the same depth.

In the areas where the sedimentary units are thin (<2 km thick) or absent, the variations in the topographic relief and in the upper continental crystalline crust exert the primary influence on the shallow thermal field. This topographic effect is related to the general increase in temperature with depth, which results in higher temperatures in the orogen than in the foreland at the same depth below sea level. The positive correlation between thickness of the upper continental crystalline crust and higher heat budget compared to the other lithospheric layers stems from these rocks being enriched in radioactive heat-producing elements due to their felsic composition (Vilà et al., 2010). These two superposed effects increase crustal temperatures in areas with high elevation (>1.5 km above mean sea level, amsl) and pronounced upper crustal thickness (>20 km). These characteristics are particularly evident in the Andean orogen, where temperatures at 2 km bmsl are up to 100°C higher with respect to the forearc, the remaining back-arc, and the foreland regions. Outside of the orogen, the average elevation and the upper continental crystalline crustal thickness decreases to 700 m amsl and 10 km, respectively, and consequently the thermal input also decreases. To further examine the effects of topographic relief and upper crustal thickness on the shallow thermal field, we extracted the temperatures at 2 and 20 km below sea level ($T_{z(bmsl)}$) and below surface ($T_{z(topo)}$) and computed the difference between the two reference levels (T_{diff}) for each depth:

$$T_{diff} = T_{z(bmsl)} - T_{z(topo)} \quad (4.7)$$

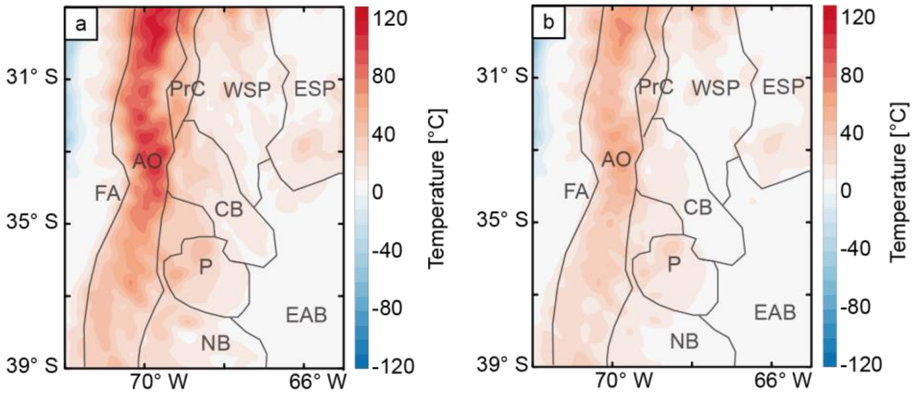

Figure 4.11: Difference between temperature distributions below sea level and below surface at depths of (a) 2 km and (b) 20 km, illustrating the topographic effect on the thermal field. Key morphotectonic provinces are shown. Refer to Fig. 4.1 for abbreviations.

The temperature differences at 2 km and 20 km are shown in Figure 4.11. We observe that at shallow depths of 2 km, the temperature differences are indeed affected by variations in the topography (~100°C in areas of 3–6 km elevation). This effect decreases with greater depth, although it is still evident at 20 km bmsl, where temperature differences are up to 50°C below areas of 5–6 km topographic elevation. Below 20 km bmsl, the influence of the upper crustal thickness outweighs the topographic effect.

Our results confirm that the lithospheric thermal field is influenced by both the cooling effect of the subducting slab and heat input from the mantle, and that below 50 km bmsl these two factors play a dominant role. The degree to which the slab dynamics affects the temperature distribution by advective cooling varies with distance from the trench and the subduction angle. To better illustrate this relationship, we obtained the overall 3D thermal field by combining the calculated steady-state conductive thermal field above the lower boundary condition (50-km approximation) with the temperatures deduced from seismic tomography between 50 and 200 km bmsl. From this combined model, the temperatures corresponding to the depth of the subduction interface as presented by Rodriguez Piceda et al. (2021) and the volumetric extent of the low-temperature CN and FS mantle domains were extracted (Fig. 4.12). These domains were defined according to the regions of the mantle of the overriding plate with temperatures lower than those of a typical continental geotherm (McKenzie et al., 2005). The mantle of the overriding plate exhibits the lowest temperatures close to the trench, within the cold nose of the forearc, and where the slab flattens (mostly at 85 km bmsl beneath the Sierras Pampeanas). In contrast, temperatures at depths > 50 km bmsl beneath the Sierras Pampeanas increase towards areas where the slab dips steeply (~30°). These results are consistent with the lower surface heat-flow values observed (Hamza et al., 2005; Hamza & Muñoz, 1996; Uyeda & Watanabe, 1982) and low v_p/v_s ratios modeled (Marot et al., 2014; Porter et al., 2012; Wagner et al., 2005, 2006) for the flat-slab area. An additional and independent constraint for the thermal state of the flat-slab area can be derived from the results from 2D thermomechanical modelling efforts done in the area (Marot et al., 2014), which suggested temperatures of 600°C at the top of the flat slab (100–120 km bmsl). This value coincides with the lower temperatures modeled across the subduction interface beneath the Sierras Pampeanas (Fig. 4.13).

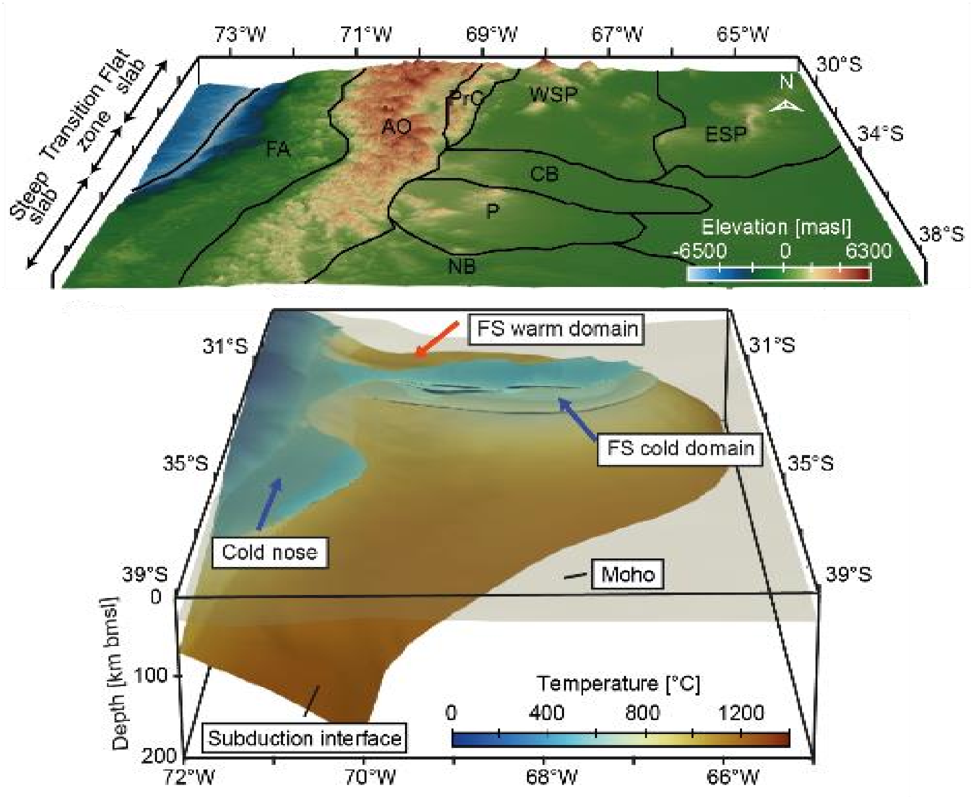

Figure 4.12: Upper panel: Topography of the study region superposed with boundaries of the main morphotectonic provinces (for abbreviations see Fig. 4.1). The extent of the subduction segments and the trench are also shown. Lower panel: Temperature at the subduction interface. The 3D configuration of cold domains in the overriding plate mantle is superimposed and indicated by blue arrows, The red arrow indicates the warmest part (~1000°C) of the flat-slab segment. The extent of the Moho is shown by the beige transparent layer.

The spatial correlation between the temperature distribution of the overriding plate and the subduction angle breaks within the northern orogen above the flat slab between 20 and 100 km bmsl (29°–30°S and 70°–70.5°W; Figs. 4.5, 4.7, 4.12). In this domain, a temperature excess of up to ~250°C is predicted along the remaining flat-slab segment, with values similar to those of the steep-slab segment (FS warm domain; Fig. 4.13). To explain the modeled temperature distribution, an additional forcing factor other than the subduction angle should be considered, a suggestion that has been discussed previously, albeit not extensively (Sánchez et al., 2018, 2019). Between 30° and 33°S, our results indicate a spatial correlation between the thermal heterogeneity derived from the v_S-to-T conversion (Assumpção et al., 2013) and the configuration of the upper crust. The lowest temperatures in the sub-horizontal slab segment occur where the upper crust is thin, while the highest temperatures occur where it thickens (cf. Fig. 4.2c). We can therefore postulate that, in the warmer, northern part of the orogen, heating from a thicker upper continental crystalline crust outweighs the cooling effect of the underlying flat oceanic slab. Conversely, areas in the flat segment with a thin upper crust and a thick lower crystalline crust are significantly colder due to a limited volumetric contribution of the lower crustal unit to the internal heat budget. North of 30°S, the thick upper crust provides an explanation for the observed patterns of low v_s and high temperature in the orogen, but not in the foreland regions where the upper crust is thinner. It is likely that the resolution of the S-wave tomography could have influenced the results within the latter area. North of the flat slab, high-resolution tomography (Calixto et al., 2013; Gao et al., 2021) identifies a N-S increase of v_s at 27°S with a sharp transition between low v_s in the southern Andean Plateau (also known as the southern Puna Plateau) and high v_s in the Sierras Pampeanas. Low v_s in the southern Puna is mainly associated with the delamination of the lower crust and the mantle (Kay et al., 1994; Schurr et al., 2006). Therefore, we postulate that this sharp velocity transition appears smoothed in the tomography of Assumpção et al. (2013) due to the coarser resolution, resulting in lower modeled v_s, and therefore higher temperatures, in the foreland north of 30°S.

To investigate the degree of influence of mantle-related temperature variations in the shallow thermal field, we compared our results to a steady-state conductive model with a simplified lower boundary condition derived from a constant geothermal gradient of 5°C km^{-1}, which represents an average value for subduction zones (Syracuse et al., 2010; Fig. B.11 in Appendix B.9). This allowed us to evaluate variations in the shallow thermal field in the case of neglecting deep-seated lateral thermal heterogeneities. At depth, there is no pronounced thermal contrast between the foreland of the flat and steep subduction segments, indicating that below 50 km bmsl, the main causative factors of the thermal heterogeneity of the foreland are the mantle heat input and the cooling effect of the slab. On the other hand, the model with a simplified boundary condition shows a more pronounced mismatch with the thermal observations (for instance, modeled temperatures are 5°C to 80°C colder than the borehole data) than the model with the lower boundary condition from the v_s-to-T conversion (Fig. B.12 in Appendix B.9). This implies that the observed data is fitted not only with the lithospheric structure above the Moho, but also with laterally variable heat input from the slab and the lithospheric mantle.

There is an ongoing debate concerning the importance of radiogenic heat production for the thermal field and the long-term evolution of orogens where the radiogenic crust is thickened and where thermal effects of shortening, exhumation, and partial melting are observed (e.g., (Chen et al., 2019; Furlong & Chapman, 2013; Gerbault et al., 2009; Jaupart et al., 2016; Mareschal & Jaupart, 2013). Some authors suggest that radiogenic heating has less influence on the thermal field of the lithosphere in the overriding plate than either shear heating along the subduction interface (Penniston-Dorland et al., 2015) or episodes of magmatic underplating (Kaislaniemi et al., 2018). Yet other authors have focused on the general thermal evolution of subduction orogens and the metamorphic record, proposing that shallow asthenospheric convection is the main process responsible for elevated temperatures in the lithosphere, while disregarding any significant contribution from radiogenic heat production (Hyndman, 2005). In the latter study, for example, it is argued that thermal equilibrium is achieved only 50 Ma after the main shortening phase, which contradicts the observation that peak metamorphism is synchronous with thickening (Collins, 2002; Thompson et al., 2001). However, the interpretations concerning thermal equilibrium conditions in an orogen have recently been disputed by geodynamic numerical modelling studies (Chen et al., 2019), which suggest that radioactive heating during crustal thickening is responsible for the observed marked temperature increase and subsequent partial melting within the mid-crust after 30 Ma of shortening. The present-day SCA are within this time window after the main phase of shortening, which implies that crustal thickening that has taken place over more than 30 Ma could indeed explain a significant part of excessive surface heat flow (Hamza et al., 2008; Hamza et al., 2005; Hamza & Muñoz, 1996) and the low seismic velocities observed across the orogen (Marot et al., 2014; Porter et al., 2012; Wagner et al., 2005, 2006; Ward et al., 2013).

In Figure 4.13, we plot variations in predicted surface heat flow compared to available observations, together with the modeled thermal field and the configuration of the main lithospheric units along three representative E-W cross sections of the flat slab, the transition zone, and the steep-slab subduction segments. Predicted surface heat flow varies between the high surface heat-flow domains over both the orogen and the Payenia volcanic province (80–100 mWm^{-2}), and low heat-flow domains over the forearc, the remaining back-arc, and foreland regions (50–60 mWm^{-2} and 40–70 mWm^{-2}, respectively). These surface heat-flow variations correlate spatially with the thickness configuration of the sedimentary strata and upper crystalline crust, namely high heat flow in areas with thin low-conductive sedimentary rocks and thick radiogenic upper crust (i.e., Andean orogen, Payenia volcanic province), and low heat flow in regions with thick sedimentary cover and/or thin upper crust (foreland basins, forearc). An additional factor leading to low modeled heat flow in most of the forearc is the shallow depth of the cold oceanic plate. This factor does not play a role in the foreland, however; despite variable dip angles and temperature distributions along and across strike, no spatial correlation is observed between the thermal field at the subduction interface and the heat-flow patterns in the orogen and foreland.

The effects of the spatially variable heat input (either from the deep mantle or from radiogenic sources) and variable efficient heat conduction demonstrate that surface heat flow alone is a poor proxy for lower crustal or lithosphere thickness (Scheck-Wenderoth et al., 2014). Nevertheless, heat-flow estimates are often compared to seismic tomography, where S-wave attenuation (measured by the quality factor Qs) anomalies correlate to some extent with the thermal field (Artemieva, 2011). While areas of high heat flow are usually related to low Qs (high attenuation of the v_s), low heat flow is commonly associated with colder areas and hence high Qs (low attenuation of v_s). These spatial correlations were also identified across the SCA. Between 31.5°S and 33.5°S, high surface heat flow predicted for the orogen coincides with low Qs (650–670; Deshayes, 2008). Accordingly, low predicted heat flow correlates with high Qs (800–1050) in the forearc and the foreland (Deshayes, 2008).

Discrepancies between observed surface heat flow (Hamza & Muñoz, 1996; Lucazeau, 2019; Uyeda & Watanabe, 1982) and the steady-state conductive model predictions in the proximity of active volcanic centers (Figs. 4.9d, 4.13) are related to unconsidered transient advective heat-transport processes, such as fluid migration or the existence of melts (e.g., Scheck-Wenderoth et al., 2014 and references therein). González-Vidal et al. (2018) demonstrated that such local effects of partial melting can be interpreted from negative S-wave anomalies imaged below the southern volcanic arc in the SCA area.

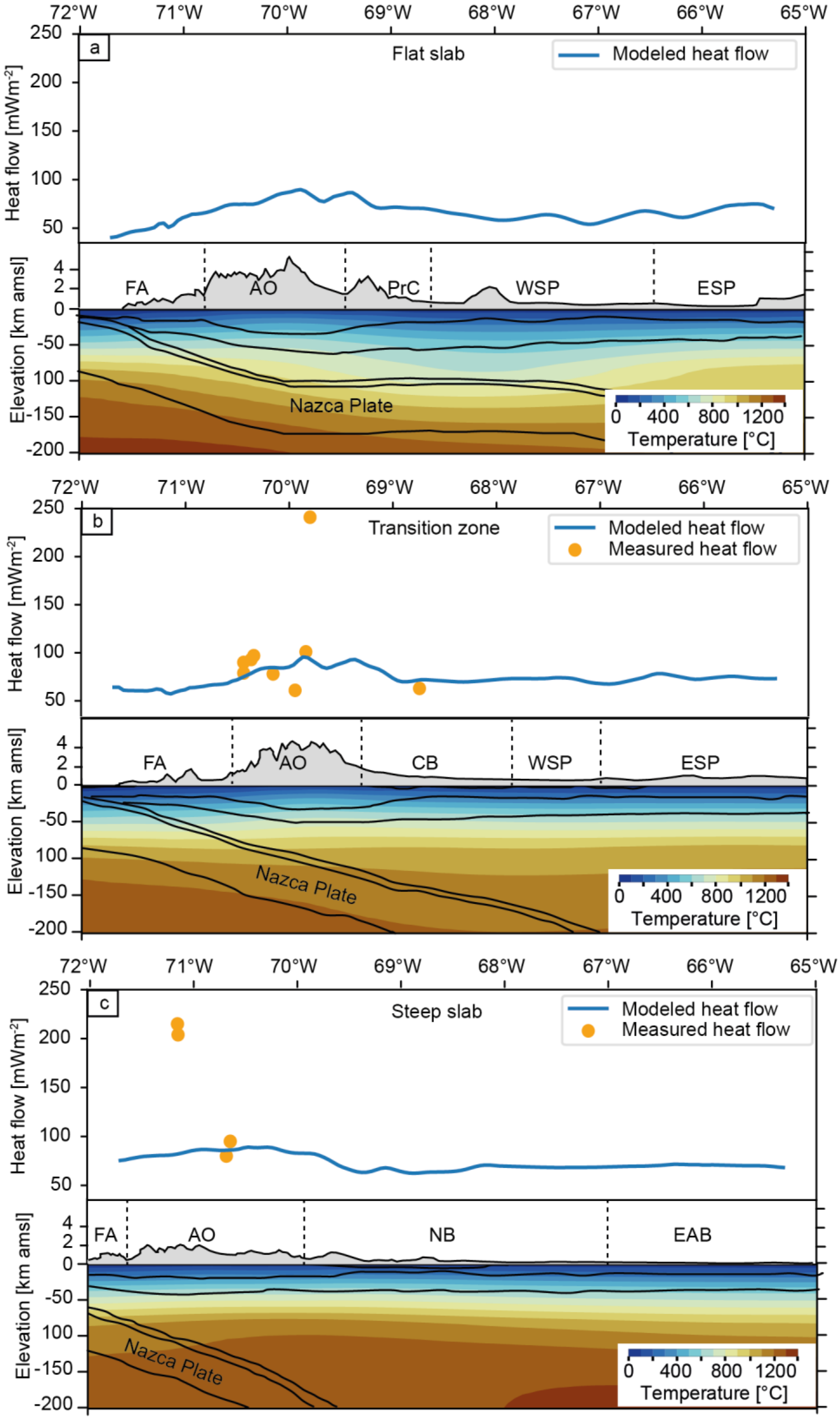

Figure 4. 13: E-W cross sections showing modeled and measured surface heat flow (upper panel) and temperature distribution (lower panel) representative of the subduction segments of: (a) flat slab; (b) transition zone and (c) steep slab. For location of the profiles and abbreviations of the main morphotectonic provinces see Fig. 4.1.

4.5.3 Implications of the thermal field for the deformation modes in the SCA

In view of the sensitivity of rock rheology to temperature, the lithological configuration from Rodriguez Piceda et al. (2021) and temperature variations derived in this study can be analyzed qualitatively in terms of their implications for the long-term strength of the lithosphere. In particular, areas that are colder and of more mafic lithology (i.e., the northern part of the forearc and foreland) are potentially stronger and can withstand higher levels of horizontal stresses before deforming viscously (Burov, 2007) compared to areas that are warm and more felsic in composition (i.e., the orogen, the Payenia volcanic province, and the foreland at the latitudes of the transition to the steeper subduction segment). The general trends in the modeled temperature distribution of the SCA lithosphere are consistent with independent elastic-thickness estimates derived from flexure analysis of the gravity field, which are an alternative, indirect proxy of lithospheric strength (Astort et al., 2019; Ibarra & Prezzi, 2019; Nacif et al., 2017; Sánchez et al., 2018; Tassara & Yáñez, 2003). High and low elastic thickness are indicative of a strong and weak lithosphere, respectively (Burov & Diament, 1995; Watts & Burov, 2003). In the SCA, areas of high elastic thickness (40–60 km) correlate spatially with the modeled cold forearc and the northern part of the foreland. Conversely, areas of low elastic thickness (<30 km) correlate spatially with the modeled warm areas of the orogen, the Payenia volcanic province, and the foreland at the latitude of the transition to the steeper subduction segment.

The inferred trends in lithospheric strength related to variations in the upper-plate configuration have strong implications for the long-term deformation processes of the Central Andes (Barrionuevo et al., 2021; Ibarra et al., 2019; Liu, 2020; Meeßen, 2019). For example, Barrionuevo et al. (2021) argued on the basis of geodynamic numerical modelling that the vergence of the orogenic wedge at 33°–36°S is mainly controlled by the E-W-oriented asymmetry of the lithosphere-asthenosphere boundary (LAB). The LAB configuration proposed by these authors agrees with our study, where a warmer lithospheric mantle, and thus shallower LAB, is encountered beneath the orogen compared to the adjacent foreland and forearc, i.e., areas where the mantle is colder and the LAB is located at greater depth. Furthermore, these authors suggest that heterogeneities in continental crustal composition could explain the observed N-S-oriented variations in the amounts of shortening and its spatial distribution within the orogen and the foreland between 33° and 36°S. In the north of their study region, the upper and lower crustal deformation maxima are aligned vertically with the strongest crustal thickening (pure-shear or coupled deformation mode), whereas to the south, upper crustal deformation is horizontally displaced with respect to the locus of lower crustal deformation (simple-shear or decoupled deformation mode). Accordingly, pure-shear deformation at 33°S would be mainly related to a more felsic and weaker crust; in contrast, simple-shear deformation at 36°S would result from a mafic and stronger crust (Barrionuevo et al., 2021). These results are compatible with gravity-constrained density distributions in the crust in the same region as proposed by Rodriguez Piceda et al. (2021) and with our results of a N-S-oriented decrease in crustal temperatures.

Furthermore, our results provide insights into the controversial debate over the governing mechanisms responsible for the formation of the spatially disparate thick-skinned deformation in the broken-foreland provinces of the Sierras Pampeanas between 27° and 33°S and the Santa Bárbara System farther north. While some authors have proposed that the setting of the flat slab is responsible for the observed deformation in that area (Horton, 2018; Jordan et al., 1983; Martinod et al., 2020), others have argued that this style of deformation is controlled by the compressional reactivation of crustal heterogeneities such as Paleozoic sutures and associated deformation fabrics between crustal terranes or the inversion of Cretaceous normal faults prior to slab flattening (Hilley et al., 2005; Hongn et al., 2007; Hongn et al., 2010; Kley et al., 1999; Kley & Monaldi, 2002; Meeßen, 2019; del Papa et al., 2013; Pearson et al., 2013; Ramos et al., 2002; Zapata et al., 2020). In the former case, the role of a flat slab is often assigned to a 'bulldozer' which continuously transfers the tectonic stresses to the front of the flat segment where the slab is already steep (Gutscher et al., 2000; Horton, 2018; Jordan et al., 1983; Ramos & Folguera, 2009). In this scenario, however, the role of the thermal and rheological fields of the overriding plate in the transmission and localization of stresses is not taken into account. More recently, Martinod et al. (2020) reinterpreted the role of the flat slab in the localization of deformation. Contrary to classical interpretations, these authors argue that, because the lithosphere above the flat slab is colder and stronger, most of it is subject to minor deformation. Therefore, deformation localizes where the slab starts to resume its steep subduction angle, triggered by slab-pull forces, rather than where the slab is already steep, as proposed by the 'bulldozed-keel' models (Gutscher et al., 2000; Horton, 2018; Jordan et al., 1983; Ramos & Folguera, 2009). The compositional and thermal characteristics of the lithosphere beneath the Sierras Pampeanas (i.e., mafic-dominated crust and cold lithosphere) derived from our results suggest that the lithosphere here is strong and may therefore inhibit the formation of crustal-scale faults, thus dismissing the 'bulldozed keel' effect as an efficient mechanism for propagating deformation. Instead, an additional process, either mechanical weakening within inherited basement heterogeneities and/or increased slab-pull where the slab resumes steep subduction, must be considered to explain the localization of deformation in the Sierras Pampeanas. The results of our study favor the hypothesis that either inherited heterogeneities and/or slab steepening controlled the geometry of faults that delimit the spatially isolated basement uplifts and the intervening sedimentary basins of the broken foreland between 27°S and 33°S, rather than slab flattening. Opting for one or the other hypotheses mentioned above requires additional geodynamic modelling studies applied to the case of the SCA.

Addressing another aspect of the debate on the mechanisms that have sustained the flat-subduction setting over the last ~20 Ma in the SCA, it has been proposed on the basis of geodynamic numerical modelling that the strength of the overriding plate influences the subduction angle of the oceanic plate (Hu et al., 2016; Manea et al., 2012; Sharples et al., 2014). This has been suggested to be the case for the northern part of the SCA (27°–33°S), where the sub-horizontal slab segment underlies the thick and dense crust of the foreland of the South American plate (Rodriguez Piceda et al., 2021). Interestingly, the cold temperatures modeled for this area in our study exhibit two effects that might also favor slab shallowing: (i) cooling of the subduction interface that enhances the coupling between the continental and oceanic plates; and (ii) efficient E-W stress transmission along the cold and strong overriding plate, which forces the trench to retreat. In this context, there is a positive feedback between the cold lithosphere in the northern foreland and the flat-subduction setting: the shallow slab, together with a thin radiogenic crust, would cause low temperatures in the lithosphere in this domain, thereby strengthening the overriding plate, which in turn would promote slab shallowing.

4.6 Conclusions

By means of conversion of S-wave seismic tomography to temperatures and steady-state conductive numerical modelling, we derived the 3D lithospheric-scale temperature distribution of the southern Central Andes and adjacent forearc and foreland regions, and conclude the following:

1. Distinct controlling factors of the thermal field are dominant at different depths. At shallow depth (<50 km bmsl), the thermal contrast between the warm orogen and the relatively cold areas of the forearc and foreland is modulated by the thickness of the upper radiogenic continental crystalline crust, which generates lateral changes of heat production. In the uppermost levels (<5 km), the effect of the sediment thickness is

superimposed, leading to depocenters of the foreland basins being warmer than the edges due to thermal blanketing. The cool oceanic slab outweighs the heating effect of the continental crust in regions with relatively shallow slab depth (<85 km bmsl) and where the upper continental crystalline crust is thin. This occurs in the forearc and in most of the northern part of the foreland (29°–33°S) where the slab flattens. At depths >50 km bmsl, the spatial correlation between crustal features and thermal heterogeneities is insignificant, and the main controlling factors become the mantle heat flow and the effect of the cold slab. However, down to 100 km bmsl, temperatures are additionally affected by the radiogenic contribution of the upper continental crystalline crust in the northern part of the orogen where this unit has a significant thickness (>30 km).

There exists a strong contrast in surface heat flow between the warm orogen (80–105 mWm^{-2}) and the relatively cold forearc and foreland areas (40–75 mWm^{-2}). These variations in heat flow are primarily controlled by the thickness configuration of the uppermost layers (sediments and upper crystalline crust). The shallow cold slab affects the pattern of surface heat flow beneath the forearc.

2. The modeled temperature configuration has implications for the rheology and, therefore, deformation patterns of the SCA. A cold, mafic, thick, and therefore potentially strong lithosphere beneath the broken foreland of the Sierras Pampeanas is prone to deformation processes that are controlled by inherited heterogeneities in the upper plate or by slab-pull, where the oceanic plate resumes steep subduction. In addition, such a lithospheric configuration may favor the coupling between the subducting and overriding plates, potentially contributing to a flat-subduction setting.
3. Sensitivity analysis of the v_s-to-T conversion shows that, at depths <100 km, mantle composition has the strongest effect on the v_s-to-T conversion for v_s larger than 4.6 km s^{-1}, as is the case for the flat-slab segment. Nevertheless, compositional variations within the range of uncertainty do not affect the main temperature and heat-flow trends found in this study.

Chapter 5: Long-term lithospheric strength and intraplate seismicity in the southern Central Andes

5.1 Abstract

We examined the relationship between the mechanical strength of the lithosphere and the distribution of seismicity within the overriding continental plate of the southern Central Andes (29°S–39°S), where the oceanic Nazca Plate changes its subduction angle between 33°S and 35°S, from subhorizontal in the north (< 5°) to steep in the south (~30°). We computed the long-term lithospheric strength based on an existing 3D model describing the variation of thickness, density and temperature of geological units forming the lithosphere of the SCA and adjacent forearc and foreland regions. The comparison between our results of rheological modeling and seismicity records within the overriding plate (hereafter: intraplate seismicity) shows that most of the events occur within the modelled brittle domain of the lithosphere, and that the depth where the deformation mode switches from brittle frictional to thermally activated ductile creep provides a conservative lower bound to the seismogenic zone in the overriding plate of the study area. We also found that the majority of intraplate earthquakes occur within the realm of first-order contrasts in the integrated strength (12.7–13.3 log Pam in the Andean orogen vs. 13.5–13.9 log Pam in the forearc and the foreland). Specific conditions characterize the mechanically strong northern foreland of the Andes, where seismicity is likely explained by the effects of slab steepening.

5.2 Introduction

The ocean-continent convergent margin of the southern Central Andes (SCA, 29°S–39°S), is characterized by the east-northeast-directed subduction of the oceanic Nazca Plate under the South American continental plate (Fig. 5.1). A distinct geodynamic feature of the subduction margin in this region is the change of the subduction angle of the Nazca Plate between 33°S and 35°S from the Chilean-Pampean flat-slab zone (< 5° dip, 27°S–33°S) in the north to a steeper sector south of 35°S (~30° dip) (Fig. 5.1). The SCA are one of the most seismically active regions along the length of the South American convergent margin, where past seismic events have had devastating impacts on the population, with loss of life and far-reaching economic repercussions (e.g. Gregori & Christiansen, 2018). In recent decades, seismological research in the SCA has mainly focused on understanding the causative dynamics of observed seismicity within the oceanic plate and along the subduction interface (e.g. Anderson et al., 2007; Cloos & Shreve, 1996; Hackney et al., 2006; Linkimer et al., 2020; Moreno et al., 2010, 2014; Wagner et al., 2020; Weiss et al., 2019), while less attention has been paid to the controlling mechanisms of intraplate seismicity (e.g. Alvarado et al., 2005, 2009; Nacif et al., 2017; Smalley et al., 1993; Smalley & Isacks, 1990).

Previous studies analyzing the distribution of intraplate earthquakes derived from local seismic networks (e.g., SIEMBRA, ESP, CHARGE, CHARSME, and CHASE seismic experiments; Alvarado et al., 2005, 2009; Nacif et al., 2013, 2017; Olivar et al., 2018; Rivas et al., 2019; Venerdini et al., 2020) have identified that seismic activity is far more frequent above the flat subduction segment, but decreases significantly towards the south, where the slab transitions into a steeper segment. These studies evaluated the spatial pattern of seismic events at crustal scale, relating seismic to localized weakening within neotectonic fault areas, either linked to Cenozoic structures directly associated with Andean mountain building or to the compressional reactivation of inherited structures and fabrics from previous deformation phases, including episodes of terrane amalgamation during the Paleozoic or rifting during the Mesozoic (e.g., Astini et al., 1995; Azcuy & Caminos, 1987; Giambiagi et al., 2003; Jordan et al., 1983; Kay et al., 2006; Llambias et al., 1993; Llambias & Sato, 1990; Mpodozis & Kay, 1990; Ramos, 1988). The analysis of focal-mechanism solutions of intraplate seismicity in the SCA (global CMT catalog, Dziewonski et al., 1981; Ekström et al., 2012) shows a predominance of reverse and strike-slip faulting (Fig. 5.1), indicating a preferential slip direction perpendicular and oblique to the plate-convergence direction, respectively (e.g. Farías et al., 2008; Tapia et al., 2015). Despite these established research results, there is still an open debate on the spatially widely distributed intraplate seismicity in the SCA, where little to no record of present-day seismicity is found in certain domains, although ubiquitous Quaternary faults have been mapped at surface (e.g. Eastern Sierras Pampeanas, Neuquén Basin; Costa et al., 2000, 2020; Grimaldi & Dorobek, 2011; Martino, 2003; Sagripanti et al., 2017). This disparity between instrumentally recorded earthquakes and paleo-seismological manifestations in the Sierras Pampeanas is noteworthy and may result from long recurrence intervals. Alternatively, some authors proposed that variations in the long-term strength of the lithosphere may be responsible for the observed lack of seismicity in areas with pervasive active faulting, provided that the integrated strength of the plate exceeds the magnitude of plate-driving stresses (e.g. Liu & Zoback, 1997).

Whether a causative relationship exists between the long-term strength of the lithosphere and the spatial distribution of seismicity has long been a matter of controversy (Burov, 2011; Chen et al., 2012; Chen & Molnar, 1983; Handy & Brun, 2004; Jackson et al., 2008; Scholz, 1988; Sibson, 1982). It has been proposed that the depth at which rocks transition from a preferentially brittle to a preferentially ductile mode of deformation in the lithosphere ('brittle-ductile transition' or BDT, Goetze & Evans, 1979) provides a conservative estimate of the down-dip extent of the seismogenic zone (e.g. Scholz, 1988; Sibson, 1982). Furthermore, compilations of crustal seismicity in different regions show that old or mafic crustal sectors are characterized by deep-seated seismicity, which supports the idea of a rheological control that is inherited from paleotectonic processes (Craig & Jackson, 2021; Jackson et al., 2008; Maggi et al., 2000). More recently, 3D observation-based modeling studies re-evaluated the role of lateral and vertical variations in the long-term mechanical configuration of the lithosphere on the distribution of seismicity (Anikiev et al., 2020; Gholamrezaie et al., 2021; Ibarra et al., 2021; Tesauro et al., 2009). Since these models are able to resolve the spatial variability of lithospheric thickness, composition, and temperature in different regions, they afford a first-order quantification of the long-term mechanical stability of the lithosphere and its direct comparison with seismicity in convergent margins and intraplate settings. A common conclusion from these studies is that there exists a spatial correlation between the distribution of lithospheric domains of different mechanical strength and the seismicity distribution.

In the SCA, recently published 3D structural and thermal models describing the first-order variation in the (i) thickness, (ii) composition, and, (iii) temperature of the main lithospheric units (crust and mantle of the continental and oceanic plates; Rodriguez Piceda et al., 2021; Chapter 3 of this dissertation) provide the opportunity to quantify the resulting thermomechanical configuration of the lithosphere and to investigate whether a causative spatial relationship exists between variations in long-term lithospheric strength and recorded active seismic deformation. In this contribution, we make use of these 3D models as input in a rheological study, where we compute (according to a method numerically implemented by Cacace & Scheck-Wenderoth, 2016) the spatial variability of crustal and lithospheric strength throughout the SCA. This enable us to obtain the first 3D rheological model of the SCA, including available structural, compositional and thermal information of the area. These results are subsequently compared to the spatial distribution of intraplate seismicity (International Seismological Centre, 2021) to determine whether and to what extent those variations in the long-term rheological configuration affect the localization of seismicity across the southern Central Andes, including the forearc and foreland regions.

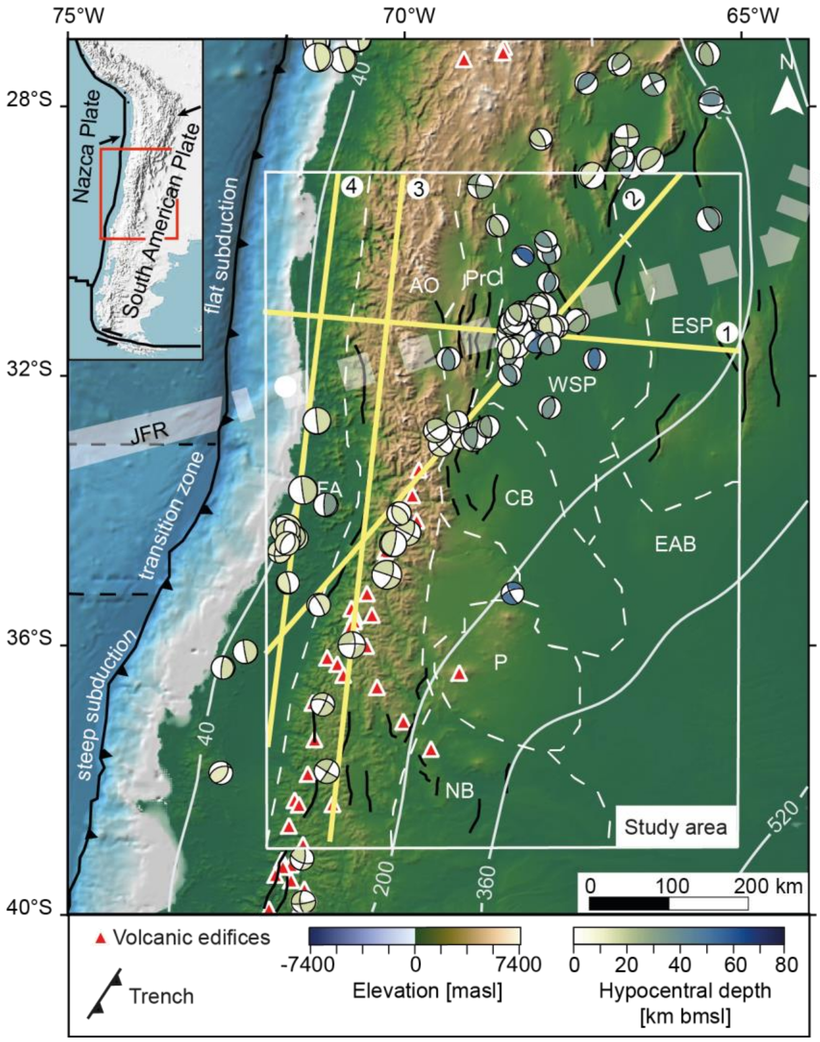

Figure 5. 1: Topography and bathymetry of the southern Central Andes taken from the ETOPO1 global relief model (Amante & Eakins, 2009) overlain with the focal mechanisms of intraplate earthquakes from the Global Centroid Moment Tensor Catalog (Dziewonski et al., 1981; Ekström et al., 2012), color-coded by their hypocentral depth. Black dashed lines in the oceanic domain indicate the boundaries between subduction segments with steepening subduction angles from north to south. White lines are isodepth contours (km below mean sea level) of the top of the oceanic crust obtained from the Slab2 model (Hayes et al., 2018). The thick and dashed white lines show the offshore and projected tracks of the Juan Fernandez Ridge (JFR), respectively (Yáñez et al., 2001). The white rectangle encloses the extent of the area modelled in this study. Thick black lines indicate the main Quaternary tectonic faults (Sagripanti et al., 2017). The boundaries between the main morphotectonic provinces are shown by white dashed lines. The red triangles indicate active volcanoes. The yellow lines show the location of the profiles in Figures 5.5 and 5.6. Abbreviations of main tectonic provinces: AO = Andean orogen, CB = Cuyo Basin, ESP = Eastern Sierras Pampeanas, EAB = extra-Andean basins, FA= forearc, NB = Neuquén Basin, P = Payenia volcanic province, Prc = Precordillera, WSP = Western Sierras Pampeanas.

5.2.1 Geologic Setting

The SCA encompass four main morphotectonic provinces: the forearc, the magmatic arc, the back-arc and the foreland, each of them characterized by distinct structural and geomorphological features. The present-day configuration of the SCA is the result of a complex tectonic evolution that spans from the Neoproterozoic to the Quaternary, including episodes of terrane amalgamation, shortening and extension (Astini et al., 1995; Azcuy & Caminos, 1987; Giambiagi et al., 2003; Jordan et al., 1983; Kay et al., 2006; Llambias & Sato, 1990; Mpodozis & Kay, 1990; Ramos, 1988). The ongoing subduction beneath the South American Plate has been active since at least the Late Jurassic (Maloney et al., 2013 and references therein), although major pulses of Andean deformation are thought to have occurred during the Late Cretaceous and the Miocene (Boyce et al., 2020; Fennell et al., 2015). The onset of the flat subduction north of 33°S is thought to have occurred at ~19 Ma (Jones et al., 2014, 2015, 2016), finally attaining its present-day subhorizontal angle at ~7–6 Ma (see Kay et al., 2006a; Kay & Mpodozis, 2002; Ramos et al., 2002). The causative dynamics responsible for the evolution in the Central Andes is not very well known. Some authors argue that episodes of flat subduction are responsible for the migration of the deformation to the foreland (e.g. Oncken et al., 2006; Yáñez & Cembrano, 2004), while others consider these compressional events as a result of reactivation of inherited tectonic heterogeneities, such as crustal-scale sutures, independent of the role of the slab (Allmendinger et al., 1983; Hongn et al., 2007, 2010; Kley et al., 1999; Kley & Monaldi, 2002; Mon & Salfity, 1995; del Papa et al., 2013; Ramos et al., 2002).

5.3 Methods

5.3.1 Modeling approach

We computed the long-term yield strength envelope of the lithosphere (i.e. for time scales longer than the characteristic relaxation time), this being the maximum differential stress that the composing rocks are able to withstand without experiencing permanent deformation (Christopher Goetze & Evans, 1979). The computation was carried out with a vertical resolution of 1 km following the approach by Cacace & Scheck-Wenderoth (2016). We assumed that rocks may exhibit frictional behavior (e. g., at shallow depths), described by Byerlee‘s law (Byerlee, 1968). According to this law, frictional behavior is temperature-independent, but sensitive to the effective confining pressure, and can be expressed as Ranalli (1995):

$$\Delta\sigma_b = f_f \rho_b g z (1 - f_p) \ (5.1)$$

where $\Delta\sigma_b$ is the brittle yield strength, f_f is the Byerlee’s friction coefficient (which depends on the internal friction coefficient μ_f and the faulting regime, Appendix C.1), ρ_b is the bulk density, g is the gravitational acceleration, z the depth below topography and f_p is the pore fluid factor (defined as the ratio $\rho_f \rho_b^{-1}$, where ρ_f is the density of the fluid).

With increasing depths and temperatures, rocks deform as viscous (non-)Newtonian fluids, with dislocation creep being the dominant deformation mechanism in the lithosphere. We also included low-temperature plasticity (Peierls creep) at differential stresses greater than 200 MPa (Goetze et al., 1978; Katayama & Karato, 2008). The power laws describing dislocation creep (eq. 5.2) and low-temperature plasticity (eq. 5.3) can be expressed as:

$$\Delta\sigma_{\mathrm{d}} = \left(\frac{\dot{\varepsilon}}{A_p}\right)^{\frac{1}{n}} \exp\left(\frac{Q_p}{nRT}\right) \; (5.2)$$

$$\Delta\sigma_{\mathrm{D}} = \sigma_D\left(1 - \left[-\frac{RT}{Q_D} ln \frac{\dot{\varepsilon}}{A_D}\right]^{\frac{1}{2}}\right) \; (5.3)$$

where $\Delta\sigma_{\mathrm{d}}$ is the ductile yield strength, $\dot{\varepsilon}$ the reference strain rate, A_p the pre-exponential scaling factor for dislocation creep, n the power law exponent, Q_p the activation energy, T the temperature, R is the universal gas constant ($R = 8.314\ JK^{-1}mol^{-1}$), σ_D the Peierls critical stress, Q_D the Dorn activation energy ($Q_D = 5.35e5\ Jmol^{-1}$) and A_D the Dorn's law strain rate ($A_D = 5.7e11\ s^{-1}$).

The yield strength ($\Delta\sigma_{\mathrm{max}}$) at a given point is then defined by the minimum of the brittle and ductile strength curves, $\Delta\sigma_{\mathrm{b}}$ and $\Delta\sigma_{\mathrm{d}}$ (Goetze & Evans, 1979). The depth at which the two curves intercept mark therefore the brittle-ductile transition ('BDT' hereafter). In an attempt to better quantify the efficiency of viscous creep, we also discuss the results in terms of the effective viscosity (η_{eff}). This parameter is expressed by a power-law dependence of temperature and strain rate as (Burov, 2011):

$$\eta_{\mathrm{eff}} = \frac{2^{\frac{1-n}{n}}}{3^{\frac{1+n}{2n}}} A^{-\frac{1}{n}} \dot{\varepsilon}^{\frac{1}{n}-1} \exp\left(\frac{H}{nRT}\right) \; (5.4)$$

where H is creep activation enthalpy, H=Q+PV, where Q is activation energy, P is pressure and V is activation volume.

The material and temperature distributions used as input for the computation of the yield strength envelopes of the lithosphere were obtained from 3D lithospheric-scale models of the SCA (Rodriguez Piceda et al., 2021; Chapter 4 of this dissertation) and described in more detail in Section 5.3.1.1. The specific mechanical properties assigned to the lithospheric units of the model are subsequently outlined in Section 5.3.1.2.

5.3.1.1 3D structural and thermal models

To estimate the present-day rheological configuration of the SCA, we used the geometries and densities of the layers forming the 3D lithospheric-scale model of Rodriguez Piceda et al. (2021) (Chapter 3). This model results from the integration of different geological and geophysical data, including seismic tomography, reflection and refraction seismic profiles, sediment isopach maps, petrological data and a gravity field model (see references in Rodriguez Piceda et al., 2021). The model covers a region that extends 1100 km in the N-S direction, 700 km in the E-W direction (white rectangle in Fig. 5.1) and 200 km in depth. The layers composing the model were defined according to the main density contrasts in the lithosphere. The layers considered for the estimation of the present-day rheology are: (1) oceanic and continental sediments; (3) upper continental crystalline crust; (4) lower continental crystalline crust; (5) continental lithospheric mantle (6) shallow oceanic crust; (7) deep oceanic crust; (8) oceanic lithospheric mantle; and (9) oceanic sub-lithospheric mantle. The main features of the model are depicted in Figure 5.2: (a) thickness of sediments; (b) thickness of continental crystalline crust; (c) thickness of upper continental crystalline crust; (d) depth to the top of the oceanic crust; and (d) average density of the continental crystalline crust.

The continental crystalline crust exhibits a first-order segmentation in terms of thickness and density, delineating three main crustal domains (Fig. 5.2b): (i) the forearc, (ii) the Andean orogen and (iii) the low-relief back-arc and foreland (‘BAF’, hereafter). The forearc is characterized by a normal continental crystalline crust (< 35 km, Fig. 5.2b) and intermediate to high average crustal densities (~2975 kgm^{-3}, Fig. 5.2f). The Andean orogen has a greater crystalline crustal thickness (~55 km, Fig. 5.2b) and less dense crust (~2900 kgm^{-3}; Fig. 5.2f) than the adjacent regions. The BAF can be segmented into three crustal domains: (i) a thick, dense northern domain (40–60 km , ~3000–3050 kgm^{-3}); (ii) a thin, high-density southern domain (~20 km, 40–60 km); and (iii) a central domain with intermediate crustal thickness (35–45 km) and low to intermediate crustal densities (~2900–2950 kgm^{-3}).

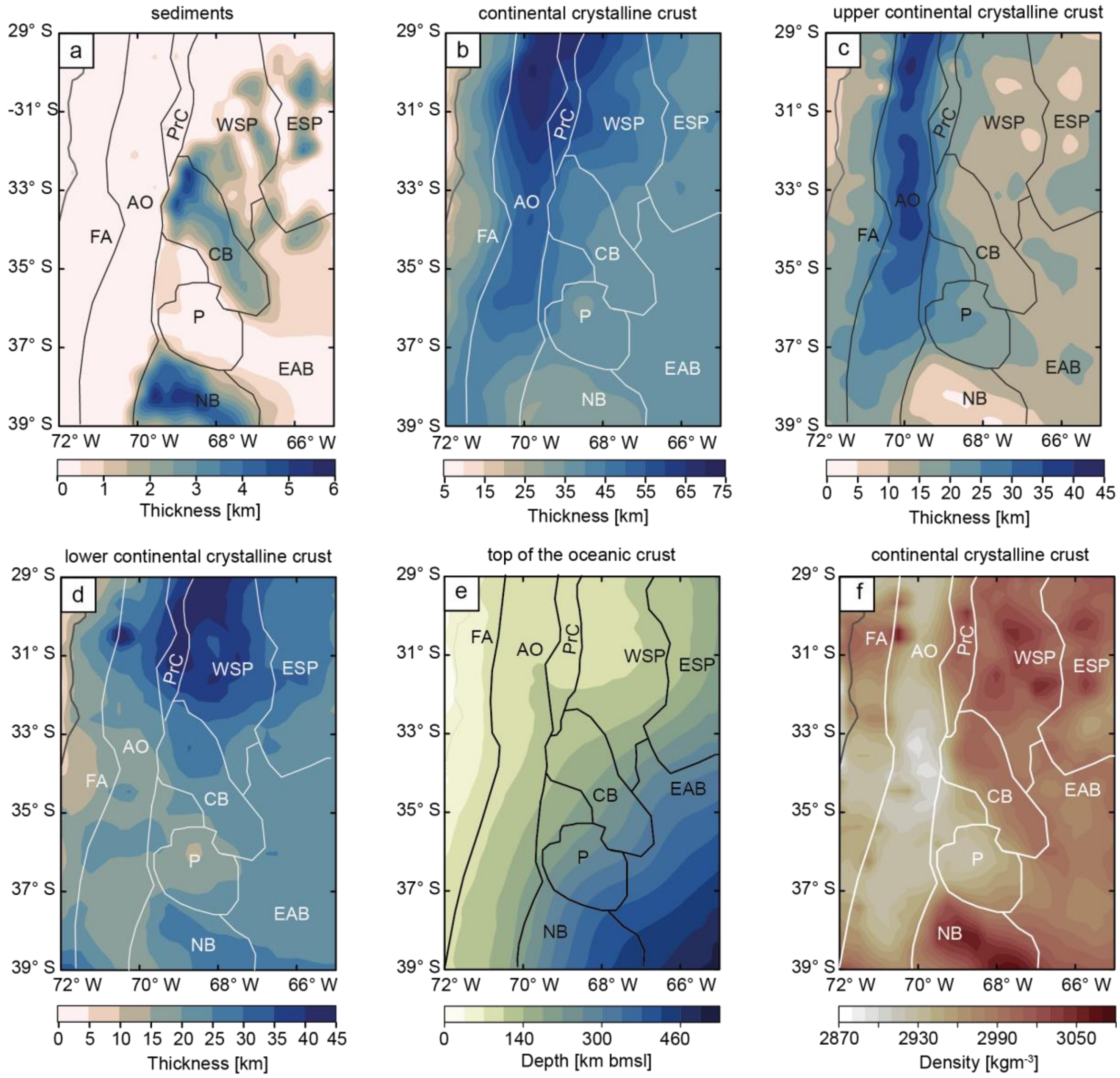

Figure 5. 2: Main structural features of the SCA lithosphere from the model of Rodriguez Piceda et al. (2021): thickness of (a) sediments; (b) continental crystalline crust; (c) felsic upper continental crystalline crust; (d) mafic lower continental crystalline crust; (e) depth to the top of the oceanic crust derived from the Slab2 subduction zone geometry model (Hayes et al., 2018); (f) average density of the continental crystalline crust. Boundaries of the main morphotectonic provinces are overlain; for abbreviations see Fig. 5.1

The temperature configuration used for the rheological calculations was extracted from a thermal model of the SCA (Chapter 4 of this dissertation) covering the same region as the structural model of Rodriguez Piceda et al. (2021). Crustal and mantle temperatures down to 50 km below mean sea level (bmsl) were computed assuming steady-state conductive conditions and using as an input the structural model of Rodriguez Piceda et al. (2021). Specific thermal properties were assigned to each layer of the model according to prevailing lithologies and to best fit wellbore temperature measurements (Collo et al., 2018) with the modelled thermal field. For the conductive thermal field calculation, the average surface temperature distribution (Copernicus Climate Change Service (C3S), 2019) was assigned as upper thermal boundary condition, whereas the temperature distribution at 50 km depth was assigned as lower thermal boundary condition. The latter was estimated from the conversion of S-wave tomography (Assumpção et al., 2013) using the approach by Goes et al. (2000) modified by Meeßen (2017) (for details, see Chapter 4 of this dissertation). The 3D thermal field between 50 and 200 km bmsl is derived directly from the seismic tomography.

Figure 5.3 shows the depth maps for the 450°C and 650°C isotherms, as they are considered to represent the thermal field of the study area at crustal and uppermost mantle levels. The 450°C isotherm shallows in the model domains of thickened upper crust enriched with radiogenic minerals (orogen), which indicates overall warmer temperatures in these domains (Fig. 5.3a). Conversely, it deepens in the crustal domains characterized by a thin upper crust, a thick mafic lower crust and where the slab is at relatively shallow depth and, therefore, is colder than where the subduction angle is steeper (forearc and BAF). As a result, the isotherm is located within the upper crust in the orogen; within the lower crust in the BAF; and within the continental lithospheric mantle in the forearc. The 650°C isotherm exhibits a similar pattern to that of the 450°C isotherm (Fig. 5.3b), shallowing in the Andean orogen and deepening in the forearc and the northern BAF. It is located mostly within the lower crust in the orogen and northernmost BAF; in the continental mantle in the remaining BAF and eastern forearc, and within the slab in the western forearc. The overall pattern of the two isotherms is partly different in that the 450°C isotherm rather mirrors the thickness of the upper crust (Fig. 5.2b) whereas the 650°C isotherm follows the pattern of the top of the oceanic crust (‘subduction interface’ hereafter) (Fig. 5.2e).

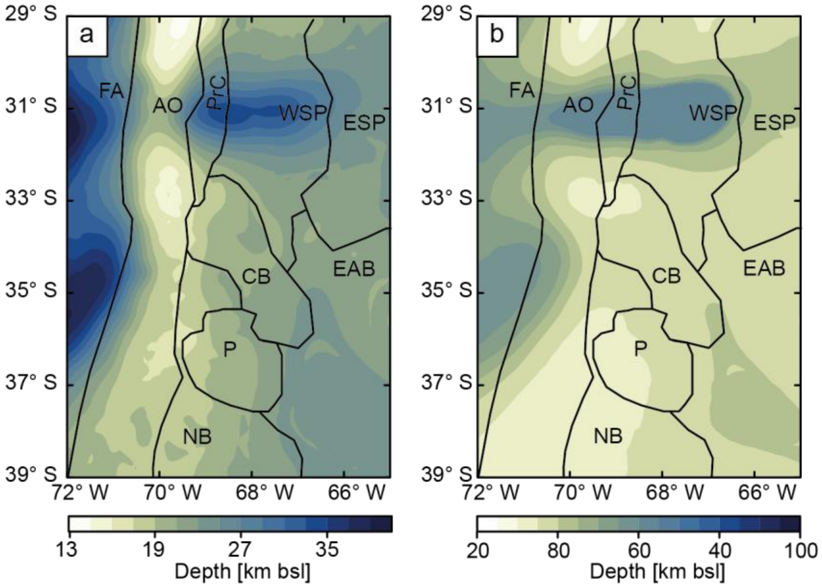

Figure 5. 3: Depth of the (a) 450°C and (b) 600°C isotherms across the modelled area according to the lithospheric-scale model of Chapter 3). Boundaries of the main morphotectonic provinces are also marked with black lines; for abbreviations see Fig. 5.1

5.3.1.2 Rheological properties

We assigned constant rheological properties for each layer of the model of Rodriguez Piceda et al. (2021) according to its prevailing lithology. These values were taken from studies based on experimental rock mechanics (Table 5.1; (Afonso & Ranalli, 2004; Gleason & Tullis, 1995; Goetze & Evans, 1979; Hirth & Kohlstedt, 1996; Ranalli & Murphy, 1987; Wilks & Carter, 1990). The lithologies were interpreted, in turn, from gravity-constrained densities (Rodriguez Piceda et al., 2021) and observed seismic velocities (Araneda et al., 2003; Contreras-Reyes et al., 2008; Marot et al., 2014; Pesicek et al., 2012; Scarfì & Barberi, 2019). Since the material properties for similar lithologies can differ between different laboratory-based studies, we selected creep parameters in a way that ensures that felsic layers are weaker than mafic ones. We provide a detailed description of our selection strategy in the Appendix C.2.

An important role in the accommodation of deformation is taken by the subduction interface (Sobolev et al., 2006), which in the model is underlain by an oceanic crustal body (~7 km thickness). The uppermost part of this body (~ 3 km thickness) is interpreted as being made up of a mèlange of metasediments, serpentinites and serpentinized peridotites, based on exhumed rock assemblages at surface related to the subduction channel (e.g. Vannucchi et al., 2008). Therefore, to model the mechanical behavior of this environment, we assigned to it a 'weak quartzite' rheology (Wilks & Carter, 1990) which would be consistent with a tectonic mélange.

The Byerlee's friction coefficient f_f of all considered layers (except for the subduction interface) was set to 2. This is consistent with the overall compressive regime at the convergent margin and it is equivalent to an internal friction coefficient μ_f of 0.65. The pore-fluid factor of these layers was set to 0.36, which is indicative of near hydrostatic conditions. For the subduction interface, in order to represent the mèlange at the subduction channel, we changed the values of both the Byerlee's friction coefficient and pore fluid factor of the uppermost oceanic crustal body to 0.03 and 0, respectively. These values are consistent with an internal friction coefficient μ_f of 0.015, which is considered appropriate of the frictional behavior of the subduction channel at the latitude of the SCA (Sobolev et al., 2006).

For all the modeled layers (except for the subduction interface), the strain rate $\dot{\varepsilon}$ was set to 6.5e-16 s^{-1}, which is consistent with the amount of shortening produced in the SCA in the last 18 Ma (Giambiagi et al., 2012) and with GNSS measurements (Drewes & Sánchez, 2017; Appendix C.3). The subduction interface, as a plate boundary, is subjected to strain rates up to 4 orders of magnitude higher than the continental and oceanic plates, as shown by petrological evidence derived from rocks exhumed from the subduction channel (Platt et al., 2018) and results from geodynamic numerical modeling of subduction zones (Muldashev, 2017). In an attempt to model this behavior, we set an $\dot{\varepsilon}$ of 1e-12 s^{-1} for the uppermost sectors of the oceanic crustal body.

Table 5.1: Rheological properties of the model units

Model Layer	Prevailing lithology	Type rheology	Dislocation creep parameters			Frictional parameters		
			Activation enthalpy Q [$Jmol^{-1}$]	**n**	**Pre-exponential factor [$Pa^{-n} s^{-1}$]**	**Pore-fluid factor f_f**	**Byerlee's friction coefficient f_f**	**Bulk Density [kgm^{-3}][7]**
Oceanic/Continental sediments	Siliciclastic	Wet granite[1]	1.37e5	1.9	7.94e-16	0.36	2	2300/2400
Upper crust	Diorite	Dry quartz diorite[1]	2.19e5	2.4	5.02e-18	0.36	2	2800
Lower crust	Mafic granulite	Dry mafic granulite[2]	4.45e5	4.2	8.83e-22	0.36	2	3100
Continental lithospheric mantle/oceanic sub-lithospheric mantle	Moderately depleted lherzolite	Dry Olivine[3]	5.10e5	3	7.00e-14	0.36	2	3340
Shallow oceanic crust (weak)	Melange (serpentinites, serpentinized peridotites, metasediments)	Wet quartzite[4]	2.23e5	4	1.00e-28	0	0.03	2900
Shallow oceanic crust (strong)	Basalt	Dry diabase[5]	4.85e5	4.7	5.05e-28	0.36	2	2900
Deep oceanic crust	Eclogite	Dry diabase[5]	4.85e5	4.7	5.05e-28	0.36	2	3200
Oceanic lithospheric mantle	Harzburgite	Dry peridotite[6]	5.35e5	3.5	5.01e-17	0.36	2	3360

[1] Ranalli & Murphy (1987); [2] Wilks & Carter (1990); [3] Goetze & Evans (1979); [4] Gleason & Tullis (1995), quartzite weakened by increasing pre-exponential factor A by 10 times (Sobolev & Babeyko, 2005) ;[5] Afonso & Ranalli (2004); [6] Hirth & Kohlstedt (1996); [7] Rodriguez Piceda et al. (2021)

5.3.2 Seismic catalogue

The computed lithospheric strengths and viscosities were compared against the distribution of seismic events for the study area between 1995 and 2018 available from the reviewed bulletin of the International Seismological Centre (International Seismological Centre, 2021). All events of which the fixed depths are associated with an error > 5 km were removed from the analyzed dataset in order to maximize reliability of the investigation. To separate intraplate events for this comparative study, we considered the depth of the top oceanic crust from the subduction zone geometry model Slab2 (Hayes et al., 2018) as their lower boundary. Our choice of this surface to represent the subduction interface stems from the consistency between fault-strike orientations inferred from the Slab2 model and GCMT focal mechanisms solutions (Chen et al., 2020). Since the Slab2 model has an uncertainty of up to tens of kilometers (Appendix C.4), we defined the maximum depth of intraplate seismicity as the depth of the top oceanic crust + the uncertainty of the Slab2 model. After filtering the data, 2174 events of moment magnitude (Mw) between 1 and 7.2 were available for comparison with our rheological model.

5.4 Results

5.4.1. Intraplate seismicity

Figure 5.4 shows the maps of event density and of the seismogenic depth D95 (depth above which 95% of events occur) of intraplate seismicity. In the forearc and in the central part of the orogen, seismic events preferentially nucleate at depths < 30 km bmsl. In the BAF regions of Precordillera, Sierras Pampeanas and Cuyo basin, i.e. largely above the flat-slab segment, the seismicity occurs at deeper crustal levels (D95=~40 km, Figs. 5.4a–b), whereas the southern and northern parts of the orogen and the remaining foreland regions are mostly aseismic.

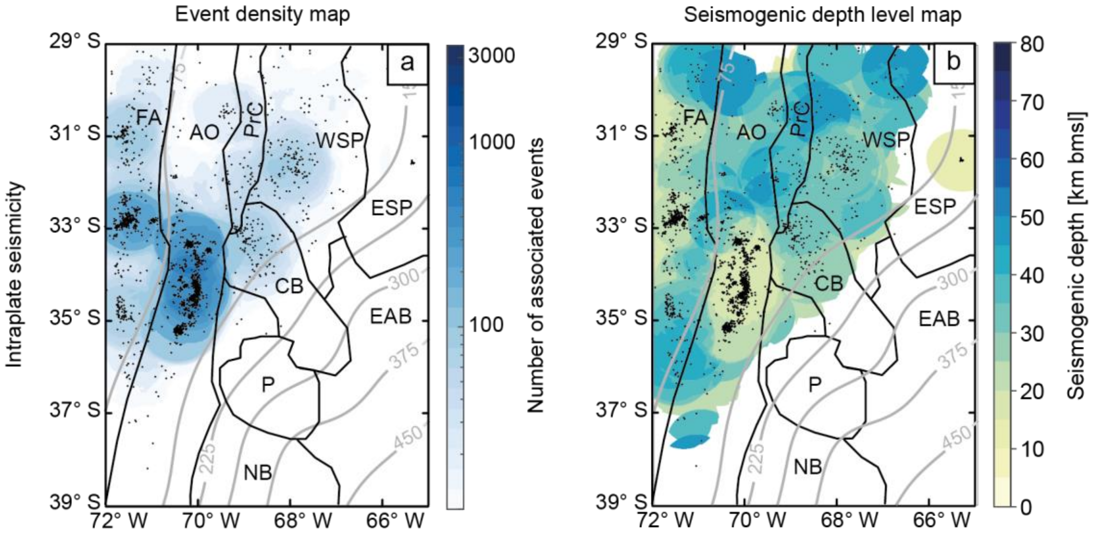

Figure 5.4: Spatial distribution of event density and of seismogenic depth D95 (depth above which 95% of events occur) derived by considering a circular bin of 75 km radius (logarithmic scale) for intraplate seismicity. Single seismic events are marked with black dots. Isodepth contours of the top of the oceanic slab (Hayes et al. 2018) are shown as grey lines. Boundaries of the main morphotectonic provinces are also marked with black lines; for abbreviations see Fig. 5.1

5.4.2 Rheological Modeling

Figure 5.5 depicts the integrated strength of (a) the continental crust (IS_c) and (b) the lithosphere (IS_L) for the study area. Both maps exhibit a heterogeneous strength distribution, with mechanically strong domains in the forearc and the northern BAF along the flat slab segment (IS_C=13.3–13.6 log Pa m; IS_L=13.5–13.9 log Pa m) and a mechanically weaker domain within the orogen proper (IS_C=12.7–13 log Pa m; IS_L=12.7–13.3 log Pa m). The orogen shows a local increase in both crustal and total lithospheric strength at approximately 31°S and between 33°S–35°S. A change in the observed overall positive correlation between IS_C and IS_L is found within the offshore part of the forearc, which displays a weak crust (IS_C<= 12.2 log Pa m) underlain by a strong mantle (IS_L>=13.6 log Pa m).

Modelled variations in both IS_C and IS_L largely correlate with the temperature distribution as represented by the isotherm examples (Fig. 5.3). Mechanically stronger domains in the forearc and the northern foreland correspond to colder domains, and the weak orogenic domain is characterized by steeper geothermal gradients. We also found a spatial relationship between the thickness distribution of the radiogenic upper continental crystalline crust (Fig. 5.2c) and the IS_L distribution. Crustal domains with a thicker upper continental crystalline crust (orogen) correlate with lower lithospheric strength values, whereas a thin upper continental crystalline crust is characterized by an increase in lithospheric strength (forearc and northern foreland).

This negative correlation between the thickness of the upper continental crust and lithospheric strength stems from the role of this layer with respect to the whole thermal budget of the plate, due to its dominant felsic lithology and high radiogenic potential, a pronounced upper crustal thickness translates into higher temperatures and, therefore, lower values of lithospheric strength. In contrast, the lower crust is comparatively depleted in heat-producing elements (Vilà et al., 2010), thus in regions with large lower crustal thickness (northern foreland) the thermal input decreases, which derives in lower temperatures and, therefore, higher values of lithospheric strength.

In an attempt to evaluate the contribution of the different layers (crust and lithospheric mantle) to the make-up of the plate integrated strength we present in Figure 5.5c a map showing the distribution of their strength ratio (Fig. 5.5c). The strength ratio can be used as a proxy of the dominance of the crustal component over the lithospheric strength. Accordingly, a ratio close to 100% means that the crust is the only contributor to the lithospheric strength, whereas a ratio close to 0% means that the lithospheric strength resides almost entirely in the mantle. The forearc and the Sierras Pampeanas exhibit a low ratio (25–40), which indicates that a great part of the strength resides in the mantle. The remaining areas of the model are characterized by higher strength ratios, with maximum values along the orogen and northernmost BAF (north of 30°S), which implies a higher contribution of the crust to the overall lithospheric strength across these domains.

To gain further insight into the rheological configuration of the area, we computed the mechanical thickness (H_L) from the modeled yield strength. H_L is the load-bearing thickness of the plate, defined as the thickness with a strength above a critical threshold, usually set at 10 MPa (Ranalli, 1994). Below this threshold, the strength of the plate becomes insignificant, thus, the dissipation of elastic energy below the depth defined by H_L is also negligible. In addition, H_L can be used to estimate the coupling-decoupling conditions of the crust and mantle in the continental plate (e.g. Tesauro et al., 2012). If H_L is greater than the thickness of the continental crust, then continental crust and mantle are considered mechanically coupled. Conversely, if H_L is smaller than the thickness of the continental crust, then the two layers are considered mechanically decoupled. Given these characteristics, H_L provides a more appropriate quantitative metric for direct comparison with the map showing seismogenic depth than other rheological parameters, such as elastic thickness Te. This is because visco-plastic models usually predict lower stresses in regions of high strain than purely elastic models (Anikiev et al., 2020; Ranalli, 1994).

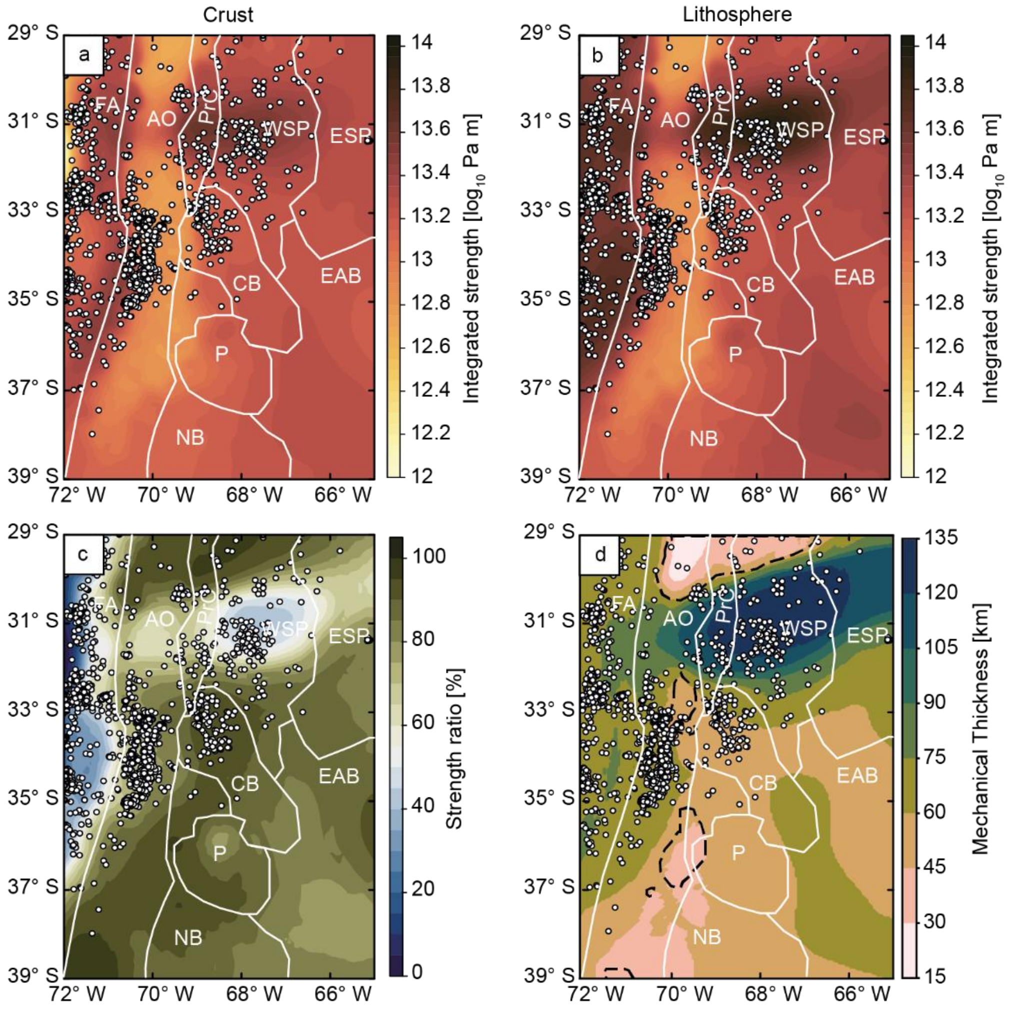

Figure 5.5: Integrated strength of (a) continental crust and (b) lithosphere; (c) strength ratio between integrated strength of the crust and of the lithosphere (strength ratio = IS_C / IS_L * 100); (d) mechanical thickness (i.e. thickness of the plate having a strength above a critical threshold of 10 MPa) with model domains where the crust and mantle of the continental plate are mechanically decoupled marked by enclosing black dashed lines. Intraplate seismicity is represented by white circles. Boundaries of the main morphotectonic provinces are also marked with white lines; for abbreviations see Fig. 5.1

Figure 5.5d illustrates the spatial variations in the mechanical thickness H_L along with the coupling-decoupling conditions of the continental crust and mantle. H_L displays a positive correlation with the IS_L (Fig. 5.5b), where larger values are found in the orogen at ~32°S, the Sierras Pampeanas, Precordillera, and the forearc (H_L=60–135 km). These values contrast with the reduced mechanical thickness of most of the orogen (H_L < 60 km). As a result, continental crust and mantle are mechanically decoupled mainly along the orogenic axis. The modeled mechanical thickness shows a similar spatial distribution as the one of the seismogenic base obtained independently from the seismic catalogue: deeper intraplate seismicity (D95=40–50 km) occurs where the mechanical thickness is > 100 km within the northern BAF regions. In contrast, shallow intraplate events (D95<30 km) takes place where the mechanical thickness is 60–75 km within the forearc and in the central part of the orogen.

Within the continental plate, mechanical strength also varies quite significantly with depth, as can be seen from four profiles that traverse our 3D model (Fig. 5.6). The location of the profiles was chosen according to the regions displaying the largest amount of seismic events: Profile 1 crosses the region from East to West across the flat slab segment; Profile 2 is oriented NE to SW; Profile 3 traverses the region along the orogen; and Profile 4 is located along the forearc (Fig. 5.1). In the forearc, strength increases up to 1.5 GPa at mantle depths of 50 km (Fig. 5.6, Profiles 1–2 and 4). Conversely, in the orogen the highest strength values (0.6 GPa) are reached at 20–25 km depth in the upper crust (Fig. 5.6, Profile 1). However, the orogen shows a local increase in strength in the mantle between 500 and 800 km along the profile (1.5 GPa, Fig. 5.6, Profile 3). This corresponds to the temperature minimum at about 34°S–36°S, as also illustrated by the deepening of the 450° and 600° isotherms at 33°S–35°S (Fig. 5.2). In the foreland, the strength maximum is 1.5 GPa and situated at lower crustal depths of ~35 km (Fig. 5.6, Profiles 1–2). Beneath the Sierras Pampeanas, the continental mantle exhibits high strength values (0.6–1.5 GPa, Fig. 5.6, Profiles 1–2). The highest strength values in the lower crust and continental lithospheric mantle correlate spatially with the deep location of the 600°C isotherm in the northern BAF.

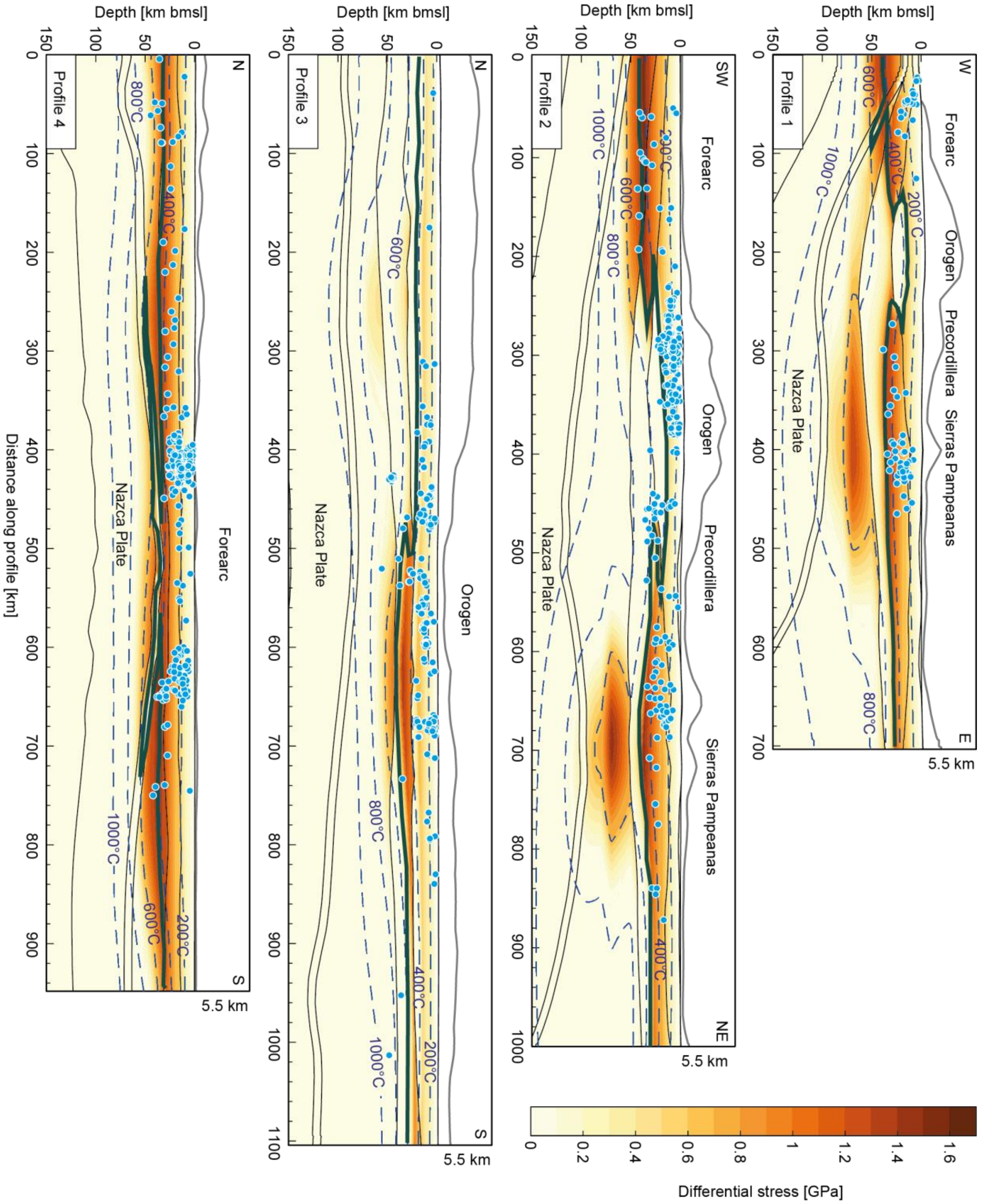

Figure 5. 6: differential stress computed along cross-sections 1–4 indicated in Figure 5.1. Light-blue dots show the location of hypocenters of seismic events within 5 km from each profile. The isotherms are marked in dashed blue lines. The BDT is shown in a thick green line. Black lines show the interfaces of the model layers. Topographic elevations are shown on top of each profile with a vertical exaggeration of 10:1. For abbreviations of main morphotectonic provinces see Fig. 5.1

These strength heterogeneities between the different morphotectonic provinces are also illustrated by depth variations in the BDT. In the orogen, the BDT occurs at upper crustal levels while in the foreland it deepens, reaching lower crustal depths (Fig. 5.6, Profiles 1–3). In the forearc, on the other hand, the BDT occurs within the lithospheric mantle or within the oceanic slab (Fig. 5.6). Within the slab, higher differential stresses (>1 GPa) occur above ~50 km depth in the western model domain (Fig. 5.6a). However, in contrast to what is observed within the continental plate, there are no significant lateral strength variations within the slab.

By analyzing the effective viscosity profiles (Fig. 5.7) extracted at the same location as those of Figure 5.6, we note that most of the continental crust is characterized by relatively high viscosity values (average 24 log Pa s) compared to values (22 log Pa s) at lower crustal and/or mantle levels. The effective viscosity decreases at shallower depths within the orogen proper. This trend is due to overall higher temperatures that characterize this model domain (Fig. 5.2). The effective viscosity also varies laterally within the continental mantle, with higher values (> 24 log Pa s) in the forearc, the northern foreland areas of the Precordillera and the Sierras Pampeanas; and low values are attained in the orogen and the remainder of the foreland (20–22 log Pa s). The oceanic plate shows a higher effective viscosity (> 24 log Pa s) at shallow depths (< 50 km) and along the flat-slab segment beneath the Precordillera and the Sierras Pampeanas (Fig. 5.7, Profiles a–b and d).

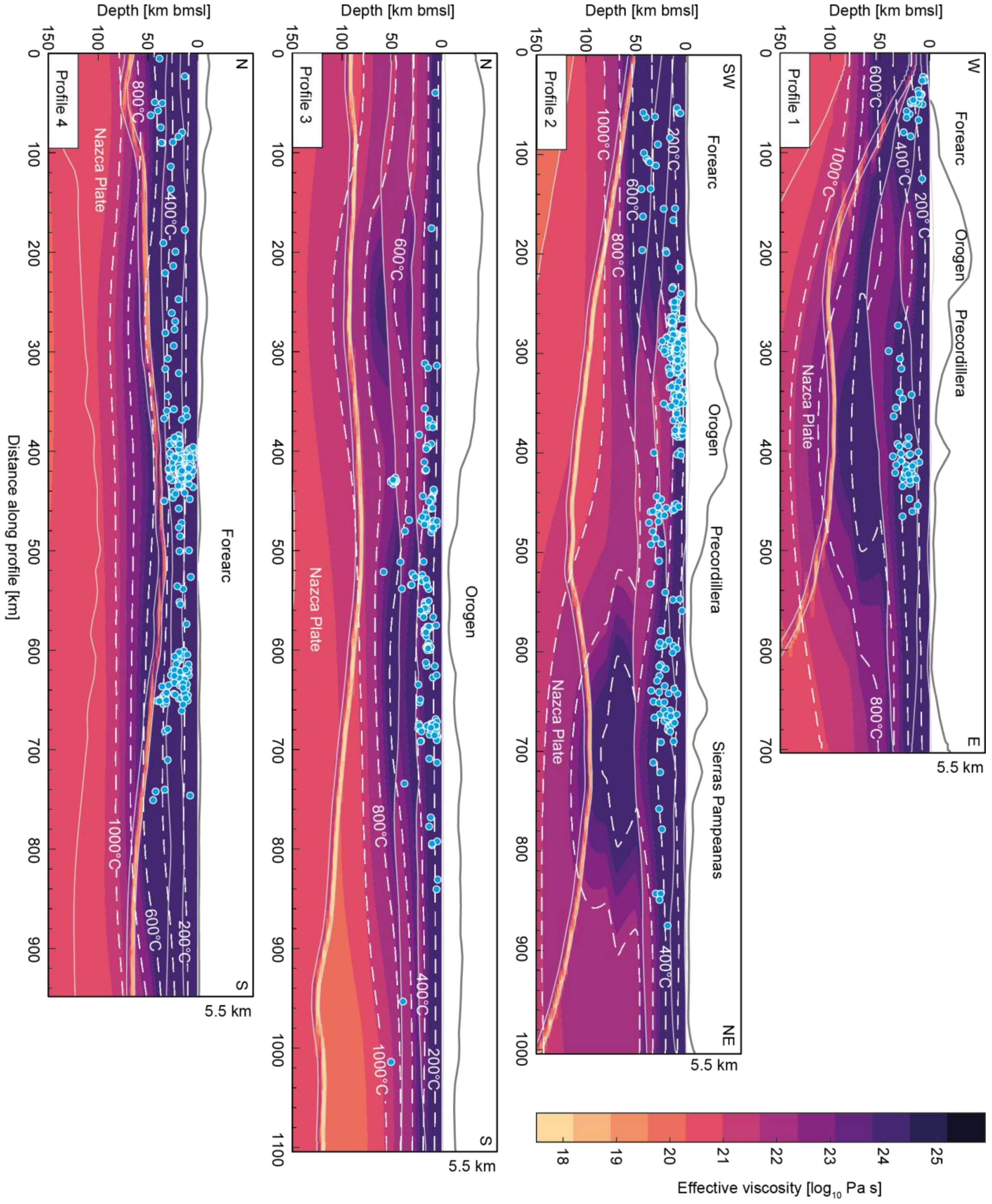

Figure 5.7: effective viscosity along cross-sections 1–4 locations shown in Figure 5.1. Light-blue dots show the location of hypocenters of seismic events within 5 km from each profile. The isotherms are marked in dashed white lines. Light-grey lines show the interfaces of the model layers. Topographic elevations are shown on top of each profile with a vertical exaggeration of 10:1. For abbreviations of main morphotectonic provinces see Fig. 5.1

5.5 Discussion and conclusions

5.5.1 Modeled mechanical strength of the lithosphere

Our results indicate a heterogeneous distribution of integrated lithospheric strength of the overriding continental plate in the different morphotectonic provinces. The mechanically strong domains of the forearc, the central-western part of the orogen, and the foreland areas of the Precordillera and Sierras Pampeanas contrast with the weak domain of most of the orogen. The remaining foreland areas display intermediate strengths.

The comparison between the 3D configuration of the thermal field and of the strength variations implies that the modelled strength distribution is mainly controlled by the lithospheric thermal field: there exists a one-to-one correspondence between strengthening and weakening of the lithosphere and the cold and warm domains, respectively. Given the first-order control of the temperature on the strength distribution, the isotherm depths can be used as a proxy for the strength of the lithosphere. More precisely, the overall rheological behavior of the lithosphere can be described by the depth variation of the 450 °C isotherm, which coincides with the BDT in most of the study area. The deepening of the 450 °C isotherm down to lower-crustal or mantle levels is associated with strengthening of the lithosphere, and vice versa. We note that variations in the thermal configuration are primarily controlled both by the distribution of the volumetric heat contribution of the upper radiogenic crust and, to a lesser extent, by superposed cooling limited to domains around the subducting slab (Chapter 4). Where the upper crustal layer thins out and the slab is relatively shallow (in the flat-slab segment or in the trench proximity), temperatures are lower and the lithosphere is therefore mechanically stronger.

Other controlling factors in the lithospheric strength distribution are the background strain rate and lithology-dependent mechanical rock properties. A key assumption of our approach is the inference of secondary (strain-rate dependent) creep across the study area. We tested two end-member models to investigate the effect of strain-rate variations on the strength distribution (Appendix C.5). Within the tested interval, variations in strain rate have almost no effect on the overall strength distribution: higher strain-rate values lead to a slight increase in total strength and vice versa. Interestingly, variations in the imposed strain-rate value do not affect the spatial distribution of coupled and decoupled conditions between the continental crust and the mantle.

To evaluate the effect of variations in rock properties on the resulting strength, we selected an alternative composition for the lower crust, the latter being the layer with the least observational constraints on lithological composition of all the model units (Table 5.1; Rodriguez Piceda et al., 2021). Gravity-constrained densities (3100 kgm^{-3}, Rodriguez Piceda et al., 2021) and mean P-wave velocities of 6.76 km s^{-1} (Marot et al., 2014; Pesicek et al., 2012; Scarfì & Barberi, 2019) are indicative of a predominantly mafic composition of the lower crust. Accordingly, we opted for 'dry diabase' (Afonso & Ranalli, 2004) as opposed to 'dry mafic granulite' (Wilks & Carter, 1990; Table 5.1) as an alternative type rheology. Although the alternative model with dry diabase depicts an overall higher strength, the chosen type rheology does not affect the general trends in the lateral distribution of integrated crustal and lithospheric strength (Appendix C.6). The highest horizontal gradient again occurs at the transition between the orogen and the foreland and between the orogen and the forearc, which suggests that the conclusions to be drawn from the rheological modeling would be the same.

The trends in the modelled lateral variability of integrated lithospheric strength found in our study (Fig. 5.5a-b) can be qualitatively compared with previous elastic thickness estimates (Te), derived from the cross-correlation between the topography and Bouguer gravity anomaly, which are indirect proxies of the strength of the plate (Astort et al., 2019; Ibarra & Prezzi, 2019; Nacif et al., 2017; Sánchez et al., 2018; Tassara & Yáñez, 2003). High values of Te usually are indicative of a strong lithosphere, whereas low values of Te correspond to a weaker lithosphere (e.g. Burov, 2011; Burov & Diament, 1995; Watts & Burov, 2003). Accordingly, Te values of 40–60 km are consistent with the cold and strong areas of the forearc, the central-western part of the orogen and the northern part of the foreland. Te values of less than 30 km correspond to warmer and weaker areas of the orogen and the central-southern BAF. Likewise, north of our study area, at the latitudes of the Andean Plateau (Altiplano-Puna Plateau; 21°S–28°S), Ibarra & Prezzi (2019) and Meeßen (2019) found similar spatial correlations between the different morphotectonic provinces and the strength distribution within the continental lithosphere, consistently encountering a mechanically weak orogenic domain that contrasts with the mechanically strong forearc and BAF regions. Therefore, the contrasting rheological characteristics between the forearc, orogen and BAF regions seems to be a distinct signature of the central Andes. The question of whether this applies to other non-colisional orogens could be addressed in future investigations.

5.5.2 Implications of modeled plate strength for intraplate seismicity

One interesting outcome of our study is the recognition of the spatial correlation between the modeled brittle domain of the continental plate and observed depth of seismicity, with maximum depths of hypocenters increasing where the BDT also deepens (forearc and northern BAF; Fig. 5.6). This modeling result is reliable since at depths greater than the modelled BDT, the onset of thermally activated viscous creep would lead to a more diffusive pattern of deformation, thus preventing strain localization, weakening and associated seismicity to occur (Handy & Brun, 2004). This observation suggests that the depth of the BDT derived from our rheological model can be considered as a first-order approximation of the lower bound of the seismogenic zone in the study region. This conclusion is consistent with previous studies that compared computed YSEs of the continental lithosphere with depth-frequency distributions of hypocentres (Anikiev et al., 2020; Chen & Molnar, 1983; Doglioni et al., 2011; Ibarra et al., 2021; Petricca et al., 2018; Rolandone et al., 2004).

We also found a spatial correlation between modeled integrated strength and intraplate seismicity in terms of their distribution with respect to the boundaries between the morphotectonic provinces. Intraplate seismicity tends to occur at the edges of the cold and strong domains (the forearc, the central-western part of the orogen and the northern part of the BAF), whereas the warm and weak morphotectonic provinces (most of the orogen and BAF) are generally characterized by a lack of intraplate seismicity. This indicates that the stronger domains are prone to resist internal deformation and can effectively transmit accumulated stresses to their edges, where the presence of a sharp lateral decay in lithospheric strength causes slip instability to develop, thereby possibly triggering seismic rupture. Similar relations between the spatial distribution of seismicity and strength of the lithosphere were encountered in a wide variety of tectonic settings including convergent (Ibarra et al., 2021) and divergent margins (Anikiev et al., 2020), as well as stable-cratonic areas (Sloan et al., 2011; Tesauro et al., 2015). Particularly, in the Central Andes, Ibarra et al. (2021) found that intraplate seismicity is restricted to the areas with high horizontal gradients of integrated strength at the transition from warm and weak to cold and strong crustal domains. The causative relationship between lateral rheological heterogeneities and strain localization has been also proposed for long-term deformation patterns in the lithosphere. Calignano et al. (2015) through analogue modeling, argued that strain localizes at the margins of strong lithospheric domains, whereas the strong domains themselves are only affected by minor deformation.

A factor that could contribute to the aseismic character of the northern part of the Andean orogen is the increase in gravitational potential energy (GPE) due to its high elevation and large crustal thickness (cf. Figs. 5.1 and 2b). An increase in GPE would prevent any internal deformation of the orogen and favor the lateral transmission of compressional stresses to adjacent areas of lower GPE (i.e. the forearc and the BAF), which, depending on their lithospheric strength, could accumulate stresses, that could subsequently be released coseismically (Mareschal & Jaupart, 2011; Stüwe, 2007). To test this hypothesis, we calculated the GPE from the load distribution of our 3D density model and compared these values with the pattern of intraplate seismicity (Appendix C.7). We found that the northern part of the orogen is indeed characterized by high GPE values (> 6.36e14 Nm^{-1}) and that this domain is overall devoid of seismic activity; instead seismicity is localized within the eastern boundary, which is characterized by a sharp decay in GPE (< 6.3e14 Nm^{-1}). In other model areas (such as the BAF and forearc regions), however, there is no evident spatial correlation between GPE magnitudes and earthquake distributions: seismic events are recorded across areas of both high and low GPE. Hence, in these areas, internal sources of stress are less suitable to explain the seismic deformation pattern than integrated strength variations.

An exception to the spatial correlation between intraplate seismicity and sharp horizontal gradients in the calculated mechanical strength of the lithosphere is found in the northern parts of the foreland. Here, seismic activity occurs in the interiors of a cold and strong lithospheric domain (Fig. 5.5a–b) and where crust and mantle are mechanically coupled (Fig. 5.5d). In addition, we observe that the seismogenic depth here is 30–40 km, which is unusually large for crustal earthquakes (e.g., Maggi et al., 2000). Furthermore, when analyzing the moment magnitude (Mw) of these earthquakes, we note that they include those intraplate events with the highest magnitudes (Mw>6) recorded in the study area (Appendix C.9). These observations raise the question as to what underlying mechanism causes the localization of deep, high-magnitude seismicity in a region that should resist deformation. One possible explanation could be that our model overestimates the integrated strength in this region. A reduction in strength could be due to higher temperatures, lower strain rate and/or weaker rheological properties. However, given that the observed trends in the distribution of lithospheric strength are not changed by those alternative model configurations, our sensitivity analysis, which is based on alternative parametrizations for both the strain rate and the rheological setup within acceptable bounds (Appendix C.5-6), seems to contradict the overestimated strengths. With respect to the thermal field, a wide range of observations independent of our study, including seismic tomography (Marot et al., 2014; Wagner et al., 2005) and wellbore temperature and heat-flow measurements (Collo et al., 2018; Hamza & Muñoz, 1996), indicate that the lithosphere in the northern foreland is significantly colder than its southern counterpart and the orogen. This is also consistent with other modeling studies of the Sierras Pampeanas lithosphere (Ibarra et al., 2021; Meeßen, 2019). Furthermore, the characteristics of the recorded seismicity (deep and high-magnitude events) may be themselves indicative of the strong mechanical behavior of the lithosphere. On the one hand, deepening of events at ~40 km depth indicates brittle conditions at this depth, which are attained if the crust there is sufficiently cold and/or has strong mechanical properties (e.g. mafic granulite composition, Craig & Jackson, 2021; Jackson et al., 2008; Maggi et al., 2000). These features are consistent with the temperatures (Chapter 4) and large thickness of the mafic lower crust modeled by Rodriguez Piceda et al. (2021) (Figs. 5.2d and 3). On the other hand, high-magnitude earthquakes as recorded in this area are compatible with a stronger lithosphere that is able to withstand larger amounts of elastic energy over time and then release it in the form of high-magnitude events. From all these observations obtained with completely independent methods, we can therefore conclude that the presence of a strong, seismically active lithosphere in the northern foreland is a robust feature. In this context, other explanation for this apparent dichotomy between the mechanical behavior of the lithosphere and the localization of seismic deformation must be called upon.

To explain the occurrence of seismicity in the northern foreland, one possible scenario is that seismic rupture occurs where the strong lithosphere is locally weakened due to the presence of crustal-scale discontinuities in the form of terrane sutures associated with pre-Andean collisional events, as proposed by Meeßen (2019) and Ibarra et al. (2021). According to this interpretation, we would expect to find a similar density of seismicity in the regions where such heterogeneities are actually observed, such as in the Sierras Pampeanas (Fig. 5.1). The observed seismicity pattern, however, is more complex, with a higher density of seismic events encountered in a specific sector of the Sierras Pampeanas between 31°S–33°S and 67°W–69°W than in the remains of the morphotectonic province, which, in turn, is characterized by scarce seismicity (Fig. 5.4a; e.g. Alvarado et al., 2009; Richardson et al., 2012).

A second possible scenario is to consider that this seismically-active region is subjected to other sources of stress as those from plate convergence, such as stresses related to a negative buoyancy of the slab where it transitions to a steep angle to the east and to the south ('slab steepening'; Fig. 5.8). When comparing the intraplate seismicity pattern with the geometry of the slab in the SCA, the epicentral distribution shows a triangular shape where the E-W extent of the seismically active area narrows from north to south, resembling the E-W variation in the width of the flat-slab segment along the strike of the subduction zone (Fig. 5.4). In particular, active seismic deformation away from the trench appears to cluster towards the south and east where the slab shifts from a sub-horizontal to a steep-dip configuration ('steepening segment', below the Sierras Pampeanas and in a narrow corridor below the Cuyo basin and the central-western part of the orogen; cf. Fig. 5.4). Similar observations were also made in previous studies (Espurt et al., 2008; Pardo et al., 2002). In contrast, only minor seismic deformation is observed in the northern orogen, i.e. inside the flat-slab segment far from where it is steepening again (cf. Fig. 5.4). In line with these observations, we propose that stresses related to geometrical variations across the slab surface are an additional controlling factor of seismicity in the region.

Although the control of the dip geometry of the slab in the localization of intraplate seismicity have received little attention in the literature so far (Gutscher, 2002), there is an ongoing debate on its effects on the Andean deformation at tectonic scales, in particular those that are ultimately responsible for the isolated basement uplifts in the broken foreland of the Sierras Pampeanas between 27°S and 33°S and the compressionally inverted Cretaceous extensional province of the Santa Bárbara System farther north (Gutscher, 2002; Horton, 2018; Jordan et al., 1983; Kley et al., 1999; Kley & Monaldi, 2002; Martinod et al., 2020). Some authors argue that the setting of the flat slab plays a pivotal role for the observed deformation in that area (Horton, 2018; Jordan et al., 1983; Martinod et al., 2020; Ramos & Folguera, 2009), opposed to other authors who suggest that compressional reactivation of inherited heterogeneities in the crust drives the spatially and temporally disparate uplift of ranges in the broken foreland and not the flat slab dynamics (e.g., Kley et al., 1999; Kley & Monaldi, 2002). Irrespective of the main mechanism involved, the question that raises is whether these relationships between dip geometry of the slab and deformation of the overriding plate could also apply to the seismicity distribution in the SCA. Answering this question requires first to assess the temporal relationship between episodes of flat subduction along the Central Andes margin. Whereas along the Central Andean margin, diachronous flat subduction evolved at the latitudes corresponding to the Altiplano-Puna Plateau (15°S–20°S) at 40–32 Ma and 27–18 Ma, in the SCA this has occurred from 19 Ma to the present day (Jones et al., 2014; Ramos & Folguera, 2009). Although still debatable, the N–S migration of the flat subduction setting is presumably triggered by the subduction of the buoyant JFR ridge (Gutscher, 2002; Kay & Mpodozis, 2002; Ramos et al., 2002; Yáñez et al., 2001), with the present-day ridge-trench intersection located at 33°S (Fig. 5.1). In this context, the present-day tectonic stresses related to the variable slab geometry and possibly affecting the localization of seismic deformation in the SCA could be analogous to those characterizing the subduction system at the latitudes of the Altiplano-Puna Plateau at 35–27 Ma. Thus, we argue that similar mechanisms to those proposed to explain the tectonic features of the foreland at the latitudes of the Altiplano-Puna Plateau between 35–27 Ma could also apply to the case of the present-day seismic deformation in the SCA. To further assess the plausibility of our conceptual model calls for, therefore, a close examination of the previously proposed models on the role of the flat slab for the foreland deformation.

On the one hand, ‘end-member’ theoretical models assign the role of a ‘bulldozer’ to the flat slab, scrapping the base of the continental lithosphere and continuously transferring tectonic stresses to the front of the flat segment itself, where the slab is already steep (e.g. Gutscher, 2018; Horton, 2018; Jordan et al., 1983; Ramos & Folguera, 2009; Fig. 5.8a). According to this model, shear stresses along the subduction interface are responsible for the eastward migration of the deformation in the overriding plate, while the role of the overriding plate rheology is negligible. If such mechanisms were indeed active in the SCA, it would be logical for intraplate seismicity to localize below the Eastern Sierras Pampeanas, a notion that contradicts the observed present-day seismicity pattern (with higher density of seismic events in the Western Sierras Pampeanas and scarce seismicity in the eastern parts; e.g., Alvarado et al., 2009; Richardson et al., 2012; Fig. 5.4a) and the manifestation of neotectonic activity (Kley et al., 1999; Kley & Monaldi, 2002). Moreover, the progressive flattening of the slab would likely result in a continuous eastward growth of the crustal wedge, which also contradicts the observed spatially diachronous deformation in the broken foreland of the Sierras Pampeanas and the Santa Bárbara System (Arnous et al., 2020; Hain et al., 2011).

On the other hand, Martinod et al. (2020) proposed more recently an alternative explanation for the role of the flat slab as a trigger of the Andean deformation at the latitudes of the Altiplano-Puna plateau (15 °S–28 °S). In their numerical study, the authors systematically analysed how the dip geometry of the slab influences the magnitude and distribution of effective stresses in the overriding plate. According to their model, maximum compressive stresses are shifted eastwards during episodes of flat subduction because of two active mechanisms: (i) increased friction applied by the subducting oceanic plate to the continental plate, and (ii) amplified negative buoyancy of the slab once the oceanic plate resumes steep subduction (Fig. 5.8b). As a result, maximum effective stresses would localize above the steepening segment of the slab (i.e. in a transition zone between the flat and steep slab), and not in locations where the slab is already steep, as proposed by the ‘bulldozer’ models. Additionally, in the remaining parts of the flat slab segment, where continental and oceanic plates are mechanically coupled, only minor deformation would occur. In the SCA, the intraplate seismicity pattern is consistent with this model proposed by Martinod et al. (2020), suggesting that similar mechanisms could be active in our study region. In view of these results, we favor a hypothesis where the flat slab generally preserves the lithosphere from deformation, and seismicity mainly localizes where the slab returns to a steep subduction angle. Geodynamic modeling experiments integrating present-day geometry, density and thermal configuration of the SCA are required to further test this hypothesis and to constrain dynamic stresses in the oceanic and continental plates.

Finally, the variable slab geometry could have a second effect in the localization of seismic deformation, which is related to the thermal and rheological state of the continental and oceanic plate. In the flat slab domain, the continental and oceanic lithosphere are cold and strong; in the transition to steep subduction, the oceanic lithosphere successively heats up and weakens, thus the integrated lithospheric strength also decreases, which would also facilitate the localization of seismic deformation in these regions.

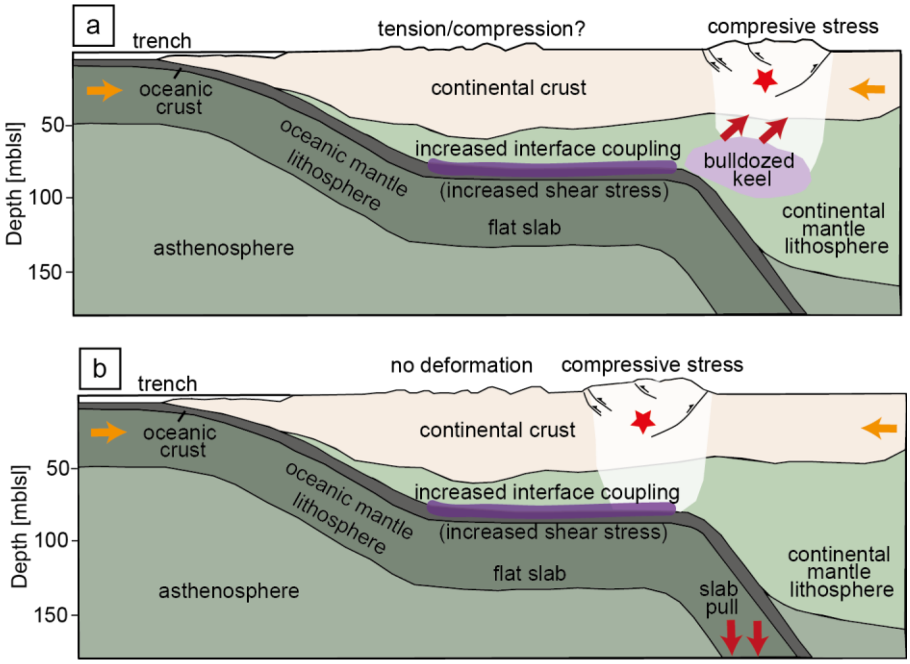

Figure 5.8: Schematic profiles of two alternative roles of the flat slab in the localization of tectonic and seismic deformation according to (a) bulldozer models (Gutscher, 2018; Horton, 2018; Jordan et al., 1983; Ramos & Folguera, 2009), modified from Gutscher (2018), and (b) Martinod et al. (2020). White shaded areas show the expected location of the maximum compressive stresses in the overriding plate. The red star shows the expected localization of intraplate seismicity. In (a), the flat slab transmits the stresses from the oceanic slab to the front due to the increased plate coupling and scrapes off the continental mantle lithosphere forming a keel in front. The tectonic and seismic compressional deformation localizes where the slab is already steep. Above the flat slab segment, the overriding plate would be subject to extension (e.g., Gutscher, 2018), which has not been observed, or compression (e.g. Horton, 2018), which has been observed. In (b) transmission of stresses occurs along the subduction interface due to increased plate coupling, but the flat slab prevents internal deformation above most of the subhorizontal segment. Compressional deformation occurs in the transition zone between the flat and steep sectors of the slab, promoted by increased slab pull.

Chapter 6: The role of mantle hydration and flexure on slab seismicity in the southern Central Andes

6.1 Abstract

The causative dynamics of earthquakes along subduction interfaces and within oceanic slabs is usually described with reference to experimental rock mechanics, but seldomly assessed in case studies based on geophysical data. Here we focus on the subduction zone of the oceanic Nazca Plate in the southern central Andes, and use a recent seismic tomography study to evaluate the controlling factors driving slab seismicity. We analyse the distribution of the ratio between compressional and shear-wave seismic velocities (v_p/v_s) as a proxy of the state of hydration of the lithospheric mantle, oceanic slab and plate interface. We postulate that seismicity in regions of high v_p/v_s, that is areas of hydrated mantle and/or partial melting, is caused by compaction effects and dehydration reactions. In contrast, seismicity in areas of low v_p/v_s and inferred low fluid content is triggered by enhanced flexural stresses due to changes in the subduction angle of the Nazca plate. The correlation between segments along the subduction interface which are characterized by a gap in background seismicity and have not experienced any recent megathrust event and low v_p/v_s values is indicative of a high plate-locking degree and an increased potential for these areas to host a large-magnitude megathrust earthquake.

6.2 Introduction

The convergent margin of the southern Central Andes (SCA, 29°S–39°S), where the oceanic Nazca Plate (NP) subducts under the continental South American Plate (SAP), is a region where the greatest amount of large-magnitude earthquakes and the greatest seismic-energy release have been recorded (e.g., Valdivia M9.5 in 1960 and M8.8 Maule in 2010; Anderson et al., 2007; Costa et al., 2020). One distinct feature of the area is the change in the subduction angle of the Nazca Plate between 33°S and 35°S from the Chilean-Pampean flat-slab zone (<5° dip, 27–33°S) in the north to a steeper sector south of it (~30° dip) (Fig. 6.1). Another characteristic of the SCA is the E-W-oriented tectonic division of the SAP into three main crustal domains: (i) the forearc, (ii) the Andean orogen and (iii) the low-relief back-arc and foreland regions.

Domains with the highest frequency of slab seismicity (International Seismological Centre, 2021), including events along the subduction interface (interplate seismicity) and within the oceanic plate (intraslab seismicity), are associated with a shallow-subducting oceanic slab either close to the trench or along the flat-slab segment, below the Andean Precordillera and Sierras Pampeanas morphotectonic provinces (Fig. 6.1 b–c).

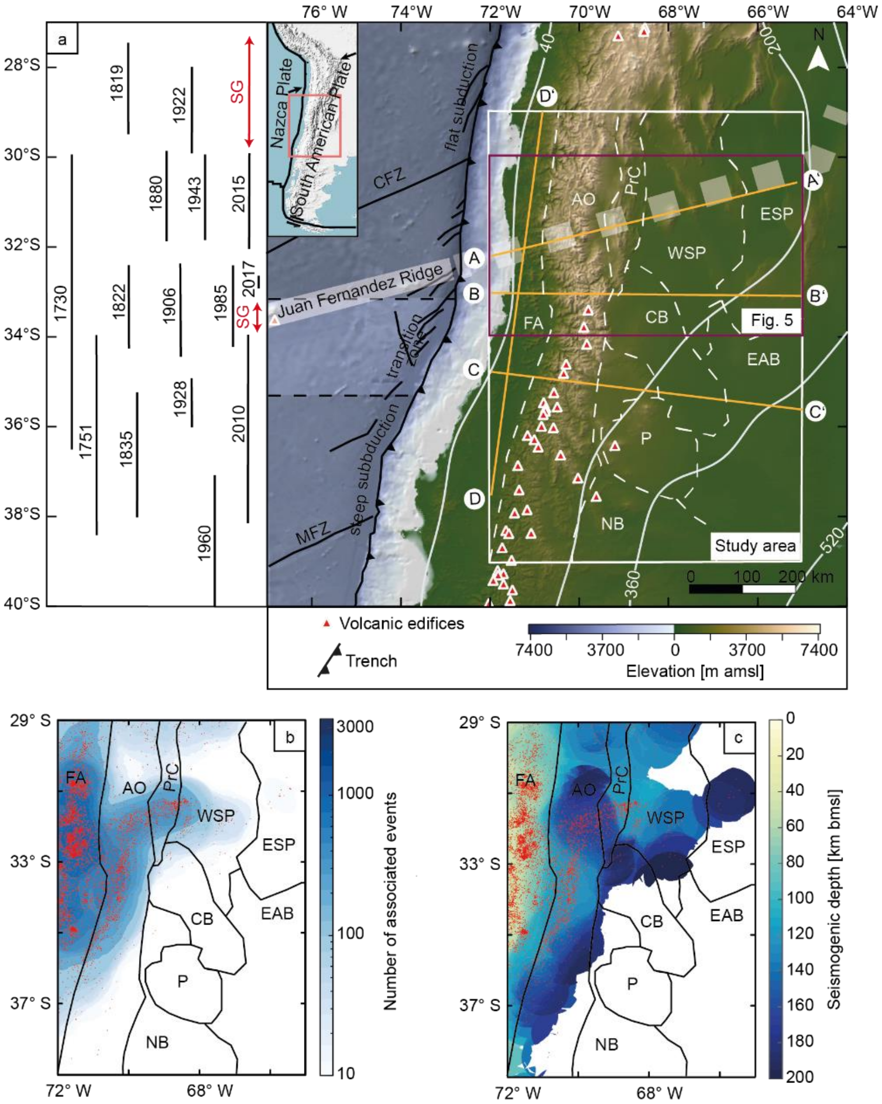

Figure 6.1: (a) Right panel: topography and bathymetry of the southern Central Andes based on the ETOPO1 global relief model(Amante & Eakins, 2009). The white rectangle encloses the extent of the area considered in this study; the purple rectangle encloses the area shown in Figure 6.5. Black-dashed lines in the oceanic domain mark the boundaries between subduction segments. The fracture zones of the Nazca Plate (Hayes et al., 2018) are highlighted by black lines. White lines show the isodepth contours (km below mean sea level) of the top of the slab (based on the Slab2 model; Hayes et al., 2018). The wide transparent white line denotes the position of offshore (full line) and projected onshore (dashed line) tracks of the Juan Fernandez Ridge (JFR) (Yáñez et al., 2001). The boundaries between the main morphotectonic provinces are shown by white dashed lines(Horton, 2018; Jordan et al., 1983). Abbreviations of main morphotectonic provinces: AO = Andean orogen, CB = Cuyo Basin, ESP = Eastern Sierras Pampeanas, EAB = extra-Andean basins, FA= forearc, NB = Neuquén Basin, P = Payenia

volcanic province, Prc = Precordillera, WSP = Western Sierras Pampeanas. Abbreviations of main fracture zones: MFZ = Mocha Fracture Zone ; CFZ = Challenger Fracture Zone. The red triangles depict locations of active volcanoes. The orange lines denote locations of profiles shown in figures 6.2 and 6.3. Left panel: extent of historical seismic ruptures (Drápela et al., 2021). Seismic gaps (SG) are shown with red lines. (b–c) event density and seismogenic depth (depth above which 95% of events occur) derived for a circular bin of 75 km radius (logarithmic scale) for slab seismicity. Seismicity marked by red dots. Boundaries of the main morphotectonic provinces are drawn in black.

Thermomechanical modelling in different tectonic settings (Anikiev et al., 2020; Gholamrezaie et al., 2021; Ibarra et al., 2021) has revealed how the long-term rheology of the lithosphere can control the distribution of seismicity, with the brittle-ductile transition (BDT) being a first-order approximation of the downdip limit of the seismogenic zone (Scholz, 1988; Sibson, 1982). A recent thermo-mechanical modelling study in the SCA incorporating the distribution of density, thickness and temperature of the layers composing the lithosphere (Appendix D.1), allowed us to test this hypothesis. Variations in the long-term yield strength of the lithosphere (i.e. maximum differential stress that rocks can withstand before permanent deformation) can reconcile the spatial distribution of slab seismicity at depths < 50 km, with earthquakes bounded within the brittle deformation domain. However, they fail to provide an explanation for the observed seismicity at depths > 50–70 km, where ductile rheological conditions are expected (Fig. 6.2). These results call for a critical revision of our current understanding of the causative dynamics driving slab seismicity at depth.

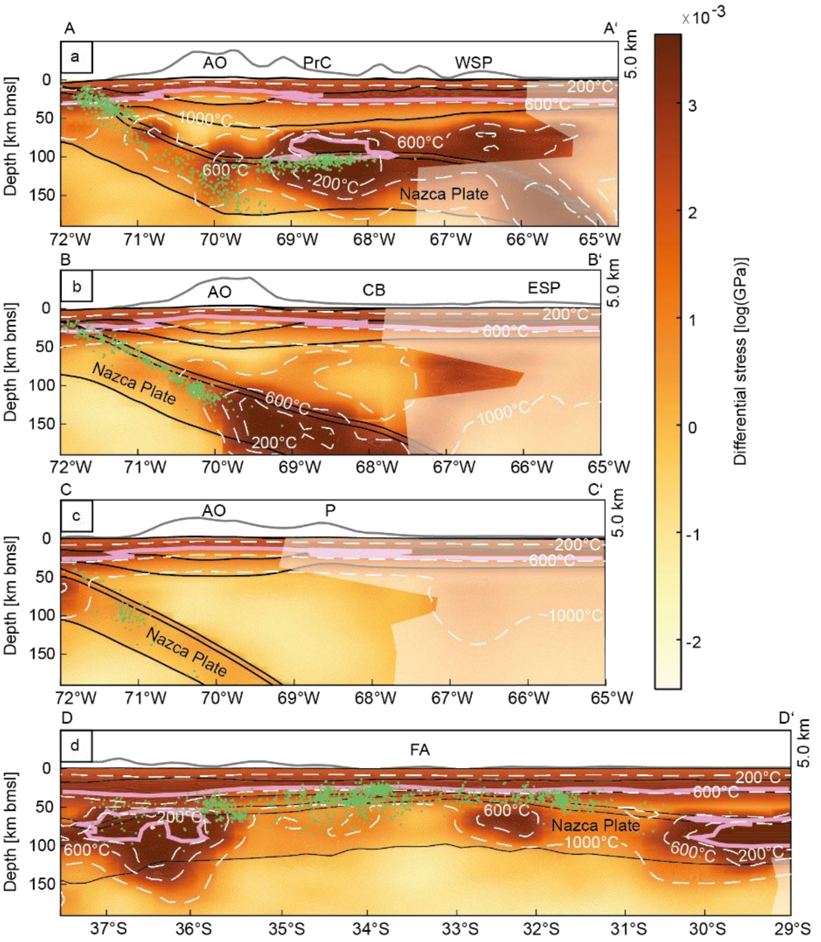

Figure 6.2: Long-term rheology of the southern Central Andes: Modelled yield strength along four cross sections (locations are provided in Figure 6.1). Light transparent sectors correspond to areas with no data coverage from seismic tomography(Gao et al., 2021). Green dots denote slab hypocentre locations(International Seismological Centre, 2021) within 5 km distance from each profile. Isotherms of the underlying thermal model are marked as dashed white lines. The BDT is shown by thick pink lines. Black lines denote the interfaces of the lithospheric model layers. On top of each profile, surface topography is shown with a vertical exaggeration of 10:1.

In this study, we make use of a recent seismic tomography model of the SCA (Gao et al., 2021) to showcase the existence of a causative relationship between the state of hydration of the mantle and recorded slab seismicity, including intraslab and interplate events(Dziewonski et al., 1981; Ekström et al., 2012; International Seismological Centre, 2021) (see chapter 6.6.1). We further demonstrate that in regions with a dry mantle, seismic activity can be explained by flexural stress due to variations in the slab geometry. Moreover, segments along the subduction interface, where gaps in the distribution of small and moderate earthquakes have been observed and which have not experienced a recent megathrust event, also correlate with domains of low v_p/v_s and high plate-locking degree, and thus these regions are likely prone to accommodate large-magnitude megathrust earthquakes.

6.3 Causative mechanisms for seismicity in subduction zones

In subduction zones, shallow (< 50 km) seismicity close to the subduction interface has been often explained as a result of the release of elastic stress accumulated during plate convergence (McCaffrey, 2007; Pacheco & Sykes, 1992) and as a function of the frictional properties of the fault interface, which is likely modulated by the release and migration of fluids (Saffer & Tobin, 2011). Below the outermost forearc, the release of fluids from the subducting sediments can lead to an increase in pore pressure and enhanced frictional weakening of the subduction interface, thereby promoting interplate processes including trenchward propagation of megathrust earthquakes and a deepening of the background seismogenic zone (Saffer & Tobin, 2011). At greater depths, the increase in lithostatic pressure should inhibit the occurrence of seismic slip. However, metamorphic reactions of constitutive minerals in the oceanic crust (e.g. amphibole and epidote breakdown during eclogitization (Hacker, et al., 2003; Incel et al., 2017) and in the mantle (e.g. serpentinite breakdown (Hacker, et al., 2003; Peacock, 2001) can weaken the rock frictional strength, thereby offering an explanation to the observed intermediate-depth (50-300 km) intraslab seismicity (Ferrand et al., 2017; Hacker et al., 2003; Ji et al., 2019; John et al., 2009; Kirby, 1995). Mechanisms proposed to be responsible for rock weakening include: (i) pore pressure increase from dehydration embrittlement (Hacker, et al., 2003; Kirby, 1995; Peacock, 2001); (ii) grain-size reduction (John et al., 2009); and, (iii) dehydration-related stress transfer from the hydrous phases to the dry host rock (Ferrand et al., 2017). These reactions affect the state of hydration of the slab and overlying lithospheric mantle; consequently, it might be expected that hydrated regions are more seismically active than dry regions (Fujie et al., 2018; Gao, 2018; Guo et al., 2021; Mochizuki et al., 2021).

It has also been argued that variations in the slab geometry may trigger seismicity within its bending and unbending portions, if the effective strain rates associated with slab flexure exceed those associated with slab pull (Engdahl & Scholz, 1977; Isacks & Molnar, 1971; Sandiford et al., 2020; Wang, 2002). Evidence for a control of slab flexure on the occurrence of seismicity comes from the observed spatial correlation between the flexural regime and the orientation of the earthquake moment tensors (Isacks & Molnar, 1971; Sandiford et al., 2020). Slab segments with positive curvature (i.e. concave down) gradients are usually characterized by earthquake moment tensors with downdip tensional axes, whereas those with negative curvature gradients display seismicity associated with downdip compressional axes.

6.4 Results of seismic tomography

To infer the driving physical mechanisms responsible for causing brittle failure requires a knowledge of parameters, e.g., state of hydration of the mantle and slab geometry, which are not accessible to direct measurements. However, seismic tomography, due to the sensitivity of P- and S-wave velocities to lithology, fluid/melt-content, and temperature, can be used as a proxy for the state of hydration of the mantle (Hacker et al., 2003). Specifically, a decrease in v_p/v_s is indicative of dry mantle conditions, whereas an increase in v_p/v_s suggests mantle hydration. An increase in v_p/v_s can be promoted by processes such as serpentinization of the mantle wedge (Hacker et al., 2003) (Figure D.1 in Appendix D) or increase in pore fluid pressures (Saffer & Tobin, 2011), as a result of compaction of sediments along the subduction interface or dewatering of hydrous minerals within the slab. Ascent of fluids from the subducting slab through the mantle of the overriding plate may also drive partial melting below the volcanic arc, leading to an increase in v_p/v_s (Hirschmann, 2000).

In this study, we analysed the v_p/v_s distribution from a recent P- and S-wave tomography model of the SCA (Gao et al., 2021), which we interpreted as a proxy for the hydration of the mantle. In the following, we discuss the results relying on (i) three E-W cross-sections, considered representative of the different subduction segments (Fig. 6.3 a–c), (ii) a N-S cross section along the forearc (Fig. 6.3d), and (ii) a map along a constant depth of 90 km, which corresponds to the overriding plate mantle just above the sub-horizontal slab in the flat-slab segment (Fig. 6.3e). All sections depict a progressive eastward dehydration of the oceanic mantle as indicated by a decrease in v_p/v_s, from values up to or greater than 1.9 below the Andean orogen to lower values below the Andean foreland further east (~1.7). Within the forearc, the ratio is intermediate to high (>1.7–1.8), suggesting hydrated conditions. We also note a significant along-strike variability in v_p/v_s. For instance, at 90 km depth, the orogenic domain displays high v_p/v_s values (> 1.8) only in its central part (between 32.5–35°S), while in the northern and southern regions v_p/v_s decreases down to 1.75 (Fig. 6.3e). We can explain the enhanced hydration in the central orogenic domain due to its proximity to the Juan Fernández Ridge, an aseismic seamount chain subducting at 33°S (Fig. 6.1). This ridge is associated with pervasive faulting (Kopp et al., 2004), which enables fluids to reach oceanic mantle depths, only to be released in the continental plate after subduction (Grevemeyer et al., 2018). South of 33°S, the orogenic mantle domain with high v_p/v_s at 90 km depth spatially correlates with the active magmatic arc (Fig. 6.3e), suggesting that the observed increase in v_p/v_s can be associated with the presence of melts. Below the back-arc and foreland, the continental mantle displays low to intermediate v_p/v_s ratios (1.72–1.8), indicative of drier conditions, while a local increase in v_p/v_s (1.84–1.9) is recorded beneath the Precordillera and the western Sierras Pampeanas.

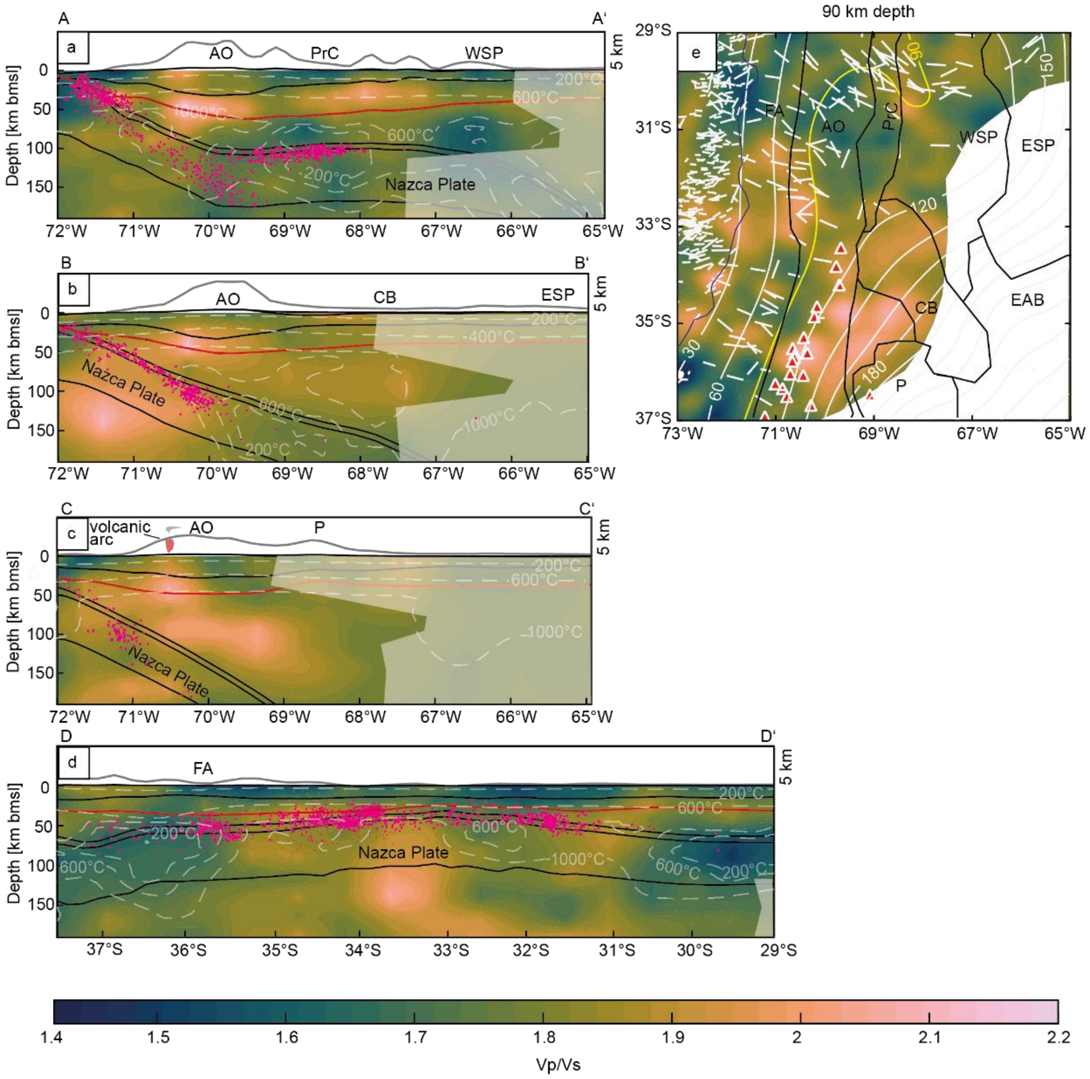

Figure 6.3: (a-d) v_p/v_s ratio along cross-sections (their locations is given in Figure 6.1). White-shaded areas with transparency denote areas with no data coverage. Magenta dots show the location of hypocentres of slab seismic events within 5 km distance from each profile. The interfaces of the lithospheric model units are marked by black lines, except for the Moho discontinuity, which is shown by red lines. Isotherms are marked as dashed white lines. On top of each profile, surface topography is displayed with a vertical exaggeration of 10:1. (e) v_p/v_s variations at 90 km depth. Overlain are also: the depth contours of the top of the slab at 30-km intervals (white thin lines, except 90 km-depth contour in yellow), the dominant orientation of the T-axes of focal mechanisms (Dziewonski et al., 1981, 1981) projected horizontally (white thick bars), the active magmatic arc (red triangles) and the coastline (grey line). For abbreviations of the main morphotectonic provinces, please refer to Fig. 6.1.

6.5 Discussion

The comparison between the v_p/v_s distribution and the interplate and intraslab seismicity, enable us to derive the following observations. First, slab seismicity at depths of less than 70 km is limited to the slab domain overlain by a hydrated continental mantle with high v_p/v_s (Figs. 6.3a-c, 72°W–70W°). This is indicative of a spatial correlation between slab seismicity and degree of hydration, with seismicity ceasing quite abruptly at depths where the slab undergoes (nearly) complete dehydration and is not able to release fluids to the mantle of the continental plate. In the transition zone and steep-slab segments, at 69°W–70°W, the change from high to low v_p/v_s in the overriding plate mantle spatially correlates with the location of the active volcanic arc (Fig. 6.3e). In the flat-slab segment, the absence of intermediate-depth seismicity between 50 km and 100 km, spatially correlates with the orogenic domain underlain by a dry mantle and characterized by the lack of active volcanism (Fig. 6.3e). This indicates that fluids responsible for the generation of partial melts, which feed the volcanic arc south of 33°S, are released west of 70°W, and that the downdip limit of intraslab seismicity is actively controlled by the availability of fluids in the slab mantle. Similar relationships between seismic velocities and distribution of seismicity have been also found in other subduction zones, such as Cascadia (Gao, 2018; Guo et al., 2021), Hirukangi (New Zealand) (Mochizuki et al., 2021), and the north-western Pacific margin (Fujie et al., 2018).

For the interface region, previous studies along the Chilean margin between 37°S and 42°S have identified a correlation between variations in the state of hydration of the mantle and in the pore-fluid content, the spatial extent of locked zones along the subduction interface (Moreno et al., 2014) and the recurrence time of great earthquakes (Moreno et al., 2018). Our findings extend the results from these studies in that we have been able to find a similar correlation between v_p/v_s and locked areas along the plate interface also for the domains of the SCA between 29°S and 39°S (Fig. 6.4). This result suggests that pore-fluid pressure variations should be considered as the main factor controlling preseismic locking along the plate interface in the SCA. In agreement with previous works (Moreno et al., 2014), we can therefore correlate the presence of such N–S variations in pore-fluid pressures to the distribution of fracture zones in the Nazca plate (Fig. 6.1). Due to this structural control, slab regions which underwent higher degree of fracturing are prone to host more fluids and are characterized by a higher degree of hydrologic connectivity. This translates to higher v_p/v_s values and in a lower degree of plate locking compared to regions where fracturing is less intense.

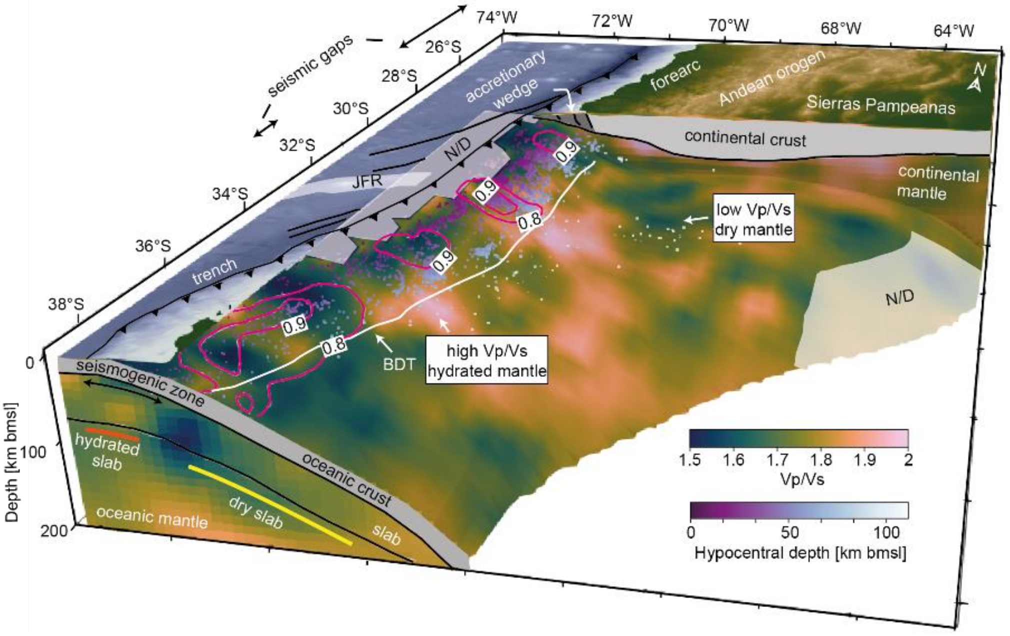

Figure 6.4: 3D diagram of v_p/v_s distribution reflecting the state of hydration within the mantle and the subduction interface, and slab seismicity color-coded by hypocentral depth. The extent of labelled dry hydrated slab only pertains to the cross-sections in figures 6.3a and b and strongly varies along the strike of the subduction zone. The continuous white line shows the brittle ductile transition (BDT). Magenta-colored contours show the areas with a high degree of locking (Moreno et al., 2010).

East of the mantle wedge corner, beneath the Precordillera and Sierras Pampeanas, the upper layer of intermediate-depth (80–100 km) seismicity close to the top surface of the slab is localized below a domain in the continental mantle that is characterized by low v_p/v_s and, therefore, interpreted to be most likely dry. This local decrease in fluid content within regions of the flat-slab domain has been previously inferred from high-resolution seismic tomography studies (Linkimer et al., 2020; Marot et al., 2014; Wagner et al., 2005). This indicates that the slab beneath this region of the Precordillera and the Sierras Pampeanas is already dehydrated. This being the case, it would be difficult to link the observed intraslab seismicity to dehydration reactions, as suggested by previous studies (Porter et al., 2012; Wagner et al., 2020). When examining the earthquake focal-mechanism solutions in the area (Dziewonski et al., 1981; Ekström et al., 2012) (Fig. 6.5a), we observe a lack of compressional mechanisms, which also rules out the effect of plate convergence as the main triggering mechanism for these earthquakes. We therefore suggest that seismicity in these domains could be related to enhanced bending and unbending stresses in locations where the slab resumes its steep subduction angle to the east, beneath the Sierras Pampeanas, and to the south, beneath the Cuyo Basin, respectively. Indeed, we found a rather striking spatial correlation between seismicity and slab geometry as based on the orientation of the T-axes of focal mechanisms (Dziewonski et al., 1981; Ekström et al., 2012) (Fig. 6.5), the latter being approximately perpendicular to the local strike direction of the top surface of the slab (Fig. 6.5b). The focal-mechanism solutions with a downdip orientation of the T-axes spatially correlate with the portions of the slab characterized by a positive curvature due to bending in the transitions to steeper subduction angles (Fig. 6.5b), which supports the notion that interplate seismicity in these regions is indeed controlled by the geometry of the slab.

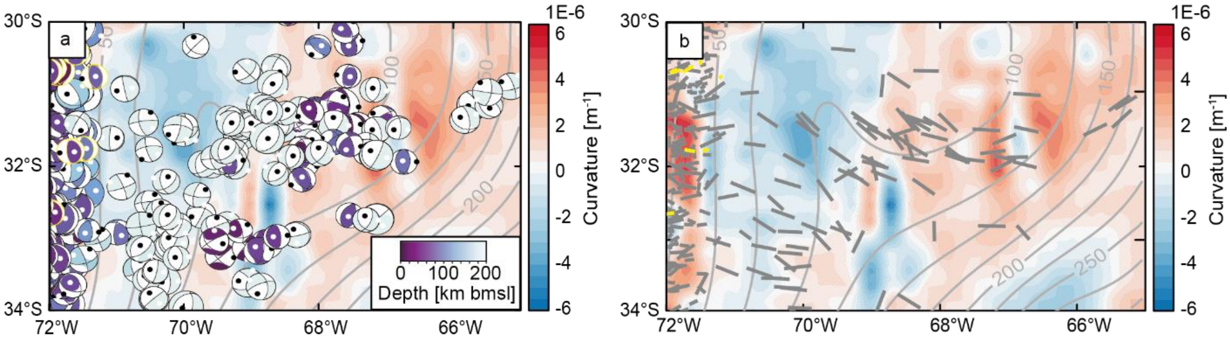

Figure 6. 5: Slab geometry and slab seismicity in the flat-slab segment. Mean curvature of the top of the slab in the region of the flat-slab to steep-dip subduction transition (Supporting Information), overlain with: (a) focal mechanism solutions of interplate earthquakes(Dziewonski et al., 1981; Ekström et al., 2012) color-coded by depth; dots show the orientation of the P- (black) and T-(white) axes; and (b) T-axes projected horizontally. The intraplate events are highlighted in yellow. The isodepth contours of the top of the slab are shown in grey lines.

Our findings provide important insights into the seismic hazard of the SCA. At approximately 29°S and between 33°S and 34°S, no megathrust earthquakes or background seismicity have been recorded during at least 40 years (Fig. 6.1a), while geodetic measurements indicate that the near-trench subduction interface at these latitudes is locked (Moreno et al., 2010) (Fig. 6.4). This raises the question as to how a seismogenic rupture will be produced along these portions of the subduction interface and if stresses will be released either in the form of frequent low-magnitude earthquakes or in the form of a few high-magnitude events. Regions that are subjected to high fluid pressures are weaker and more unstable under the build-up of stresses than faults under dry conditions (Hubbert & Rubey, 1959; Saffer & Tobin, 2011), and thus are more prone to seismic rupture in the form of frequent earthquakes of moderate magnitude (Moreno et al., 2018). Conversely, regions with a drier mantle are able to accumulate elastic energy during longer periods of time, which will be released by infrequent high-magnitude earthquakes. We found that in regions characterized by a gap in seismic activity, the subduction interface displays low v_p/v_s, thereby indicating dry conditions. These results provide indications for these domains to be the likely host of a large-magnitude earthquake in the future (Fig. 6.4), a conclusion that calls for increased geodetic monitoring of the seafloor to better assess the potential sites for future megathrust earthquakes.

In summary, our synopsis of v_p/v_s data in the SCA suggests that local fluid overpressure resulting from disequilibrium compaction beneath the outermost forearc and dehydration reactions of hydrous minerals below the remaining regions are responsible for embrittlement of the lithosphere and the triggering of intraslab and interplate seismicity at depths < 80 km. In contrast, deeper intraslab seismicity (80–100 km) within the flat-slab segment is driven by flexural stresses due to variations in the slab geometry. Our analysis demonstrates the added value of seismic tomographic methods to help in better elucidating the mechanisms responsible for the distribution of slab seismicity and their potential for assessing seismic activity, especially in regions with scarce geodetic instrumentation.

6.6 Methods

6.6.1 Seismic catalogue

We derived the seismicity distribution for the study area between 1964 and 2018 from the reviewed bulletin of the International Seismological Centre (International Seismological Centre, 2021), from which we removed all events with fixed depth and having a depth error > 5 km. We additionally filtered the events related to the oceanic slab (‘slab seismicity’), according to their proximity to the subduction interface, which is represented by the top of the slab from the Slab2 subduction zone geometry model (Hayes et al., 2018). We considered the Slab2 model as a good representation of the subduction interface, given the consistency between focal mechanisms solutions from the GCMT catalogue (Dziewonski et al., 1981; Ekström et al., 2012) and the fault-strike orientations inferred from Slab2 (Hayes et al., 2018). The events with depths greater than the depth of the top slab – given the uncertainty of the Slab2 model – were also considered as belonging to the slab seismicity. As a result of the filtering process, we extracted a total of 9125 intraslab earthquakes. To classify the events into ‘intraslab’ and ‘interplate’ seismicity, we relied on the focal mechanism solutions from the GCMT catalogue (Dziewonski et al., 1981; Ekström et al., 2012). 873 events were available for classification. An earthquake was considered as interplate seismicity if it fulfilled four criteria (Tichelaar & Ruff, 1993): (i) it occurs in the interval defined by the depth of the top slab ± the uncertainty of the

Slab2 model (Hayes et al., 2018); (ii) the slip vector orientation represents thrusting; (iii) the strike of one of the nodal planes is equal to the strike of the top slab surface from Slab2 (Hayes et al., 2018) (± 15°); and, (iv) the dip angle of one of the nodal planes differs less than 35° from the dip angle of the top of the slab surface (Hayes et al., 2018). The remaining earthquakes were considered as intraslab seismicity. After respective filtering, we ended up with a total of 839 and 34 events classified as intraslab and interplate events, respectively.

6.6.2 P- and S- wave seismic tomography

We derived the v_p/v_s model from the isotropic P and S velocity models presented in Gao et al. (2021). Here, we only provide a brief summary of the methodology followed to construct the tomography model; more technical details about the inversion workflow can be found in the original publication[4].

The seismic velocity model is the result of a multi-scale full waveform inversion (Gao et al., 2021) based on the adjoint methodology (Fichtner et al., 2010; Tape et al., 2010), starting from the 3D seismic velocity model SP12RTS (Fichtner et al., 2010). Solutions of the visco-elastic wave equation in a radially anisotropic Earth model are obtained from Salvus (Afanasiev et al., 2019).

Long-wavelength surface topography from the EGM2008 Geoid (Pavlis et al., 2012) and Earth2014 global topography model (Hirt & Rexer, 2015) with Earth ellipticity according to WGS84 and the Moho depth from the global model CRUST1.0 (Laske et al., 2013) were implemented by deforming the mesh grid vertically. The surface topography and Moho depth have been filtered with a maximum angular order of 128, equivalent to a spatial resolution of 155 km. In order to constrain the deep structure of the upper mantle, we initialized our inversion from long-period surface wave data at 60–120 s and progressed in seven stages to a final period range of 12–120 s. The progressive extension to shorter periods mitigates the risk of falling into local minima. The model updates are driven by the Limited-Memory Broyden–Fletcher–Goldfarb–Shanno algorithm (L-BFGS; Liu & Nocedal, 1989). We employ the Time-Frequency Phase Shift and Cross-Correlation-Coefficient misfits as misfit functions during stages 1–5 and 6–7, respectively, with the assistance of the Large-scale Seismic Inversion Framework 2.0 (Krischer et al., 2015; Thrastarson et al., 2021).

Chapter 7: Discussion

From a larger perspective and in light of the conclusions drawn from the different manuscripts that constitute this thesis which addressed the three main questions posed in the Introduction, this chapter aims at discussing the results from the 3D data-integrative modelling approach. At the outset, I asked the following principal research questions that helped me to structure my analytical approach:

(i) Which are the lithological, structural and thermo-mechanical characteristics of the lithosphere in the SCA?

(ii) How does long-term strength of the lithosphere vary in response to the characteristics of the overriding plate and with respect to the dip angle of the subducting slab?

(iii) How does the long-term thermo-mechanical configuration of the SCA relate to tectonic and seismic deformation patterns?

The outcomes from the structural, thermal, and rheological models (chapters 3, 4, 5) indicate that there is a strong variation in the composition, temperature, and strength of the lithosphere between the domains of the forearc, the orogen, and the foreland. Different factors, including the lithology and thickness of the layers of the overriding plate and the subduction angle, affect the thermomechanical field of the lithosphere at different depths (chapters 4 and 5). Moreover, these variations in the long-term lithospheric strength may also exert a control on regional deformation patterns within the overriding plate and the subduction angle (Chapter 5). Finally, seismicity related to the subducting oceanic plate can be explained by other mechanisms, including fluid-mediated processes and flexural stresses within this plate (Chapter 6).

7.1 The structural and thermo-mechanical segmentation of the Andean continental lithosphere

The 3D structural model built in Chapter 3 was the key to investigate the thermo-mechanical configuration of the lithosphere and constituted the basis to discuss the effects of both the structure of the overriding plate and slab-dip geometry on active deformation in the southern Central Andes. Essential characteristics of the differentiated lithospheric domains, along with the corresponding dip angle of the slab, are synthesized in Table 7.1. As proxy of the thermal state of each domain, the geothermal gradient between 0 and 20 km bmsl was used. In turn, the rheological state of each domain is exemplified by the strength ratio between the integrated strength of the domain in question and the orogen. According to these characteristics and a first-order approximation, the SCA lithosphere can be subdivided into five domains:

(i) **Forearc**: normal to thin crust (20–35 km) with intermediate to high densities (~2975 kgm$^{-3,}$ indicating intermediate to mafic composition) and small sediment thickness (<500 m). Cold and relatively strong (strength ratio = 5) lithosphere.

(ii) **Andean orogen**: thick crust (~40–65 km) with low densities (~2900 kgm^{-3}, indicating felsic composition with high radiogenic heat production) and small sediment thickness (< 500 m). Mostly warm and relatively weak (strength ratio = 1) lithosphere.

(iii) **Northern foreland and low-relief back-arc (29°S–33°S, flat-slab domain)**: thick (40–60 km) crust with high density (~3000–3050 kgm^{-3}; indicating mafic composition). Isolated basins (1-km-thick sediments) bounded by faults. Cold and strong (strength ratio = 5) lithosphere in the south (30°S–33°S); warm and slightly stronger than the orogen (strength ratio = 3) in the north (29°S–30°S). Slab subducts sub-horizontally (dip < 5°)

(iv) **Central foreland and low-relief back-arc (33°–35°S, transition zone)**: crust of intermediate thickness (35–45 km) and low to intermediate densities (2900–2950 kgm^{-3}, probably intermediate composition). Large sediment thickness in the Cuyo basin (2–5 km). Warm and slightly stronger than the orogenic lithosphere (strength ratio = 2). Slab dips with a transitional angle (5°–30°) from north to south.

(iv) Southern foreland and low-relief back-arc (35°S–39°S, steep-slab domain): thin (~20 km) and dense crust (~3050 kgm^{-3}, probably mafic). Large sediment thickness in the Neuquén basin (2–5 km). Warm and slightly stronger than the orogenic lithosphere (strength ratio = 2). Slab dips with a steep angle (~30°)

`

Table 7.1: Main morphotectonic provinces of the southern Central Andes with structural, thermal and rheological features, and the dip angle of the oceanic slab.

	Forearc	**Andean Orogen**	**Northern Foreland (29°S-33°S)**	**Central Foreland (33°S-35°S)**	**Southern Foreland (35°S-39°S)**
Crustal thickness [km]	20-35	40–65	40–60	35–45	~20
Crustal density [kgm^{-3}]	~2975	~2900	~3000–3050	2900 –2950	~3050
Sediment thickness [km]	< 0.5	<0.5	1	2–5	2 –5
Slab-dip angle	<5°-30°	<5°-30°	<5°	5°–30°	~30°
Geothermal gradient 0-20 km [°C/km]	13	19	17 (north) 13 (south)	18	19
Strength-ratio domain:orogen	5	1	5 (north) 3 (south)	2	2

7.1.1 Model robustness and sensitivity analysis

The design of the 3D structural model relied on the integration of different geological and geophysical data sets, including seismic, gravity and petrological data to define the first-order variations of thickness and density of the continental crust. A major drawback of this approach was the scarcity of data in some regions of the study area. For instance, the southern foreland regions lack accurate constraints on the thickness of the continental crust from seismic receiver functions (Assumpção et al., 2013; Fig. 3.2). Therefore, the southward extent of the area of seismic coverage would help to reduce the uncertainties regarding the crustal thickness in these regions. Moreover, it would be desirable to obtain more accurate constraints on the 3D crustal density distribution. One way to do this is to convert crustal P-wave velocities to densities using empirical relationships (e.g., Birch, 1964; Christensen & Mooney, 1995) and subsequently cross-check the results with gravity data. However, due to the lack of P-wave crustal tomography in the SCA, I followed an alternative approach in which the crystalline crust was simply divided into two layers (upper and lower crust) with different average densities, by means of inverse gravity modelling. To estimate potential uncertainties that could arise from this approach, the model sensitivity to the specific error ranges of the chosen density configuration was tested (see sensitivity analysis in Chapter 3.6). Nevertheless, this method estimates potential uncertainties for this specific model, which means that future models incorporating more data from P-wave tomography would require to carry out the sensitivity analysis again. Although some advances towards a greater seismic-tomography coverage in the

SCA have been made in the recent years (Gao et al., 2021), large parts of the south of the study area have remained uncovered, mainly due to the scarcity of seismic stations in these domains. This is another reason why to extend the coverage of seismic stations farther south.

The 3D structural model was used as a basis to calculate the thermal and rheological fields of the SCA (Chapters 4 and 5, respectively). These modelling results depended strongly on the chosen thermal and rheological properties. Although there is an inherent non-uniqueness in the way thermal and rheological properties influence the results, the range over which these properties can vary is limited (see sensitivity analysis in Appendixes B.4, C.5 and C.6). In addition to testing the effect of end-member property values, the use of a wide variety of independent lithology-constraining data sets, including borehole temperatures, seismic tomography and heat-flow measurements, helped to reduce the range of property variability. One caveat of the use of borehole temperature and heat-flow measurements is their uneven spatial distribution, with the northern foreland being more extensively sampled than the remaining areas. Most of these measurements come from the oil and gas industry (Collo et al., 2018) and they usually target sedimentary basins with large hydrocarbon potential, such as the foreland basins, whereas other regions that are not of primary interest, such as the orogen and the forearc, have little to no coverage. Despite these limitations, first-order thermal variations proved to be robust for the tested range in imposed properties.

In addition, the thermal and rheological results are conditioned by seismic tomography data used to convert velocities to mantle temperatures. The tomography by Assumpção et al. (2013) was used in chapters 4 and 5, whereas the results of Chapter 6 were derived from the tomography of Gao et al. (2021b). This choice stems from the fact that the most recent tomographic model was not available by the time of development of the thermal and rheological models in chapters 4 and 5, respectively. When comparing the integrated crustal and lithospheric strength derived from both tomographic models, although they differ in absolute value, the first-order spatial trends (relatively weak orogen with respect to adjacent forearc and foreland areas), persist (Fig. E.1 in Appendix E). This indicates that the first-order rheological segmentation of the lithosphere is a robust result. Moreover, the thermal and rheological contrasts show remarkable correlations with independent observations, such as the distribution of seismicity and tectonic deformation patterns. Therefore, these contrasts were considered useful to extract conclusions with regards to the controlling factors of the thermal and strength distributions in the lithosphere and, ultimately, how the latter influence the short-(seismic) and long-(tectonic) term deformation patterns.

7.2 Controls on the thermo-mechanical segmentation of the lithosphere

Despite the above-mentioned limitations, there are robust findings related to controls of the thermomechanical state of the lithosphere. One of these controlling features is the crustal configuration, mainly the thickness of the upper continental crust. Given its larger concentration of radiogenic elements (e.g., Vilà et al., 2010), the upper continental crust is a large contributor to the heat budget of the lithosphere. Previous studies in other regions demonstrate that the crust can contribute more than 50% to the total heat budget (Furlong & Chapman, 2013; Scheck-Wenderoth & Maystrenko, 2013). Temperature, in turn, strongly controls the depth range at which rocks transition from dominantly brittle to dominantly ductile deformation (eqs. 5.2 and 5.3; e.g., Heard, 1960). Therefore, variations in upper crustal thickness directly result in variations of the predicted temperature and strength of the plate. Where the upper continental crust is thick (i.e., the Andean orogen) the lithosphere is warm and mechanically weak. In contrast, where the upper crust thins, the lithosphere is relatively cold and mechanically strong (i.e., forearc and foreland). Besides its effect on temperature, crustal composition exerts a control on the strength of the plate which is related to the mechanical properties. The chosen upper crustal composition (dry quartz diorite; Ranalli & Murphy, 1987) is weaker than the chosen lower crustal composition (dry mafic granulite; Wilks & Carter, 1990). Therefore, regions with thicker upper crust will have a larger part that is weak, in contrast to regions with smaller upper crustal thickness.

The second factor governing the thermal and rheological field of the lithosphere is the dip geometry of the oceanic slab. While the mantle thermal structure was derived from a tomography model (Assumpção et al., 2013), the slab-dip geometry was extracted from the Slab2 model (Hayes et al., 2018). The thermal and rheological fields of the continental plate are mainly affected by the oceanic slab in regions where the latter is characterized by a relatively shallow depth (< 85 km bmsl) and where, in addition, the radiogenic continental crust is thin. This is the case in the forearc and most of the northern foreland. Here, the lithosphere is colder and, therefore, has greater mechanical strength compared to regions where the radiogenic continental crust is thick and the oceanic slab is steep.

Additionally, slab-dip geometry may have distinct implications for the strength of the subduction interface. Figure 7.1 shows (a) the differential stress acting on the subduction interface and the yield strength envelopes (YSE) of the (b) differential and (c) shear stresses along three profiles that are representative of the different subduction segments. It can be seen that the subduction interface in the flat slab segment is up to 30 MPa stronger than in the transition zone and in steep slab segments. This also implies a stronger mechanical coupling between the two plates where the slab dips subhorizontally, with a strong crust above a strong mantle. This has important implications for the transmission of tectonic stresses, as discussed in Section 7.3. It is worth mentioning that the strength variations described here are temperature-driven, while constant frictional properties (i.e. pore-fluid pressure and Byerlee's friction coefficient) were set. However, previous studies have identified a considerable variation of pore-fluid pressure along the interface in some areas of the SCA (e.g. Hicks et al., 2014; Moreno et al., 2014). This could result in additional changes of the mechanical behavior of the plate interface. Future models should incorporate such variations which could be derived from the analysis of the v_p/v_s ratio distribution (Gao et al., 2021b).

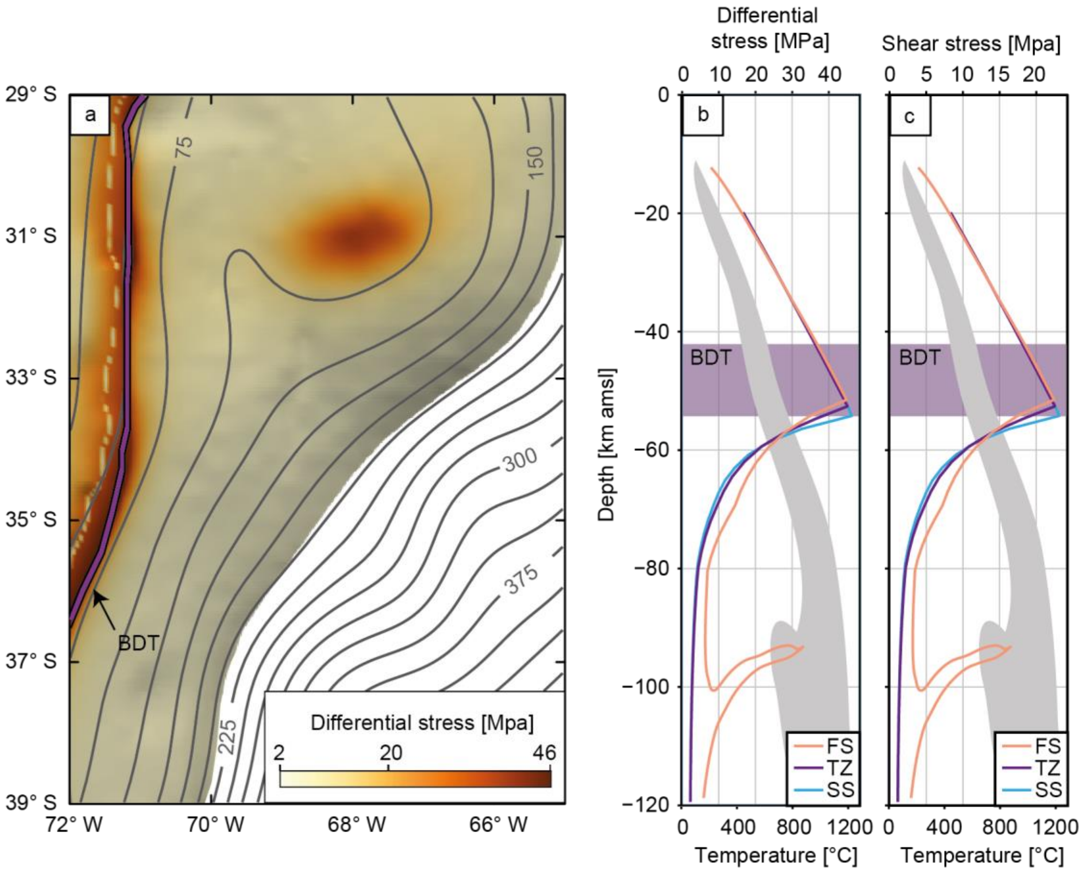

Figure 7.1: (a) Yield strength at the subduction interface overlain with location of brittle-ductile transition (BDT; thick purple area. Yield strength envelope of (b) differential stress and (c) shear stress for E-W oriented cross sections across the model domain, color-coded according to the dip domains of the slab ('FL': flat slab; TZ: transition zone; SS: steep slab). The purple-shaded area in (b-c) shows the depth of the BDT for the entire SCA region. Grey shaded area in (b-c) encompasses the geotherms of the cross sections.

There is an exception to the spatial correlation between shallow-dipping slab and the thermo-mechanical field of the lithosphere in the northernmost sectors of the foreland (29°S–30°S). Here, despite its crustal configuration (i.e., thin radiogenic upper crust and thick mafic lower crust) and underlying flat slab, the mantle exhibits high temperatures; thus, the lithosphere is weak compared to the foreland part immediately south (30°S–33°S). These high temperatures in the northernmost foreland are derived from the low v_s detected in the tomography of Assumpção et al. (2013). Therefore, an important question is whether the low v_s is a robust feature or if it is related to a smoothing effect due to the resolution of the seismic tomography used to convert S-wave velocities to temperatures.

In Chapter 4.5.2, I assessed the likelihood that the low v_s in the northernmost foreland is linked to the resolution of the seismic tomography (Assumpção et al., 2013). Farther north, at 27°S, other seismic tomography studies (Calixto et al., 2013; Gao et al., 2021a) identified a sharp transition between a low v_s region in the in the southern Andean Plateau (also known as the southern Puna Plateau) and a high v_s region in the Sierras Pampeanas. Therefore, I suggested that this transition appears to be smoothed in the tomography of Assumpção et al. (2013) due to its coarser resolution, resulting in lower modelled v_s, thus leading to higher converted temperatures and weaker rheology in the foreland north of 30°S. This hypothesis was further tested with the more recent seismic tomography data of Gao et al. (2021b), which was not available during the development of the thermal and rheological models. These authors also detected a low- v_s anomaly between 60 km bmsl and 80 km bmsl (Figs. E.2a-b in Appendix E), which spatially correlates with the low v_s domain in the northernmost foreland imaged by Assumpção et al. (2013), and high temperature-low strength modelled in this dissertation. This supports the conclusion that the low v_s feature in the region is robust, although it remains unclear, however, what the reason for this decrease could be.

The decrease of v_s in the region could be related to the accumulation of fluids released from the subducting slab (Gao et al., 2021). Interestingly, a thorough analysis of the v_p/v_s ratio distribution at 80 km bmsl (Fig. E.2c in Appendix E) indicates that the v_p/v_s ratio there is high (>1.8). This, in turn, suggests that the mantle is probably hydrated, thus supporting the notion that the decrease of v_s is caused by the presence of fluids, rather than an increase of temperature. Therefore, it is plausible that the temperatures derived from the seismic tomography are slightly overestimated, not because of the resolution of the tomography of Assumpção et al. (2013), but because of the presence of fluids in the mantle. In light of these findings, I suggest that the northernmost foreland could be indeed colder and mechanically stronger than what has been predicted by the models presented in this dissertation. Thus, the thermal imprint of the cold oceanic slab on the thermal and rheological fields of the lithosphere of the upper plate should be discernible along the entire northern foreland, where the slab dips sub-horizontally. Importantly, this hypothesis is supported by the magnitude and spatial distribution of intraplate seismicity (ISC and GCMT seismic catalogues; Dziewonski et al., 1981; Ekström et al., 2012; International Seismological Centre, 2021). The characteristic deep (D95>30 km, Fig. 5.4b) and large-magnitude intraplate seismicity of the entire northern foreland (Mw>=6, Fig. C.9) indicates that the BDT here is located at great depth and that the lithosphere is able to withstand large amounts of elastic energy, which is compatible with a strong rheological configuration.

A general outcome from this analysis of the v_p/v_s ratio of the tomography of Gao et al. (2021) is that the mantle exhibits lateral compositional variations due to different degrees of hydration, which were not included initially in the conversion of seismic velocity to temperature (Chapter 4). The orogen above the steep subduction segment and the above-mentioned northernmost foreland is characterized by high v_p/v_s ratios (>1.8), which indicates hydration and/or partial melting, in contrast to the remaining drier areas of the orogenic system, where v_p/v_s ratios are lower (Fig 6.3e). In regions where the mantle is hydrated, a serpentinite composition seems more appropriate than a spinel/garnet lherzolite composition (Hacker et al., 2003). These heterogeneous mantle composition is the result of the oceanic slab transporting fluids from the surface to larger depths (e.g., Bostock et al., 2002; Deschamps et al., 2013). In future studies, the mantle structure could be refined by subdividing it according to its degree of hydration, which would translate into the recognition of different domains with characteristic compositional, thermal, and rheological properties that would ultimately influence deformation processes.

7.3 Influence of the thermo-mechanical segmentation of the lithosphere on deformation patterns in the SCA

7.3.1 Forearc

The characteristics of the deformation of the forearc (i.e., small amount of shortening and seismicity mainly located at the borders of the strong domain) are consistent with the modelled cold and strong lithosphere, which is consequently able to resist deformation and divert it laterally to areas where the strength of the overriding plate is lower (i.e., trenchward and within the borders of the orogenic domains) and stress release is possible. This interesting concept of the forearc acting as a rigid pseudo-indenter has also been suggested in the context of deformation at the latitude of the central part of the Andean Plateau (also known as Altiplano Plateau) at about 21°S (Tassara, 2005); thus, it may be possible that similar mechanisms are potentially acting in the forearc sectors of the entire central Andean margin.

7.3.2 Andean orogen

In contrast to the forearc area, the Andean orogen has experienced pervasive tectonic deformation, as shown by the high shortening rates of the Frontal and Principal cordilleras (Fig. 2.2). The high amount of shortening is compatible with the felsic-dominated, warm and weak upper crust of this domain. Thus, the orogen is prone to localize higher amounts of strain under the same stress field than the mechanically stronger foreland and forearc. The weak character of the orogenic lithosphere is partly related to the vertical stacking of radiogenic upper crustal rocks during the Andean orogenic cycle. Restoration of balanced cross sections (L. Giambiagi et al., 2012; Ramos et al., 2002) indicates that the orogenic crust was significantly thickened at 9 Ma before the last pulse of large-scale orogenic deformation, and thus already contained a significantly large amount of upper crustal rocks. This strongly suggests that the last stage of shortening in the orogen was additionally enhanced by the existence of weak orogenic lithosphere. Present-day deformation, however, is almost absent within the orogen, as shown by the scarce seismicity (Fig. 5.4) and low shortening rates (Fig. 2.2). The absence of contractional deformation could be related to the interaction of tectonic and gravitational forces. During the last shortening stage (5 Ma), the orogen could have reached a critical thickness and elevation, resulting also in an increase in gravitational potential energy (GPE). This higher GPE could provide a counterbalance to plate-tectonic forces originating from plate convergence and plate coupling. This superposition of gravitational forces could prevent contractional deformation in the domain of the orogen, but would facilitate the migration of the deformation front to areas with lower GPE in the foreland (Mareschal & Jaupart, 2013; Molnar & Lyon-Caen, 1988; Stüwe, 2007). Indeed, widely distributed Pliocene and Quaternary normal faults within the southern sectors of the Andean Plateau (Puna) and coeval thrusting and reverse faulting in the adjacent broken foreland support this notion (Allmendinger, 1986; Montero Lopez et al., 2010; Schoenbohm & Strecker, 2009).

The modelled compositional and thermal fields of the orogenic lithosphere have other implications for the observed modes of deformation, as proposed by Barrionuevo et al. (2021). To illustrate this, Figure 7.2 shows (a) the average crystalline crustal density distribution from the structural model and (b) the depth of the 450°C isotherm from the thermal model, overlain with the E-W transects modelled by Barrionuevo et al. (2021). The N-S oriented increase of the average crustal densities and decrease of temperatures suggest that the lower crust in the southern sector is potentially more mafic than in the northern sector. These modelling results indicate that the processes proposed by Barrionuevo et al. (2021) could be taking place in the orogenic domain. A more intermediate composition and weaker lower crust in the north would promote lower-crustal thickening, which would coincide with the locus of maximum topography and upper-crustal shortening. This would be associated with pure-shear(coupled) deformation. In contrast, the more mafic and stronger lower crust in the south would prevent its crustal flow; thus, the deformation here would be shifted to the west compared to the deformation in the upper crust. This would result in simple-shear(decoupled) deformation.

The thermal field provides additional insights into the LAB geometry and, therefore, the fault-vergence of the Principal Cordillera between 34°S and 36°S (Barrionuevo et al., 2021). The temperatures modelled in chapter 4 indicate a warmer lithospheric mantle, and thus a shallower position of the LAB, beneath the orogen compared to the adjacent foreland and forearc, where the mantle is colder and, thus, the LAB is located at greater depth (Fig. 7.2b). According to the predictions by Barrionuevo et al., (2021), such an asymmetric LAB configuration would promote the formation of a west-vergent orogenic wedge, in accordance with recent kinematic models (Riesner et al., 2018).

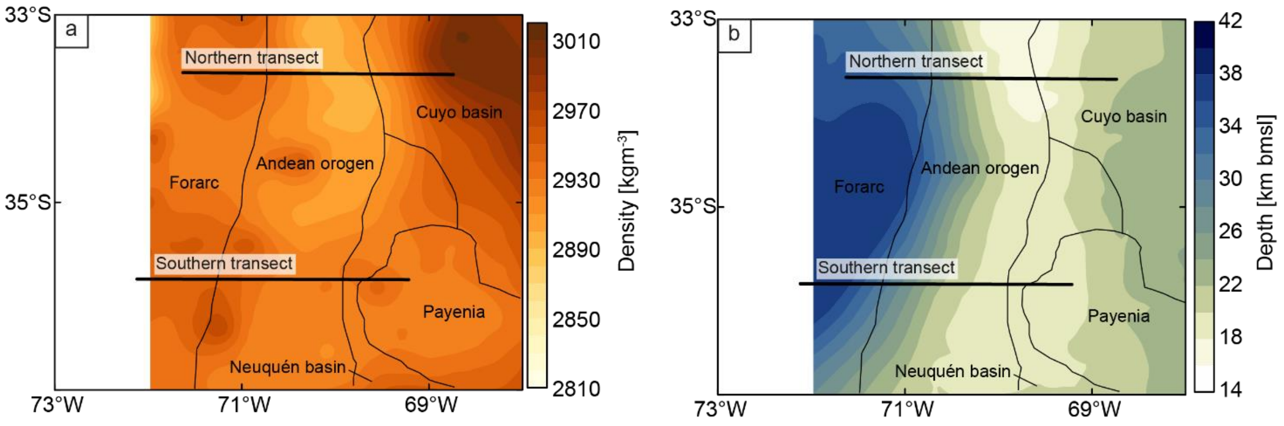

Figure 7.2: (a) Average crystalline crustal density and (b) depth to the 450°C isotherm in the region of the southern Central Andes studied by Barrionuevo et al. (2021). The location of the representative transects of different

orogenic deformation modes are overlain: northern transect (pure-shear mode), southern transect (simple-shear deformation mode).

7.3.3 Foreland

To assess the control of long-term deformation in the foreland, I focus on the main characteristics of the lithosphere that influence the deformation style according to Liu (2020): the strength ratio between the orogen and the foreland, the thickness of the lithosphere, the crust, and the sediments and the GPE of the orogen. The control of these parameters on foreland-deformation patterns is schematized in Figure 7.3. Two exemplary areas were selected based on their distinct deformation style: (i) the central-southern (33°S–39°S) and (ii) the northern (29°S–33°S) foreland. The central-southern part exhibits a mixed thin- and thick-skinned deformation pattern, which is identified in the fold-and-thrust belts of Aconcagua, La Ramada, and Malargüe (Giambiagi et al., 2012; Fig. 2.1). In contrast to the central-southern foreland, the northern foreland is dominated by a thick-skinned deformation style. This region comprises two main morphotectonic provinces: The Precordillera with thin- and thick skinned deformation (Alonso et al., 2005; Cristallini & Ramos, 2000) and the Sierras Pampeanas, which is a region characterized by thick-skinned deformation (Giambiagi et al., 2011, 2015; Fig. 2.1). In the Sierras Pampeanas morphotectonic province evidence of faults that sole out at mid-to lower crustal depths, potentially to Moho depths, has been found (e.g., Perarnau et al., 2012).

It is important to note, however, that while some of the characteristics required to link lithospheric strength with deformation patterns, such as the thickness of the crust and the sediments or the mechanical behavior of the lithosphere can be directly deduced from the presented models, the depth of the thermal LAB cannot be directly derived from the results. The computed temperatures at the base of the model (200 km) range between 1200°C and 1350°C (Fig. 4.5d), which indicate that in some sectors of the study area the thermal LAB lies below this depth. The only region where the base of the lithosphere can be traced in the model is along the flat subduction segment: here, the thickness of the continental lithosphere is structurally constrained by the depth of the subduction interface. To reconcile the problem of lacking direct constraints on the depth of the LAB, I compared different models of the global depth distribution of the LAB and selected the one that is more consistent with the modelled thermal field (Fig. E.4 in Appendix E; Artemieva, 2006; Conrad & Lithgow-Bertelloni, 2006; Hamza & Vieira, 2012; Koptev & Ershov, 2011; Priestley et al., 2018). Between the tested configurations, the model of Hamza & Vieira (2012) (Fig. E.4c) appears to be more in agreement with the computed temperatures at 200 km (Fig. 4.5d). Therefore, for the sake of simplicity, when analyzing the thickness of the lithosphere in the different regions of the SCA, I refer to the results by Hamza & Vieira (2012).

In the central-southern foreland, the continental lithosphere is ~160 km thick beneath the orogen and ~190 km thick beneath the foreland (Hamza & Vieira (2012; Fig. E.4c). The orogenic lithosphere is weaker than the lithosphere in the foreland region, but the strength contrast between the two regions (strength ratio = 2) is less pronounced than in the model areas farther north (strength ratio = 5). In addition, the central-southern foreland is characterized by the thick sediments of the Neuquén basin (Fig. 3.5b). In the northern foreland, the continental lithosphere is relatively thin (~90 km) due to the shallow dip of the slab (Fig.E.4c). The northern foreland is mechanically stronger than the orogen (strength ratio = 5) and the mechanically weak sediments are distributed in a series of shallow sedimentary basins (Fig. 3.5b). These characteristics of the lithosphere of the overriding plate in both sectors are consistent with the model predictions of Liu (2020) (Fig. 7.3), which indicate that the first-order variations of strength in the overriding plate are able to explain the main patterns of foreland-deformation style.

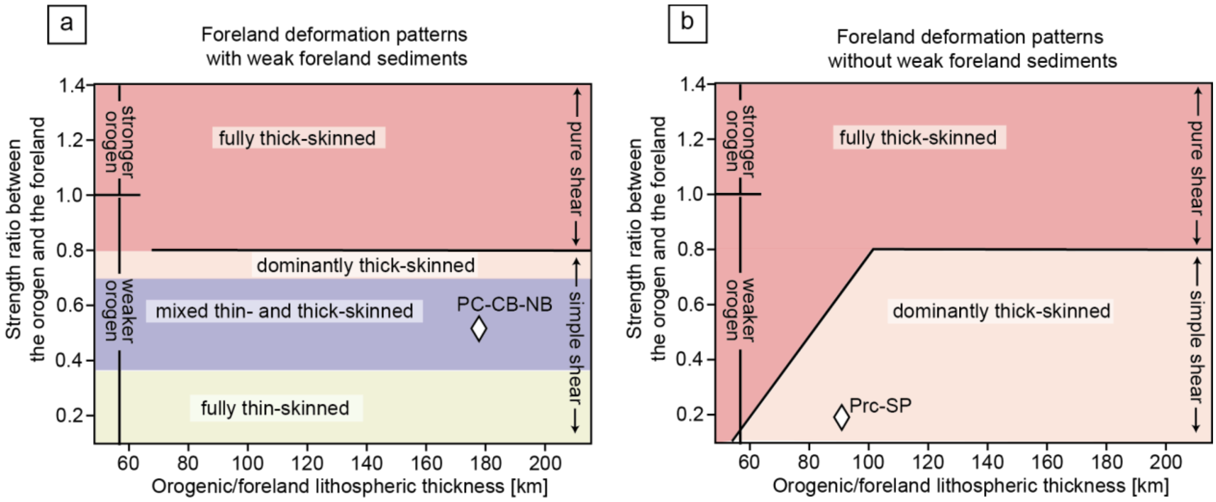

Figure 7.3: Foreland-deformation patterns (a) with or (b) without weak sediments, modified from Liu (2020). White diamonds show the structural and thermal characteristics of the main orogen-foreland systems of the SCA derived from the present dissertation. PC, Principal Cordillera; CB, Cuyo basin; NB, Neuquén basin; Prc, Precordillera; SP, Sierras Pampeanas.

The deformation styles of the two foreland areas described above imply that the principal faults extend to different depths. In the north, high-angle faults related to the spatially disparate, thick-skinned, broken-foreland of the Sierras Pampeanas occur at upper and lower crustal levels, whereas in the central-southern foreland thin-skinned faults constitute an integral part of low-angle décollements rooted in the upper crust (e.g. Giambiagi et al., 2012; Hain et al., 2011; Kley et al., 1999; Ramos, 1988). When analyzing the stress magnitudes needed to overcome the crustal strength and to generate these faults, some interesting observations were made. The strength of the upper crust in the central-southern foreland reaches up to 0.4 GPa, which is below the value of normal tectonic stresses (Fig. E.5b–c, e.g., Burov, 2011; Cloetingh & Wortel, 1986; Molnar & Lyon-Caen, 1988). Thus, the modelling results can explain why faults develop at upper crustal levels in this foreland sector. In turn, the strength in the northern foreland (up to 1.6 GPa, Fig. E.5a) far exceeds the normal tectonic stresses, which apparently contradicts the observed deformation. Therefore, additional mechanisms of crustal weakening, allowing for strain localization at lower-crustal levels must exist. This topic has been a matter of controversial debate. One proposed weakening mechanism has been related to the flat slab acting as a 'bulldozer', which weakens the upper plate due to partial removal of the mantle of the overriding plate and propagates the deformation to the east where the slab returns to a steeper subduction angle (Gutscher, 2018; Horton, 2018; Jordan et al., 1983; Ramos & Folguera, 2009). More recent interpretations (e.g., Martinod et al., 2020) questioned this concept and it was instead suggested that the flattening of the slab creates a cold and strong core in the overriding plate that prevents the lithosphere from being deformed. According to this alternative interpretation, deformation would rather localize where the slab resumes its steep subduction angle, caused by enhanced slab-pull forces due to the buoyancy contrast between the flat and steep segments. The modeled strength configuration of the northern foreland is, therefore, more consistent with this last interpretation, since the 'bulldozer' effect would be an inefficient mechanism to continuously propagate deformation in a cold and strong lithosphere. Furthermore, the spatial distribution of intraplate seismicity with the highest density of events above the steepening segments of the slab might be an indication that the mechanisms suggested by Martinod et al. (2020) may be operating in the foreland regions of the SCA.

The modeled strong overriding plate of the northern foreland makes it necessary though to explain the widely observed uplifts in the corresponding broken foreland; these different issues can be reconciled if the compressional reactivation of pre-existent faults and other heterogeneities in the crust are taken into account. In the Sierras Pampeanas such structures are either related to Paleozoic sutures and associated deformation fabrics between crustal terranes or the inversion of Cretaceous normal faults formed prior to slab flattening. These zones would act as zones of enhanced weakening, favoring strain localization (Hilley et al., 2005; Hongn et al., 2007; Hongn et al., 2010; Kley et al., 1999; Kley & Monaldi, 2002; del Papa et al., 2013; Zapata et al., 2020). Additionally, magmatic events could contribute to further crustal weakening due to local temperature increase (Meeßen, 2019; Ramos et al., 2002). For instance, Meeßen (2019) demonstrated that this could be the case of the Sierras Pampeanas, if a reduction of Byerlee's friction coefficient from 2 to 8 and a temperature increase of 100°C is inferred. In that case the crust would fail under tectonic stresses of 100 to 600 MPa (e.g., Burov, 2011; Cloetingh & Wortel, 1986; Molnar & Lyon-Caen, 1988). It is noteworthy, however, that no strict positive spatial correlation between the distribution of intraplate seismicity and the crustal faults mapped at surface is observed (Fig. 5.1). Faults between 31°S and 33°S are more seismically active than structures north of 31°S. The shorter recurrence intervals of earthquakes in the southern sector of the Sierras Pampeanas might be explained by additional tectonic forces related to the steepening segments of the slab.

Overall, the static models presented here suggest that slab steepening and weakening along inherited structures are plausible mechanisms that help explain the deformation patterns within the Sierras Pampeanas. Defining the degree of relevance of one or another process would require additional geodynamic modeling studies applied to the SCA.

7.3.4 Seismicity within the oceanic slab

While the long-term strength of the lithosphere can explain the first-order deformation patterns of the overriding plate, it fails to explain part of the active deformation within the slab. Seismicity at intermediate depths between 50 and 300 km is observed in regions modelled as ductile, where elastic energy should be preferably dissipated by viscous creep instead of seismic slip. Therefore, other mechanisms beyond the long-term mechanical strength of the lithosphere must be taken into account. The downdip limit of slab seismicity was found to spatially correlate with the transition between hydrated and dry mantle regions, as interpreted from the distribution of the v_p/v_s ratio from seismic tomography data obtained in the SCA (Gao et al., 2021b). Thus, I propose that different degrees of hydration in the mantle caused by disequilibrium compaction and dehydration of hydrous minerals may control the distribution of slab seismicity above 80 km depth. However, seismicity at 80–100 km depth within the flat-slab segment, is overlain by the mantle of an overriding plate that is more likely dry, hence ruling out fluid-mediated processes as the main mechanism to cause this seismic cluster. Here, I alternatively suggest that seismicity is triggered by enhanced flexural stresses related to the steepening of the slab.

7.4. Implications of the thermo-mechanical segmentation of the lithosphere regarding the slab-subduction angle

So far, only the implications of the slab-dip geometry on the strength configuration and associated deformation patterns have been discussed. However, the rheological variations within the overriding plate could have also exerted a control on the dip angle of the slab during the past ~20 Myr, as proposed in previous studies (Hu et al., 2016; Manea et al., 2012; Rodríguez-González et al., 2012; Schellart & Strak, 2021; Sharples et al., 2014). The structural characteristics and the strength configuration of the overriding plate at the latitudes of the Precordillera and the Sierras Pampeanas (i.e., mafic composition, cold and strong) indicates that there is an enhanced coupling between the continental and oceanic plates, as shown by the high strength of the subduction interface within the flat-slab segment (Fig. 7.1). This condition enables an efficient transmission of stresses from the continental to the oceanic plate, which forces the trench to retreat and favors the shallowing of the slab (Schellart & Strak, 2021). Moreover, the strengthening of the overriding plate causes the reduction of shortening rates and crustal thickening over time, delaying the opening of the mantle wedge and the reduction in mantle-wedge suction (Schellart & Strak, 2021). This process also facilitates the sustenance of the flat-subduction setting. Interestingly, the results presented here suggest that there is a positive feedback loop between the flat-subduction setting and the strength configuration of the overriding plate. The advection of cold material at shallow depths by the slab strengthens the overriding plate, which in turn becomes stiffer and stronger, as explained in Section 7.2. Consequently, the strong overriding plate would prevent the slab to steepen, which explains the long-lived character of the flat-subduction setting. The complex interactions between crustal structure, slab dip geometry, temperature, and strength for the SCA are summarized in Figure 7.4.

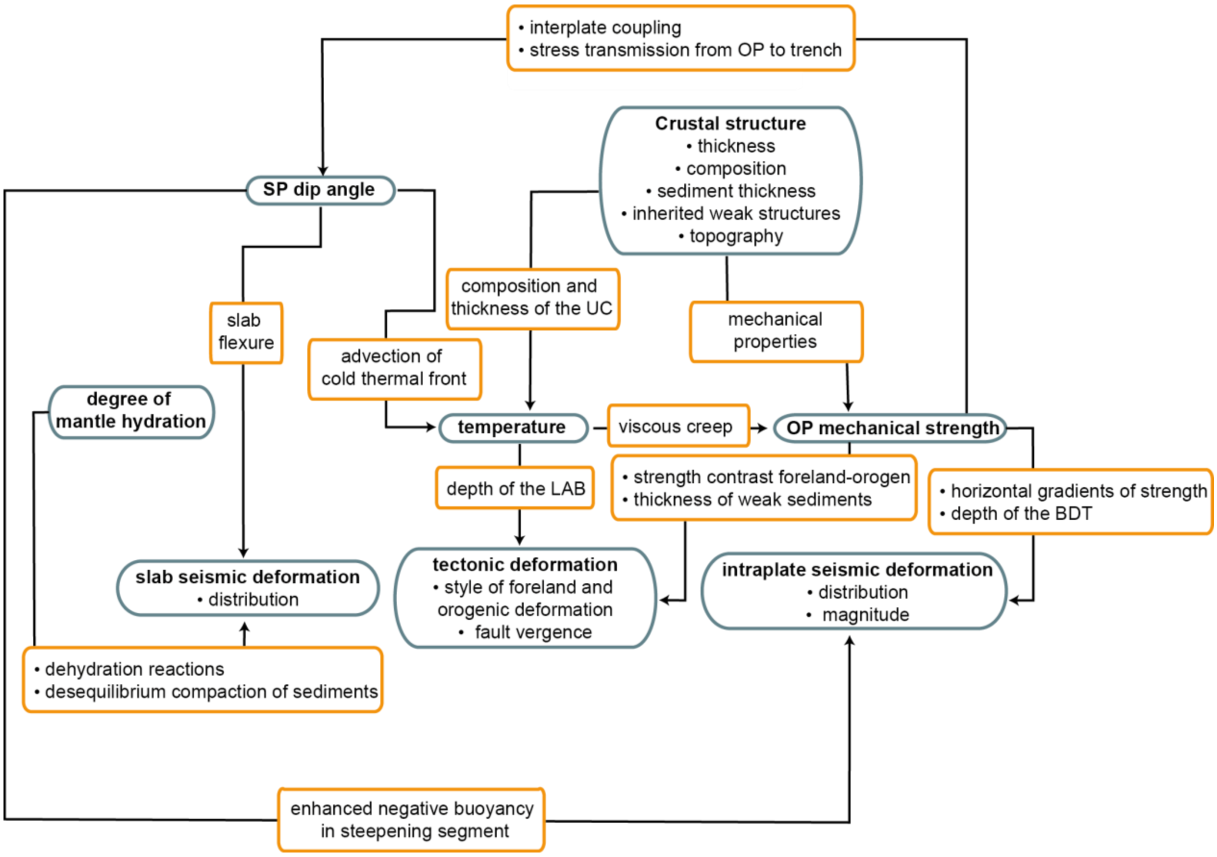

Figure 7.4: Schematic diagram summarizing the relationships between crustal inheritance, dip angle of the oceanic slab, temperature, mechanical strength, and deformation for the SCA. LAB, lithosphere-asthenosphere boundary; UC, upper crust; BDT: brittle-ductile transition; OP, overriding plate.

Chapter 8: Conclusions

Through a data-integrative approach, I aimed to characterize the present-day structural and thermomechanical configuration of the lithosphere in the southern Central Andes (SCA) and assess the related control on neotectonic structures and seismicity. The most relevant findings of this study are summarized below:

1. The lithosphere of the SCA exhibits a structural and thermomechanical segmentation and the boundaries of individual segments coincide with the main morphotectonic domains of the forearc, orogen and foreland. The orogen is characterized by thicker, more felsic, warmer and weaker lithosphere than the adjacent forearc and foreland regions.

2. The main controls on the shallow thermal field (< 50 km bmsl) are related to sedimentary blanketing and the thickness of the upper crystalline crust. Low-conductive sediments have a higher capability to store heat; the upper crystalline crust has a higher concentration of radiogenic elements, which increases the heat budget. This leads to higher temperatures where the upper crystalline crust and/or sediments are thick. In addition, the thermal overprint of the cold oceanic slab is detectable where the oceanic slab is shallow (< 85 km bmsl) and the radiogenic crust is thin, resulting in lower temperatures compared to regions where the slab is steep and the radiogenic crust is thick. In turn, the deep thermal field (> 50 km bmsl) is controlled by the mantle heat input and the slab dip geometry. Regions with lower temperatures coincide with the regions where the cold descending slab is detected.

3. The mechanical strength of the lithosphere is primarily dominated by the thermal field: there exists a negative spatial correlation between temperature and strength. Strong and weak domains correspond to cold and warm domains respectively. The heterogeneous configuration of the crust also affects the strength in terms of the lithology-related mechanical properties: the thick, felsic orogenic crust is characterized by a smaller integrated crustal strength and a shallower brittle-ductile transition than the adjacent forearc and foreland areas. Conversely, due to a thinner and more mafic crust, most of the forearc and foreland areas display higher crustal integrated strength and deeper brittle-ductile transition.

4. The mechanical strength configuration of the lithosphere appears to exert a fundamental control in the localization of intraplate seismicity. First, intraplate events occur above the brittle-ductile transition (BDT). Within the cold and strong lithosphere (i.e. forearc and most of foreland), the BDT occurs at larger depths same as the seismic events. Furthermore, these regions are characterized by large-magnitude seismicity, which indicates that the lithosphere is

able to sustain larger amounts of elastic energy before seismic rupture. Conversely, within the warm and weak lithosphere of the orogen, the BDT and the seismogenic depth are smaller than the contiguous forearc and foreland. Secondly, most of the intraplate seismicity is localized at the transition from strong and weak domains, suggesting that tectonic stresses related to plate convergence are transmitted from the mechanically strong to the weak regions of the lithosphere, where they are released.

5. Slab seismicity occurs also where long-term ductile conditions are expected. Different mechanisms can explain the occurrence of slab seismicity for these regions. Most of these earthquakes are interpreted to occur due to compaction effects and dehydration reactions in regions of hydrated mantle. However, slab seismicity is also observed in an area of dry mantle within the flat slab segment. Here seismicity is likely triggered by enhanced flexural stresses where the slab transition from a flat to a steeper subduction angle.

6. The mechanical strength of the lithosphere also explains the first-order variations in tectonic deformation observed in the orogen and the foreland. (i) Mechanically strong areas (i.e. forearc and foreland), display smaller amounts of shortening than the weak orogenic areas due to their resistance to deformation. (ii) The structural and thermomechanical characteristics defined in this dissertation are also consistent with predictions of foreland and orogenic deformation style from geodynamical models. For instance, the combination of multiple modelled characteristics, including the strength ratio between orogen and foreland, the lithospheric and crustal thickness, the presence of weak sediments and the gravitational potential energy of the orogen, appears to explain the first-order variations in foreland deformation style. This likely indicates that the overriding plate lithosphere exerts a fundamental control on tectonic deformation patterns in the SCA.

7. Where the oceanic slab is shallow, the cold oceanic plate causes strengthening of the overriding plate, increasing its resistance to deformation. In the northern foreland, the modelled crustal strength exceeds the typical values of externally applied tectonic stresses, although being characterized by active seismicity and thick-skinned structures. Therefore, two additional mechanisms were proposed to explain the strain localization in regions that should resist deformation: (i) external forces related to the steepening of the oceanic slab and (ii) localized weakening in inherited faults corresponding to Pre-Andean tectonic phases.

8. The denser and stronger lithosphere beneath the northern foreland likely favoured the strong coupling between the oceanic and continental plates, preserving the flat subduction angle.

9. Differences in crustal thickness and density of each morphotectonic domain are likely reflecting variations in their long-term tectono-magmatic evolution. For instance, development of Andean-type magmatic arcs and stacking of upper crustal rocks by thrusting could have led to a thicker and more felsic orogenic crust. In the foreland, most of the compositional and thickness heterogeneities are thought to be developed after the Neoproterozoic-Early-Paleozoic accretion of terranes to the Gondwanan margin. These events include crustal thinning of the southern foreland during Mesozoic extensional phases or extrusion of felsic magmas and intrusion of granitic material in the central Foreland during the Late Permian-Triassic.

10. This dissertation opens up new prospects for future research. For instance, the density structure of the crystalline and mantle could be refined by making use of recently published seismic tomography of the SCA. Additionally, this seismic dataset could be used to obtain a more realistic characterization of the rheological behaviour of the subduction interface, by quantifying the pore-pressure variations from the v_p/v_s ratio. These results could be subsequently compared with the seismicity at the interface to infer possible causative relationships. Finally, a topic of future investigation is the quantification of the effects of internal forces related to the structural inheritance of the overriding plate and to the slab dip geometry on the localization of deformation. To that aim, the static structural and thermal models presented in this dissertation could be incorporated into geodynamic simulations.

Appendix A: Structural and density modelling

A.1 Conversion of seismic velocity to density

Following the approach by Goes et al. (2000), the shear wave velocity of a rock with a given composition X and different temperature and pressure conditions can be calculated as:

$$v_s(P,T,X,\omega) = \sqrt{\frac{\mu(P,T,X)}{\rho(P,T,X)}} - (1 - \varepsilon(w,T,a) \text{ (A.1)}$$

Where P is pressure, T is Temperature, X the rock composition, ω the wave frequency, μ the shear modulus, ρ the density, a the frequency exponent (0.15) and ε the attenuation term, which can be defined as:

$$\varepsilon(\omega,T,a) = \frac{2}{Q(\omega,T)\tan(\frac{\pi a}{2})} \text{ (A.2)}$$

Where Q is defined as the attenuation due to anelasticity and is calculated as:

$$Q(\omega,T) = A\omega^{a}\exp\left[\frac{a(H+PV}{RT}\right] \text{ (A.3)}$$

A and R are the anelastic and universal gas constants, H is the activation energy and V is the activation volume.

For each mineral phase and pressures up to 6 GPa density ρ and M (shear modulus μ or compressibility K) can be calculated as:

$$\rho(P,T) = \rho_0\left[1 - \alpha(T - T_0) + \frac{P - P_0}{K}\right] \text{ (A.4)}$$

$$M(P,T) = M_0 + (T - T_0)\frac{\partial M}{\partial T} + (P - P_0)\frac{\partial M}{\partial P} \text{ (A.5)}$$

Where α is the thermal expansion coefficient. Mineral properties α, ρ_0, M_0, ∂M/∂T, ∂M/∂P for olivine, diopside (ortopyroxene) and enstatite (clinopyroxene) were taken from Cammarano et al. (2003), for spinel from Goes et al. (2000), while A (0.48), H(5e5 J mol^{-1}) and V (2e-5 m^3mol^{-1}) were extracted from Sobolev et al. (1996).

For each depth in the seismic tomography the algorithm calculates the S-wave velocity for temperatures between 300 and 3000K in steps of 1 K and the corresponding density, storing them subsequently in a table. For the latter calculation, pressure values are converted from depth using the AK135 seismic model (Kennett et al., 1995). In each grid point, it compares the obtained velocities with the ones from the tomographic model, by performing a look- up method over the table and choosing the two closest values to the velocity from the tomography. Then it linearly interpolates the temperatures and corresponding densities to obtain the final values.

A.2 Composition of mantle xenoliths

Table A.1: Petrological and geochemical composition of mantle xenoliths of the Agua Poca volcanic Area (see Fig.1 for the location of the xenoliths). Ol= olivine, Opx= orthopyroxene, Cpx = clinopyroxene, Sp = spinel, Xfe = iron content (1-Mg#)/100, where Mg# is the magnesium number. lherz = lherzolite, webst = websterite, cpto = clinopyroxenite.

	Composition [%]					
Sample	**Ol**	**Opx**	**Cpx**	**Sp**	**Xfe**	**Classification**
AP-75[1]	58.1	18.2	20	3.7	0.11	lherz
AP-80[1]	71.3	15.6	10.4	2.7	0.08	lherz
AP91b[1]	64.3	18.7	13.9	3.1	0.10	lherz
AP03[2]	52.3	34.8	7.1	5.8	0.11	lherz
AP06[2]	70.5	13.6	12.1	3.8	0.11	lherz
AP07[2]	52.6	33.9	8.6	4.9	0.11	lherz
AP12[2]	62.4	15.4	17.1	5.1	0.11	lherz
AP13[2]	68.2	12.3	15.2	4.3	0.11	lherz
AP45[2]	71.2	20.1	5.2	3.5	0.11	lherz
AP75[2]	52.5	22.3	19.8	1.4	0.11	lherz
AP80[2]	73.4	17.4	8	1.2	0.11	lherz
AP91[2]	57.6	19.7	18	4.8	0.12	lherz
AP10[2]	67.5	25.6	0.7	6.2	0.12	lherz
AP15[2]	84	13	2	1	0.12	lherz
AP78[2]	0.8	33.3	55.9	10	0.12	webst
AP11[2]	0.9	4	90.2	4.9	0.12	cpto
Average	**59.74**	**18.96**	**17.38**	**3.77**	**0.11**	

[1]Conceição et al. (2005); [2] Jalowitzki et al. (2010)

Appendix B: Thermal modelling

B.1 S-wave velocity

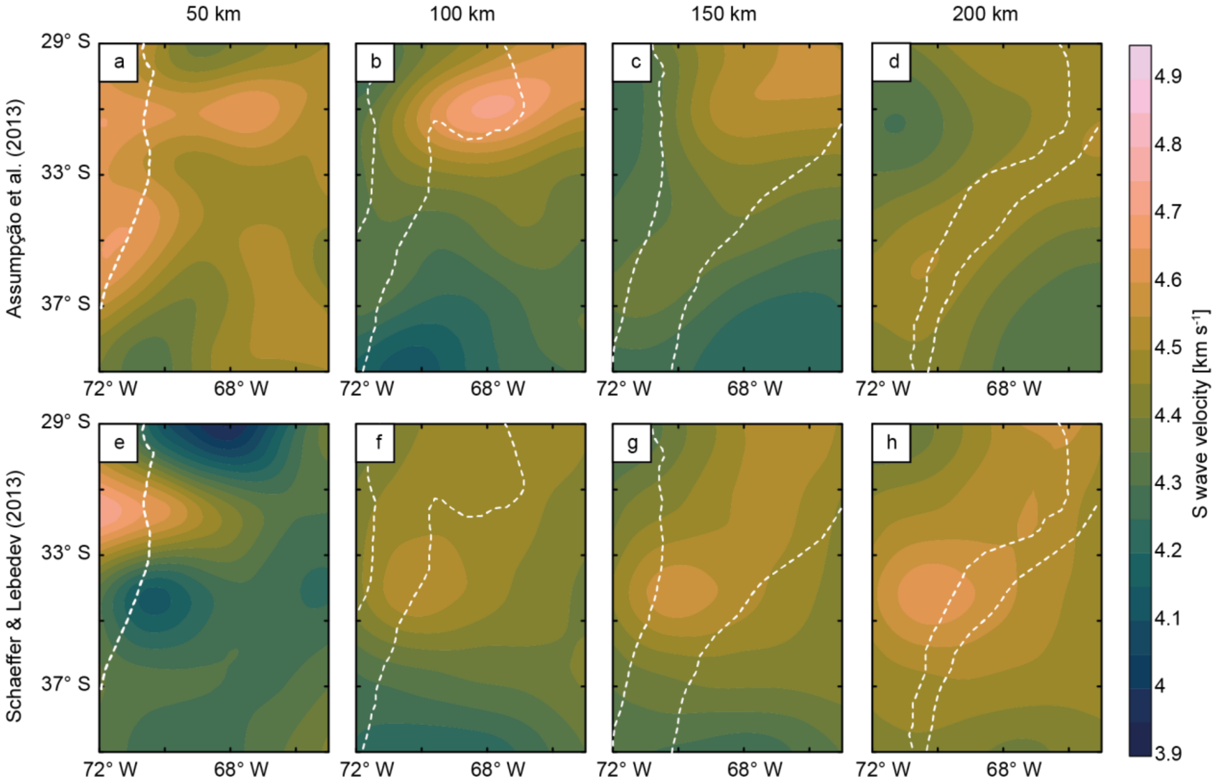

Figure B.1: S-wave velocity (v_S) distribution at depths of 50, 100, 150 and 200 km from seismic tomography of (a-e) Assumpção et al. (2013) and (e-h) Schaeffer & Lebedev (2013). Dashed lines indicate the top and bottom of the oceanic slab. There is a higher spatial correlation between high v_S (> 4.4 km s^{-1}) and the slab location in the tomography by Assumpção et al. (2013) compared to the tomography by Schaeffer & Lebedev (2013).

B.2 Sensitivity analysis of the v_S-to-T conversion

Four models were defined to evaluate the sensitivity of the v_S-to-T conversion results to variations of different parameters or conversion method: mantle composition (spinel model), thermal expansion coefficient (α model), attenuation (Q2 Model) and conversion method by Priestley & Mckenzie (2006).

To test the compositional effect on the model, the spinel lherzolite from Conceição et al. (2005) and Jalowitzki et al. (2010) was selected as alternative mantle composition (spinel model; Table 4.1). In contrast to the reference model, this composition is richer in clinopyroxene and iron and has spinel, instead of garnet, as aluminium phase. Within the compositional parameters, seismic velocities are most sensitive to the iron content, where an increase in the magnesium number Mg/(Mg+Fe) by 10 is estimated to produce a velocity increase of 2-3% (Cammarano et al., 2003; Goes et al., 2000).

Secondly, we assessed the effect of the temperature (T) dependence of the thermal expansion coefficient α on the resulting temperature distribution (αT model; Cammarano et al., 2003; Goes et al., 2000 based on Saxena & Shen, 1992). Figure B.2 shows the variation of α with T for different mantle minerals.

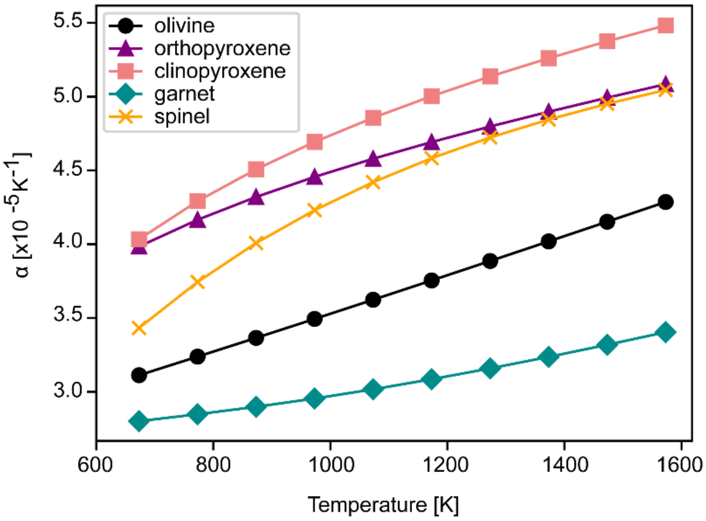

Figure B.2: Variation of the thermal expansion coefficient α with temperature for the main mineral phases of the mantle. Values for olivine, orthopyroxene and garnet were taken from (Cammarano et al., 2003). Values for spinel were taken from Goes et al. (2000). Both publications are based on experimental estimations of Saxena & Shen (1992).

In a third stage, we used the parameters provided by Berckhemer et al. (1982) to investigate the effect of anelasticity Q (Q2 model; $a = 0.25$, $A = 2e\text{-}4$, $H = 584\ \mathrm{kJ\ mol^{-1}}$, $V = 20\ \mathrm{cm^3\ mol^{-1}}$). This database is entirely derived from an experimental model for synthetic forsterite, in contrast to the attenuation parameters by Sobolev et al. (1996), which result from average values for a wide range of experiments. Therefore, the latter represents a more averaged Q model than the database of Berckhemer et al., (1982; Goes et al., 2000). The Q2 model has a weaker attenuation than the reference model, thus the effect on anelasticity is smaller. Both models are considered to represent extreme values for the anelastic correction and, therefore, they allow for a rough estimation of the uncertainty in the v_S-to-T conversion due to unknowns related to Q (Shapiro et al., 2004).

As a final step of the sensitivity analysis, we tested the alternative conversion method of (Priestley & Mckenzie, 2006; PM model), using the conversion tool VeloDT (Meeßen, 2020). In contrast to the Goes et al., (2000) mineral-physics-based approach, Priestley & Mckenzie (2006) derived an empirical relationship between *S-wave* and temperature, dependent on pressure but not on composition. Despite being calibrated mainly for oceanic lithosphere, the conversion was also applied to continental lithosphere using thermal models from mantle nodules in kimberlites, thus it was considered appropriate for our study area as well.

Figure B.3 shows the temperature residual (i.e. difference between the reference model and each alternative configuration tested) as a function of v_s and depth. By relying on the Goes et al. (2000) approach, a modification of the mantle mineral composition yields up to 160°C difference at depths shallower than 100 km and high v_s (4.6 km s^{-1}) with respect to the reference model (Fig. B.3a). Variations in the expansion coefficient or seismic attenuation lead to temperature differences up to 80°C for v_s of 4.6 km s^{-1} (Fig. B.3b-c). In contrast, the method by Priestley & Mckenzie (2006) predicts higher temperatures for v_s < 4.6 km s^{-1} than the reference model, up to 450°C higher for v_s between 4.6 and 4.8 km s^{-1} (Fig. B.3d).

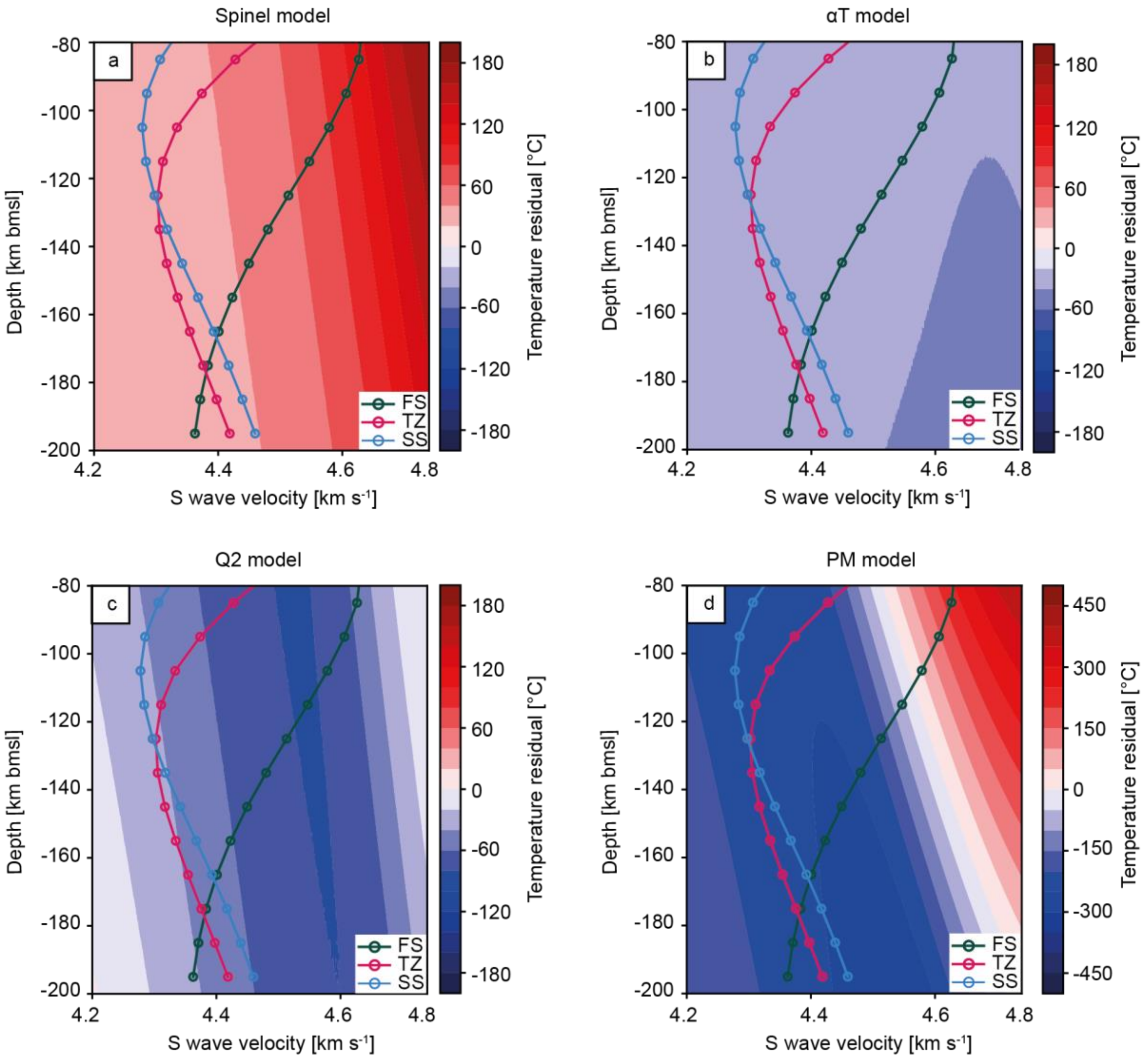

Figure B.3: Residual temperature maps showing the difference between the reference model and the alternative configurations in the v_s-depth parameter space. a) Spinel model: mantle composition of spinel lherzolite (Conceição et al., 2005; Jalowitzki et al., 2010); b) αT model: T-dependent thermal expansion coefficient (Saxena & Shen, 1992); c) Q2 model: attenuation parameters by Berckhemer et al. (1982); d) PM model: v_s-to-T conversion method of Priestley & Mckenzie (2006). 1-D v_s profiles of the tomography of Assumpção et al. (2013) are overlain: FS = flat slab area; TZ = transition zone; SS = steep slab area.

B.3 Thermal properties for the calculation of the steady-state conductive thermal field

The assignment of thermal properties to the units of the structural model of Rodriguez Piceda et al. (2021) was done according to the comparison between gravity-constrained densities (Rodriguez Piceda et al., 2021) and mean P-wave velocities (v_p, Araneda et al., 2003; Contreras-

Reyes et al., 2008; Marot et al., 2014; Scarfi & Barbieri, 2019), combined with rock property compilations (Brocher, 2005; Christensen & Mooney, 1995).

For the sedimentary layers, based on a mean density of 2350 kg m^{-3} (Rodriguez Piceda et al., 2021) and a mean velocity of 4.6 km s^{-1} (Araneda et al., 2003), we assigned a siliciclastic composition (Brocher, 2005). Thus, we attributed to both sedimentary units a thermal conductivity of 2 $Wm^{-1}K^{-1}$ (Čermák & Rybach, 1982) and a radiogenic heat production of 1 μWm^{-3} (Vilà et al., 2010), consistent with this lithology.

The physical properties of the upper crust (density of 2800 kgm^{-3}; v_P of 6.3 km s^{-1}) are indicative of diorites (Christensen & Mooney, 1995). According to this lithology, the thermal conductivity was set to 3.4 $Wm^{-1}K^{-1}$ (Čermák & Rybach, 1982) and the heat production to 2 μWm^{-3} (Vilà et al., 2010).

In the case of the lower crust, its composition is not precisely determined throughout the entire region, apart from a modeled density of 3100 kgm^{-3} (Rodriguez Piceda et al., 2021), a mean v_P of 6.76 km s^{-1} (Marot et al., 2014; Pesicek et al., 2012; Scarfi & Barbieri, 2019) and the occurrence of partial eclogitization suggested by several studies in the region of the flat slab (e.g. Alvarado et al., 2007; 2009; Ammirati et al., 2013, 2015, 2018; Gilbert et al., 2006; Marot et al., 2014). The comparison of these physical properties with the compilation of Christensen & Mooney (1995) points to a mafic granulite composition. Conforming to this rock type, we used a lower crustal thermal conductivity of 2.5 $Wm^{-1}K^{-1}$ (Čermák & Rybach, 1982) and a heat production of 0.4 μWm^{-3} (Hasterok & Chapman, 2011).

For the shallow oceanic crust, a density of 2900 kgm^{-3} (Rodriguez Piceda et al., 2021) and a mean v_P of 6.7 km s^{-1} (Araneda et al., 2003; Contreras-Reyes et al., 2008) suggest that this layer is represented by a basaltic composition (Christensen & Mooney, 1995). Thus, we chose a thermal conductivity of 1.8 $Wm^{-1}K^{-1}$ (Čermák & Rybach, 1982) and radiogenic heat production of 0.35 μWm^{-1} (Vilà et al., 2010), consistent with this lithology. For the deep oceanic crust, based on a modeled density of 3200 kg m^{-3} and a mean v_P of 7.1 km s^{-1} (Araneda et al., 2003; Contreras-Reyes et al., 2008), we assumed an eclogitic composition (Christensen & Mooney, 1995). Hence, we assigned to this layer a thermal conductivity of 2.87 $Wm^{-1}K^{-1}$ (He et al., 2008) and a radiogenic heat production of 0.25 μWm^{-3} (Vilà et al., 2010).

Lastly, for the mantle layers, based on the average density of 3360 kgm^{-3} (oceanic lithospheric mantle) and 3340 kgm^{-3} (continental lithospheric/oceanic sub-lithospheric mantle), we assigned a composition of moderately depleted lherzolite (Rodriguez Piceda et al., 2021).

This is also coherent with geochemical data of mantle xenoliths (Bertotto et al., 2013), v_s of 4.6—4.7 km s^{-1} (Wagner et al., 2005) and v_p/v_s ratios of 1.75–1.77 (Marot et al., 2014). Accordingly, we set a mantle radiogenic heat production of 0.01 μWm^{-3} (Vilà et al., 2010). The thermal conductivity of the mantle was determined based on the empirical relationship of (Xu et al., 2004). This expression quantifies the P(pressure)-T(temperature) dependency of the thermal conductivity λ of olivine from thermal diffusivity measurements at pressures up to 20 GPa and temperatures up to 1373 K and is described as:

$$\lambda = 4.10\left(\frac{298}{T}\right)^{0.493}(1 + 0.032P) \quad \text{(B.1)}$$

where T is in K and P is in GPa.

Figure B.4a shows the variation of thermal conductivity with P and T for the upper mantle (up to 10 GPa and 1750 K), overlain with 3 representative geotherms of the study area derived from the v_s-to-T conversion (see Chapter 4.3.1). Overall, thermal conductivity decreases with increasing temperature and decreasing pressure. The largest variation of λ occurs at low temperatures (< 750 K). Figure B.4b depicts the histogram of thermal conductivities for the P-T range of the results of v_s-to-T conversion. For this range, the mean value of λ is 2.24 $Wm^{-1}K^{-1}$ with a standard deviation of 0.12 $Wm^{-1}K^{-1}$. Therefore, the variations of λ are sufficiently small to consider taking a constant value of 2.24 $Wm^{-1}K^{-1}$ as a valid assumption for the entire modeled P-T range of the lithospheric mantle.

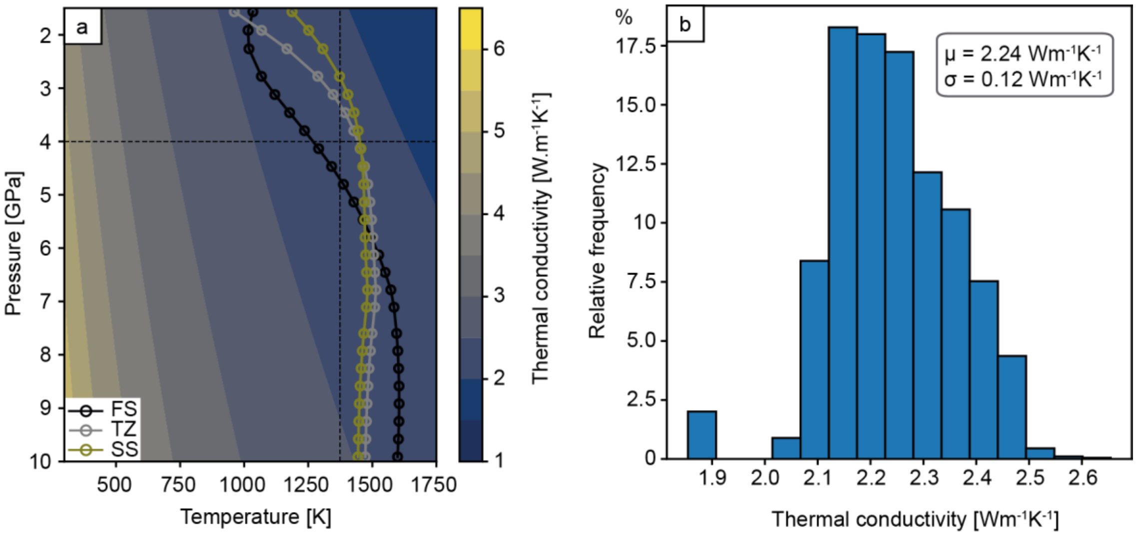

Figure B.4: (a) Thermal conductivity v_s. pressure and temperature according to eq. 1 (Xu et al., 2004) overlain with 1-D geotherms of the study area. FS= Flat slab area, TZ=Transition zone, SS=Steep slab area. (b) Histogram of thermal conductivity calculated for the (P-T) range of the results of the v_s -to-T conversion (Chapter 4.3.1; Goes et al., 2000; Meeßen, 2017). μ is the mean value and σ the standard deviation.

B.4 Sensitivity analysis of the steady-state conductive thermal modelling

We performed a sensitivity analysis of the modeled temperatures to variations of the thermal properties (thermal conductivity λ and radiogenic heat production S) of the units composing the structural model. To this end, we carried out a steady-state conductive simulation on alternative configurations of the final structural model, varying one thermal parameter at a time. The imposed variations of each property are based on the range of its natural variability according to the composition of each unit (Table B.1, Carter & Tsenn, 1987; Čermák & Rybach, 1982; Hasterok & Chapman, 2011; He et al., 2008; Majorowicz et al., 2019; Russell et al., 2001; Vilà et al., 2010; Xu et al., 2004). Figures B.5 and B.6 displays the temperature difference between the preferred model described in Chapter 4.3.2 and each alternative configuration at depths of 10 and 30 km bmsl. A preliminary analysis of these depth slices shows that the greatest temperature differences occur when varying the radiogenic heat production of the upper crust. However, since perturbations of different magnitude are imposed to each thermal property, in order to properly compare the results, we compute a normalization factor f by dividing the maximum induced variation in temperature by the relative variation of the thermal property that induced such temperature perturbation (Table B.1). This factor quantifies how the temperature changes according to variations in the predefined thermal properties of the units. A comparison of the factor f corresponding to the thermal conductivity and the radiogenic heat production of each unit is depicted in Figure B.7. Contrary to our preliminary analysis, this approach indicates that temperatures are most sensitive to perturbations in the thermal conductivity of the upper continental crystalline crust and the mantle (f=10.9 °C/%).

Table B. 1: Summary of results from sensitivity analysis of the steady state conductive thermal modelling to variations in thermal conductivity λ and radiogenic heat production S. The factor f is calculated by dividing the absolute value of the maximum ΔT (i.e., temperature difference between final and alternative models) by the relative variation of the thermal property

		Thermal conductivity λ			**Radiogenic heat production S**		
Layers		**λ [$Wm^{-1}K^{-1}$] / Absolute λ variation [$m^{-1}K^{-1}$] / Relative λ variation (%)**	**Maximum ΔT, abs. value [°C]**	**Factor f [%/°C]**	**S [μWm^{-3}] / Absolute S variation / [μWm^{-3}] / Relative variation (%)**	**Maximum ΔT, abs.value [km]**	**Factor f [%/°C]**
Continental/oceanic sediments		1.81[1] /-0.19 / 9.5	12	1.2	0.12[2] / -0.88 / 87.7	5	0.06
		2.50[1] / +0.50 / 25	25	1	2.50[2] / +1.5 / 150	8	0.05
Upper continental crystalline crust		1.72[1] / -1.68 / 49	65	1.3	0.25[2] / -1.75 / 87.4	200	2.30
		4.14[1] / +0.74 / 21.8	237	10.9	3.8 / +1.8 / 90	206	2.30
Lower continental crystalline crust		2.10[3] / -0.4 / -16	48	3	0.20[5] / -0.2 / -50	39	0.78
		2.80[4] / +0.3 / 12	40	2.4	0.75[5] / +0.35 / 87.5	60	0.70
Oceanic plate	Shallow crust	1.40[1] /-0.4 / -22.2	53	2.39	0.009[2] /-0.341 / 97.4	42	0.43
		5.33[1] / +3.53 / 196	63	0.30	1.2[2] / +0.85 / 243	62	0.26
	Deep crust	2.20[6] /-0.67 / -23.3	34	1.46	0.02[2] / -0.23 / 90.4	33	0.37
		3.60[6] / +0.73 / 25.4	32	1.26	0.70[2] / +0.45 /180	42	0.23
Continental and Oceanic lithospheric mantle/Oceanic sub-lithospheric mantle		2.10[7] / -0.14 / -6.25	38	6.08	0.00[2] / -0.01 / 100	41	0.41
		3.30[8] / +1.06 / 47.3	84	1.78	0.80[2] / +0.79 / 7900	102	0.01

[1] Čermák & Rybach (1982); [2] Vilà et al. (2010); [3] Majorowicz et al. (2019); [4]; Carter & Tsenn (1987); [5] Hasterok & Chapman (2011); [6] He et al. (2008); [7] Xu et al., 2004); [8]Russell et al. (2001)

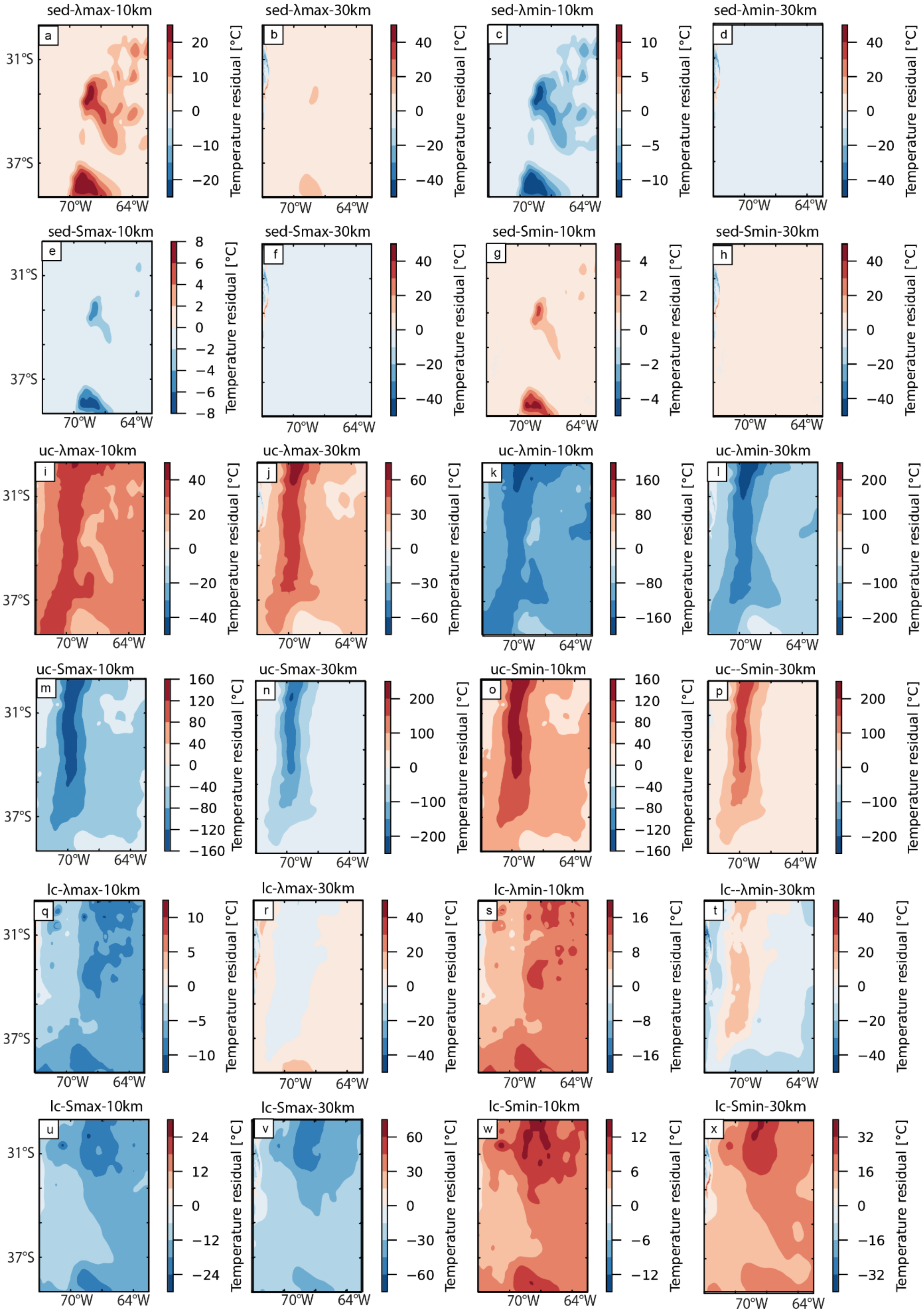

Figure B.5: Slices at depths of 10 and 30 km bmsl (below mean sea level) showing the temperature residual (i.e. difference between the temperature fields of the final steady-state conductive model and alternative configurations tested in the sensitivity analysis) for the thermal properties of the sediments and the continental crystalline crust. λ = bulk thermal conductivity; S = radiogenic heat production. Sed=sediments; uc=upper continental crystalline crust; lc=lower continental crystalline crust.

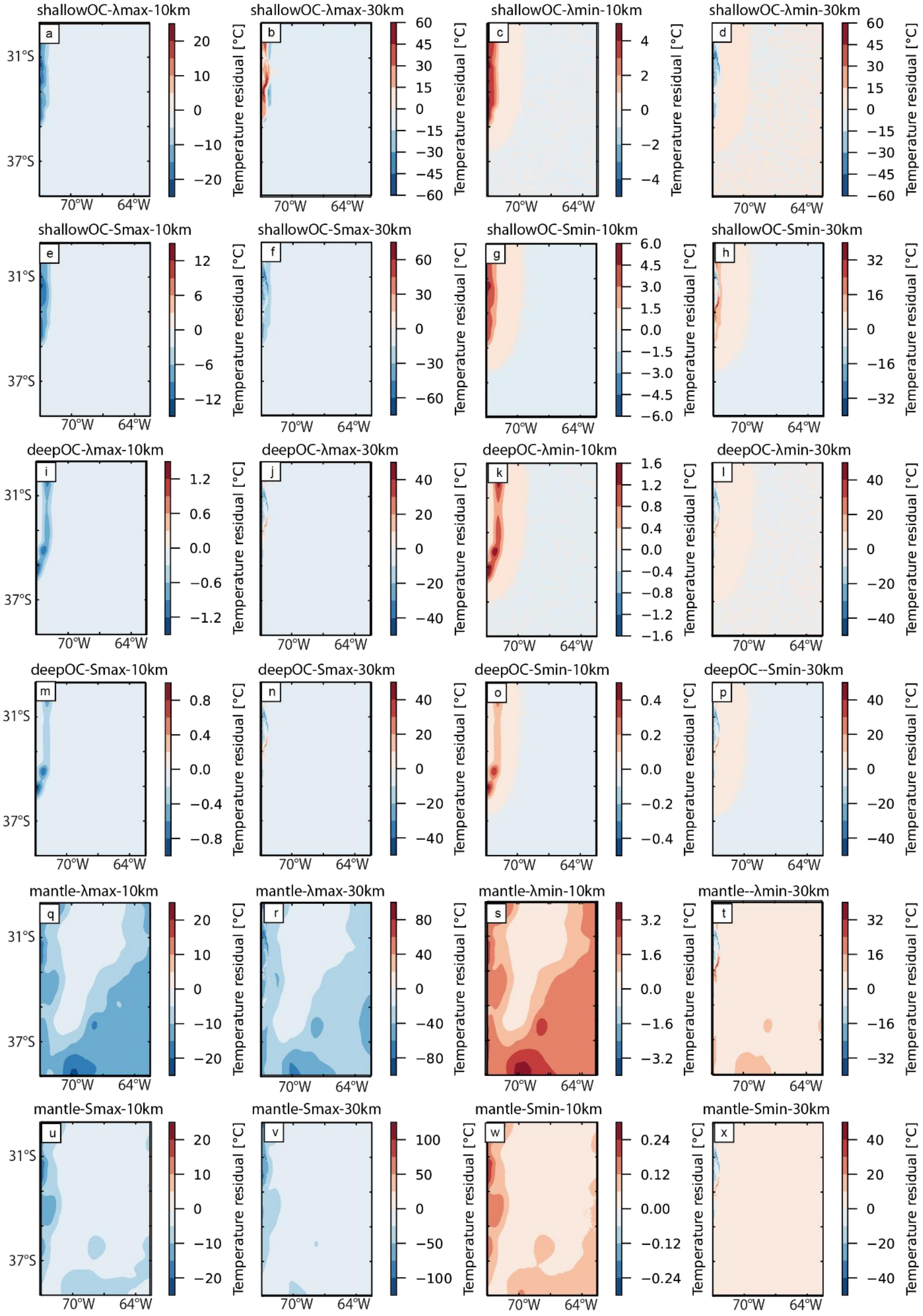

Figure B.6: Slices at depths of 10 and 30 km bmsl (below mean sea level) showing the temperature residual for thermal properties of the oceanic crust (a-p) and the mantle (q-x). shallowOC= shallow oceanic crust; deepOC=deep oceanic crust.

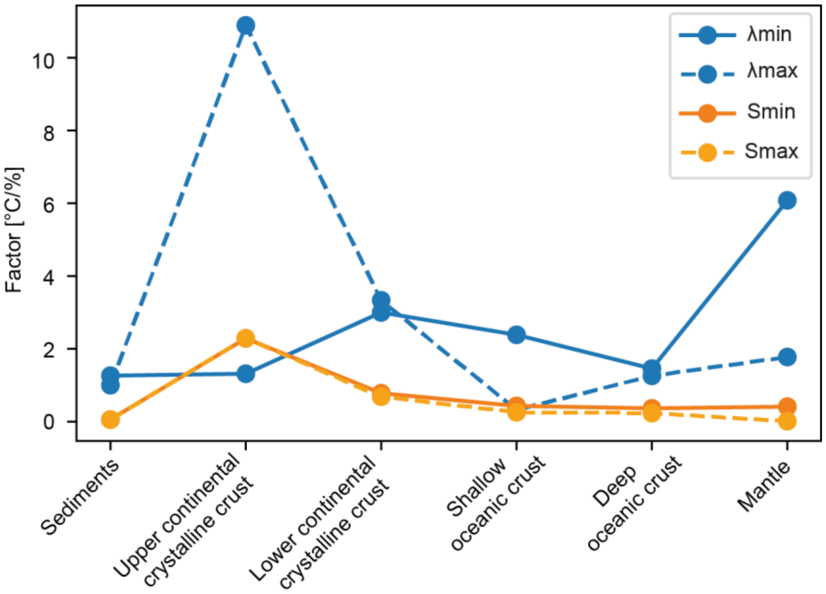

Figure B.7: Variation of the sensitivity factor f corresponding to the variation of the thermal properties of the model units. λ = bulk thermal conductivity; S = radiogenic heat production.

B.5 Upper thermal boundary condition

For the upper thermal boundary condition in the continental domain, we considered the yearly average surface temperature from 1981 to 2020, provided by the ERA-5 land database (Copernicus Climate Change Service (C3S), 2019). In the oceanic domain, we used a constant temperature of 4 °C, which is an average estimate at sea floor (Pawlowicz, 2013).

B.6 Calculation of heat flow

The heat flow in GOLEM (Cacace & Jacquey, 2017; Jacquey & Cacace, 2017) is calculated at every nodal point of the model as a vector, so the output is the following:

$$\boldsymbol{q}(x, y, z) = -\lambda(\nabla T_x, \nabla T_y, \nabla T_z) \text{ (B.2)}$$

Where λ is the thermal conductivity and ∇Tx, ∇Ty, ∇Tz are the gradient in x,y and z directions, respectively.

B.7 Transient thermal modelling approach

B.7.1 Advective thermal modelling of the subduction interface

In a first modelling stage, we computed the thermal evolution of the subduction interface in 7 Ma due to advection and conduction with the Finite Element numerical simulator LYNX (Jacquey & Cacace, 2019, 2020). We used a 2D mesh that represents a horizontal projection of the subduction interface with a horizontal resolution of 5 km and an extension of 1400 km by 1400 km. Temperatures are computed in LYNX by solving the energy equation, which accounts for both heat transfer by conduction and by advection of solid material. If we neglect the effect of radiogenic heat production and shear heating, the equation reads as follows:

$$\frac{\partial T}{\partial t} + \boldsymbol{v} \nabla T - \nabla \left(\frac{\lambda}{C_p \rho} \nabla T \right) = 0 \quad \text{(B.3)}$$

where T is temperature, t is time, ν is the solid velocity, λ is the thermal conductivity, C_p is the heat capacity and ρ is the bulk density. λ was set to 1.8 $Wm^{-1}K^{-1}$, ρ to 2900 kgm^{-3} and C_p to 1200 m^2s^{-1}, which is consistent with a basaltic composition representative of the top slab (Petitjean et al., 2006). As ν we used the absolute velocity of the Nazca Plate at present-day (ν_n=0.04 myr^{-1}, Sdrolias & Müller, 2006) projected horizontally by applying the following equation:

$$v = cos \propto_s v_n \quad \text{(B.4)}$$

where α_s is the subduction angle of the oceanic plate extracted from the 3D structural model (Rodriguez Piceda et al., 2021). ν was set to 0 myr^{-1} at the nodes where the depth of the subduction interface is > 200 km bmsl (i.e., base of the steady-state conductive thermal model of Chapter 4). The velocity field is shown in Figure B.8a. The model was initialized with the temperature distribution at the subduction interface extracted from the S-wave tomography (Figure B.8b, Assumpção et al., 2013).

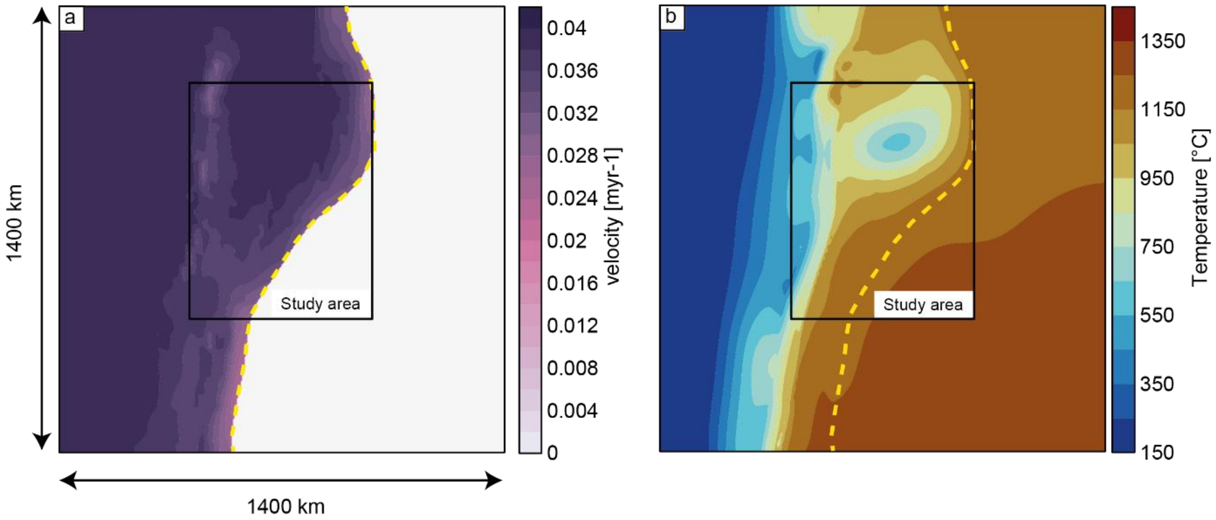

Figure B.8: Set up of the advective-conductive thermal model of the subduction interface. (a) absolute plate velocity of the oceanic plate projected horizontally according to eq. 3. v was set to 0 cmyr^{-1} at the nodes right of the dashed yellow line since the slab there is deeper than 200 km bmsl.; (b) initial temperature distribution from the S-wave tomography of Assumpção et al. (2013). The black rectangle bounds the study area.

Figure B.9 shows the W-E progression of the cold thermal front along the subduction interface after (a) 2 Ma, (b) 5 Ma and (c) 7 Ma of model run.

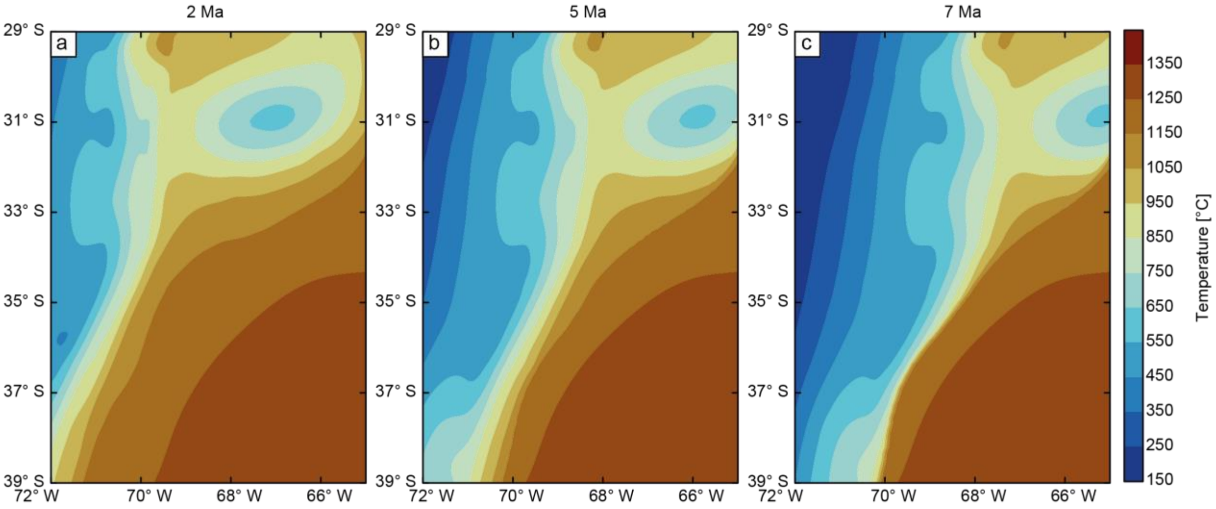

Figure B.9: Thermal evolution of the subduction interface in the study area after (a) 2 Ma, (b) 5 Ma and (c) 7 Ma of the advective-conductive model run.

B.7.2 Transient thermal modelling of the upper plate

The second modelling stage aimed to assess the effect of transient conduction and advection in the thermal field of the overriding plate. We used a subarea of the structural and density model of Rodriguez Piceda et al. (2021) with the same refinement and resolution of the model described in Chapter 4.3.2 to solve for the conductive transient thermal field with GOLEM (Cacace & Jacquey, 2017; Jacquey & Cacace, 2017). The formulation that describes the temperature calculation under transient conditions is:

$$\frac{\partial T}{\partial t} - \nabla\left(\frac{\lambda}{C_p \rho}\nabla T\right) = S \text{ (B.5),}$$

where S is the radiogenic heat production. The thermal properties S and λ were applied for each model unit as described in text S2. Densities were taken from the model of Rodriguez Piceda et al. (2021). A heat capacity of 1200 $m^2 s^{-1}$ (Petitjean et al., 2006) was assigned for all the model units. Thermal properties are summarized in Table B.2.

Table B.2: Thermal properties assigned to the units of the 3D structural model (Rodriguez Piceda et al., 2020) to calculate the transient thermal field in the overriding plate. λ = bulk thermal conductivity; Cp = heat capacity; ρ = bulk density; S = radiogenic heat production. [1]Čermák & Rybach (1982); [2] Petitjean et al. (2006); [3] Vilà et al. (2010); [4] Hasterok & Chapman (2011); [5] Xu et al. (2004)

Layers	**λ [$Wm^{-1}K^{-1}$]**	**Cp [m^2s^{-1}]**	**ρ [kg m^{-3}]**	**S [μWm^{-3}]**
Continental/oceanic sediments	2.00[1]	1200[2]	2300/2400	1.00[3]
Upper continental crystalline crust	3.40[1]	1200[2]	2800	2.00[3]
Lower continental crystalline crust	2.50[1]	1200[2]	3100	0.40[4]
Continental lithospheric mantle	2.24[5]	1200[2]	3320	0.01[3]

Dirichlet thermal boundary conditions were assigned along the top and the base of the model. The surface temperature of ERA-5 data set described in Appendix B.5 was set as fixed upper boundary condition. As time-dependent lower boundary condition, we used the thermal progression along this interface previously computed and explained in Appendix B.7.1. We initialized the simulation with the 3D thermal field of the model presented in Chapter 4.4 and run the model for 7 Ma. The initial model set up is schematized in Figure B.10.

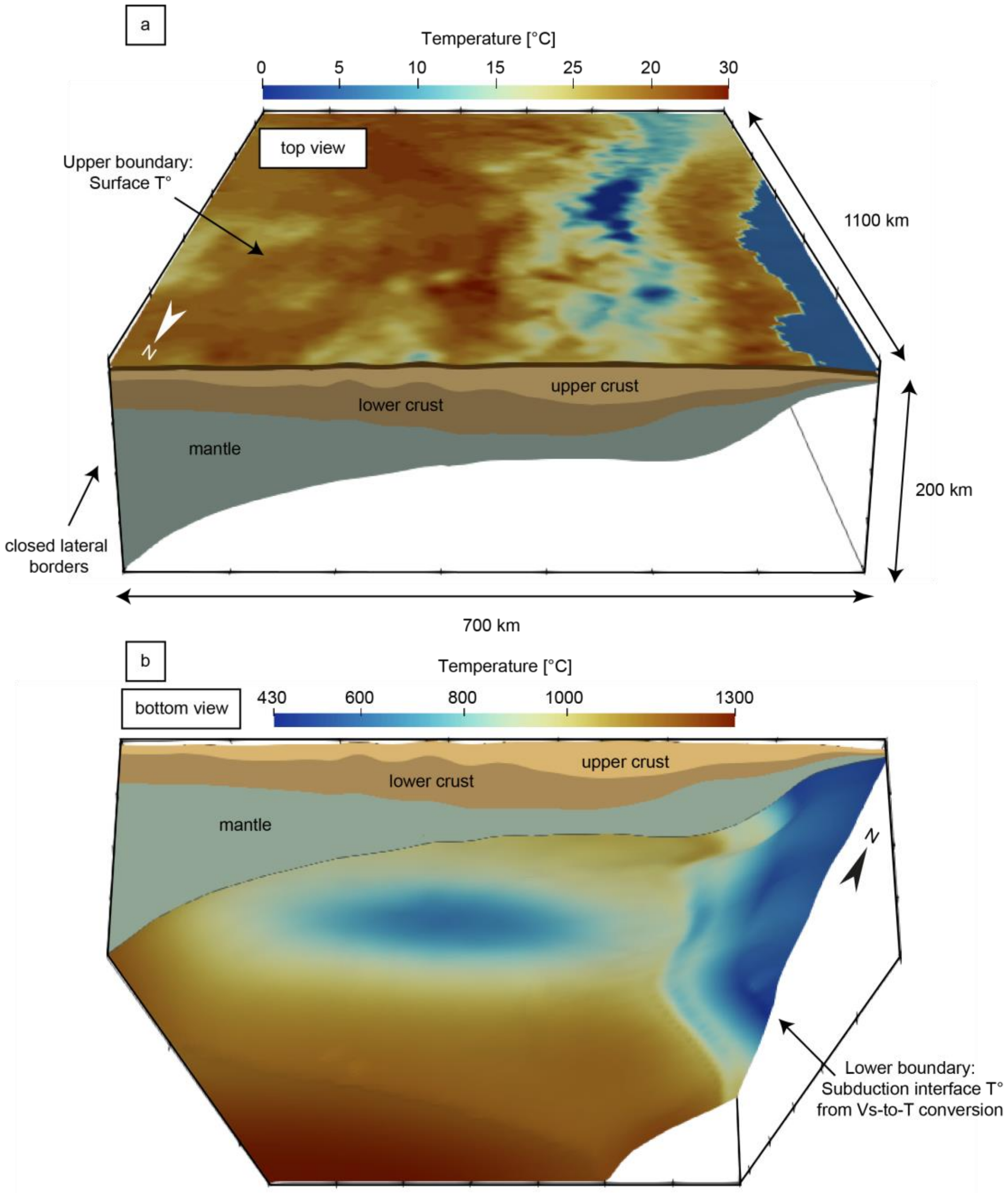

Figure B.10: initial set up of the 3D transient model showing the thermal boundary conditions at the (a) top and (b) bottom of the model. During the simulation, the upper boundary condition was fixed, while the thermal progression along the subduction interface previously computed and explained in Appendix B.7.1 was set as the lower transient boundary.

B.8 Lower boundary condition with garnet lherzolite

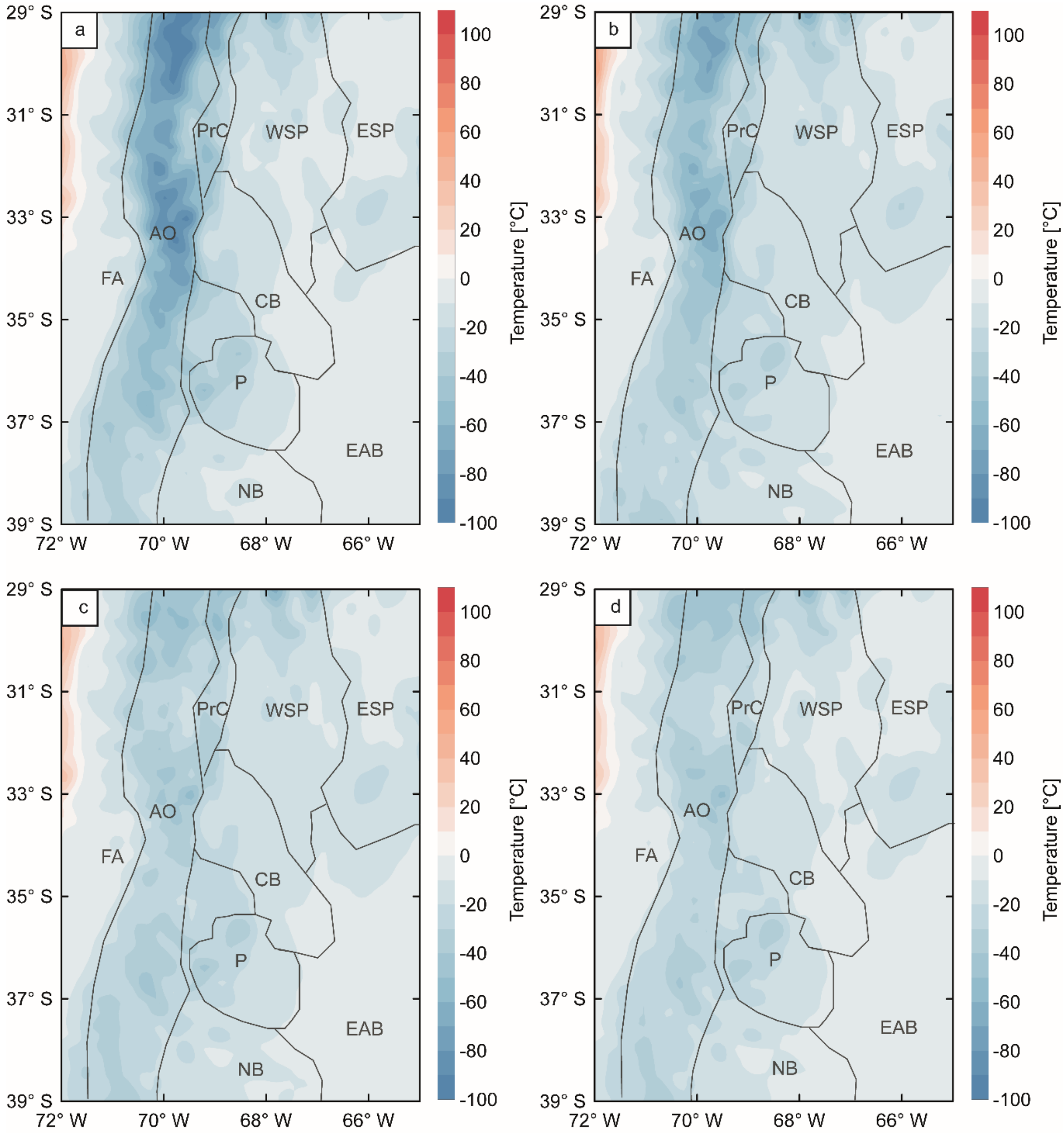

Figure B.11: Difference maps between temperature slices using a lower boundary condition from the v_s-to-T conversion with spinel and garnet lherzolite at depths of a) 10 km, b) 20 km, c) 30 km and d) 40 km. Key tectonic features are overlain (see Fig. 4.1 for abbreviations).

B.9 Lower boundary condition with a linear gradient

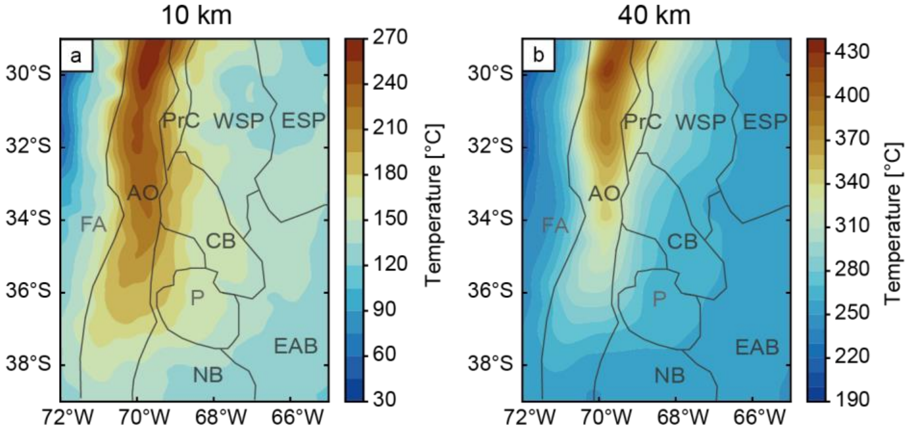

Figure B.12: Temperature maps at depths of (a) 10 km and (b) 40 km of the model with a lower boundary condition derived from a linear gradient of 5°C km^{-1} (Syracuse et al., 2010)

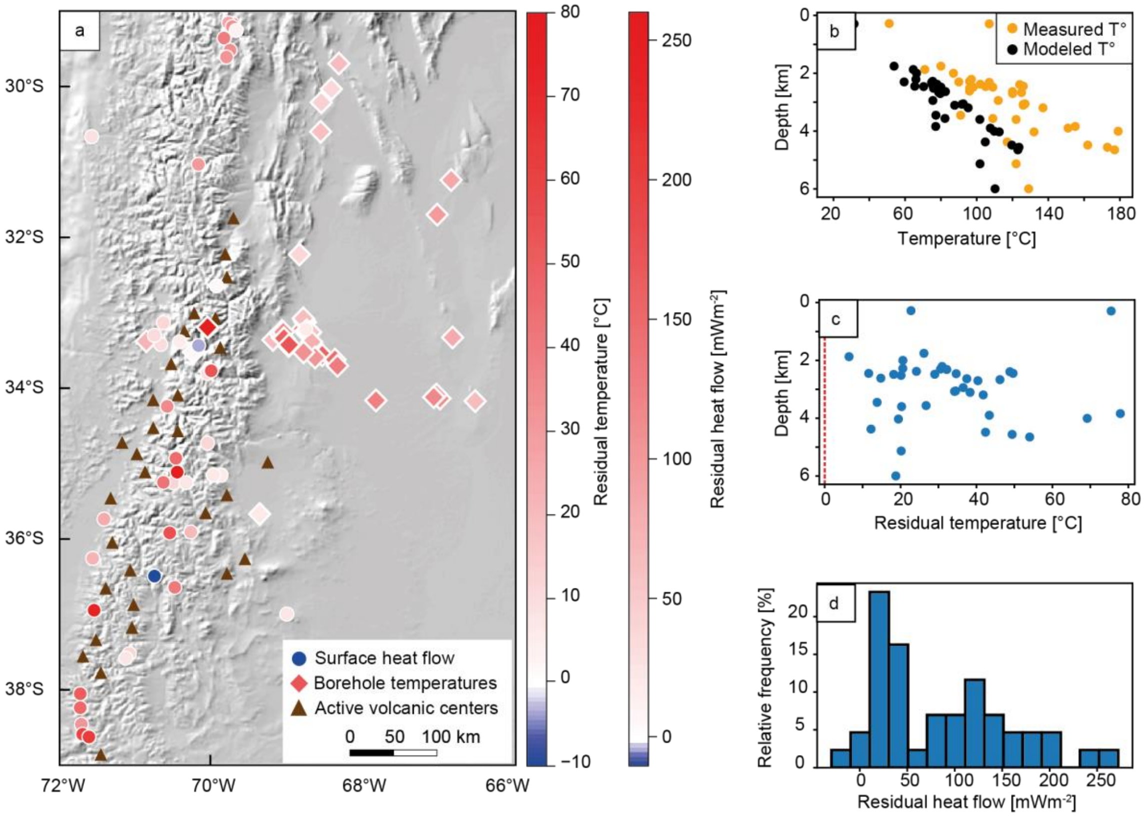

Figure B.13: Comparison between thermal measurements (Collo et al., 2018; Hamza & Muñoz, 1996; Lucazeau, 2019; Uyeda & Watanabe, 1982) and results from the model with a lower boundary condition derived from a linear gradient of 5°C km^{-1} (Syracuse et al., 2010). (a) residual temperature and residual heat flow, defined as the difference between measured and modeled values, at the location of the measurements. Triangles show the location of active volcanic centers; (b) comparison between measured (orange) and modeled (black) temperatures v$_s$. depth; (c) residual temperature v$_s$. depth; and (d) histogram of residual heat flow.

Appendix C: Rheological modelling

C.1 Calculation of Byerlee‘s friction coefficient

Byerlee‘s friction coefficient (f_f) depends on the faulting regime (thrusting, strike-slip or normal faulting). For thrusting, f_f is expressed as:

$$f_f = R - 1 \text{ (C.1)}$$

where R depends on the internal friction angle Φ as:

$$R = \left(\sqrt{1 + \Phi^2} - \Phi\right)^{-2} \text{ (C.2)}$$

R can also be expressed in terms of internal friction coefficient μ_f ($\mu_f = \tan\Phi$) as:

$$R = \left(\sqrt{1 + (\mathrm{atan}\mu_f)^2} - \mathrm{atan}\mu_f\right)^{-2} \text{(C.3)}$$

C.2 Selection of rheological properties

Secondary creep parameters were chosen from studies based on experimental rock mechanics (Afonso & Ranalli, 2004; Gleason & Tullis, 1995; Goetze & Evans, 1979; Hirth & Kohlstedt, 1996; Ranalli & Murphy, 1987; Wilks & Carter, 1990). Since parameters from different authors for similar lithologies can differ in the literature, we compared synthetic yield strength envelopes for a given strain rate in order to visually inspect the relative strength of different compositions (Fig. C.1). In the selection of rheological properties, we ensured that mafic layers are mechanically stronger than felsic layers and, that the slab is mechanically stronger than the continental lithospheric mantle.

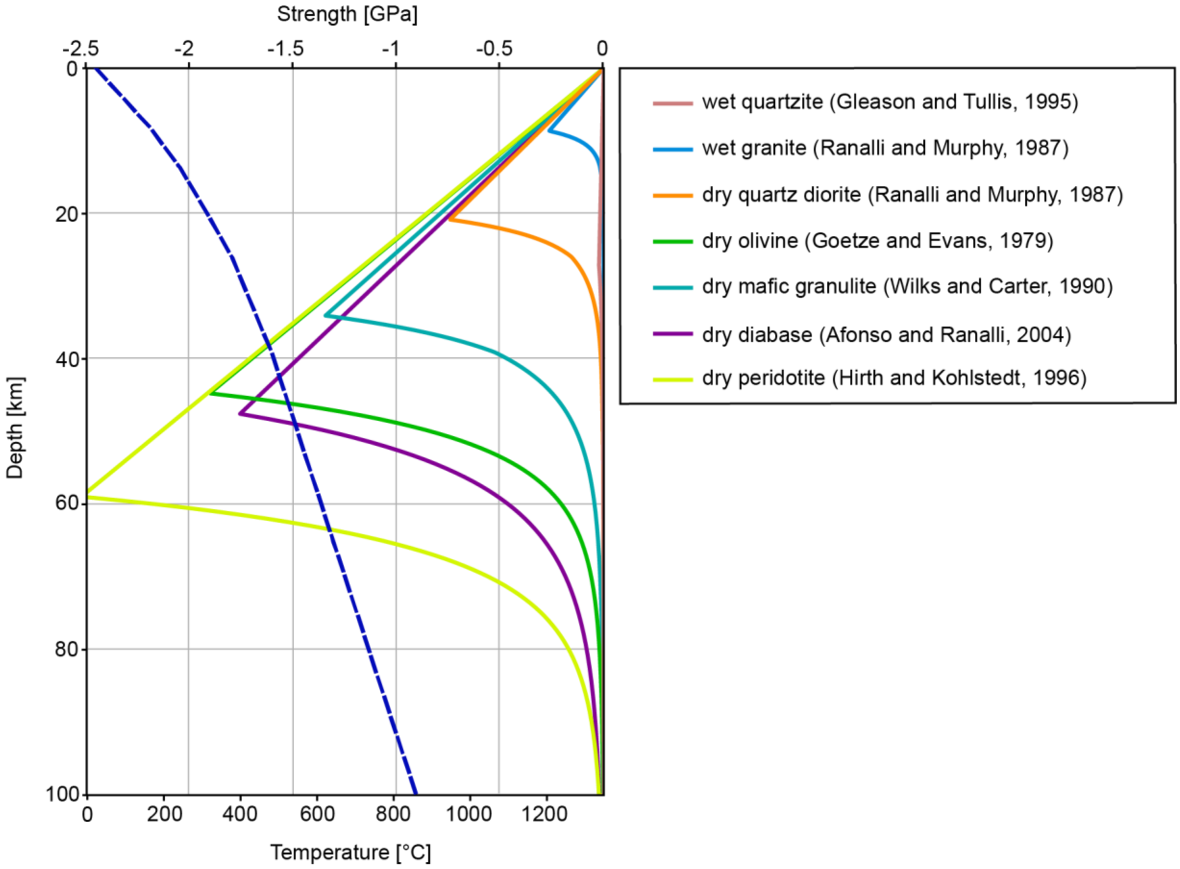

Figure C.1: synthetic yield strength envelopes for the different rock-type rheologies assigned to the model units and described in Table 5.1, considering a uniform strain rate of 6.5e-16 s^{-1} and the geotherm from McKenzie et al. (2005).

C.3 Calculation of strain rate

Giambiagi et al. (2012) computed the amount of horizontal shortening for different profiles across the northern, the central and southern sector of the SCA. Given the length of the profiles (L = 90 km) and the largest amount of shortening (L-Lo, Table C.1), we calculated the strain taking place in each sector as:

$$\varepsilon = \frac{(L-Lo)}{Lo} \quad \text{(C.4)}$$

Using the average strain of the area (0.28), we then calculated the strain rate as:

$$\dot{\varepsilon} = \frac{\varepsilon}{t} \quad \text{(C.5)}$$

where t is 18 Ma, corresponding to the set-up of the main pulse of deformation in the SCA. From eq. C.5, the resulting strain rate for the SCA is 4.93e-16s^{-1}.

Table C.1: Horizontal shortening in the SCA from Giambiagi et al. (2012) and strain used to calculate the reference strain rate for the rheology modeling

Sector	**Largest horizontal Shortening [km]**	**Strain ε**
Northern (33°30'-34°40')	55	0.38
Central (34°40'-35°20')	33	0.26
Southern (35°30'-36°10')	23	0.20
Mean		0.28

Alternatively, Drewes & Sánchez (2017) calculated the strain rate distribution from GNSS time series of a velocity model of South-America (VEMOS2017). Figure C.2 depicts the frequency distribution of strain rate extracted from the model by Drewes & Sánchez (2017). The average strain rate derived from this model is 6.5e-16 s^{-1}. Given the consistency in terms of order of magnitude between the strain rate obtained from Giambiagi et al. (2012) and Drewes & Sánchez (2017), we considered is 6.5e-16 s^{-1} as representative value of the SCA.

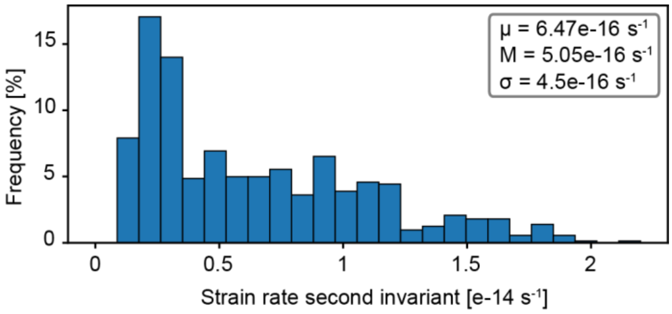

Figure C. 2: frequency distribution of strain rate derived from GNSS velocity model in the SCA (Drewes & Sánchez, 2017). μ = mean, M = median, σ = standard deviation.

C.4 Depth uncertainty of the Slab2 model

The subduction interface was extracted from the subduction zone geometry model Slab2 (Hayes et al., 2018). This model was constrained with different data sources, including active-source seismic data, receiver functions, seismicity catalogs and seismic tomography. The uncertainty of the top surface of the slab (Fig. C.3) was determined by accounting for the vertical uncertainty related to each data source used in the model (see the Supplementary Materials of Hayes et al. (2018) for more details).

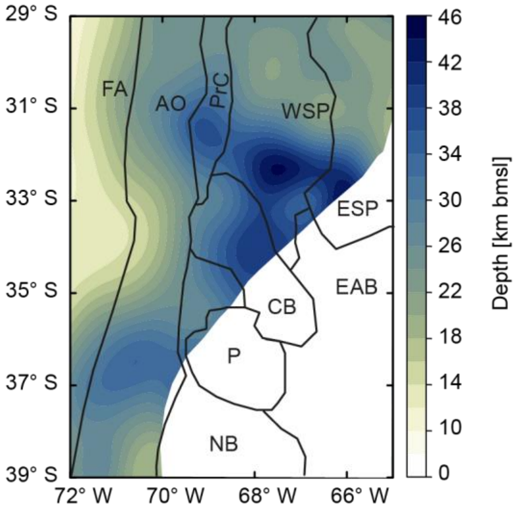

Figure C. 3: Depth uncertainty of the top of the slab from the Slab2 geometry model (Hayes et al., 2018). Domains shown in white are areas where the depth to the top of the slab is larger than 200 km (base of the rheological model). Main morphotectonic provinces are overlain. For abbreviations, see Fig. 5.1.

C.5 Model sensitivity to variations in the strain rate

We tested two end-member models to investigate the effect of strain rate variations on the strength distribution of the lithosphere. We selected 1e-15 s^{-1} and 1e-16 s^{-1} as alternative values for the strain rate. Figure C.4 shows the yield strength envelope for an exemplarily chosen location in the SCA study area showing the variations of differential stress for the models with different strain rate.

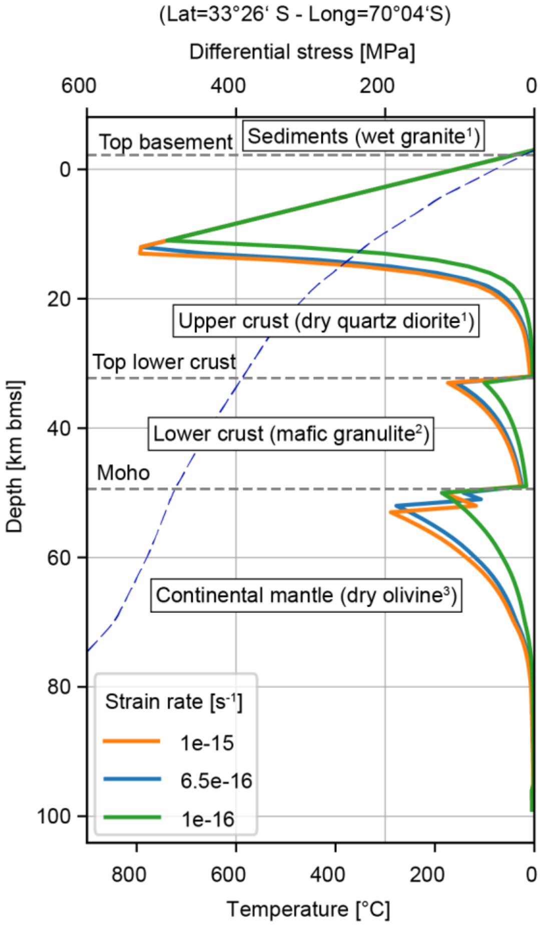

Figure C.4: Yield strength envelopes for an exemplarily chosen location in the SCA study area showing the variations of differential stress for models with different values of strain rate. The corresponding geotherm (derived from the thermal model of Chapter 4) is shown as a blue line. Rock type rheologies applied are based on: [1] Ranalli & Murphy (1987); [2] Wilks & Carter (1990); [3] Goetze & Evans (1979).

C.6. Model sensitivity to variations in the rheology properties of the lower crust

We tested the sensitivity of our results to the alternative parametrization of the lower crustal composition. To that end, we computed the yield strength of the lithosphere assigning a 'dry diabase' composition (Afonso & Ranalli, 2004), instead of 'mafic granulite' composition (Wilks & Carter, 1990). Figure C.5 shows the crustal and lithospheric integrated strength and Figure C.6 displays the differential stress along 4 profiles cutting though the 3D model (cf. Fig. 5.1)

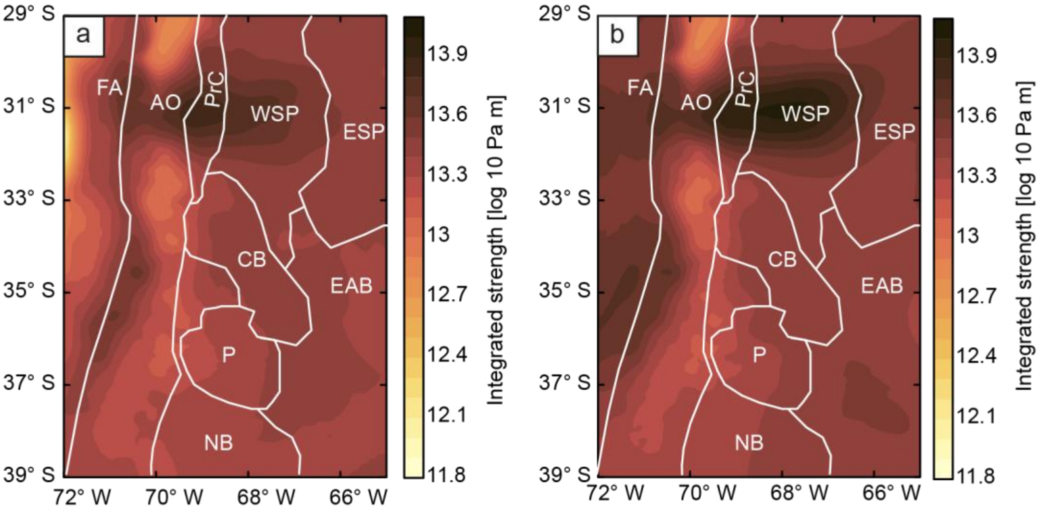

Figure C.5: Integrated strength of (a) continental crust and (b) lithosphere for a model considering dry diabase (Afonso & Ranalli, 2004) as alternative composition for the lower crust (to be compared to the model with a 'mafic granulite'-type lower crust described in Chapter 5.3.1.2). Boundaries of the main morphotectonic provinces are also marked with white lines; for abbreviations see Fig. 5.1.

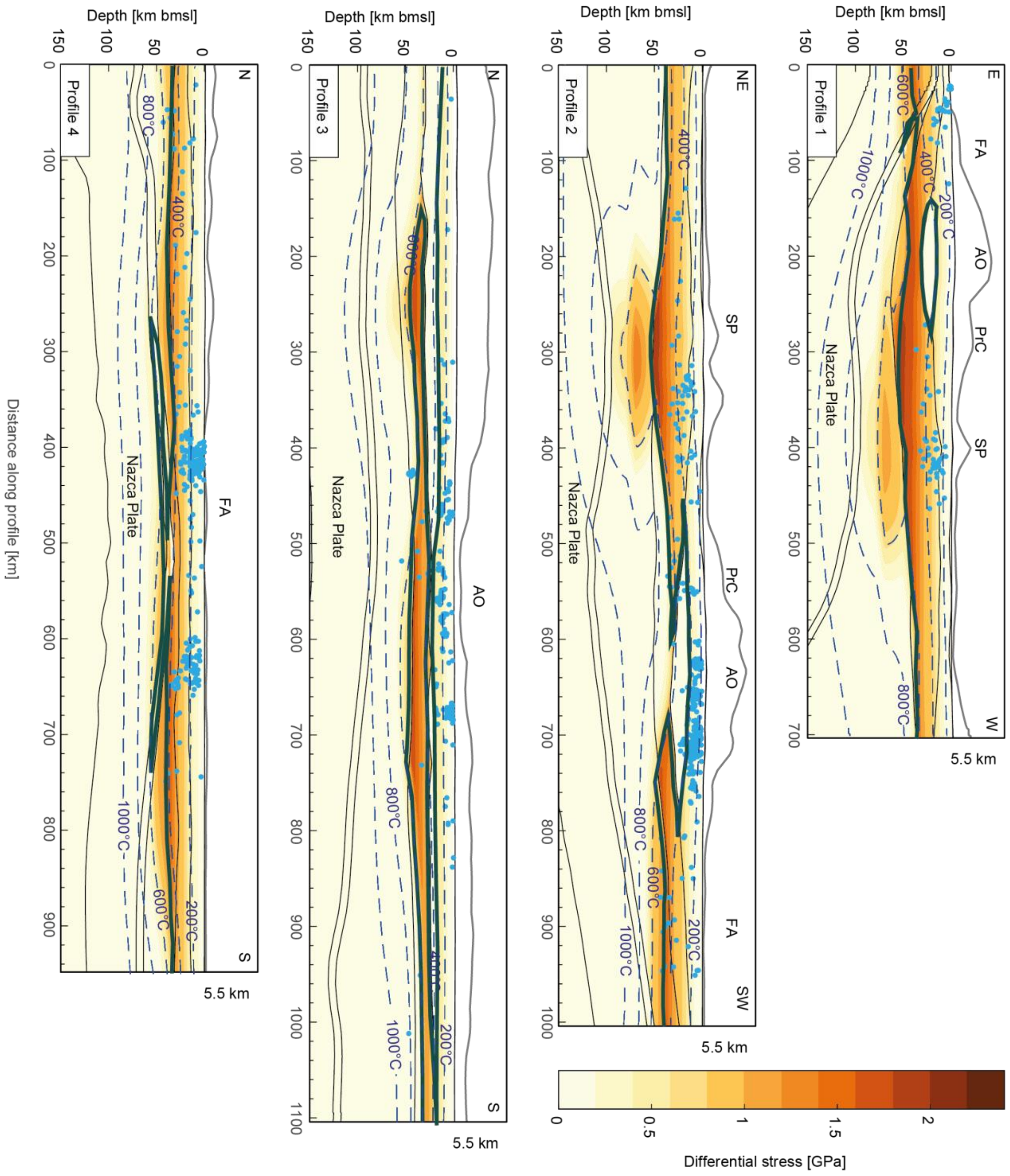

Figure C.6: differential stress along cross-sections displayed in Fig. 5.1, for a model considering dry diabase (Afonso & Ranalli, 2004)as alternative composition for the lower crust (to be compared to the model with a 'mafic granulite'-type lower crust described in Chapter 5.3.1.2). Light-blue dots show the location of hypocenters of seismic events within 5 km distance from each profile (International Seismological Centre, 2021). The isotherms are marked in dashed blue lines. The BDT is shown in thick green line. Black lines show the interfaces of the model layers. For abbreviations of main morphotectonic provinces see Fig. 5.1

C.7 Gravitational potential energy

We calculated the gravitational potential energy from the structural density model of (Rodriguez Piceda et al., 2021) with the gravity modelling software IGMAS+ (Götze & Lahmeyer, 1988; Schmidt et al., 2010). The gravitational potential energy (GPE) at each lithospheric column of the model area is computed as:

$$GPE = G \sum \rho_i {h_i}^2 \quad \text{(C.6)}$$

Where g is the gravity acceleration (9.81 ms^{-2}), ρ_i and h_i are the thickness and the density of each lithospheric model unit, respectively. Figure C.7 shows the GPE for our model area overlain with intraplate seismicity.

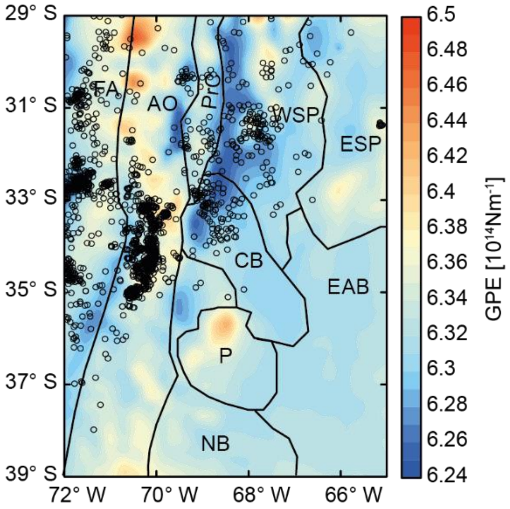

Figure C.7: Gravitational potential energy (GPE) overlain with intraplate seismicity. Boundary between morphotectonic provinces are also shown; for abbreviations see Fig. 5.1.

C.8. Moment magnitude of seismic events

From the ISC seismic catalogue (International Seismological Centre, 2019), 320 events had reported values of moment magnitude (Mw). After analysis of the catalogue completeness using the maximum curvature approach by Wiemer & Wyss (2000) (Fig. C.8), 174 events remained for comparison to the distribution of integrated strength (Fig. C.9).

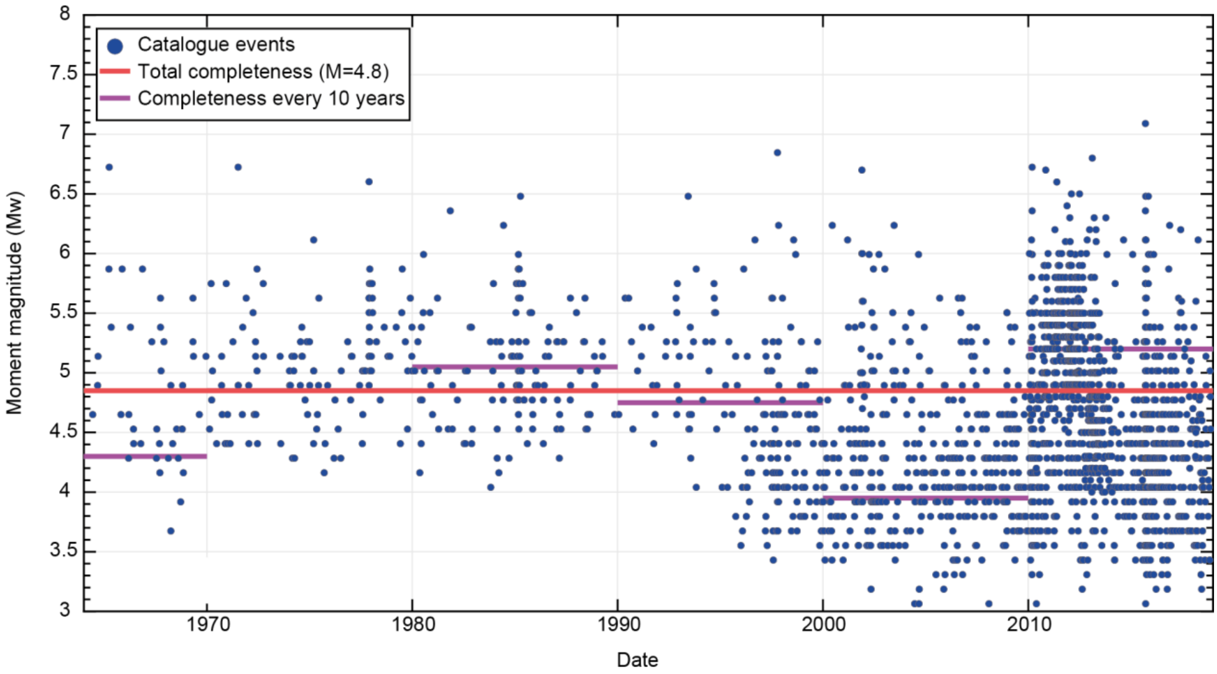

Figure C.8: Analysis of completeness of the ISC seismic catalog for events with reported moment magnitude (Mw) between 1964 and 2018 (inclusive), using the maximum curvature approach by Wiemer and Wyss (2000)

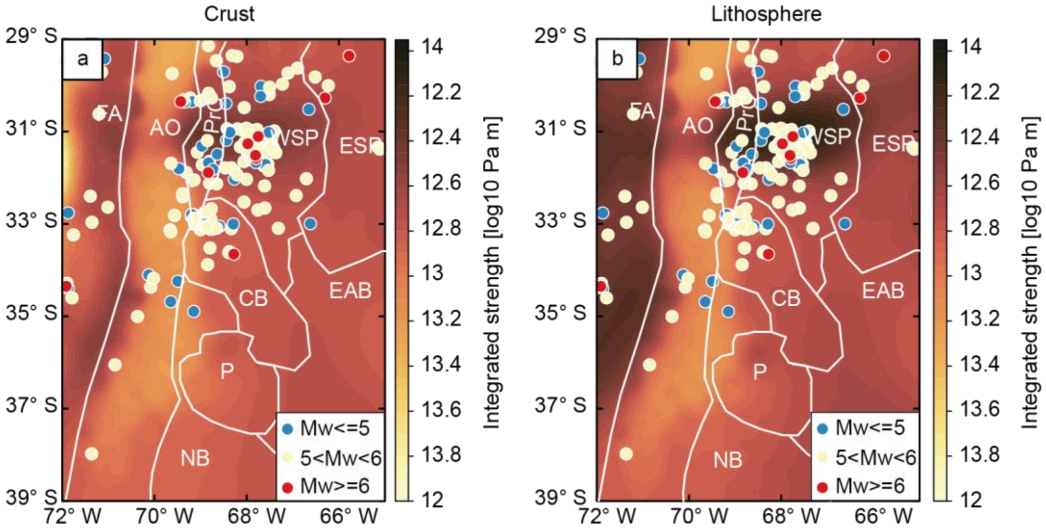

Figure C.9: Integrated strength of (a) continental crust and (b) lithosphere overlain with intraplate seismic events color-coded by moment magnitude Mw. Boundaries of the main morphotectonic provinces are also marked with white lines; for abbreviations see Fig. 5.1.

Appendix D: Slab seismicity

D.1. Calculation of the long-term strength of the lithosphere

To compute the present-day lithospheric strength of the southern Central Andes, we relied on a 3D lithospheric-scale geological model of the study area, which we used to constrain the thickness variations and density distribution for all layers (Rodriguez Piceda et al., 2021). The model extends 1100 km in the N-S direction, 700 km in the E-W direction and 200 km in depth (Fig. 1 of the main text). Geological and geophysical data, including gravity field modelling, seismic tomography, seismic reflection and refraction profiles and petrological data were integrated in order to define the thickness and density of the main lithospheric layers. These layers are, from top to bottom: (1) oceanic and continental sediments; (3) upper continental crystalline crust; (4) lower continental crystalline crust; (5) continental lithospheric mantle (6) shallow oceanic crust; (7) deep oceanic crust; (8) oceanic lithospheric mantle; and (9) oceanic sub-lithospheric mantle.

The temperatures used to compute the lithospheric strength of the southern Central Andes were computed following a workflow as explained in more details in chapter 5. Mantle temperatures between 50 and 200 km were estimated from the conversion of S-wave velocity (Gao et al., 2021) to temperatures using a mineral-physics based approach (Goes et al., 2000; Meeßen, 2017). Complementary, crustal and mantle temperatures down to 50 km bmsl were calculated using the Finite Element simulator GOLEM (Cacace & Jacquey, 2017; Jacquey & Cacace, 2017), assuming steady-state conductive conditions and using as an input the 3D structural model of the southern central Andes (Rodriguez Piceda et al., 2021). Thermal properties were assigned to each layer of the model according to its lithology, which we defined based on gravity-constrained densities (Rodriguez Piceda et al., 2021) and mean P-wave velocities (Araneda et al., 2003; Contreras-Reyes et al., 2008; Marot et al., 2014; Pesicek et al., 2012; Scarfì & Barberi, 2019). We applied fixed boundary conditions along the top and the base of the thermal model. As upper boundary condition, the average surface temperature distribution (Copernicus Climate Change Service (C3S), 2019) was used. The lower boundary condition was set at 50 km and at 5 km below the Moho in the model domain where this interface is deeper than 50 km. The temperature of the lower boundary condition was estimated using the same conversion approach as for the calculation of mantle temperatures.

We computed the long-term lithospheric strength of the lithosphere with a vertical resolution of 1km using the pressure (mean stress) and temperature from the structural and thermal models of the southern Central Andes following the same procedure as outlined in Cacace & Scheck-Wenderoth (2016). According to this approach, static frictional rock behaviour is described by Byerlee's law (Byerlee, 1968) as:

$$\Delta\sigma_{\mathrm{b}} = \mathrm{f_f}\rho_{\mathrm{b}}\mathrm{gz}(1 - \mathrm{f_p}) \text{ (D.1),}$$

where $\Delta\sigma_b$ is the differential stress (yield strength) under a brittle rheology, f_f is the Byerlee's friction coefficient (which is a function of the internal friction coefficient μ_f and the faulting regime), ρ_b is the bulk density, g is the gravitational acceleration, z the depth below topography and f_p is the pore fluid factor (defined as the ratio ρ_f/ρ_b, where ρ_f is the density of the fluid). The f_f of all the layers (except for the top of the slab) was set to 2, this being equivalent to an internal friction coefficient, μ_f, of 0.65 and accounting for the overall convergent regime in the study area. The f_p of these layers was set to 0.36, which is indicative of near hydrostatic conditions. For the uppermost oceanic crustal layer, in order to represent the mèlange at the subduction channel (Vannucchi et al., 2008), Byerlee's friction coefficient and pore fluid factor were set to 0.03 and 0, respectively. These values are consistent with an internal friction coefficient μ_f of 0.015 (Sobolev et al., 2006).

With increasing temperature and pressure, the mechanical behavior of the lithosphere is described by dislocation creep for differential stresses < 200 MPa, while by low-temperature plasticity as parametrized in Dorn's law for differential stresses greater than 200 MPa. The equations that describe dislocation creep (eq. D.2) and low temperature plasticity (eq. D.3) are:

$$\Delta\sigma_{\mathrm{b}} = \left(\frac{\dot{\varepsilon}}{A_p}\right)^{\frac{1}{n}} \exp\left(\frac{Q_p}{nRT}\right) \text{ (D.2)}$$

$$\Delta\sigma_{\mathrm{d}} = \sigma_D\left(1 - \left[-\frac{RT}{Q_D} ln\frac{\dot{\varepsilon}}{A_D}\right]^{\frac{1}{2}}\right) \text{ (D.3)}$$

where $\Delta\sigma_b$ is the ductile yield strength, $\dot{\varepsilon}$ the reference strain rate, A_p the pre-exponential scaling factor for dislocation creep, n the power law exponent, Q_p the activation energy, T the temperature, R is the universal gas constant ($R = 8.314\ JK^{-1}mol^{-1}$), σ_D the Peierls critical stress, Q_D the Dorn activation energy ($Q_D = 5.35e5\ Jmol^{-1}$) and A_D the Dorn's law strain rate ($A_D = 5.7e11\ s^{-1}$). Constant rheological properties were assigned for each model layer according to its lithology(Afonso & Ranalli, 2004; Gleason & Tullis, 1995; Goetze & Evans, 1979; Hirth & Kohlstedt, 1996; Ranalli, 1995; Ranalli & Murphy, 1987; Wilks & Carter, 1990) (Table D.1).

To the uppermost oceanic crustal layer, we assign a ‘weak quartzite rheology’ according to the weak mechanical behavior of the tectonic mélange at the subduction channel. $\dot{\varepsilon}$ was set to 6.5e-16 s^{-1} for all the layers (except for the uppermost oceanic crustal layer), which is consistent with the amount of shortening produced in the southern Central Andes during the last 18 Ma (Giambiagi et al., 2012) and with GNSS measurements (Drewes & Sánchez, 2017)

Table D.1: Rheological properties of the model units

			Dislocation creep parameters			Frictional parameters		
Model Layer	**Prevailing lithology**	**Type rheology**	**Activation enthalpy Q [$Jmol^{-1}$]**	**n**	**Pre-exponential factor [$Pa^{-n} s^{-1}$]**	**Pore-fluid factor f_f**	**Byerlee's friction coefficient f_f**	**Bulk Density [kgm^{-3}][7]**
Oceanic/Continental sediments	Siliciclastic	wet granite[1]	1.37e5	1.9	7.94e-16	0.36	2	2300/2400
Upper crust	Dioritoid	Dry quartz diorite[1]	2.19e5	2.4	5.02e-18	0.36	2	2800
Lower crust	Mafic granulite	Dry mafic granulite[2]	4.45e5	4.2	8.83e-22	0.36	2	3100
Continental lithospheric mantle/oceanic sub-lithospheric mantle	Moderately depleted lherzolite	Dry Olivine[3]	5.10e5	3	7.00e-14	0.36	2	3340
Shallow oceanic crust (weak)	Melange (serpentinites, serpentinized peridotites, metasediments)	Wet quartzite[4]	2.23e5	4	1.00e-28	0	0.03	2900
Shallow oceanic crust (strong)	Basalt	Dry diabase[5]	4.85e5	4.7	5.05e-28	0.36	2	2900
Deep oceanic crust	Eclogite	Dry diabase[5]	4.85e5	4.7	5.05e-28	0.36	2	3200
Oceanic lithospheric mantle	Harzburgite	Dry peridotite[6]	5.35e5	3.5	5.01e-17	0.36	2	3360

[1] Ranalli & Murphy (1987); [2] Wilks & Carter (1990); [3] Goetze & Evans (1979); [4] Gleason & Tullis (1995), quartzite weakened by increasing pre-exponential factor A by 10 times (Sobolev & Babeyko, 2005) ;[5] Afonso & Ranalli (2004); [6] Hirth & Kohlstedt (1996); [7] Rodriguez Piceda et al. (2021)

D.2. v_p/v_s and hydration of the mantle

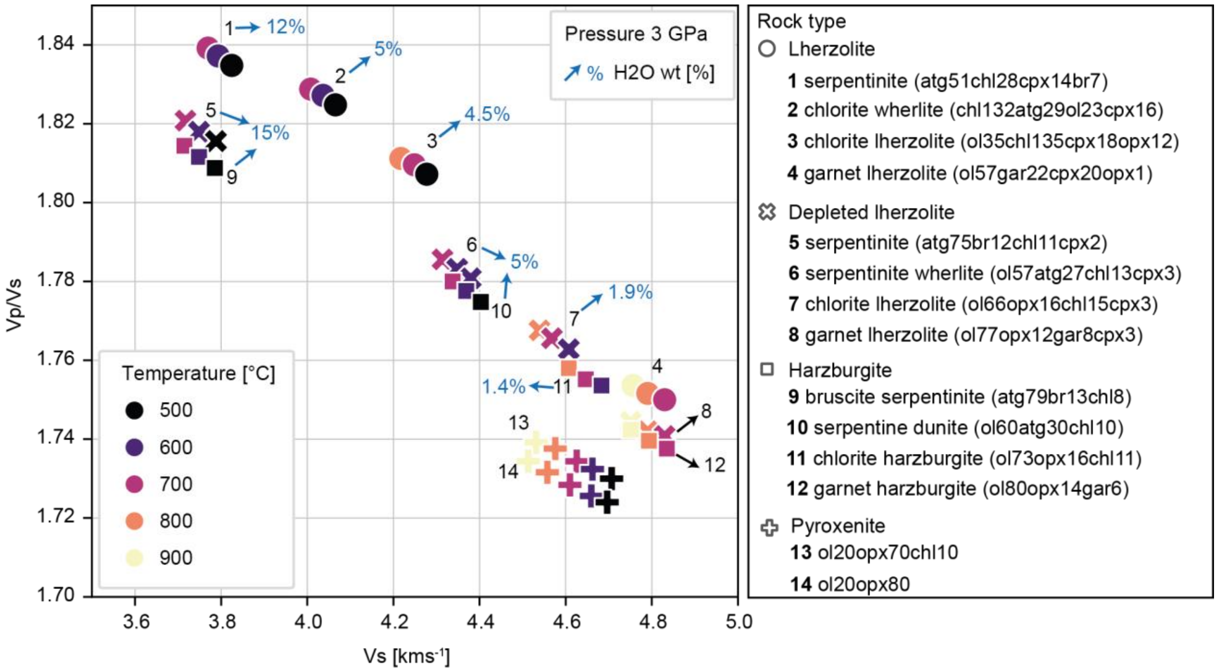

Figure D. 1: Predicted S-wave velocities (v_s) vs. P-wave to S-wave ratio (v_p/v_s) and corresponding state of hydration for common mantle peridotitic rocks stable at 3 GPa and temperatures from 500°C to 900°C (Hacker et al., 2003; Linkimer et al., 2020)

D.3 Calculation of curvature of the slab

For a given surface σ, the intersection between σ and any plane containing the normal n to the surface at a point P is represented by the curve Γ (Fig. D.2).

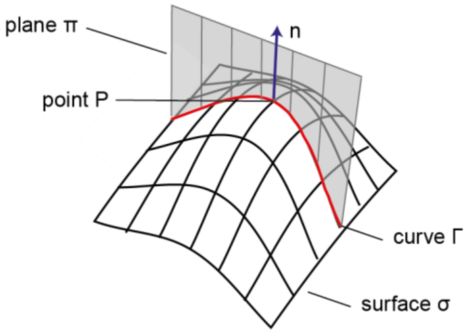

Figure D.2: schematic diagram of the curvature of a surface

Γ has a curvature γ and a radius of curvature R, which is defined as:

$$R = \frac{1}{\gamma} \text{ (D.4)}$$

There are infinite planes that contains the normal n. However, there is only one direction that has the absolute maximum radius of curvature and only one direction that has the absolute minimum. These curvatures are called *principal curvatures* k_1 and k_2 (maximal and minimal curvatures, respectively). The Euler's formula describes the relationship between the radius of curvature R in the direction of the plane and the principal curvatures:

$$\frac{1}{R} = \frac{sin^2\theta}{R_1} + \frac{cos^2\theta}{R_2} \text{ (D.5)},$$

where θ is the angle is the angle formed by the plane π that contains the normal n and the plane π_2 which corresponds to the maximum principal curvature; R_2 is the maximum radius of curvature and R_1 the minimum radius of curvature. The *mean curvature* was calculated using the Petrel software (Schlumberger, 2011) as:

$$H = \frac{1}{R_n} = \frac{2}{R_1 + R_2} \ (D.6)$$

Appendix E: Discussion

E.1 Strength sensitivity to different seismic tomography

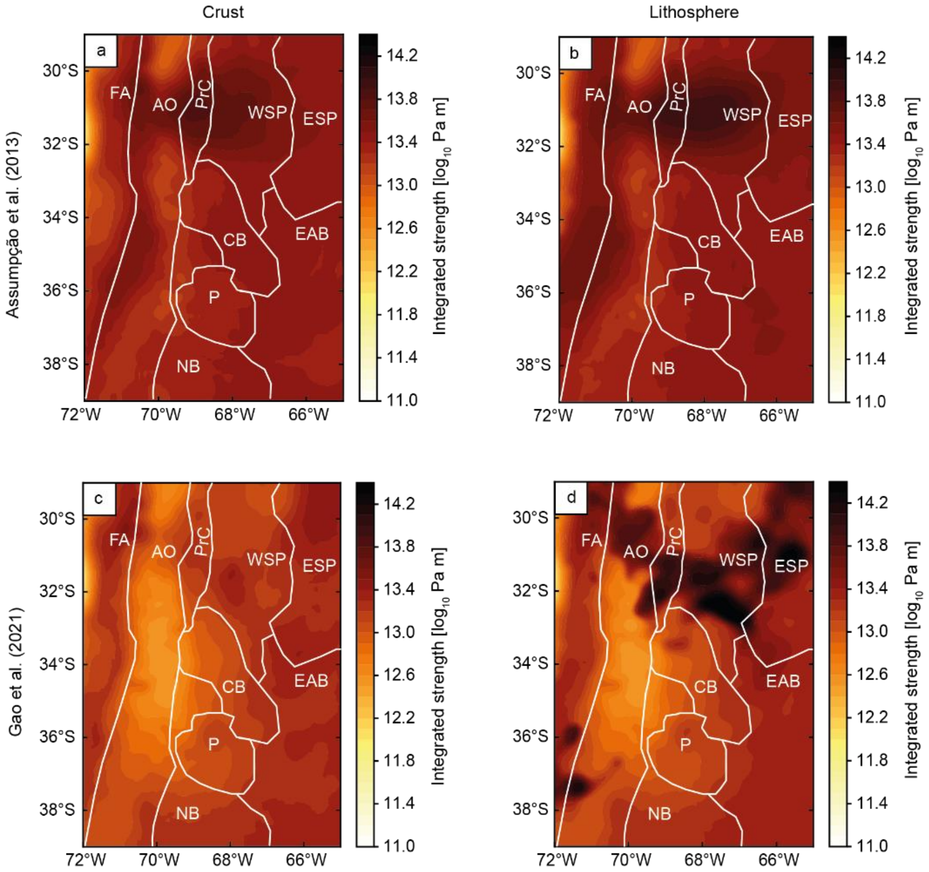

Figure E.1: Integrated strength of continental crust and lithosphere using the temperatures derived from the seismic tomography of (a-b) Assumpção et al. (2013) and (c-d) Gao et al. (2021b). Key tectonic features are overlain (see Fig. 4.1 for abbreviations)

E.2 Seismic tomography by Gao et al. (2021b)

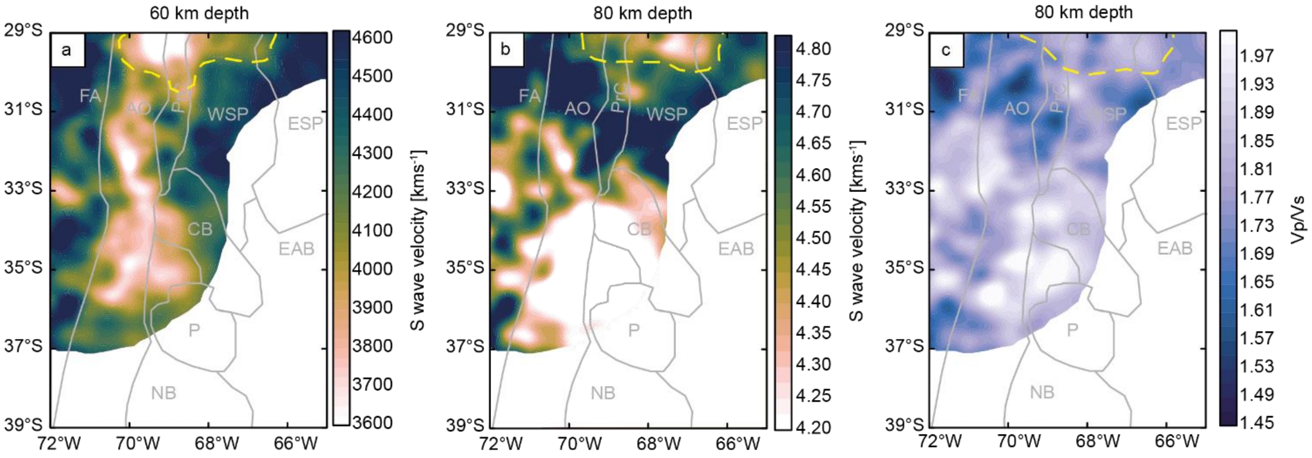

Figure E.2: Results from seismic tomography of Gao et al. (2021b): v_s distribution at depths of (a) 60 km and (b) 80 km; (c) v_p/v_s ratio distribution at 90 km depth. The low v_s -high v_p/v_s anomaly in the northern foreland is enclosed by the yellow dashed line. Boundaries of the main morphotectonic provinces are also marked with grey lines; for abbreviations see Fig. 4.1.

E.3 Brittle-ductile transition

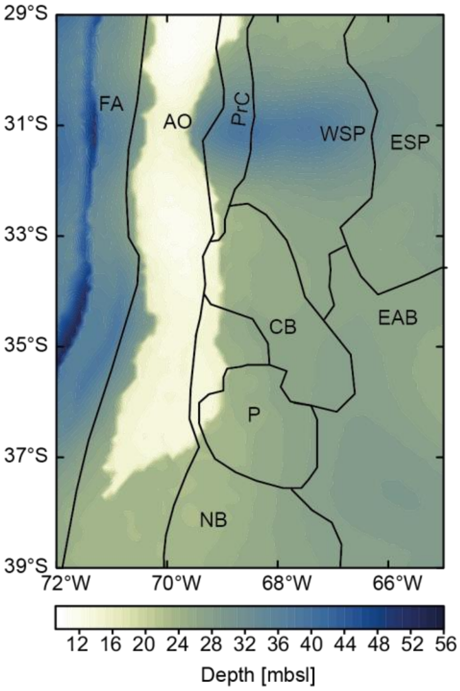

Figure E.3: Depth of the brittle-ductile transition obtained from rheological modelling presented in Chapter 4. Boundaries of the main morphotectonic provinces are also marked with black lines; for abbreviations see Fig. 4.1.

E.4 Global models of LAB depth

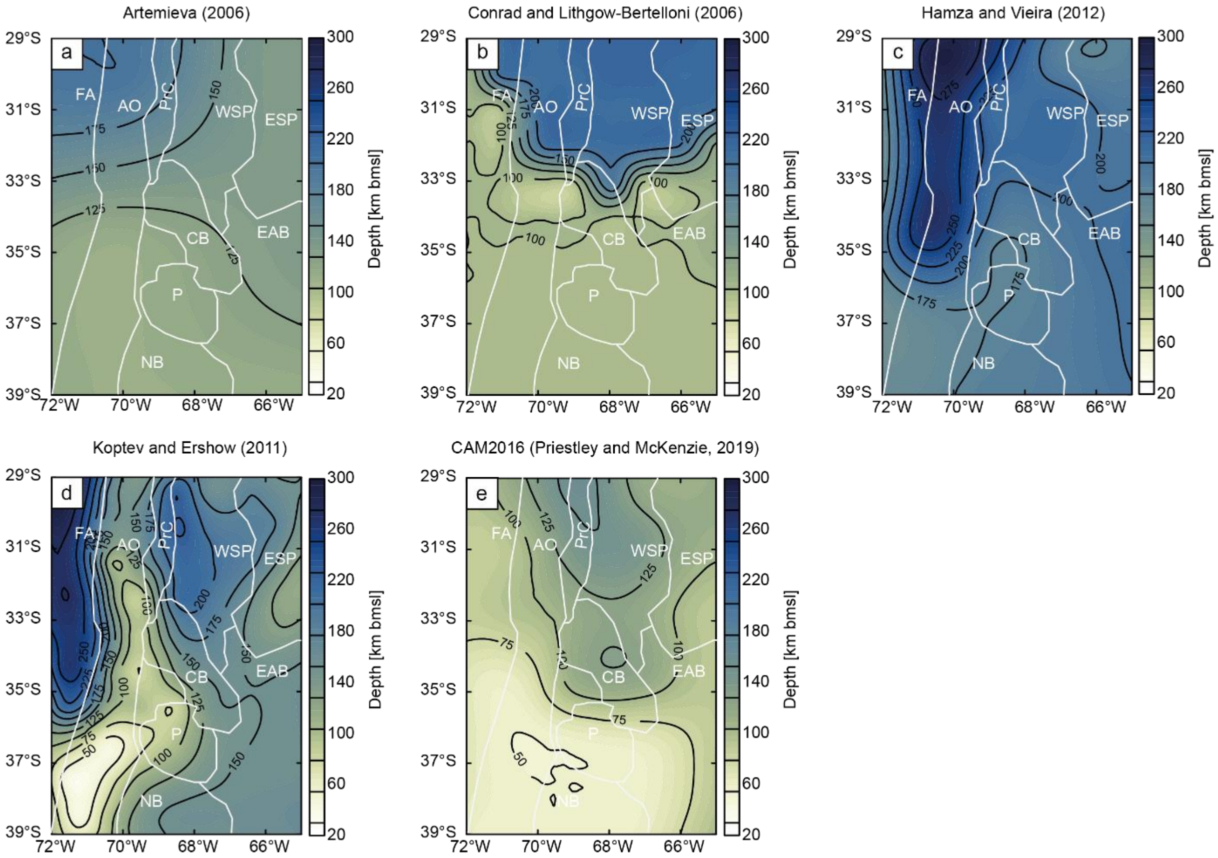

Figure E.4: Depth of the lithospheric-asthenospheric boundary (LAB) from the models of (a) (Artemieva, 2006), (b) (Conrad & Lithgow-Bertelloni, 2006), (c) Hamza & Vieira (2012), (d) Koptev & Ershov (2011) and (c) CAM 2016 (Priestley et al., 2018). Boundaries of the main morphotectonic provinces are also marked with black lines; for abbreviations see Fig. 4.1.

E.5 Strength profiles

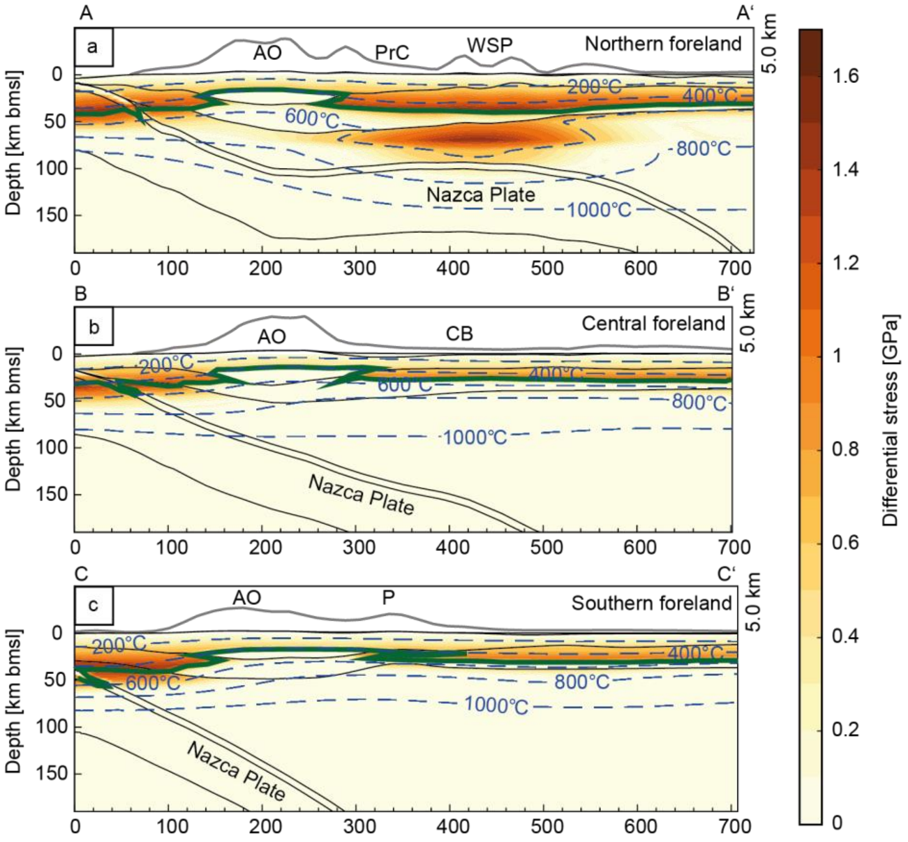

Figure E.5: differential stress computed along cross-sections indicated in Figure 6.1. The isotherms are marked in dashed blue lines. The BDT is shown in a thick green line. Black lines show the interfaces of the model layers. Topographic elevations are shown on top of each profile with a vertical exaggeration of 10:1. For abbreviations of main morphotectonic provinces see Fig. 6.1.

Software and data availability

Python 2.7 and 3.7 were used for data analysis and plotting (Van Rossum & Drake, 2009; Van Rossum & Drake, 1995), including the packages Matplotlib (Hunter, 2007), NumPy (Harris et al., 2020), pandas (McKinney, 2010) and Scipy (Virtanen et al., 2020). MATLAB R2020a (Mathworks Inc.) was used for plotting and analysis of the seismic catalogue completeness. Surfer® *(Golden Software, LLC),* Adobe® Illustrator *(Adobe Inc.)* and QGIS (QGIS Development Team, 2009) were used for plotting. ParaView was used for data analysis (Ahrens et al. 2005). Pyrocko was used for retrieving of the seismic catalogues (The pyrocko Developers, 2018).

Seismic catalogues were taken from the International Seismological Centre (http://www.isc.ac.uk/iscbulletin/) and the Global Centroid Moment Catalog (https://www.globalcmt.org/CMTsearch.html). The structural, thermal and rheological models presented in chapters 3, 4, 5 and 6 and the seismic tomography used in Chapter 6 can be accessed through GFZ data services (https://dataservices.gfz-potsdam.de/portal/).

Acknowledgements

Doing a PhD has been far from lonely. Here I would like to dedicate some words to all the people that helped me on both sides of the Atlantic to get to the place I am today.

This thesis is part of the StRATEGy project funded by the DFG (Deutsche Forschungsgemeinschaft) and the federal state of Brandenburg. My sincere thanks to all the people in Germany and Argentina who granted and secure the funding to achieve this work; especially to Manfred Strecker, Verónica Torres Acosta and Graciela Da Poian. Many thanks to the StRATEGy PhD students, with whom I enjoyed our activities together, including the field trip to Argentina, seminars, workshops and our meetings outside of the office playing Laser Tag or drinking Glühwein in the Christmas Market. Special thanks to Federico Ibarra, Claudia Prezzi and Matias Barrionuevo, who shared with me their experience on modelling and about the Central Andes.

To my supervisors Leni Scheck-Wenderoth and Manfred Strecker. It was a great pleasure to work along your side. To Leni, for always encouraging me to follow my research interests and for helping me to get back on track in the moments when '*my nose was in the canteen and my feet were still in the office*'. Thank you also for being such a good leader and for fostering the communication and collaboration between the members of our group. You made us feel like a big international family. To Manfred, for his very constructive feedback in multiple stages of my project and to share with me his profound knowledge about the Andes. I am deeply grateful for all your support.

Big thanks to the (past and current) members of the Section 4.5 (Basin Modeling) at the GFZ: Ajay, Angela, Antoine, Cameron, Christian, Denis, Ershad, Judith, Lew, Mauro, Maria Laura, Max, Naiara, Nora and Vivien. I enjoyed every moment up in the hill and outside the office. Special thanks to Judith Bott and Maria Laura Gomez Dacal who mentored me during these years and helped me to become a better researcher; to Mauro Cacace for having the patience to assist me with the numerical modelling part; and to Denis Anikiev, for all your technical support, from using MATLAB to every kind of hardware problems. I would also like to thank other people that has advised me and/or provided me with part of the data that was used in this dissertation: Hajo Götze, Sabine Schmidt, Christian Meeßen, Marcelo Assumpção, Mei Feng, Yajian Gao, Laura Giambiagi and Frederik Tilmann.

Most certainly, I could have not gotten here if it was not for the support of my friends and family of both continents. To the friends I met in Germany: Derek, Michele, Nikos, Camille, Roman and Sara. Thank you for making my days brighter in the often rough German weather. To my old friends of Argentina, including the ones of the North, my former partner Tomás and my beloved friends Wanda, Sofia, Daniela and Luana, for being there in different stages of my PhD. To my family, for encouraging me to begin this adventure abroad: my mother Analia, my siblings Victoria and Ignacio and my grandparents Beatriz and Edgardo, my aunt, my cousin, and my father Gustavo. And finally, thanks to my partner Michael, to walk with me this road and to support me in every dimension I can think of: from sharing your passion on Geodynamics, believing in me and, importantly, encouraging me to assert myself.

¡Muchas gracias!

References

Aceñolaza, F. G., & Toselli, A. J. (1976). Consideraciones estratigráficas y tectónicas sobre el Paleozoico Inferior del noroeste argentino (pp. 755–764). Presented at the 2 Congreso Latinoamericano de Geología, Buenos Aires.

Afanasiev, M., Boehm, C., Van Driel, M., Krischer, L., Rietmann, M., May, D., et al. (2019). Modular and flexible spectral-element waveform modelling in two and three dimensions. *Geophysical Journal International*, *216*(3), 1675–1692.

Afonso, J. C., & Ranalli, G. (2004). Crustal and mantle strengths in continental lithosphere: is the jelly sandwich model obsolete? *Tectonophysics*, *394*(3–4), 221–232. https://doi.org/10.1016/j.tecto.2004.08.006

Alasino, P. H., Casquet, C., Pankhurst, R. J., Rapela, C. W., Dahlquist, J. A., Galindo, C., et al. (2016). Mafic rocks of the Ordovician Famatinian magmatic arc (NW Argentina): New insights into the mantle contribution. *Geological Society of America Bulletin*, *128*(7–8), 1105–1120. https://doi.org/10.1130/B31417.1

Allmendinger, R., Figueroa, D., Snyder, D., Beer, J., Mpodozis, C., & Isacks, B. (1990). Foreland shortening and crustal balancing in the Andes at 30 S latitude. *Tectonics*, *9*(4), 789–809. https://doi.org/10.1029/TC009i004p00789

Allmendinger, R. W. (1986). Tectonic development, southeastern border of the Puna Plateau, northwestern Argentine Andes. *GSA Bulletin*, *97*(9), 1070–1082. https://doi.org/10.1130/0016-7606(1986)97<1070:TDSBOT>2.0.CO;2

Allmendinger, R. W., & Judge, P. A. (2014). The Argentine Precordillera: A foreland thrust belt proximal to the subducted plate. *Geosphere*, *10*(6), 1203–1218. https://doi.org/10.1130/GES01062.1

Allmendinger, R. W., Ramos, V. A., Jordan, T. E., Palma, M., & Isacks, B. L. (1983). Paleogeography and Andean structural geometry, northwest Argentina. *Tectonics*, *2*(1), 1–16. https://doi.org/10.1029/TC002i001p00001

Allmendinger, R.W., & Gubbels, T. (1996). Pure and simple shear plateau uplift, Altiplano-Puna, Argentina and Bolivia. *Tectonophysics*, *259*(1–3), 1–13. https://doi.org/10.1016/0040-1951(96)00024-8

Alonso, J., Rodríguez Fernández, L., García-Sansegundo, J., Heredia, N., Farias, P., & Gallastegui, J. (2005). Gondwanic and Andean structure in the Argentine central Precordillera: the Río San Juan section revisited (pp. 36–39). Presented at the 6th International Symposium on Andean Geodynamics. IRD Editions (Institut de Recherche pour le Développement), Extended Abstracts.

Alvarado, P., Beck, S., & Zandt, G. (2007). Crustal structure of the south-central Andes Cordillera and backarc region from regional waveform modelling. *Geophysical Journal International*, *170*(2), 858–875. https://doi.org/10.1111/j.1365-246X.2007.03452.x

Alvarado, P., Beck, S., Zandt, G., Araujo, M., & Triep, E. (2005). Crustal deformation in the south-central Andes backarc terranes as viewed from regional broad-band seismic waveform modelling. *Geophysical Journal International*, *163*(2), 580–598. https://doi.org/10.1111/j.1365-246X.2005.02759.x

Alvarado, P., Pardo, M., Gilbert, H., Miranda, S., Anderson, M., Saez, M., & Beck, S. (2009). Flat-slab subduction and crustal models for the seismically active Sierras Pampeanas region of Argentina. In Suzanne Mahlburg Kay, V. A. Ramos, & W. R. Dickinson, *Backbone of the Americas: Shallow Subduction, Plateau Uplift, and Ridge and Terrane Collision*. Geological Society of America. https://doi.org/10.1130/2009.1204(12)

Álvarez, O., Gimenez, M., Braitenberg, C., & Folguera, A. (2012). GOCE satellite derived gravity and gravity gradient corrected for topographic effect in the South Central Andes region: GOCE derivatives in the South Central Andes. *Geophysical Journal International*, *190*(2), 941–959. https://doi.org/10.1111/j.1365-246X.2012.05556.x

Amante, C., & Eakins, B. (2009). *ETOPO1 1 Arc-Minute Global Relief Model: Procedures, Data Sources and Analysis* (NOAA Technical Memorandum NESDIS NGDC-24). National Geophysical Data Center, NOAA. Retrieved from doi:10.7289/V5C8276M

Ammirati, J.-B., Alvarado, P., Perarnau, M., Saez, M., & Monsalvo, G. (2013). Crustal structure of the Central Precordillera of San Juan, Argentina (31°S) using teleseismic receiver functions. *Journal of South American Earth Sciences*, *46*, 100–109. https://doi.org/10.1016/j.jsames.2013.05.007

Ammirati, J.-B., Alvarado, P., & Beck, S. (2015). A lithospheric velocity model for the flat slab region of Argentina from joint inversion of Rayleigh wave phase velocity dispersion and teleseismic receiver functions. *Geophysical Journal International*, *202*(1), 224–241. https://doi.org/10.1093/gji/ggv140

Ammirati, J.-B., Pérez Luján, S., Alvarado, P., Beck, S., Rocher, S., & Zandt, G. (2016). High-resolution images above the Pampean flat slab of Argentina (31–32°S) from local receiver functions: Implications on regional tectonics. *Earth and Planetary Science Letters*, *450*, 29–39. https://doi.org/10.1016/j.epsl.2016.06.018

Ammirati, J.-B., Venerdini, A., Alcacer, J. M., Alvarado, P., Miranda, S., & Gilbert, H. (2018). New insights on regional tectonics and basement composition beneath the eastern Sierras Pampeanas (Argentine back-arc region) from seismological and gravity data. *Tectonophysics*, *740–741*, 42–52. https://doi.org/10.1016/j.tecto.2018.05.015

An, M., Wiens, D. A., Zhao, Y., Feng, M., Nyblade, A., Kanao, M., et al. (2015). Temperature, lithosphere-asthenosphere boundary, and heat flux beneath the Antarctic Plate inferred from seismic velocities. *Journal of Geophysical Research: Solid Earth*, *120*(12), 8720–8742. https://doi.org/10.1002/2015JB011917

Anderson, M., Alvarado, P., Zandt, G., & Beck, S. (2007). Geometry and brittle deformation of the subducting Nazca Plate, Central Chile and Argentina. *Geophysical Journal International*, *171*(1), 419–434. https://doi.org/10.1111/j.1365-246X.2007.03483.x

Anikiev, D., Cacace, M., Bott, J., Gomez Dacal, M. L., & Scheck-Wenderoth, M. (2020). Influence of Lithosphere Rheology on Seismicity in an Intracontinental Rift: The Case of the Rhine Graben. *Frontiers in Earth Science*, *8*, 492. https://doi.org/10.3389/feart.2020.592561

Araneda, M., Asch, G., Bataille, K., Bohm, M., Bruhn, C., Giese, P., et al. (2003). A crustal model along 39° S from a seismic refraction profile-ISSA 2000. *Revista Geológica de Chile*, *30*(1), 83–101. http://dx.doi.org/10.4067/S0716-02082003000100006

Armijo, R., Rauld, R., Thiele, R., Vargas, G., Campos, J., Lacassin, R., & Kausel, E. (2010). The West Andean Thrust, the San Ramón Fault, and the seismic hazard for Santiago, Chile. *Tectonics*, *29*(2). https://doi.org/10.1029/2008TC002427

Armijo, R., Lacassin, R., Coudurier-Curveur, A., & Carrizo, D. (2015). Coupled tectonic evolution of Andean orogeny and global climate. *Earth-Science Reviews*, *143*, 1–35. https://doi.org/10.1016/j.earscirev.2015.01.005

Arnous, A., Zeckra, M., Venerdini, A., Alvarado, P., Arrowsmith, R., Guillemoteau, J., et al. (2020). Neotectonic Activity in the Low-Strain Broken Foreland (Santa Bárbara System) of the North-Western Argentinean Andes (26°S). *Lithosphere*, *2020*(1), 1–25. https://doi.org/10.2113/2020/8888588

Arriagada, C., Ferrando, R., Córdova, L., Morata, D., & Roperch, P. (2013). The Maipo Orocline: A first scale structural feature in the Miocene to Recent geodynamic evolution in the central Chilean Andes. *Andean Geology*, *40*(3), 419–437. http://dx.doi.org/10.5027/andgeoV40n3-a02

Artemieva, I. (2011). *Lithosphere: an interdisciplinary approach*. Cambridge University Press.

Artemieva, I. M. (2006). Global 1°×1° thermal model TC1 for the continental lithosphere: Implications for lithosphere secular evolution. *Tectonophysics*, *416*(1), 245–277. https://doi.org/10.1016/j.tecto.2005.11.022

Assumpção, M., Feng, M., Tassara, A., & Julià, J. (2013). Models of crustal thickness for South America from seismic refraction, receiver functions and surface wave tomography. *Tectonophysics*, *609*, 82–96. https://doi.org/10.1016/j.tecto.2012.11.014

Astini, R. A., & Dávila, F. M. (2004). Ordovician back arc foreland and Ocloyic thrust belt development on the western Gondwana margin as a response to Precordillera terrane accretion. *Tectonics*, *23*(4). https://doi.org/10.1029/2003TC001620

Astini, R.A, Benedetto, J., & Vaccari, N. (1995). The early Paleozoic evolution of the Argentine Precordillera as a Laurentian rifted, drifted, and collided terrane: A geodynamic model. *Geological Society of America Bulletin*, *107*(3), 253–273. https://doi.org/10.1130/0016-7606(1995)107<0253:TEPEOT>2.3.CO;2

Astini, R.A. (2003). Ordovician basins of Argentina. In *Ordovician Fossils of Argentina* (pp. 1–74). Córdoba, Argentina: Univ. Nac. de Córdoba.

Astort, A., Colavitto, B., Sagripanti, L., García, H., Echaurren, A., Soler, S., et al. (2019). Crustal and Mantle Structure Beneath the Southern Payenia Volcanic Province Using Gravity and Magnetic Data. *Tectonics*, *38*(1), 144–158. https://doi.org/10.1029/2017TC004806

Ávila, J. N., Chemale, F., Jr., Mallmann, G., Kawashita, K., & Armstrong, R. A. (2006). Combined stratigraphic and isotopic studies of Triassic strata, Cuyo Basin, Argentine Precordillera. *GSA Bulletin*, *118*(9–10), 1088–1098. https://doi.org/10.1130/B25893.1

Azcuy, C., & Caminos, R. (1987). El Sistema Carbonifero en la Republica Argentina. Diastrofismo. In *El sistema carbonífero en la República Argentina* (pp. 239–251). Córdoba, Argentina: Academia Nacional de Ciencias.

Bahlburg, H. (1990). *The Ordovician basin in the Puna of NW Argentina and N Chile: Geodynamic evolution from back-arc to foreland basin*. Stuttgart, Germany: Schweizerbart Science Publishers. Retrieved from http://www.schweizerbart.de//publications/detail/isbn/9783510500413/Geotekt_Forsch_H_75

Bahlburg, H., & Hervé, F. (1997). Geodynamic evolution and tectonostratigraphic terranes of northwestern Argentina and northern Chile. *GSA Bulletin*, *109*(7), 869–884. https://doi.org/10.1130/0016-7606(1997)109<0869:GEATTO>2.3.CO;2

Bahlburg, H., Vervoort, J. D., Du Frane, S. A., Bock, B., Augustsson, C., & Reimann, C. (2009). Timing of crust formation and recycling in accretionary orogens: Insights learned from the western margin of South America. *Earth-Science Reviews*, *97*(1), 215–241. https://doi.org/10.1016/j.earscirev.2009.10.006

Barazangi, M., & Isacks, B. L. (1976). Spatial distribution of earthquakes and subduction of the Nazca plate beneath South America. *Geology*, *4*(11), 686–692.

Barredo, S. P. (2012). Geodynamic and tectonostratigrafic study of a continental rift: the Triassic Cuyana Basin, Argentina. In *Tectonics—Recent Advances* (Vol. 346, pp. 99–130). Rijeka, Croatia: InTech.

Barrionuevo, M., Liu, S., Mescua, J., Yagupsky, D., Quinteros, J., Giambiagi, L., et al. (2021). The influence of variations in crustal composition and lithospheric strength on the evolution of deformation processes in the southern Central Andes: Insights from geodynamic models. *International Journal of Earth Sciences*. https://doi.org/10.1007/s00531-021-01982-5

Barrows, L., & Barrows, V. (2010). The mechanics of gravity-driven faulting. *Solid Earth Discussions*, *2*(1), 105–144.

Barrows, Larry, & Langer, C. J. (1981). Gravitational potential as a source of earthquake energy. *Tectonophysics*, *76*(3), 237–255. https://doi.org/10.1016/0040-1951(81)90099-8

Bebout, G. E., Scholl, D. W., Stern, R. J., Wallace, L. M., & Agard, P. (2018). Twenty Years of Subduction Zone Science: Subduction Top to Bottom 2 (ST2B-2). *GSA Today*, 4–10. https://doi.org/10.1130/GSATG354A.1

Bellahsen, N., Sebrier, M., & Siame, L. (2016). Crustal shortening at the Sierra Pie de Palo (Sierras Pampeanas, Argentina): near-surface basement folding and thrusting. *Geological Magazine*, *153*(5–6), 992–1012. https://doi.org/10.1017/S0016756816000467

Berckhemer, H., Kampfmann, W., Aulbach, E., & Schmeling, H. (1982). Shear modulus and Q of forsterite and dunite near partial melting from forced-oscillation experiments. *Physics of the Earth and Planetary Interiors*, *29*(1), 30–41. https://doi.org/10.1016/0031-9201(82)90135-2

Bertotto, G. W., Mazzucchelli, M., Zanetti, A., & Vannucci, R. (2013). Petrology and geochemistry of the back-arc lithospheric mantle beneath eastern Payunia (La Pampa, Argentina): Evidence from Agua Poca peridotite xenoliths. *Geochemical Journal*, *47*(2), 219–234. https://doi.org/10.2343/geochemj.2.0256

Birch, F. (1964). Density and composition of mantle and core. *Journal of Geophysical Research (1896-1977)*, *69*(20), 4377–4388. https://doi.org/10.1029/JZ069i020p04377

Boedo, F. L., Willner, A. P., Vujovich, G. I., & Massonne, H.-J. (2016). High-pressure/low-temperature metamorphism in the collision zone between the Chilenia and Cuyania microcontinents (western Precordillera, Argentina). *Journal of South American Earth Sciences*, *72*, 227–240. https://doi.org/10.1016/j.jsames.2016.09.009

Boonma, K., Kumar, A., Garcia-Castellanos, D., Jiménez-Munt, I., & Fernández, M. (2019). Lithospheric mantle buoyancy: the role of tectonic convergence and mantle composition. *Scientific Reports*, *9*(1), 17953. https://doi.org/10.1038/s41598-019-54374-w

Bostock, M. G., Hyndman, R. D., Rondenay, S., & Peacock, S. M. (2002). An inverted continental Moho and serpentinization of the forearc mantle. *Nature, 417*(6888), 536–538. https://doi.org/10.1038/417536a

Boyce, D., Charrier, R., & Farías, M. (2020). The First Andean Compressive Tectonic Phase: Sedimentologic and Structural Analysis of Mid-Cretaceous Deposits in the Coastal Cordillera, Central Chile (32°50′S). *Tectonics, 39*(2). https://doi.org/10.1029/2019TC005825

Brocher, T. M. (2005). Empirical Relations between Elastic Wavespeeds and Density in the Earth’s Crust. *Bulletin of the Seismological Society of America*, *95*(6), 2081–2092. https://doi.org/10.1785/0120050077

Burov, E.B., & Diament, M. (1995). The effective elastic thickness (Te) of continental lithosphere: What does it really mean? *Journal of Geophysical Research*, *100,* 3905–3927. https://doi.org/10.1029/94JB02770

Burov, E. B. (2011). Rheology and strength of the lithosphere. *Marine and Petroleum Geology, 28*(8), 1402–1443. https://doi.org/10.1016/j.marpetgeo.2011.05.008

Burov, E.B. (2007). Coupled lithosphere-surface processes in collision context. In *Thrust Belts and Foreland Basins* (pp. 3–40). Springer.

Byerlee, J. D. (1968). Brittle-ductile transition in rocks. *Journal of Geophysical Research (1896-1977), 73*(14), 4741–4750. https://doi.org/10.1029/JB073i014p04741

Cacace, M., & Scheck-Wenderoth, M. (2016). Why intracontinental basins subside longer: 3-D feedback effects of lithospheric cooling and sedimentation on the flexural strength of the lithosphere: Subsidence at Intracontinental Basins. *Journal of Geophysical Research: Solid Earth*, *121*(5), 3742–3761. https://doi.org/10.1002/2015JB012682

Cacace, M., & Jacquey, A. B. (2017). Flexible parallel implicit modelling of coupled thermal–hydraulic–mechanical processes in fractured rocks. *Solid Earth, 8*(5), 921–941. https://doi.org/10.5194/se-8-921-2017

Cahill, T., & Isacks, B. L. (1992). Seismicity and shape of the subducted Nazca Plate. *Journal of Geophysical Research*, *97*(B12), 17503. https://doi.org/10.1029/92JB00493

Calignano, E., Sokoutis, D., Willingshofer, E., Gueydan, F., & Cloetingh, S. (2015). Strain localization at the margins of strong lithospheric domains: Insights from analog models. *Tectonics*, *34*(3), 396–412. https://doi.org/10.1002/2014TC003756

Calixto, F. J., Sandvol, E., Kay, S., Mulcahy, P., Heit, B., Yuan, X., et al. (2013). Velocity structure beneath the southern Puna plateau: Evidence for delamination: Velocity Structure in The Southern Puna. *Geochemistry, Geophysics, Geosystems*, *14*(10), 4292–4305. https://doi.org/10.1002/ggge.20266

Cammarano, F., Goes, S., Vacher, P., & Giardini, D. (2003). Inferring upper-mantle temperatures from seismic velocities. *Physics of the Earth and Planetary Interiors*, *138*(3), 197–222. https://doi.org/10.1016/S0031-9201(03)00156-0

Carter, N., & Tsenn, M. (1987). Flow properties of continental lithosphere. *Tectonophysics, 136,* 27–63.

Casquet, C., Dahlquist, J. A., Verdecchia, S. O., Baldo, E. G., Galindo, C., Rapela, C. W., et al. (2018). Review of the Cambrian Pampean orogeny of Argentina; a displaced orogen formerly attached to the Saldania Belt of South Africa? *Earth-Science Reviews, 177*, 209–225. https://doi.org/10.1016/j.earscirev.2017.11.013

Čermák, V., & Rybach, L. (1982). Thermal conductivity and specific heat of minerals and rocks. *Landolt-Börnstein: Numerical Data and Functional Relationships in Science and Technology, New Series, Group V (Geophysics and Space Research), Volume Ia,(Physical Properties of Rocks), Edited by G. Angenheister, Springer, Berlin-Heidelberg*, 305–343.

Čížková, H., & Bina, C. R. (2013). Effects of mantle and subduction-interface rheologies on slab stagnation and trench rollback. *Earth and Planetary Science Letters*, *379*, 95–103. https://doi.org/10.1016/j.epsl.2013.08.011

Charrier, R. (1979). El Triásico en Chile y regiones adyacentes de Argentina. Universidad de Chile, Departamento de geologia. *Comunicaciones*, *26*, 1–37.

Charrier, R., Ramos, V. A., Tapia, F., & Sagripanti, L. (2015). Tectono-stratigraphic evolution of the Andean Orogen between 31 and 37°S (Chile and Western Argentina). *Geological Society, London, Special Publications*, *399*(1), 13–61. https://doi.org/10.1144/SP399.20

Chen, K., Liu, Z., & Song, Y. T. (2020). Automated GNSS and Teleseismic Earthquake Inversion (AutoQuake Inversion) for Tsunami Early Warning: Retrospective and Real-Time Results. *Pure and Applied Geophysics*, *177*(3), 1403–1423. https://doi.org/10.1007/s00024-019-02252-x

Chen, L., Song, X., Gerya, T. V., Xu, T., & Chen, Y. (2019). Crustal melting beneath orogenic plateaus: Insights from 3-D thermo-mechanical modeling. *Tectonophysics*, *761*, 1–15. https://doi.org/10.1016/j.tecto.2019.03.014

Chen, W.-P., & Molnar, P. (1983). Focal depths of intracontinental and intraplate earthquakes and their implications for the thermal and mechanical properties of the lithosphere. *Journal of Geophysical Research: Solid Earth*, *88*(B5), 4183–4214. https://doi.org/10.1029/JB088iB05p04183

Chen, W.-P., Hung, S.-H., Tseng, T.-L., Brudzinski, M., Yang, Z., & Nowack, R. L. (2012). Rheology of the continental lithosphere: Progress and new perspectives. *Tectonic Evolution of Tibet and Surrounding Regions*, *21*(1), 4–18. https://doi.org/10.1016/j.gr.2011.07.013

Chlieh, M., Perfettini, H., Tavera, H., Avouac, J.-P., Remy, D., Nocquet, J.-M., et al. (2011). Interseismic coupling and seismic potential along the Central Andes subduction zone. *Journal of Geophysical Research: Solid Earth*, *116*(B12). https://doi.org/10.1029/2010JB008166

Christensen, N. I., & Mooney, W. D. (1995). Seismic velocity structure and composition of the continental crust: A global view. *Journal of Geophysical Research: Solid Earth*, *100*(B6), 9761–9788. https://doi.org/10.1029/95JB00259

Christensen, U. R., & Hofmann, A. W. (1994). Segregation of subducted oceanic crust in the convecting mantle. *Journal of Geophysical Research: Solid Earth*, *99*(B10), 19867–19884. https://doi.org/10.1029/93JB03403

Cloetingh, S., & Wortel, R. (1986). Stress in the Indo-Australian plate. *Tectonophysics*, *132*(1), 49–67. https://doi.org/10.1016/0040-1951(86)90024-7

Cloos, M., & Shreve, R. L. (1996). Shear-zone thickness and the seismicity of Chilean- and Marianas-type subduction zones. *Geology*, *24*(2), 107–110. https://doi.org/10.1130/0091-7613(1996)024<0107:SZTATS>2.3.CO;2

Collins, W. J. (2002). Hot orogens, tectonic switching, and creation of continental crust. *Geology*, *30*(6), 535–538. https://doi.org/10.1130/0091-7613(2002)030<0535:HOTSAC>2.0.CO;2

Collo, G., Ezpeleta, M., Dávila, F. M., Giménez, M., Soler, S., Martina, F., et al. (2018). Basin Thermal Structure in the Chilean-Pampean Flat Subduction Zone. In *The Evolution of the Chilean-Argentinean Andes* (pp. 537–564). Springer.

Conceição, R. V., Mallmann, G., Koester, E., Schilling, M., Bertotto, G. W., & Rodriguez-Vargas, A. (2005). Andean subduction-related mantle xenoliths: Isotopic evidence of Sr–Nd decoupling during metasomatism. *Lithos*, *82*(3–4), 273–287. https://doi.org/10.1016/j.lithos.2004.09.022

Conrad, C. P., & Lithgow-Bertelloni, C. (2006). Influence of continental roots and asthenosphere on plate-mantle coupling. *Geophysical Research Letters*, *33*(5). https://doi.org/10.1029/2005GL025621

Contreras-Reyes, E., Grevemeyer, I., Flueh, E. R., & Reichert, C. (2008). Upper lithospheric structure of the subduction zone offshore of southern Arauco peninsula, Chile, at ∼38°S. *Journal of Geophysical Research*, *113*(B7), B07303. https://doi.org/10.1029/2007JB005569

Contreras-Reyes, E., Becerra, J., Kopp, H., Reichert, C., & Díaz-Naveas, J. (2014). Seismic structure of the north-central Chilean convergent margin: Subduction erosion of a paleomagmatic arc. *Geophysical Research Letters*, *41*(5), 1523–1529. https://doi.org/10.1002/2013GL058729

Contreras-Reyes, E., Ruiz, J. A., Becerra, J., Kopp, H., Reichert, C., Maksymowicz, A., & Arriagada, C. (2015). Structure and tectonics of the central Chilean margin (31°–33°S): implications for subduction erosion and shallow crustal seismicity. *Geophysical Journal International*, *203*(2), 776–791. https://doi.org/10.1093/gji/ggv309

Copernicus Climate Change Service (C3S). (2019). *ERA5-Land monthly averaged data from 1981 to present*. Retrieved from 10.24381/cds.68d2bb3

Costa, C., Machette, M., Dart, R., Bastia, H., Paredes, J., Perucca, L., et al. (2000). *Map and database of Quaternary faults and folds in Argentina* (Open-File Report No. 00–0108) (p. 76). Denver, Colorado, USA: U.S. Geological Survey.

Costa, C., Alvarado, A., Audemard, F., Audin, L., Benavente, C., Bezerra, F. H., et al. (2020a). Hazardous faults of South America; compilation and overview. *Journal of South American Earth Sciences*, *104*, 102837. https://doi.org/10.1016/j.jsames.2020.102837

Costa, C., Alvarado, A., Audemard, F., Audin, L., Benavente, C., Bezerra, F. H., et al. (2020b). Hazardous faults of South America; compilation and overview. *Journal of South American Earth Sciences*, *104*, 102837. https://doi.org/10.1016/j.jsames.2020.102837

Craig, T. J., & Jackson, J. A. (2021). Variations in the Seismogenic Thickness of East Africa. *Journal of Geophysical Research: Solid Earth*, *126*(3), e2020JB020754. https://doi.org/10.1029/2020JB020754

Cristallini, E., & Ramos, V. (2000). Thick-skinned and thin-skinned thrusting in the La Ramada fold and thrust belt: crustal evolution of the High Andes of San Juan, Argentina (32 SL). *Tectonophysics*, *317*(3–4), 205–235. https://doi.org/10.1016/S0040-1951(99)00276-0

Dahlen, F. A. (1990). Critical taper model of fold-and-thrust belts and accretionary wedges. *Annual Review of Earth and Planetary Sciences*, *18*(1), 55–99. https://doi.org/10.1146/annurev.ea.18.050190.000415

Davis, D., Suppe, J., & Dahlen, F. A. (1983). Mechanics of fold-and-thrust belts and accretionary wedges. *Journal of Geophysical Research: Solid Earth*, *88*(B2), 1153–1172. https://doi.org/10.1029/JB088iB02p01153

Davy, Ph., & Cobbold, P. R. (1991). Experiments on shortening of a 4-layer model of the continental lithosphere. *Experimental and Numerical Modelling of Continental Deformation*, *188*(1), 1–25. https://doi.org/10.1016/0040-1951(91)90311-F

Deschamps, F., Godard, M., Guillot, S., & Hattori, K. (2013). Geochemistry of subduction zone serpentinites: A review. *Serpentinites from Mid-Oceanic Ridges to Subduction*, *178*, 96–127. https://doi.org/10.1016/j.lithos.2013.05.019

Deschamps, F., Trampert, J., & Snieder, R. (2002). Anomalies of temperature and iron in the uppermost mantle inferred from gravity data and tomographic models. *Physics of the Earth and Planetary Interiors*, *129*(3), 245–264. https://doi.org/10.1016/S0031-9201(01)00294-1

Deshayes, P. (2008, November). *Velocity and attenuation tomography of the subduction zone in central Chile-western Argentina (29°S-34°S) from local seismic data: contribution to the mineralogical composition study.* (Theses). Université Nice Sophia Antipolis. Retrieved from https://tel.archives-ouvertes.fr/tel-00360063

van Dinther, Y., Morra, G., Funiciello, F., & Faccenna, C. (2010). Role of the overriding plate in the subduction process: Insights from numerical models. *Tectonophysics*, *484*(1–4), 74–86. https://doi.org/10.1016/j.tecto.2009.08.038

Doglioni, C., Barba, S., Carminati, E., & Riguzzi, F. (2011). Role of the brittle–ductile transition on fault activation. *Physics of the Earth and Planetary Interiors*, *184*(3–4), 160–171. https://doi.org/10.1016/j.pepi.2010.11.005

Drápela, J., Calisto, I., & Moreno, M. (2021). Locking-derived tsunami scenarios for the most recent megathrust earthquakes in Chile: implications for tsunami hazard assessment. *Natural Hazards*, *107*(1), 35–52. https://doi.org/10.1007/s11069-021-04572-5

Drewes, H., & Sánchez, L. (2017). The varying surface kinematics in Latin America: VEMOS 2009, 2015, and 2017. Presented at the Symposium SIRGAS2017.

Ducea, M. N., Otamendi, J. E., Bergantz, G. W., Jianu, D., & Petrescu, L. (2015). The origin and petrologic evolution of the Ordovician Famatinian-Puna arc. In P. G. DeCelles, M. N. Ducea, B. Carrapa, & P. A. Kapp, *Geodynamics of a Cordilleran Orogenic System: The Central Andes of Argentina and Northern Chile*. Geological Society of America. https://doi.org/10.1130/2015.1212(07)

Dziewonski, A. M., Chou, T.-A., & Woodhouse, J. H. (1981). Determination of earthquake source parameters from waveform data for studies of global and regional seismicity. *Journal of Geophysical Research: Solid Earth*, *86*(B4), 2825–2852. https://doi.org/10.1029/JB086iB04p02825

Ekström, G., Nettles, M., & Dziewoński, A. M. (2012). The global CMT project 2004–2010: Centroid-moment tensors for 13,017 earthquakes. *Physics of the Earth and Planetary Interiors*, *200–201*, 1–9. https://doi.org/10.1016/j.pepi.2012.04.002

Encinas, A., Maksaev, V., Pinto, L., Le Roux, J. P., Munizaga, F., & Zentilli, M. (2006). Pliocene lahar deposits in the Coastal Cordillera of central Chile: implications for uplift, avalanche deposits, and porphyry copper systems in the Main Andean Cordillera. *Journal of South American Earth Sciences*, *20*(4), 369–381.

Engdahl, E. R., & Scholz, C. H. (1977). A double Benioff Zone beneath the central Aleutians: An unbending of the lithosphere. *Geophysical Research Letters*, *4*(10), 473–476. https://doi.org/10.1029/GL004i010p00473

England, P. (2018). On Shear Stresses, Temperatures, and the Maximum Magnitudes of Earthquakes at Convergent Plate Boundaries. *Journal of Geophysical Research: Solid Earth*, *123*(8), 7165–7202. https://doi.org/10.1029/2018JB015907

Escayola, M. P., van Staal, C. R., & Davis, W. J. (2011). The age and tectonic setting of the Puncoviscana Formation in northwestern Argentina: An accretionary complex related to Early Cambrian closure of the Puncoviscana Ocean and accretion of the Arequipa-Antofalla block. *Journal of South American Earth Sciences*, *32*(4), 438–459. https://doi.org/10.1016/j.jsames.2011.04.013

Espurt, N., Funiciello, F., Martinod, J., Guillaume, B., Regard, V., Faccenna, C., & Brusset, S. (2008). Flat subduction dynamics and deformation of the South American plate: Insights from analog modeling. *Tectonics*, *27*(3). https://doi.org/10.1029/2007TC002175

Evans, B., & Kohlstedt, D. L. (1995). Rheology of rocks. *Rock Physics and Phase Relations: A Handbook of Physical Constants, AGU Ref. Shelf*, *3*, 148–165.

Faccenda, M., & Dal Zilio, L. (2017). The role of solid–solid phase transitions in mantle convection. *Lithos*, *268*, 198–224. https://doi.org/10.1016/j.lithos.2016.11.007

Faccenna, C., Oncken, O., Holt, A. F., & Becker, T. W. (2017). Initiation of the Andean orogeny by lower mantle subduction. *Earth and Planetary Science Letters*, *463*, 189–201. https://doi.org/10.1016/j.epsl.2017.01.041

Farías, M., Charrier, R., Carretier, S., Martinod, J., Fock, A., Campbell, D., et al. (2008). Late Miocene high and rapid surface uplift and its erosional response in the Andes of central Chile (33°–35°S). *Tectonics*, *27*(1). https://doi.org/10.1029/2006TC002046

Feng, M., van der Lee, S., & Assumpção, M. (2007). Upper mantle structure of South America from joint inversion of waveforms and fundamental mode group velocities of Rayleigh waves. *Journal of Geophysical Research: Solid Earth*, *112*(B4). https://doi.org/10.1029/2006JB004449

Fennell, L. M., Folguera, A., Naipauer, M., Gianni, G., Rojas Vera, E. A., Bottesi, G., & Ramos, V. A. (2015). Cretaceous deformation of the southern Central Andes: synorogenic growth strata in the Neuquén Group (35° 30′–37° S). *Basin Research*, 51–72. https://doi.org/10.1111/bre.12135

Fennell, L. M., Quinteros, J., Iannelli, S. B., Litvak, V. D., & Folguera, A. (2018). The role of the slab pull force in the late Oligocene to early Miocene extension in the Southern Central Andes (27°-46°S): Insights from numerical modeling. *Journal of South American Earth Sciences*, *87*, 174–187. https://doi.org/10.1016/j.jsames.2017.12.012

Ferrand, T. P., Hilairet, N., Incel, S., Deldicque, D., Labrousse, L., Gasc, J., et al. (2017). Dehydration-driven stress transfer triggers intermediate-depth earthquakes. *Nature Communications*, *8*(1), 15247. https://doi.org/10.1038/ncomms15247

Fichtner, A., Kennett, B. L. N., Igel, H., & Bunge, H.-P. (2010). Full waveform tomography for radially anisotropic structure: New insights into present and past states of the Australasian upper mantle. *Earth and Planetary Science Letters*, *290*(3), 270–280. https://doi.org/10.1016/j.epsl.2009.12.003

Flueh, E. R., Vidal, N., Ranero, C. R., Hojka, A., von Huene, R., Bialas, J., et al. (1998). Seismic investigation of the continental margin off- and onshore Valparaiso, Chile. *Tectonophysics*, *288*(1–4), 251–263. https://doi.org/10.1016/S0040-1951(97)00299-0

Fock, A. (2005). *Cronología y tectónica de la exhumación en el Neógeno de los Andes de Chile Central entre los 33° y los 34°S*. Facultad De Ciencias Físicas y Matemáticas Departamento De Geología; Universidad de Chile.

Folguera, A., & Zárate, M. (2009). La sedimentación neógena continental en el sectorextrandino de Argentina central. *Revista de La Asociación Geológica Argentina*, *64*(4), 692–712.

Folguera, A., Zapata, T., & Ramos, V. A. (2006). Late Cenozoic extension and the evolution of the Neuquén Andes. In Suzanne Mahlburg Kay & V. A. Ramos (Eds.), *Evolution of an Andean Margin: A Tectonic and Magmatic View from the Andes to the Neuque´n Basin (35°-39°S lat)* (Vol. 407, p. 0). Geological Society of America. https://doi.org/10.1130/2006.2407(12)

Folguera, A., Naranjo, J. A., Orihashi, Y., Sumino, H., Nagao, K., Polanco, E., & Ramos, V. A. (2009). Retroarc volcanism in the northern San Rafael Block (34–35 30′ S), southern Central Andes: Occurrence, age, and tectonic setting. *Journal of Volcanology and Geothermal Research*, *186*(3–4), 169–185.

Förste, C., Bruinsma, S., Abrikosov, O., Flechtner, F., Marty, J.-C., Lemoine, J.-M., et al. (2014). EIGEN-6C4-The latest combined global gravity field model including GOCE data up to degree and order 1949 of GFZ Potsdam and GRGS Toulouse. In *EGU general assembly conference abstracts* (Vol. 16).

Forsythe, R. (1982). The late Palaeozoic to early Mesozoic evolution of southern South America: a plate tectonic interpretation. *Journal of the Geological Society*, *139*(6), 671–682. https://doi.org/10.1144/gsjgs.139.6.0671

French, S., Lekic, V., & Romanowicz, B. (2013). Waveform tomography reveals channeled flow at the base of the oceanic asthenosphere. *Science*, *342*(6155), 227–230.

Freymark, J., Sippel, J., Scheck-Wenderoth, M., Bär, K., Stiller, M., Fritsche, J.-G., & Kracht, M. (2017). The deep thermal field of the Upper Rhine Graben. *Tectonophysics*, *694*, 114–129. https://doi.org/10.1016/j.tecto.2016.11.013

Fuentes, F., & Horton, B. K. (2020). The Andean Foreland Evolution of the Neuquén Basin: A Discussion. In D. Kietzmann & A. Folguera (Eds.), *Opening and Closure of the Neuquén Basin in the Southern Andes* (pp. 341–370). Cham: Springer International Publishing. https://doi.org/10.1007/978-3-030-29680-3_14

Fujie, G., Kodaira, S., Kaiho, Y., Yamamoto, Y., Takahashi, T., Miura, S., & Yamada, T. (2018). Controlling factor of incoming plate hydration at the north-western Pacific margin. *Nature Communications*, *9*(1), 3844. https://doi.org/10.1038/s41467-018-06320-z

Furlong, K. P., & Chapman, D. S. (2013). Heat Flow, Heat Generation, and the Thermal State of the Lithosphere. *Annual Review of Earth and Planetary Sciences*, *41*(1), 385–410. https://doi.org/10.1146/annurev.earth.031208.100051

Gao, H. (2018). Three-dimensional variations of the slab geometry correlate with earthquake distributions at the Cascadia subduction system. *Nature Communications*, *9*(1), 1204. https://doi.org/10.1038/s41467-018-03655-5

Gao, Y., Tilmann, F., van Herwaarden, D., Thrastarson, S., Fichtner, A., Heit, B., et al. (2021a). Full Waveform Inversion beneath the Central Andes: Insight into the dehydration of the Nazca slab and delamination of the back-arc lithosphere. *Journal of Geophysical Research: Solid Earth*. https://doi.org/10.1029/2021JB021984

Gao, Y., Yuan, X., Heit, B., Tilmann, F., van Herwaarden, D.-P., Thrastarson, S., et al. (2021b). Impact of the Juan Fernandez Ridge on the Pampean Flat Subduction Inferred From Full Waveform Inversion. *Geophysical Research Letters*, *48*(21), e2021GL095509. https://doi.org/10.1029/2021GL095509

Gerbault, M., Cembrano, J., Mpodozis, C., Farias, M., & Pardo, M. (2009). Continental margin deformation along the Andean subduction zone: Thermo-mechanical models. *Physics of the Earth and Planetary Interiors*, *177*(3), 180–205. https://doi.org/10.1016/j.pepi.2009.09.001

Gholamrezaie, E., Scheck-Wenderoth, M., Cacace, M., Bott, J., Heidbach, O., Bohnhoff, M., & Strecker, M. R. (2021). Lithospheric strength variations and seismotectonic segmentation below the Sea of Marmara. *Tectonophysics*, *815*, 228999. https://doi.org/10.1016/j.tecto.2021.228999

Giambiagi, L., Tassara, A., Mescua, J., Tunik, M., Alvarez, P. P., Godoy, E., et al. (2015). Evolution of shallow and deep structures along the Maipo–Tunuyán transect (33 40′ S): from the Pacific coast to the Andean foreland. *Geological Society, London, Special Publications*, *399*(1), 63–82. https://doi.org/10.1144/SP399.14

Giambiagi, L., Mescua, J., Heredia, N., Farías, P., García-Sansegundo, J., Fernández, C., et al. (2014). Reactivation of Paleozoic structures during Cenozoic deformation in the Cordón del Plata and Southern Precordillera ranges (Mendoza, Argentina). *Journal of Iberian Geology*, *40*(2). https://doi.org/10.5209/rev_JIGE.2014.v40.n2.45302

Giambiagi, L., Mescua, J., Bechis, F., Tassara, A., & Hoke, G. (2012). Thrust belts of the southern Central Andes: Along-strike variations in shortening, topography, crustal geometry, and denudation. *Geological Society of America Bulletin*, *124*(7–8), 1339–1351. https://doi.org/10.1130/B30609.1

Giambiagi, L., Mescua, J., Bechis, F., Martínez, A., & Folguera, A. (2011). Pre-Andean deformation of the Precordillera southern sector, southern Central Andes. *Geosphere*, *7*(1), 219–239. https://doi.org/10.1130/GES00572.1

Giambiagi, L., Bechis, F., García, V., & Clark, A. H. (2008). Temporal and spatial relationships of thick- and thin-skinned deformation: A case study from the Malargüe fold-and-thrust belt, southern Central Andes. *Tectonophysics*, *459*(1–4), 123–139. https://doi.org/10.1016/j.tecto.2007.11.069

Giambiagi, L., Ramos, V. A., Godoy, E., Alvarez, P. P., & Orts, S. (2003). Cenozoic deformation and tectonic style of the Andes, between 33° and 34° south latitude. *Tectonics*, *22*(4), n/a-n/a. https://doi.org/10.1029/2001TC001354

Giambiagi, L, & Ramos, V. (2002). Structural evolution of the Andes in a transitional zone between flat and normal subduction (33 300–33 450S), Argentina and Chile. *Journal of South American Earth Sciences*, *15*(1), 101–116.

Giambiagi, L, & Ramos, V. A. (2002). Structural evolution of the Andes in a transitional zone between flat and normal subduction (33°30′–33°45′S), Argentina and Chile. *Flat-Slab Subduction in the Andes*, *15*(1), 101–116. https://doi.org/10.1016/S0895-9811(02)00008-1

Giambiagi, L., Tunik, M. A., & Ghiglione, M. (2001). Cenozoic tectonic evolution of the Alto TunuyaÂn foreland basin above the transition zone between the flat and normal subduction segment (338300±348S), western Argentina. *Journal of South American Earth Sciences*, 18.

Gilbert, H., Beck, S., & Zandt, G. (2006). Lithospheric and upper mantle structure of central Chile and Argentina. *Geophysical Journal International*, *165*(1), 383–398. https://doi.org/10.1111/j.1365-246X.2006.02867.x

Gleason, G. C., & Tullis, J. (1995). A flow law for dislocation creep of quartz aggregates determined with the molten salt cell. *30 Years of Tectonophysics a Special Volume in Honour of Gerhard Oertel*, *247*(1), 1–23. https://doi.org/10.1016/0040-1951(95)00011-B

Godoy, E., Yañez, G., & Vera, E. (1999). Inversion of an Oligocene volcano-tectonic basin and uplifting of its superimposed Miocene magmatic arc in the Chilean Central Andes: first seismic and gravity evidences. *Tectonophysics*, *306*(2), 217–236. https://doi.org/10.1016/S0040-1951(99)00046-3

Goes, S, Govers, R., & Vacher, and P. (2000). Shallow mantle temperatures under Europe from P and S wave tomography. *Journal of Geophysical Research: Solid Earth*, *105*(B5), 11153–11169. https://doi.org/10.1029/1999JB900300

Goes, S., Hasterok, D., Schutt, D. L., & Klöcking, M. (2020). Continental lithospheric temperatures: A review. *Physics of the Earth and Planetary Interiors*, *306*, 106509. https://doi.org/10.1016/j.pepi.2020.106509

Goetze, C., Poirier, J. P., Kelly, A., Cook, A. H., & Greenwood, G. W. (1978). The mechanisms of creep in olivine. *Philosophical Transactions of the Royal Society of London. Series A, Mathematical and Physical Sciences*, *288*(1350), 99–119. https://doi.org/10.1098/rsta.1978.0008

Goetze, C., & Evans, B. (1979). Stress and temperature in the bending lithosphere as constrained by experimental rock mechanics. *Geophysical Journal International*, *59*(3), 463–478. https://doi.org/10.1111/j.1365-246X.1979.tb02567.x

Götze, H-J. (1984). Über den Einsatz interaktiver Computergraphik im Rahmen 3-dimensionaler Interpretationstechniken in Gravimetrie und Magnetik.

Götze, H-J, & Lahmeyer, B. (1988). Application of three-dimensional interactive modeling in gravity and magnetics. *Geophysics*, *53*(8), 1096–1108. https://doi.org/10.1190/1.1442546

Gregori, S. D., & Christiansen, R. (2018). Seismic hazard analysis for central-western Argentina. *Seismological Advances in Latin America*, *9*(1), 25–33. https://doi.org/10.1016/j.geog.2017.07.006

Grevemeyer, I., Ranero, C. R., & Ivandic, M. (2018). Structure of oceanic crust and serpentinization at subduction trenches. *Geosphere*, *14*(2), 395–418. https://doi.org/10.1130/GES01537.1

Grimaldi, G. O., & Dorobek, S. L. (2011). Fault framework and kinematic evolution of inversion structures: Natural examples from the Neuquén Basin, Argentina. *AAPG Bulletin*, *95*(1), 27–60. https://doi.org/10.1306/06301009165

Guo, H., McGuire, J. J., & Zhang, H. (2021). Correlation of porosity variations and rheological transitions on the southern Cascadia megathrust. *Nature Geoscience, 14*(5), 341–348. https://doi.org/10.1038/s41561-021-00740-1

Gutscher, M., Spakman, W., Bijwaard, H., & Engdahl, E. R. (2000). Geodynamics of flat subduction: Seismicity and tomographic constraints from the Andean margin. *Tectonics, 19*(5), 814–833.

Gutscher, M. (2002). Andean subduction styles and their effect on thermal structure and interplate coupling. *Journal of South American Earth Sciences, 15*(1), 3–10. https://doi.org/10.1016/S0895-9811(02)00002-0

Gutscher, M. (2018). Scraped by flat-slab subduction. *Nature Geoscience, 11*(12), 889–890. https://doi.org//10.1038/s41561-018-0270-x

Hacker, B. R., Abers, G. A., & Peacock, S. M. (2003). Subduction factory 1. Theoretical mineralogy, densities, seismic wave speeds, and H $_2$ O contents: SUBDUCTION ZONE MINERALOGY AND PHYSICAL PROPERTIES. *Journal of Geophysical Research: Solid Earth*, *108*(B1). https://doi.org/10.1029/2001JB001127

Hacker, B. R., Peacock, S. M., Abers, G. A., & Holloway, S. D. (2003). Subduction factory 2. Are intermediate-depth earthquakes in subducting slabs linked to metamorphic dehydration reactions? *Journal of Geophysical Research: Solid Earth*, *108*(B1). https://doi.org/10.1029/2001JB001129

Hacker, B. R., Kelemen, P. B., & Behn, M. D. (2011). Differentiation of the continental crust by relamination. *Earth and Planetary Science Letters*, *307*(3–4), 501–516. https://doi.org/10.1016/j.epsl.2011.05.024 Get

Hackney, R. I., Echtler, H. P., Franz, G., Götze, H.-J., Lucassen, F., Marchenko, D., et al. (2006). The Segmented Overriding Plate and Coupling at the South-Central Chilean Margin (36–42°S). In O. Oncken, G. Chong, G. Franz, P. Giese, H.-J. Götze, V. A. Ramos, et al. (Eds.), *The Andes* (pp. 355–374). Springer Berlin Heidelberg. https://doi.org/10.1007/978-3-540-48684-8_17

Hain, M. P., Strecker, M. R., Bookhagen, B., Alonso, R. N., Pingel, H., & Schmitt, A. K. (2011). Neogene to Quaternary broken foreland formation and sedimentation dynamics in the Andes of NW Argentina (25°S). *Tectonics, 30*(2). https://doi.org/10.1029/2010TC002703

Haller, M., & Ramos, V. (1984). Las ofiolitas famatinianas (Eopaleozoico) de las provincias de San Juan y Mendoza. In *IX Congreso Geológico Argentino* (Vol. 2, pp. 66–83).

Hamza, V. M., & Vieira, F. P. (2012). Global distribution of the lithosphere-asthenosphere boundary: a new look. *Solid Earth*, *3*(2), 199–212. https://doi.org/10.5194/se-3-199-2012

Hamza, V. M., Cardoso, R. R., & Ponte Neto, C. F. (2008). Spherical harmonic analysis of earth's conductive heat flow. *International Journal of Earth Sciences*, *97*(2), 205–226. https://doi.org/10.1007/s00531-007-0254-3

Hamza, V. M, & Muñoz, M. (1996a). Heat flow map of South America, 47.

Hamza, V. M., & Muñoz, M. (1996b). Heat flow map of South America. *Geothermics, 25*(6), 599–646. https://doi.org/10.1016/S0375-6505(96)00025-9

Hamza, V. M., Dias, F. J. S. S., Gomes, A. J. L., & Terceros, Z. G. D. (2005). Numerical and functional representations of regional heat flow in South America. *Physics of the Earth and Planetary Interiors*, *152*(4), 223–256. https://doi.org/10.1016/j.pepi.2005.04.009

Handy, M. R., & Brun, J.-P. (2004). Seismicity, structure and strength of the continental lithosphere. *Earth and Planetary Science Letters*, *223*(3–4), 427–441. https://doi.org/10.1016/j.epsl.2004.04.021

Harris, C. R., Millman, K. J., van der Walt, S. J., Gommers, R., Virtanen, P., Cournapeau, D., et al. (2020). Array programming with NumPy. *Nature*, *585*, 357–362. https://doi.org/10.1038/s41586-020-2649-2

Hasterok, D. (2013). A heat flow based cooling model for tectonic plates. *Earth and Planetary Science Letters*, *361*, 34–43. https://doi.org/10.1016/j.epsl.2012.10.036

Hasterok, D., & Chapman, D. (2011). Heat production and geotherms for the continental lithosphere. *Earth and Planetary Science Letters*, *307*(1–2), 59–70. https://doi.org/10.1016/j.epsl.2011.04.034

Hayes, G. P., Moore, G. L., Portner, D. E., Hearne, M., Flamme, H., Furtney, M., & Smoczyk, G. M. (2018). Slab2, a comprehensive subduction zone geometry model. *Science*, *362*(6410), 58. https://doi.org/10.1126/science.aat4723

He, L., Hu, S., Huang, S., Yang, W., Wang, J., Yuan, Y., & Yang, S. (2008). Heat flow study at the Chinese Continental Scientific Drilling site: Borehole temperature, thermal conductivity, and radiogenic heat production. *Journal of Geophysical Research*, *113*(B2), B02404. https://doi.org/10.1029/2007JB004958

Heard, H. C. (1960). Chapter 7: Transition from Brittle Fracture to Ductile Flow in Solenhofen Limestone as a Function of Temperature, Confining Pressure, and Interstitial Fluid Pressure. In D. Griggs & J. Handin (Eds.), *Rock Deformation (A Symposium)* (Vol. 79, p. 0). Geological Society of America. https://doi.org/10.1130/MEM79-p193

Heine, C. (2007). *Formation and Evolution of intracontinental basins*. University of Sidney, Sydney.

Heit, B., Yuan, X., Bianchi, M., Sodoudi, F., & Kind, R. (2008). Crustal thickness estimation beneath the southern central Andes at 30°S and 36°S from *S* wave receiver function analysis. *Geophysical Journal International*, *174*(1), 249–254. https://doi.org/10.1111/j.1365-246X.2008.03780.x

Henry, S. G., & Pollack, H. N. (1988). Terrestrial heat flow above the Andean Subduction Zone in Bolivia and Peru. *Journal of Geophysical Research: Solid Earth*, *93*(B12), 15153–15162. https://doi.org/10.1029/JB093iB12p15153

Heredia, N., García-Sansegundo, J., Gallastegui, G., Farias, P., Giacosa, R. E., Giambiagi, L. B., et al. (2018). Review of the geodynamic evolution of the SW margin of Gondwana preserved in the Central Andes of Argentina and Chile (28°-38° S latitude). *Journal of South American Earth Sciences*, *87*, 87–94. https://doi.org/10.1016/j.jsames.2017.11.019

Heredia, N., García-Sansegundo, J., Gallastegui, G., Farias, P., Giacosa, R., Hongn, F., et al. (2018). The Pre-Andean Phases of Construction of the Southern Andes Basement in Neoproterozoic–Paleozoic Times. In Andrés Folguera, E. Contreras-Reyes, N. Heredia, A. Encinas, S. B. Iannelli, V. Oliveros, et al. (Eds.), *The Evolution of the Chilean-Argentinean Andes* (pp. 111–131). Cham: Springer International Publishing. https://doi.org/10.1007/978-3-319-67774-3_5

Hervé, F., Munizaga, F., Parada, M. A., Brook, M., Pankhurst, R. J., Snelling, N. J., & Drake, R. (1988). Granitoids of the Coast Range of central Chile: Geochronology and geologic setting. *Journal of South American Earth Sciences*, *1*(2), 185–194. https://doi.org/10.1016/0895-9811(88)90036-3

Herve, F., Calderón, M., Fanning, C., Pankhurst, R. J., & Godoy, E. (2013). Provenance variations in the Late Paleozoic accretionary complex of central Chile as indicated by detrital zircons. *Gondwana Research*, *23*(3), 1122–1135. https://doi.org/10.1016/j.gr.2012.06.016

Hicks, S. P., Rietbrock, A., Ryder, I. M. A., Lee, C.-S., & Miller, M. (2014). Anatomy of a megathrust: The 2010 M8.8 Maule, Chile earthquake rupture zone imaged using seismic tomography. *Earth and Planetary Science Letters*, *405*, 142–155. https://doi.org/10.1016/j.epsl.2014.08.028

Hildreth, W., & Moorbath, S. (1988). Crustal contributions to arc magmatism in the Andes of Central Chile. *Contributions to Mineralogy and Petrology*, *98*(4), 455–489. https://doi.org/10.1007/BF00372365

Hilley, G. E., Blisniuk, P. M., & Strecker, M. R. (2005). Mechanics and erosion of basement-cored uplift provinces. *Journal of Geophysical Research: Solid Earth*, *110*(B12). https://doi.org/10.1029/2005JB003704

Hirschmann, M. M. (2000). Mantle solidus: Experimental constraints and the effects of peridotite composition. *Geochemistry, Geophysics, Geosystems*, *1*(10). https://doi.org/10.1029/2000GC000070

Hirt, C., & Rexer, M. (2015). Earth2014: 1 arc-min shape, topography, bedrock and ice-sheet models – Available as gridded data and degree-10,800 spherical harmonics. *International Journal of Applied Earth Observation and Geoinformation*, *39*, 103–112. https://doi.org/10.1016/j.jag.2015.03.001

Hirth, G., & Kohlstedt, D. L. (1996). Water in the oceanic upper mantle: implications for rheology, melt extraction and the evolution of the lithosphere. *Earth and Planetary Science Letters*, *144*(1), 93–108. https://doi.org/10.1016/0012-821X(96)00154-9

Hofmann, A. W. (1997). Mantle geochemistry: the message from oceanic volcanism. *Nature*, *385*(6613), 219–229. https://doi.org/10.1038/385219a0

Holt, A. F., & Condit, C. B. (2021). Slab Temperature Evolution Over the Lifetime of a Subduction Zone. *Geochemistry, Geophysics, Geosystems*, *22*(6). https://doi.org/10.1029/2020GC009476

Hongn, F., Papa, C. del, Powell, J., Petrinovic, I., Mon, R., & Deraco, V. (2007a). Middle Eocene deformation and sedimentation in the Puna-Eastern Cordillera transition (23°-26°S): Control by preexisting heterogeneities on the pattern of initial Andean shortening. *Geology*, *35*(3), 271–274. https://doi.org/10.1130/G23189A.1

Hongn, F., Papa, C. del, Powell, J., Petrinovic, I., Mon, R., & Deraco, V. (2007b). Middle Eocene deformation and sedimentation in the Puna-Eastern Cordillera transition (23°-26°S): Control by preexisting heterogeneities on the pattern of initial Andean shortening. *Geology*, *35*(3), 271–274. https://doi.org/10.1130/G23189A.1

Hongn, F., & Riller, U. (2007). Tectonic Evolution of the Western Margin of Gondwana Inferred from Syntectonic Emplacement of Paleozoic Granitoid Plutons in Northwest Argentina. *The Journal of Geology*, *115*(2), 163–180. https://doi.org/10.1086/510644

Hongn, F., Mon, R., Petrinovic, I., del Papa, C., & Powell, J. (2010). Inversión y reactivación tectónicas cretácico-cenozoicas en el noroeste argentino: influencia de las heterogeneidades del basamento Neoproterozoico-Paleozoico inferior. *Revista de La Asociación Geológica Argentina*, *66*(1–2), 38–53.

Horton, B. K. (2018a). Sedimentary record of Andean mountain building. *Earth-Science Reviews*, *178*, 279–309. https://doi.org/10.1016/j.earscirev.2017.11.025

Horton, B. K. (2018b). Tectonic Regimes of the Central and Southern Andes: Responses to Variations in Plate Coupling During Subduction. *Tectonics*, *37*(2), 402–429. https://doi.org/10.1002/2017TC004624

Howell, J. A., Schwarz, E., Spalletti, L. A., & Veiga, G. D. (2005). The Neuquén Basin: an overview. *Geological Society, London, Special Publications*, *252*(1), 1. https://doi.org/10.1144/GSL.SP.2005.252.01.01

Hu, J., Liu, L., Hermosillo, A., & Zhou, Q. (2016). Simulation of late Cenozoic South American flat-slab subduction using geodynamic models with data assimilation. *Earth and Planetary Science Letters*, *438*, 1–13. https://doi.org/10.1016/j.epsl.2016.01.011

Hubbert, M. K., & Rubey, W. W. (1959). Role of fluid pressure in mechanics of overthrust faulting: I. Mechanics of fluid-filled porous solids and its application to overthrust faulting. *GSA Bulletin*, *70*(2), 115–166. https://doi.org/10.1130/0016-7606(1959)70[115:ROFPIM]2.0.CO;2

von Huene, R., Corvalán, J., Flueh, E. R., Hinz, K., Korstgard, J., Ranero, C. R., & Weinrebe, W. (1997). Tectonic control of the subducting Juan Fernández Ridge on the Andean margin near Valparaiso, Chile. *Tectonics*, *16*(3), 474–488. https://doi.org/10.1029/96TC03703

van Hunen, J., van den Berg, A. P., & Vlaar, N. J. (2000). A thermo-mechanical model of horizontal subduction below an overriding plate. *Earth and Planetary Science Letters*, *182*(2), 157–169. https://doi.org/10.1016/S0012-821X(00)00240-5

van Hunen, J., van den Berg, A. P., & Vlaar, N. J. (2002). On the role of subducting oceanic plateaus in the development of shallow flat subduction. *Tectonophysics*, *352*(3–4), 317–333.

van Hunen, J., van den Berg, A. P., & Vlaar, N. J. (2004). Various mechanisms to induce present-day shallow flat subduction and implications for the younger Earth: a numerical parameter study. *Physics of the Earth and Planetary Interiors*, *146*(1), 179–194. https://doi.org/10.1016/j.pepi.2003.07.027

Hunter, J. D. (2007). Matplotlib: A 2D graphics environment. *Computing in Science & Engineering*, *9*(3), 90–95.

Hyndman, R. D. (2005). Subduction zone backarcs, mobile belts, and orogenic heat. *GSA TODAY*, 7.

Iannelli, S. B., Fernández Paz, L., Litvak, V. D., Gianni, G., Fennell, L. M., González, J., et al. (2020). Southward-Directed Subduction of the Farallon–Aluk Spreading Ridge and Its Impact on Subduction Mechanics and Andean Arc Magmatism: Insights From Geochemical and Seismic Tomographic Data. *Frontiers in Earth Science*, *8*, 121. https://doi.org/10.3389/feart.2020.00121

Ibarra, F., Liu, S., Meeßen, C., Prezzi, C. B., Bott, J., Scheck-Wenderoth, M., et al. (2019a). 3D data-derived lithospheric structure of the Central Andes and its implications for deformation: Insights from gravity and geodynamic modelling. *Tectonophysics*, *766*, 453–468. https://doi.org/10.1016/j.tecto.2019.06.025

Ibarra, F., Liu, S., Meeßen, C., Prezzi, C. B., Bott, J., Scheck-Wenderoth, M., et al. (2019b). 3D data-derived lithospheric structure of the Central Andes and its implications for deformation: Insights from gravity and geodynamic modelling. *Tectonophysics*, *766*, 453–468. https://doi.org/10.1016/j.tecto.2019.06.025

Ibarra, F., Prezzi, C. B., Bott, J., Scheck-Wenderoth, M., & Strecker, M. R. (2021a). Distribution of Temperature and Strength in the Central Andean Lithosphere and Its Relationship to Seismicity and Active Deformation. *Journal of Geophysical Research: Solid Earth*, *126*(5). https://doi.org/10.1029/2020JB021231

Ibarra, F., & Prezzi, C. B. (2019). The thermo-mechanical state of the Andes in the Altiplano-Puna region: insights from Curie isotherm and effective elastic thickness determination. *Revista de La Asociación Geológica Argentina*, *76*(4), 352–362.

Ince, E. S., Barthelmes, F., Reißland, S., Elger, K., Förste, C., Flechtner, F., & Schuh, H. (2019). ICGEM – 15 years of successful collection and distribution of global gravitational models, associated services, and future plans. *Earth System Science Data*, *11*(2), 647–674. https://doi.org/10.5194/essd-11-647-2019

Incel, S., Hilairet, N., Labrousse, L., John, T., Deldicque, D., Ferrand, T., et al. (2017). Laboratory earthquakes triggered during eclogitization of lawsonite-bearing blueschist. *Earth and Planetary Science Letters*, *459*, 320–331. https://doi.org/10.1016/j.epsl.2016.11.047

International Seismological Centre. (2021). *On-line Bulletin*. Retrieved from https://doi.org/10.31905/D808B830

Irigoyen, M. V., Buchan, K. L., & Brown, R. L. (2000). Magnetostratigraphy of Neogene Andean foreland-basin strata, lat 33°S, Mendoza Province, Argentina. *GSA Bulletin*, *112*(6), 803–816. https://doi.org/10.1130/0016-7606(2000)112<803:MONAFS>2.0.CO;2

Isacks, B., & Molnar, P. (1971). Distribution of stresses in the descending lithosphere from a global survey of focal-mechanism solutions of mantle earthquakes. *Reviews of Geophysics*, *9*(1), 103. https://doi.org/10.1029/RG009i001p00103

Isacks, B. L. (1988). Uplift of the Central Andean Plateau and bending of the Bolivian Orocline. *Journal of Geophysical Research: Solid Earth*, *93*(B4), 3211–3231. https://doi.org/10.1029/JB093iB04p03211

Jackson, J., McKenzie, D., Priestley, K., & Emmerson, B. (2008). New views on the structure and rheology of the lithosphere. *Journal of the Geological Society*, *165*(2), 453–465. https://doi.org/10.1144/0016-76492007-109

Jacquey, A. B., & Cacace, M. (2017). GOLEM, a MOOSE-based application (Version v1.0). Zenodo. https://doi.org/10.5281/zenodo.999401

Jacquey, A. B., & Cacace, M. (2019). LYNX: Lithosphere dYnamic Numerical toolboX, a MOOSE-based application (Version 1.0). Zenodo. https://doi.org/10.5281/zenodo.3355376

Jacquey, A. B., & Cacace, M. (2020). Multiphysics Modeling of a Brittle-Ductile Lithosphere: 1. Explicit Visco-Elasto-Plastic Formulation and Its Numerical Implementation. *Journal of Geophysical Research: Solid Earth*, *125*(1). https://doi.org/10.1029/2019JB018474

Jalowitzki, T. L. R., Conceição, R. V., Orihashi, Y., Bertotto, G. W., Nakai, S., & Schilling, M. E. (2010). Evolução geoquímica de peridotitos e piroxenitos do Manto Litosférico Subcontinental do vulcão Agua Poca, Terreno Cuyania, Argentina. *Pesquisas em Geociências*, *37*(2), 143. https://doi.org/10.22456/1807-9806.22656

Japas, M., & Kleiman, L. (2004). El ciclo Choiyoi en el bloque de San Rafael (Mendoza): de la orogénesis tardía a la relajación mecánica. *Avances En Microtectónica y Geología Estructural, Asoc. Geol. Argent. Serie D-Publ. Espec*, *7*, 89–100.

Jarrard, R. D. (1986). Relations among subduction parameters. *Reviews of Geophysics*, *24*(2), 217–284. https://doi.org/10.1029/RG024i002p00217

Jaupart, C., Mareschal, J.-C., & Iarotsky, L. (2016). Radiogenic heat production in the continental crust. *Lithos*, *262*, 398–427. https://doi.org/10.1016/j.lithos.2016.07.017

Ji, Y., Yoshioka, S., Manea, V. C., Manea, M., & Suenaga, N. (2019). Subduction thermal structure, metamorphism and seismicity beneath north-central Chile. *Journal of Geodynamics*, *129*, 299–312. https://doi.org/10.1016/j.jog.2018.09.004

John, T., Medvedev, S., Rüpke, L. H., Andersen, T. B., Podladchikov, Y. Y., & Austrheim, H. (2009). Generation of intermediate-depth earthquakes by self-localizing thermal runaway. *Nature Geoscience*, *2*(2), 137–140. https://doi.org/10.1038/ngeo419

Jones, R. E., De Hoog, J. C., Kirstein, L. A., Kasemann, S. A., Hinton, R., Elliott, T., & Litvak, V. D. (2014). Temporal variations in the influence of the subducting slab on Central Andean arc magmas: Evidence from boron isotope systematics. *Earth and Planetary Science Letters*, *408*, 390–401. https://doi.org/10.1016/j.epsl.2014.10.004

Jones, R. E., Kirstein, L. A., Kasemann, S. A., Dhuime, B., Elliott, T., Litvak, V. D., et al. (2015). Geodynamic controls on the contamination of Cenozoic arc magmas in the southern Central Andes: Insights from the O and Hf isotopic composition of zircon. *Geochimica et Cosmochimica Acta*, *164*, 386–402.

Jones, R. E., Kirstein, L. A., Kasemann, S. A., Litvak, V. D., Poma, S., Alonso, R. N., & Hinton, R. (2016). The role of changing geodynamics in the progressive contamination of Late Cretaceous to Late Miocene arc magmas in the southern Central Andes. *Lithos*, *262*, 169–191. https://doi.org/10.1016/j.lithos.2016.07.002

Jones, R. E. (2014). *Subduction zone processes and continental crust formation in the southern Central Andes : insights from geochemistry and geochronology* (Ph.D.). University of Edinburgh. Retrieved from http://hdl.handle.net/1842/9672

Jordan, T.E., Schlunegger, F., & Cardozo, N. (2001). Unsteady and spatially variable evolution of the Neogene Andean Bermejo foreland basin, Argentina. *Journal of South American Earth Sciences*, *14*(7), 775–798. https://doi.org/10.1016/S0895-9811(01)00072-4

Jordan, T. E, & Allmendinger, R. W. (1986). The Sierras Pampeanas of Argentina; a modern analogue of Rocky Mountain foreland deformation. *American Journal of Science*, *286*(10), 737–764. https://doi.org/10.2475/ajs.286.10.737

Jordan, T. E, Isacks, B. L., Allmendinger, R. W., Brewer, J. A., Ramos, V. A., & Ando, C. J. (1983). Andean tectonics related to geometry of subducted Nazca plate. *Geological Society of America Bulletin*, *94*(3), 341–361.

Jordan, T.E., Kay, S. M., & Isacks, B. L. (1997). The evolution of the Altiplano-Puna plateau of the Central Andes. *Annual Review of Earth and Planetary Sciences*, *25*(1), 139–174. https://doi.org/10.1146/annurev.earth.25.1.139.

Kaban, M. K., Tesauro, M., Mooney, W. D., & Cloetingh, S. A. P. L. (2014). Density, temperature, and composition of the North American lithosphere-New insights from a joint analysis of seismic, gravity, and mineral physics data: 1. Density structure of the crust and upper mantle. *Geochemistry, Geophysics, Geosystems*, *15*(12), 4781–4807. https://doi.org/10.1002/2014GC005483

Kaislaniemi, L., Hunen, J., & Bouilhol, P. (2018). Lithosphere Destabilization by Melt Weakening and Crust-Mantle Interactions: Implications for Generation of Granite-Migmatite Belts, 15.

Karner, G., Taylor, B., Driscoll, N., & Kohlstedt, D. (Eds.). (2004). *Rheology and Deformation of the Lithosphere at Continental Margins*. Columbia University Press. https://doi.org/10.7312/karn12738

Katayama, I., & Karato, S. (2008). Low-temperature, high-stress deformation of olivine under water-saturated conditions. *Physics of the Earth and Planetary Interiors*, *168*(3), 125–133. https://doi.org/10.1016/j.pepi.2008.05.019

Kay, S.M. (1991). Magma source variations for mid-late Tertiary magmatic rocks associated with a shallowing subduction zone and a thickening crust in the central Andes (28 to 33°S). *Pecial Paper of the Geological Society of America*, *265*, 113–137. http://dx.doi.org/10.1130/SPE265-p113

Kay, S.M., & Copeland, P. (2006). Early to middle Miocene backarc magmas of the Neuquén Basin: Geochemical consequences of slab shallowing and the westward drift of South America. https://doi.org/10.1130/2006.2407(09)

Kay, S.M., & Mpodozis, C. (2002). Magmatism as a probe to the Neogene shallowing of the Nazca plate beneath the modern Chilean ¯at-slab. *Journal of South American Earth Sciences*, 19.

Kay, S.M., Ramos, V. A., Mpodozis, C., & Sruoga, P. (1989). Late Paleozoic to Jurassic silicic magmatism at the Gondwana margin: Analogy to the Middle Proterozoic in North America? *Geology*, *17*(4), 324–328. https://doi.org/10.1130/0091-7613(1989)017<0324:LPTJSM>2.3.CO;2

Kay, S.M., Coira, B., & Viramonte, J. (1994). Young mafic back arc volcanic rocks as indicators of continental lithospheric delamination beneath the Argentine Puna Plateau, central Andes. *Journal of Geophysical Research: Solid Earth*, *99*(B12), 24323–24339. https://doi.org/10.1029/94JB00896

Kay, S.M., Godoy, E., & Kurtz, A. (2005). Episodic arc migration, crustal thickening, subduction erosion, and magmatism in the south-central Andes. *GSA Bulletin*, *117*(1–2), 67–88. https://doi.org/10.1130/B25431.1

Kay, S.M., Mancilla, O., & Copeland, P. (2006a). Evolution of the late Miocene Chachahuén volcanic complex at 37°S over a transient shallow subduction zone under the Neuquén Andes. https://doi.org/10.1130/2006.2407(10)

Kay, S.M., Burns, W. M., Copeland, P., & Mancilla, O. (2006b). Upper Cretaceous to Holocene magmatism and evidence for transient Miocene shallowing of the Andean subduction zone under the northern Neuquén Basin. In Suzanne Mahlburg Kay & V. A. Ramos (Eds.), *Evolution of an Andean Margin: A Tectonic and Magmatic View from the Andes to the Neuquén Basin (35°-39°S lat)* (Vol. 407, p. 0). Geological Society of America. https://doi.org/10.1130/2006.2407(02)

van Keken, P. E., Wada, I., Sime, N., & Abers, G. A. (2019). Thermal Structure of the Forearc in Subduction Zones: A Comparison of Methodologies. *Geochemistry, Geophysics, Geosystems*, *20*(7), 3268–3288. https://doi.org/10.1029/2019GC008334

Kennett, B. L. N., Engdahl, E. R., & Buland, R. (1995). Constraints on seismic velocities in the Earth from traveltimes. *Geophysical Journal International*, *122*(1), 108–124. https://doi.org/10.1111/j.1365-246X.1995.tb03540.x

Kirby, S. (1995). Interslab earthquakes and phase changes in subducting lithosphere. *Reviews of Geophysics*, *33*(S1), 287–297. https://doi.org/10.1029/95RG00353

Kleiman, L. E., & Japas, M. S. (2009). The Choiyoi volcanic province at 34°S–36°S (San Rafael, Mendoza, Argentina): Implications for the Late Palaeozoic evolution of the southwestern margin of Gondwana. *Tectonophysics*, *473*(3), 283–299. https://doi.org/10.1016/j.tecto.2009.02.046

Kley, J., Monaldi, C. R., & Salfity, J. A. (1999). Along-strike segmentation of the Andean foreland: causes and consequences. *Tectonophysics*, *301*(1), 75–94. https://doi.org/10.1016/S0040-1951(98)90223-2

Kley, J., & Monaldi, C. R. (1998). Tectonic shortening and crustal thickness in the Central Andes: How good is the correlation? *Geology*, *26*(8), 723–726. https://doi.org/10.1130/0091-7613(1998)026<0723:TSACTI>2.3.CO;2

Kley, J., & Monaldi, C. R. (2002). Tectonic inversion in the Santa Barbara System of the central Andean foreland thrust belt, northwestern Argentina. *Tectonics*, *21*(6), 11-1-11–18. https://doi.org/10.1029/2002TC902003

Kopp, H., Flueh, E. R., Papenberg, C., & Klaeschen, D. (2004). Seismic investigations of the O'Higgins Seamount Group and Juan Fernández Ridge: Aseismic ridge emplacement and lithosphere hydration. *Tectonics*, *23*(2). https://doi.org/10.1029/2003TC001590

Koptev, A. I., & Ershov, A. V. (2011). Thermal thickness of the Earth's lithosphere: a numerical model. *Moscow University Geology Bulletin*, *66*(5), 323–330. https://doi.org/10.3103/S014587521105005X

Krawczyk, C. M., Mechie, J., Lüth, S., Tašárová, Z., Wigger, P., Stiller, M., et al. (2006). Geophysical Signatures and Active Tectonics at the South-Central Chilean Margin. In O. Oncken, G. Chong, G. Franz, P. Giese, H.-J. Götze, V. A. Ramos, et al. (Eds.), *The Andes* (pp. 171–192). Springer Berlin Heidelberg. https://doi.org/10.1007/978-3-540-48684-8_8

Krischer, L., Megies, T., Barsch, R., Beyreuther, M., Lecocq, T., Caudron, C., & Wassermann, J. (2015). ObsPy: a bridge for seismology into the scientific Python ecosystem. *Computational Science & Discovery*, *8*(1), 014003. https://doi.org/10.1088/1749-4699/8/1/014003

KRISP Working Party. (1991). Large-scale variation in lithospheric structure along and across the Kenya rift. *Nature*, *354*(6350), 223–227. https://doi.org/10.1038/354223a0

Kumar, N., Aoudia, A., Guidarelli, M., Babu, V. G., Hazarika, D., & Yadav, D. K. (2019). Delineation of lithosphere structure and characterization of the Moho geometry under the Himalaya–Karakoram–Tibet collision zone using surface-wave tomography. *Geological Society, London, Special Publications*, *481*(1), 19. https://doi.org/10.1144/SP481-2017-172

Kusznir, N. J., & Park, R. G. (1984). Intraplate lithosphere deformation and the strength of the lithosphere. *Geophysical Journal International*, *79*(2), 513–538. https://doi.org/10.1111/j.1365-246X.1984.tb02238.x

Lamb, S., & Davis, P. (2003). Cenozoic climate change as a possible cause for the rise of the Andes. *Nature*, *425*(6960), 792–797. https://doi.org/10.1038/nature02049

Lara, L. E., Flores, F., Calderón, R., & Cardona, C. (2021). Chapter 17 - Volcano hazards and risks in Chile. In P. Papale (Ed.), *Forecasting and Planning for Volcanic Hazards, Risks, and Disasters* (Vol. 2, pp. 617–633). Elsevier. https://doi.org/10.1016/B978-0-12-818082-2.00017-2

Laske, G., Masters, G., Ma, Z., & Pasyanos, M. (2013). Update on CRUST1.0 -A 1-degree Global Model of Earth's Crust. Presented at the EGU2013.

Leech, M. L. (2001). Arrested orogenic development: eclogitization, delamination, and tectonic collapse. *Earth and Planetary Science Letters*, *185*(1–2), 149–159. https://doi.org/10.1016/S0012-821X(00)00374-5

Legarreta, L, & Gulisano, C. (1989). Análisis estratigráfico secuencial de la Cuenca Neuquina (Triásico Superior-Terciario Inferior). In *Cuencas Sedimentarias Argentinas* (pp. 221–243). Tucumán: Universidad Nacional de Tucumán.

Legarreta, L., & Uliana, M. (1999). El Jurásico y Cretácico de la Cordillera Principal y la cuenca Neuquina. 1. Facies sedimentarias. In *Geología Argentina* (Vol. Anales no. 29, pp. 399–416). Servicio Geológico y Minero Argentino.

Leng, W., & Mao, W. (2015). Geodynamic modeling of thermal structure of subduction zones. *Science China Earth Sciences*, *58*(7), 1070–1083. https://doi.org/10.1007/s11430-015-5107-5

Linkimer, L., Beck, S., Zandt, G., Alvarado, P., Anderson, M., Gilbert, H., & Zhang, H. (2020). Lithospheric structure of the Pampean flat slab region from double-difference tomography. *Journal of South American Earth Sciences*, *97*, 102417. https://doi.org/10.1016/j.jsames.2019.102417

Litvak, V. D., Poma, S., & Kay, S. M. (2007). Paleogene and Neogene magmatism in the Valle del Cura region: New perspective on the evolution of the Pampean flat slab, San Juan province, Argentina. *Journal of South American Earth Sciences*, *24*(2), 117–137. https://doi.org/10.1016/j.jsames.2007.04.002

Litvak, V. D., Poma, S., Jones, R. E., Fernández Paz, L., Iannelli, S. B., Spagnuolo, M., et al. (2018). The Late Paleogene to Neogene Volcanic Arc in the Southern Central Andes (28°–37° S). In Andrés Folguera, E. Contreras-Reyes, N. Heredia, A. Encinas, S. B. Iannelli, V. Oliveros, et al. (Eds.), *The Evolution of the Chilean-Argentinean Andes* (pp. 503–536). Cham: Springer International Publishing. https://doi.org/10.1007/978-3-319-67774-3_20

Liu, D. C., & Nocedal, J. (1989). On the limited memory BFGS method for large scale optimization. *Mathematical Programming*, *45*(1), 503–528. https://doi.org/10.1007/BF01589116

Liu, L., & Zoback, M. D. (1997). Lithospheric strength and intraplate seismicity in the New Madrid seismic zone. *Tectonics*, *16*(4), 585–595. https://doi.org/10.1029/97TC01467

Liu, S. (2020). *Controls of foreland-deformation patterns in the orogen-foreland shortening system*. Retrieved from https://publishup.uni-potsdam.de/frontdoor/index/index/docId/44573

Llambias, E. J., & Sato, A. M. (1990). El Batolito de Colangüil (29-31° S) cordillera frontal de Argentina: estructura y marco tectonico. *Andean Geology*, *17*(1), 89–108. http://dx.doi.org/10.5027/andgeoV17n1-a04

Llambias, E. J., Kleiman, L. E., & Salvarredi, J. A. (1993). El magmatismo gondwánico (pp. 53–64). Presented at the Geología y Recursos Naturales de Mendoza (Ramos, V.; editor). Congreso Geológico Argentino.

Llambias, E. J., Bertotto, G. W., Risso, C., & Hernando, I. (2010). El volcanismo cuaternario en el retroarco de Payenia: una revisión. *Revista de La Asociación Geológica Argentina*, *67*(2), 278–300.

López-Gamundí, O. (2006). Permian plate margin volcanism and tuffs in adjacent basins of west Gondwana: Age constraints and common characteristics. *Comparison between Intracratonic and Active Margin 4 Basins: Examples from the Late Paleozoic of Western Gondwana*, *22*(3), 227–238. https://doi.org/10.1016/j.jsames.2006.09.012

Lossada, A. C., Giambiagi, L., Hoke, G., Mescua, J., Suriano, J., & Mazzitelli, M. (2018). Cenozoic Uplift and Exhumation of the Frontal Cordillera Between 30° and 35° S and the Influence of the Subduction Dynamics in the Flat Slab Subduction Context, South Central Andes. In *The Evolution of the Chilean-Argentinean Andes* (pp. 387–409). Springer.

Lucazeau, F. (2019). Analysis and Mapping of an Updated Terrestrial Heat Flow Data Set. *Geochemistry, Geophysics, Geosystems*, *20*(8), 4001–4024. https://doi.org/10.1029/2019GC008389

Lucazeau, F., & Le Douaran, S. (1985). The blanketing effect of sediments in basins formed by extension: a numerical model. Application to the Gulf of Lion and Viking graben. *Earth and Planetary Science Letters*, *74*(1), 92–102. https://doi.org/10.1016/0012-821X(85)90169-4

Maaløe, S., & Aoki, K. (1977). The major element composition of the upper mantle estimated from the composition of lherzolites. *Contributions to Mineralogy and Petrology*, *63*(2), 161–173. https://doi.org/10.1007/BF00398777

Maggi, A., Jackson, J. A., McKenzie, D., & Priestley, K. (2000). Earthquake focal depths, effective elastic thickness, and the strength of the continental lithosphere. *Geology*, *28*(6), 495–498.

Majorowicz, J., Polkowski, M., & Grad, M. (2019). Thermal properties of the crust and the lithosphere–asthenosphere boundary in the area of Poland from the heat flow variability and seismic data. *International Journal of Earth Sciences*, *108*(2), 649–672. https://doi.org/10.1007/s00531-018-01673-8

Maloney, K. T., Clarke, G. L., Klepeis, K. A., & Quevedo, L. (2013). The Late Jurassic to present evolution of the Andean margin: Drivers and the geological record: evolution of the Andean margin. *Tectonics*, *32*(5), 1049–1065. https://doi.org/10.1002/tect.20067

Manea, V.C., Manea, M., Ferrari, L., Orozco-Esquivel, T., Valenzuela, R. W., Husker, A., & Kostoglodov, V. (2017). A review of the geodynamic evolution of flat slab subduction in Mexico, Peru, and Chile. *Tectonophysics*, *695*, 27–52. https://doi.org/10.1016/j.tecto.2016.11.037

Manea, V. C, & Manea, M. (2011). Flat-slab thermal structure and evolution beneath central Mexico. *Pure and Applied Geophysics*, *168*(8–9), 1475–1487.

Manea, V. C., Pérez-Gussinyé, M., & Manea, M. (2012). Chilean flat slab subduction controlled by overriding plate thickness and trench rollback. *Geology*, *40*(1), 35–38. https://doi.org/10.1130/G32543.1

Mareschal, J.-C., & Jaupart, C. (2011). Energy Budget of the Earth. In H. K. Gupta (Ed.), *Encyclopedia of Solid Earth Geophysics* (pp. 285–291). Dordrecht: Springer Netherlands. https://doi.org/10.1007/978-90-481-8702-7_64

Mareschal, J.-C., & Jaupart, C. (2013). Radiogenic heat production, thermal regime and evolution of continental crust. *Moho: 100 Years after Andrija Mohorovicic*, *609*, 524–534. https://doi.org/10.1016/j.tecto.2012.12.001

Marot, M., Monfret, T., Gerbault, M., Nolet, G., Ranalli, G., & Pardo, M. (2014). Flat versus normal subduction zones: a comparison based on 3-D regional traveltime tomography and petrological modelling of central Chile and western Argentina (29°–35°S). *Geophysical Journal International*, *199*(3), 1633–1654. https://doi.org/10.1093/gji/ggu355

Martínez, F., Arriagada, C., Peña, M., Deckart, K., & Charrier, R. (2016). Tectonic styles and crustal shortening of the Central Andes “Pampean” flat-slab segment in northern Chile (27–29°S). *Tectonophysics*, *667*, 144–162. https://doi.org/10.1016/j.tecto.2015.11.019

Martínez, F., Parra, M., Arriagada, C., Mora, A., Bascuñan, S., & Peña, M. (2017). Late Cretaceous to Cenozoic deformation and exhumation of the Chilean Frontal Cordillera (28°–29°S), Central Andes. *Journal of Geodynamics*, *111*, 31–42. https://doi.org/10.1016/j.jog.2017.08.004

Martínez, F., Arriagada, C., & Bascuñán, S. (2018). Mechanisms and Episodes of Deformation Along the Chilean–Pampean Flat-Slab Subduction Segment of the Central Andes in Northern Chile. In Andrés Folguera, E. Contreras-Reyes, N. Heredia, A. Encinas, S. B. Iannelli, V. Oliveros, et al. (Eds.), *The Evolution of the Chilean-Argentinean Andes* (pp. 273–290). Cham: Springer International Publishing. https://doi.org/10.1007/978-3-319-67774-3_11

Martino, R. D. (2003). Las fajas de deformación dúctil de las Sierras Pampeanas de Córdoba: Una reseña general. *Revista de La Asociación Geológica Argentina*, *58*(4), 549–571.

Martinod, J., Gérault, M., Husson, L., & Regard, V. (2020). Widening of the Andes: An interplay between subduction dynamics and crustal wedge tectonics. *Earth-Science Reviews*, *204*, 103170. https://doi.org/10.1016/j.earscirev.2020.103170

McCaffrey, R. (2007). The Next Great Earthquake. *Science*, *315*(5819), 1675. https://doi.org/10.1126/science.1140173

McGlashan, N., Brown, L., & Kay, S. (2008). Crustal thickness in the central Andes from teleseismically recorded depth phase precursors. *Geophysical Journal International*, *175*(3), 1013–1022. https://doi.org/10.1111/j.1365-246X.2008.03897.x

McKenzie, D., Jackson, J., & Priestley, K. (2005). Thermal structure of oceanic and continental lithosphere. *Earth and Planetary Science Letters*, *233*(3–4), 337–349. https://doi.org/10.1016/j.epsl.2005.02.005

McKinney, W. (2010). Data Structures for Statistical Computing in Python. In S. van der Walt & J. Millman (Eds.), *Proceedings of the 9th Python in Science Conference* (pp. 56–61). https://doi.org/10.25080/Majora-92bf1922-00a

Meeßen. (2017). *VelocityConversion. V. v1.0.1*. GFZ Data Services. Retrieved from http://doi.org/10.5880/GFZ.6.1.2017.001

Meeßen, C., Sippel, J., Scheck-Wenderoth, M., Heine, C., & Strecker, M. R. (2018). Crustal Structure of the Andean Foreland in Northern Argentina: Results From Data-Integrative

Three-Dimensional Density Modeling. *Journal of Geophysical Research: Solid Earth*, *123*(2), 1875–1903. https://doi.org/10.1002/2017JB014296

Meeßen, C. (2019). *The thermal and rheological state of the Northern Argentinian foreland basins* (doctoralthesis). Universität Potsdam. https://doi.org/10.25932/publishup-43994

Meeßen, C. (2020). VeloDT v1.2 (Version v1.2). Zenodo. https://doi.org/10.5281/zenodo.3895784

Mescua, J. F., Giambiagi, L. B., Tassara, A., Gimenez, M., & Ramos, V. A. (2014). Influence of pre-Andean history over Cenozoic foreland deformation: structural styles in the Malargüe fold-and-thrust belt at 35 S, Andes of Argentina. *Geosphere*, *10*(3), 585–609. https://doi.org/10.1130/GES00939.1

Mescua, J. F., Giambiagi, L., Barrionuevo, M., Tassara, A., Mardonez, D., Mazzitelli, M., & Lossada, A. (2016). Basement composition and basin geometry controls on upper-crustal deformation in the Southern Central Andes (30–36°S). *Geological Magazine*, *153*(5–6), 945–961. https://doi.org/10.1017/S0016756816000364

MKenzie, D., & Priestley, K. (2008). The influence of lithospheric thickness variations on continental evolution. *Continental Volcanism and the Chemistry of the Earth's Interior*, *102*(1), 1–11. https://doi.org/10.1016/j.lithos.2007.05.005

Mochizuki, K., Henrys, S., Haijima, D., Warren-Smith, E., & Fry, B. (2021). Seismicity and velocity structure in the vicinity of repeating slow slip earthquakes, northern Hikurangi subduction zone, New Zealand. *Earth and Planetary Science Letters*, *563*, 116887. https://doi.org/10.1016/j.epsl.2021.116887

Molnar, P., & Lyon-Caen, H. (1988). Some simple physical aspects of the support, structure, and evolution of mountain belts. https://doi.org/10.1130/SPE218-p179

Mon, R., & Salfity, J. (1995). Tectonic evolution of the Andes of northern Argentina. In *Petroleum Basins of South America* (Vol. 62). Houston: AAPG Special Volumes.

Montero-Lopez, M. C., Hongn, F. D., Strecker, M. R., Marrett, R., Seggiaro, R., & Sudo, M. (2010). Late Miocene–early Pliocene onset of N–S extension along the southern margin of the Central Andean Puna Plateau: Evidence from magmatic, geochronological and structural observations. *Tectonophysics*, *494*(1), 48–63. https://doi.org/10.1016/j.tecto.2010.08.010

Montero-López, C., Hongn, F., López Steinmetz, R. L., Aramayo, A., Pingel, H., Strecker, M. R., et al. (2020). Development of an incipient Paleogene topography between the present-day Eastern Andean Plateau (Puna) and the Eastern Cordillera, southern Central Andes, NW Argentina. *Basin Research*, *n/a*(n/a). https://doi.org/10.1111/bre.12510

Moreno, M., Li, S., Melnick, D., Bedford, J. R., Baez, J. C., Motagh, M., et al. (2018). Chilean megathrust earthquake recurrence linked to frictional contrast at depth. *Nature Geoscience*, *11*(4), 285–290. https://doi.org/10.1038/s41561-018-0089-5

Moreno, M., Rosenau, M., & Oncken, O. (2010). 2010 Maule earthquake slip correlates with pre-seismic locking of Andean subduction zone. *Nature*, *467*(7312), 198–202. https://doi.org/10.1038/nature09349

Moreno, M., Haberland, C., Oncken, O., Rietbrock, A., Angiboust, S., & Heidbach, O. (2014). Locking of the Chile subduction zone controlled by fluid pressure before the 2010 earthquake. *Nature Geoscience*, *7*(4), 292–296. https://doi.org/10.1038/ngeo2102

Moscoso, E., Grevemeyer, I., Contreras-Reyes, E., Flueh, E. R., Dzierma, Y., Rabbel, W., & Thorwart, M. (2011). Revealing the deep structure and rupture plane of the 2010 Maule, Chile earthquake (Mw=8.8) using wide angle seismic data. *Earth and Planetary Science Letters*, *307*(1–2), 147–155. https://doi.org/10.1016/j.epsl.2011.04.025

Mpodozis, C., & Kay, S. M. (1990). Provincias magmáticas ácidas y evolución tectónica de Gondwana: Andes chilenos (28-31 S). *Andean Geology*, *17*(2), 153–180. http://dx.doi.org/10.5027/andgeoV17n2-a03

Mpodozis, C., & Ramos, V. (1990). The Andes of Chile and Argentina.

Muldashev, I. (2017). *Modeling of the great earthquake seismic cycles*. Retrieved from https://publishup.uni-potsdam.de/opus4-ubp/frontdoor/index/index/docId/39892

Müller, R. D., Sdrolias, M., Gaina, C., & Roest, W. R. (2008). Age, spreading rates, and spreading asymmetry of the world's ocean crust. *Geochemistry, Geophysics, Geosystems*, *9*(4). https://doi.org/10.1029/2007GC001743

Muñoz, J., Troncoso, R., Duhart, P., Crignola, P., Farmer, L., & Stern, C. R. (2000). The relation of the mid-Tertiary coastal magmatic belt in south-central Chile to the late Oligocene increase in plate convergence rate. *Revista Geológica de Chile*, *27*, 177–203.

Nacif, S., Triep, E., Furlani, R., & Spagnotto, S. (2013). Stripe of normal mechanisms for crustal earthquakes with M ≤ 3.5 flanking the western side of the thrust front zone in the Andes backarc. *Natural Science*, *05*(08), 18–26. https://doi.org/10.4236/ns.2013.58A1003

Nacif, S., Lupari, M., Triep, E. G., Nacif, A., Álvarez, O., Folguera, A., & Gímenez, M. (2017). Change in the pattern of crustal seismicity at the Southern Central Andes from a local seismic network. *Tectonophysics*, *708*, 56–69. https://doi.org/10.1016/j.tecto.2017.04.012

Nasi, C., Mpodozis, C., Cornejo, P., Moscoso, R., & Maksaev, V. (2010). El batolito Elqui-Limari (Paleozoico Superior-Triásico): características petrográficas, geoquímicas y significado tectónico. *Andean Geology*, (25–26), 77–11. https://doi.org/10.5027/andgeoV12n2-3-a06

Olivar, J., Nacif, S., Fennell, L., & Folguera, A. (2018). Within plate seismicity analysis in the segment between the high Cordillera and the Precordillera of northern Mendoza (Southern Central Andes). *Geodesy and Geodynamics*, *9*(1), 13–24. https://doi.org/10.1016/j.geog.2017.09.004

Oliveros, V., Morata, D., Aguirre, L., Feraud, G., & Fornari, M. (2010). Jurassic to Early Cretaceous subduction-related magmatism in the Coastal Cordillera of northern Chile (18°30'-24°S): geochemistry and petrogenesis. *Revista Geológica de Chile*, *34*(2), 209–232. http://dx.doi.org/10.5027/andgeoV34n2-a03

Oliveros, V., González, J., Espinoza Vargas, M., Vásquez, P., Rossel, P., Creixell, C., et al. (2018). The Early Stages of the Magmatic Arc in the Southern Central Andes. In Andrés Folguera, E. Contreras-Reyes, N. Heredia, A. Encinas, S. B. Iannelli, V. Oliveros, et al. (Eds.), *The Evolution of the Chilean-Argentinean Andes* (pp. 165–190). Cham: Springer International Publishing. https://doi.org/10.1007/978-3-319-67774-3_7

Oncken, O., Hindle, D., Kley, J., Elger, K., Victor, P., & Schemmann, K. (2006). Deformation of the Central Andean Upper Plate System — Facts, Fiction, and Constraints for Plateau Models. In O. Oncken, G. Chong, G. Franz, P. Giese, H.-J. Götze, V. A. Ramos, et al. (Eds.), *The Andes: Active Subduction Orogeny* (pp. 3–27). Berlin, Heidelberg: Springer Berlin Heidelberg. https://doi.org/10.1007/978-3-540-48684-8_1

Oncken, O., Chong, G., Gerhard, F., Giese, P., Götze, H.-J., Ramos, V. A., et al. (2006). *The Andes: Active Subduction Orogeny* (1st ed.). Heidelberg: Springer-Verlag Berlin Heidelberg. Retrieved from https://www.springer.com/gp/book/9783540243298

Otamendi, J. E., Vujovich, G. I., de la Rosa, J. D., Tibaldi, A. M., Castro, A., Martino, R. D., & Pinotti, L. P. (2009). Geology and petrology of a deep crustal zone from the Famatinian paleo-arc, Sierras de Valle Fértil and La Huerta, San Juan, Argentina. *Journal of South American Earth Sciences*, *27*(4), 258–279. https://doi.org/10.1016/j.jsames.2008.11.007

Pacheco, J. F., & Sykes, L. R. (1992). Seismic moment catalog of large shallow earthquakes, 1900 to 1989. *Bulletin of the Seismological Society of America*, *82*(3), 1306–1349.

del Papa, C., Hongn, F., Powell, J., Payrola, P., Do Campo, M., Strecker, M. R., et al. (2013). Middle Eocene-Oligocene broken-foreland evolution in the Andean Calchaqui Valley, NW Argentina: insights from stratigraphic, structural and provenance studies. *Basin Research*, *25*(5), 574–593. https://doi.org/10.1111/bre.12018

Parada, M.A, Nyström, J. O., & Levi, B. (1999). Multiple sources for the Coastal Batholith of central Chile (31–34°S): geochemical and Sr–Nd isotopic evidence and tectonic implications. *Lithos*, *46*(3), 505–521. https://doi.org/10.1016/S0024-4937(98)00080-2

Parada, M. A., López-Escobar, L., Oliveros, V., Fuentes, F., Morata, D., Calderón, M., et al. (2007). Andean magmatism. In *The Geology of chile* (pp. 115–146). Retrieved from http://www.scopus.com/inward/record.url?scp=34347328140&partnerID=8YFLogxK

Pardo, M., Comte, D., & Monfret, T. (2002). Seismotectonic and stress distribution in the central Chile subduction zone. *Journal of South American Earth Sciences*, *15*(1), 11–22.

Pavlis, N. K., Holmes, S. A., Kenyon, S. C., & Factor, J. K. (2012). The development and evaluation of the Earth Gravitational Model 2008 (EGM2008). *Journal of Geophysical Research: Solid Earth*, *117*(B4). https://doi.org/10.1029/2011JB008916

Pawlowicz, R. (2013). Key physical variables in the ocean: temperature, salinity, and density. *Nature Education Knowledge*, *4*(4), 13.

Peacock, S. M. (2001). Are the lower planes of double seismic zones caused by serpentine dehydration in subducting oceanic mantle? *Geology*, *29*(4), 299–302. https://doi.org/10.1130/0091-7613(2001)029<0299:ATLPOD>2.0.CO;2

Peacock, S. M. (2020). Advances in the thermal and petrologic modeling of subduction zones. *Geosphere*, *16*(4), 936–952. https://doi.org/10.1130/GES02213.1

Pearson, D. M., Kapp, P., DeCelles, P. G., Reiners, P. W., Gehrels, G. E., Ducea, M. N., & Pullen, A. (2013). Influence of pre-Andean crustal structure on Cenozoic thrust belt kinematics and shortening magnitude: Northwestern Argentina. *Geosphere*, *9*(6), 1766–1782. https://doi.org/10.1130/GES00923.1

Penniston-Dorland, S. C., Kohn, M. J., & Manning, C. E. (2015). The global range of subduction zone thermal structures from exhumed blueschists and eclogites: Rocks are hotter than models. *Earth and Planetary Science Letters*, *428*, 243–254. https://doi.org/10.1016/j.epsl.2015.07.031

Perarnau, M., Gilbert, H., Alvarado, P., Martino, R., & Anderson, M. (2012). Crustal structure of the Eastern Sierras Pampeanas of Argentina using high frequency local receiver functions. *Tectonophysics*, *580*, 208–217. https://doi.org/10.1016/j.tecto.2012.09.021

Pérez Luján, S. B., Ammirati, J.-B., Alvarado, P., & Vujovich, G. I. (2015). Constraining a mafic thick crust model in the Andean Precordillera of the Pampean flat slab subduction region. *Journal of South American Earth Sciences*, *64*, 325–338. https://doi.org/10.1016/j.jsames.2015.09.005

Pesicek, J. D., Engdahl, E. R., Thurber, C. H., DeShon, H. R., & Lange, D. (2012). Mantle subducting slab structure in the region of the 2010 M8.8 Maule earthquake (30-40°S), Chile: Mantle subducting slab structure in Chile. *Geophysical Journal International*, *191*(1), 317–324. https://doi.org/10.1111/j.1365-246X.2012.05624.x

Petitjean, S., Rabinowicz, M., Grégoire, M., & Chevrot, S. (2006). Differences between Archean and Proterozoic lithospheres: Assessment of the possible major role of thermal conductivity: ARCHEAN CRATON THICKNESS. *Geochemistry, Geophysics, Geosystems*, *7*(3), n/a-n/a. https://doi.org/10.1029/2005GC001053

Petricca, P., Carminati, E., Doglioni, C., & Riguzzi, F. (2018). Brittle-ductile transition depth versus convergence rate in shallow crustal thrust faults: Considerations on seismogenic volume and impact on seismicity. *Physics of the Earth and Planetary Interiors*, *284*, 72–81. https://doi.org/10.1016/j.pepi.2018.09.002

Platt, J. P., Xia, H., & Schmidt, W. L. (2018). Rheology and stress in subduction zones around the aseismic/seismic transition. *Progress in Earth and Planetary Science*, *5*(1), 24. https://doi.org/10.1186/s40645-018-0183-8

Poma, S., Ramos, A., Litvak, V. D., Quenardelle, S., Maisonnave, E. B., & Díaz, I. (2017). Southern Central Andes Neogene magmatism over the Pampean Flat Slab: implications on crustal and slab melts contribution to magma generation in Precordillera, Western Argentina. *Andean Geology*, *44*(3), 249–274. https://doi.org/10.5027/andgeoV44n3-a02

Porter, R., Gilbert, H., Zandt, G., Beck, S., Warren, L., Calkins, J., et al. (2012). Shear wave velocities in the Pampean flat-slab region from Rayleigh wave tomography: Implications for slab and upper mantle hydration: PAMPEAN FLAT SLAB SHEAR VELOCITIES. *Journal of Geophysical Research: Solid Earth*, *117*(B11), n/a-n/a. https://doi.org/10.1029/2012JB009350

Prezzi, C., Iglesia Llanos, M. P., Götze, H.-J., & Schmidt, S. (2014). Thermal and geodynamic contributions to the elevation of the Altiplano–Puna plateau. *Physics of the Earth and Planetary Interiors*, *237*, 51–64. https://doi.org/10.1016/j.pepi.2014.10.002

Prezzi, C., Götze, H.-J., & Schmidt, S. (2009). 3D density model of the Central Andes. *Physics of the Earth and Planetary Interiors*, *177*(3–4), 217–234. https://doi.org/10.1016/j.pepi.2009.09.004

Priestley, K, & McKenzie, D. (2006). The thermal structure of the lithosphere from shear wave velocities. *Earth and Planetary Science Letters*, *244*(1–2), 285–301. https://doi.org/10.1016/j.epsl.2006.01.008

Priestley, K., & McKenzie, D. (2013). The relationship between shear wave velocity, temperature, attenuation and viscosity in the shallow part of the mantle. *Earth and Planetary Science Letters*, *381*, 78–91. https://doi.org/10.1016/j.epsl.2013.08.022

Priestley, K., McKenzie, D., & Ho, T. (2018). A Lithosphere–Asthenosphere Boundary—a Global Model Derived from Multimode Surface-Wave Tomography and Petrology. In *Lithospheric Discontinuities* (pp. 111–123). American Geophysical Union (AGU). https://doi.org/10.1002/9781119249740.ch6

Prieto, G. A., Froment, B., Chunquan, Y., Poli, P., & Abercrombie, R. (2017). Earthquake rupture below the brittle-ductile transition in continental lithospheric mantle. *Science Advances*, *3*(3), e1602642. https://doi.org/10.1126/sciadv.1602642

QGIS Development Team. (2009). *QGIS Geographic Information System*. Open Source Geospatial Foundation. Retrieved from http://qgis.osgeo.org

Ramos, V.A, Jordan, T., Allmendinger, R. W., Mpodozis, C., Kay, S. M., Cortés, J., & Palma, M. (1986). Paleozoic terranes of the central Argentine-Chilean Andes. *Tectonics*, *5*(6), 855–880.

Ramos, V. A. (1988). The tectonics 0f the Central Andes; 30 to 33 S latitude. *Processes in Continental Lithospheric Deformation*, *218*, 31.

Ramos, V. A. (1988). The tectonics of the Central Andes; 30° to 33° S latitude. In S. P. Clark Jr., B. C. Burchfiel, & J. Suppe (Eds.), *Processes in Continental Lithospheric Deformation* (Vol. 218, p. 0). Geological Society of America. https://doi.org/10.1130/SPE218-p31

Ramos, V. A. (2008). The Basement of the Central Andes: The Arequipa and Related Terranes. *Annual Review of Earth and Planetary Sciences*, *36*(1), 289–324. https://doi.org/10.1146/annurev.earth.36.031207.124304

Ramos, V. A. (2010). The Grenville-age basement of the Andes. *The Grenville Orogen in Central and South America*, *29*(1), 77–91. https://doi.org/10.1016/j.jsames.2009.09.004

Ramos, V. A. (2018). The Famatinian Orogen Along the Protomargin of Western Gondwana: Evidence for a Nearly Continuous Ordovician Magmatic Arc Between Venezuela and Argentina. In Andrés Folguera, E. Contreras-Reyes, N. Heredia, A. Encinas, S. B. Iannelli, V. Oliveros, et al. (Eds.), *The Evolution of the Chilean-Argentinean Andes* (pp. 133–161). Cham: Springer International Publishing. https://doi.org/10.1007/978-3-319-67774-3_6

Ramos, V. A., & Folguera, A. (2009). Andean flat-slab subduction through time. *Geological Society, London, Special Publications*, *327*(1), 31–54. https://doi.org/10.1144/SP327.3

Ramos, V. A, & Kay, S. M. (1991). Triassic rifting and associated basalts in the Cuyo basin, central Argentina. In *Andean magmatism and its tectonic setting* (Vol. 265, pp. 79–91). Geological Society of America Boulder.

Ramos, V. A, Cegarra, M., & Cristallini, E. (1996). Cenozoic tectonics of the High Andes of west-central Argentina (30–36 S latitude). *Tectonophysics*, *259*(1–3), 185–200. https://doi.org/10.1016/0040-1951(95)00064-X

Ramos, V. A., Dallmeyer, R. D., & Vujovich, G. (1998). Time constraints on the Early Palaeozoic docking of the Precordillera, central Argentina. *Geological Society, London, Special Publications*, *142*(1), 143–158. https://doi.org/10.1144/GSL.SP.1998.142.01.08

Ramos, V.A., Cristallini, E. O., & Pérez, D. J. (2002). The Pampean flat-slab of the Central Andes. *Flat-Slab Subduction in the Andes*, *15*(1), 59–78. https://doi.org/10.1016/S0895-9811(02)00006-8

Ramos, V.A., Vujovich, G., Martino, R., & Otamendi, J. (2010). Pampia: A large cratonic block missing in the Rodinia supercontinent. *Journal of Geodynamics*, *50*(3–4), 243–255. https://doi.org/10.1016/j.jog.2010.01.019

Ramos, V. A., Litvak, V. D., Folguera, A., & Spagnuolo, M. (2014). An Andean tectonic cycle: From crustal thickening to extension in a thin crust (34°–37°SL). *Geoscience Frontiers*, *5*(3), 351–367. https://doi.org/10.1016/j.gsf.2013.12.009

Ramos, V. A., & Kay, S. M. (2006). Overview of the tectonic evolution of the southern Central Andes of Mendoza and Neuquén (35°–39°S latitude). https://doi.org/10.1130/2006.2407(01)

Ranalli, G. (1994). Nonlinear flexure and equivalent mechanical thickness of the lithosphere. *Tectonophysics*, *240*(1–4), 107–114. https://doi.org/10.1016/0040-1951(94)90266-6

Ranalli, G. (1995). *Rheology of the Earth* (2nd ed.). Springer Netherlands.

Ranalli, G. (1997). Rheology and deep tectonics. *Annals of Geophysics*, *40*(3), 3. https://doi.org/10.4401/ag-3893

Ranalli, G., & Murphy, D. C. (1987). Rheological stratification of the lithosphere. *Tectonophysics*, *132*(4), 281–295. https://doi.org/10.1016/0040-1951(87)90348-9

Rapalini, A. E. (2005). The accretionary history of southern South America from the latest Proterozoic to the Late Palaeozoic: some palaeomagnetic constraints. *Geological Society, London, Special Publications*, *246*(1), 305–328. https://doi.org/10.1144/GSL.SP.2005.246.01.12

Rapela, C., Pankhurst, R., Casquet, C., Baldo, E., Saavedra, J., Galindo, C., & Fanning, C. (1998). The Pampean Orogeny of the southern proto-Andes: Cambrian continental collision in the Sierras de Córdoba. *Geological Society, London, Special Publications*, *142*(1), 181–217. https://doi.org/10.1144/GSL.SP.1998.142.01.10

Richardson, T., Gilbert, H., Anderson, M., & Ridgway, K. D. (2012). Seismicity within the actively deforming Eastern Sierras Pampeanas, Argentina: Seismicity in the actively deforming ESP. *Geophysical Journal International*, *188*(2), 408–420. https://doi.org/10.1111/j.1365-246X.2011.05283.x

Riesner, M., Lacassin, R., Simoes, M., Carrizo, D., & Armijo, R. (2018). Revisiting the Crustal Structure and Kinematics of the Central Andes at 33.5°S: Implications for the Mechanics of Andean Mountain Building. *Tectonics*, *37*(5), 1347–1375. https://doi.org/10.1002/2017TC004513

Rivas, C., Ortiz, G., Alvarado, P., Podesta, M., & Martin, A. (2019). Modern crustal seismicity in the northern Andean Precordillera, Argentina. *Tectonophysics, 762,* 144–158. https://doi.org/10.1016/j.tecto.2019.04.019

Rodriguez Piceda, C., Scheck Wenderoth, M., Gomez Dacal, M. L., Bott, J., Prezzi, C. B., & Strecker, M. R. (2021). Lithospheric density structure of the southern Central Andes constrained by 3D data-integrative gravity modelling. *International Journal of Earth Sciences*, *110*(7), 2333–2359. https://doi.org/10.1007/s00531-020-01962-1

Rodríguez-González, J., Negredo, A. M., & Billen, M. I. (2012). The role of the overriding plate thermal state on slab dip variability and on the occurrence of flat subduction. *Geochemistry, Geophysics, Geosystems*, *13*(1). https://doi.org/10.1029/2011GC003859

Rolandone, F., Bürgmann, R., & Nadeau, R. M. (2004). The evolution of the seismic-aseismic transition during the earthquake cycle: Constraints from the time-dependent depth distribution of aftershocks: AN EVOLVING SEISMIC-ASEISMIC TRANSITION. *Geophysical Research Letters*, *31*(23). https://doi.org/10.1029/2004GL021379

Rudnick, R. L., & Gao, S. (2003). 3.01 - Composition of the Continental Crust. In H. D. Holland & K. K. Turekian (Eds.), *Treatise on Geochemistry* (pp. 1–64). Oxford: Pergamon. https://doi.org/10.1016/B0-08-043751-6/03016-4

Russell, J. K., Dipple, G. M., & Kopylova, M. G. (2001). Heat production and heat flow in the mantle lithosphere, Slave craton, Canada. *Physics of the Earth and Planetary Interiors*, *123*(1), 27–44. https://doi.org/10.1016/S0031-9201(00)00201-6

Saffer, D. M., & Tobin, H. J. (2011). Hydrogeology and Mechanics of Subduction Zone Forearcs: Fluid Flow and Pore Pressure. *Annual Review of Earth and Planetary Sciences*, *39*(1), 157–186. https://doi.org/10.1146/annurev-earth-040610-133408

Sagripanti, L., Colavitto, B., Jagoe, L., Andrés, F., & Costa, C. (2017). A review about the quaternary upper-plate deformation in the Southern Central Andes (36–38°S): A plausible interaction between mantle dynamics and tectonics. *Journal of South American Earth Sciences*, *87*, 221–231. https://doi.org/10.1016/j.jsames.2017.11.008

Sánchez, M. A., Ariza, J. P., García, H. P., Gianni, G. M., Weidmann, M. C., Folguera, A., et al. (2018). Thermo-mechanical analysis of the Andean lithosphere over the Chilean-Pampean flat-slab region. *Journal of South American Earth Sciences*, *87*, 247–257. https://doi.org/10.1016/j.jsames.2017.09.036

Sánchez, M. A., García, H. P. A., Acosta, G., Gianni, G. M., Gonzalez, M. A., Ariza, J. P., et al. (2019). Thermal and lithospheric structure of the Chilean-Pampean flat-slab from gravity and magnetic data. In *Andean Tectonics* (pp. 487–507). Elsevier. https://doi.org/10.1016/B978-0-12-816009-1.00005-8

Sandiford, D., Moresi, L. M., Sandiford, M., Farrington, R., & Yang, T. (2020). The Fingerprints of Flexure in Slab Seismicity. *Tectonics*, *39*(8). https://doi.org/10.1029/2019TC005894

Sato, A. M., Llambías, E. J., Basei, M. A. S., & Castro, C. E. (2015). Three stages in the Late Paleozoic to Triassic magmatism of southwestern Gondwana, and the relationships with the volcanogenic events in coeval basins. *Journal of South American Earth Sciences*, *63*, 48–69. https://doi.org/10.1016/j.jsames.2015.07.005

Saxena, S. K., & Shen, G. (1992). Assessed data on heat capacity, thermal expansion, and compressibility for some oxides and silicates. *Journal of Geophysical Research*, *97*(B13), 19813. https://doi.org/10.1029/92JB01555

Scarfi, L., & Barbieri, G. (2019). New insights on the tectonic structure of the Southern Central Andes – Western Argentina – from seismic tomography. *Geology, Earth & Marine Sciences*, *1*(1). https://doi.org/10.31038/GEMS.2019113

Schaeffer, A. J., & Lebedev, S. (2013). Global shear speed structure of the upper mantle and transition zone. *Geophysical Journal International*, *194*(1), 417–449. https://doi.org/10.1093/gji/ggt095

Scheck-Wenderoth, M., & Maystrenko, Y. P. (2013). Deep Control on Shallow Heat in Sedimentary Basins. *Energy Procedia*, *40*, 266–275. https://doi.org/10.1016/j.egypro.2013.08.031

Scheck-Wenderoth, M., Cacace, M., Maystrenko, Y. P., Cherubini, Y., Noack, V., Kaiser, B. O., et al. (2014). Models of heat transport in the Central European Basin System: Effective mechanisms at different scales. *Marine and Petroleum Geology*, *55*, 315–331. https://doi.org/10.1016/j.marpetgeo.2014.03.009

Schellart, W. P., & Strak, V. (2021). Geodynamic models of short-lived, long-lived and periodic flat slab subduction. *Geophysical Journal International*, *226*(3), 1517–1541. https://doi.org/10.1093/gji/ggab126

Scheuber, E., Bogdanic, T., Jensen, A., & Reutter, K.-J. (1994). Tectonic Development of the North Chilean Andes in Relation to Plate Convergence and Magmatism Since the Jurassic. In K.-J. Reutter, E. Scheuber, & P. J. Wigger (Eds.), *Tectonics of the Southern Central Andes: Structure and Evolution of an Active Continental Margin* (pp. 121–139). Berlin, Heidelberg: Springer Berlin Heidelberg. https://doi.org/10.1007/978-3-642-77353-2_9

Schlumberger. (2011). *Petrel Seismic-to-Evaluation Software*. Houston: Schlumberger Information Solutions.

Schmidt, S., Götze, H.-J., Fichler, C., & Alvers, M. (2010). IGMAS+–a new 3D gravity, FTG and magnetic modeling software. *GEO-INFORMATIK Die Welt Im Netz, Edited by: Zipf, A., Behncke, K., Hillen, F., and Scheffermeyer, J., Akademische Verlagsgesellschaft AKA GmbH, Heidelberg, Germany*, 57–63.

Schoenbohm, L. M., & Strecker, M. R. (2009). Normal faulting along the southern margin of the Puna Plateau, northwest Argentina. *Tectonics*, *28*(5). https://doi.org/10.1029/2008TC002341

Scholz, C. H. (1988). The brittle-plastic transition and the depth of seismic faulting. *Geologische Rundschau*, *77*(1), 319–328. https://doi.org/10.1007/BF01848693

Schurr, B., Rietbrock, A., Asch, G., Kind, R., & Oncken, O. (2006). Evidence for lithospheric detachment in the central Andes from local earthquake tomography. *Tectonophysics*, *415*(1), 203–223. https://doi.org/10.1016/j.tecto.2005.12.007

Schwartz, J. J., Gromet, L. P., & Miró, R. (2008). Timing and Duration of the Calc‐Alkaline Arc of the Pampean Orogeny: Implications for the Late Neoproterozoic to Cambrian Evolution of Western Gondwana. *The Journal of Geology*, *116*(1), 39–61. https://doi.org/10.1086/524122

Sdrolias, M., & Müller, R. D. (2006). Controls on back-arc basin formation. *Geochemistry, Geophysics, Geosystems*, *7*(4), n/a-n/a. https://doi.org/10.1029/2005GC001090

Shapiro, N. M., Ritzwoller, M. H., Mareschal, J. C., & Jaupart, C. (2004). Lithospheric structure of the Canadian Shield inferred from inversion of surface-wave dispersion with thermodynamic *a priori* constraints. *Geological Society, London, Special Publications*, *239*(1), 175–194. https://doi.org/10.1144/GSL.SP.2004.239.01.12

Sharples, W., Jadamec, M. A., Moresi, L. N., & Capitanio, F. A. (2014). Overriding plate controls on subduction evolution. *Journal of Geophysical Research: Solid Earth*, *119*(8), 6684–6704. https://doi.org/10.1002/2014JB011163

Sibson, R. H. (1982). Fault zone models, heat flow, and the depth distribution of earthquakes in the continental crust of the United States. *Bulletin of the Seismological Society of America*, *72*(1), 151–163. https://doi.org/10.1785/BSSA0720010151

Sick, C., Yoon, M.-K., Rauch, K., Buske, S., Lüth, S., Araneda, M., et al. (2006). Seismic Images of Accretive and Erosive Subduction Zones from the Chilean Margin. In O. Oncken, G. Chong, G. Franz, P. Giese, H.-J. Götze, V. A. Ramos, et al. (Eds.), *The Andes* (pp. 147–169). Springer Berlin Heidelberg. https://doi.org/10.1007/978-3-540-48684-8_7

Sigismondi, M. E. (2012). Estudio de la deformación litosférica de la cuenca Neuquina: estructura termal, datos de gravedad y sísmica de reflexión. (Thesis) University of Buenos Aires, Argentina

Sippel, J., Meeßen, C., Cacace, M., Mechie, J., Fishwick, S., Heine, C., et al. (2017). The Kenya rift revisited: insights into lithospheric strength through data-driven 3-D gravity and thermal modelling. *Solid Earth*, *8*(1), 45–81. https://doi.org/10.5194/se-8-45-2017

Sloan, R. A., Jackson, J. A., McKenzie, D., & Priestley, K. (2011). Earthquake depth distributions in central Asia, and their relations with lithosphere thickness, shortening and extension. *Geophysical Journal International*, *185*(1), 1–29. https://doi.org/10.1111/j.1365-246X.2010.04882.x

Smalley, R., & Isacks, B. L. (1990). Seismotectonics of thin- and thick-skinned deformation in the Andean Foreland from local network data: Evidence for a seismogenic lower crust. *Journal of Geophysical Research*, *95*(B8), 12487. https://doi.org/10.1029/JB095iB08p12487

Smalley, R., Pujol, J., Regnier, M., Chiu, J.-M., Chatelain, J.-L., Isacks, B. L., et al. (1993). Basement seismicity beneath the Andean precordillera thin-skinned thrust belt and implications for crustal and lithospheric behavior. *Tectonics*, *12*(1), 63–76. https://doi.org/10.1029/92TC01108

Sobel, E. R., & Strecker, M. R. (2003). Uplift, exhumation and precipitation: tectonic and climatic control of Late Cenozoic landscape evolution in the northern Sierras Pampeanas, Argentina. *Basin Research*, *15*(4), 431–451. https://doi.org/10.1046/j.1365-2117.2003.00214.x

Sobolev, S.V., Zeyen, H., Stoll, G., Werling, F., Altherr, R., & Fuchs, K. (1996). Upper mantle temperatures from teleseismic tomography of French Massif Central including effects of composition, mineral reactions, anharmonicity, anelasticity and partial melt. *Earth and Planetary Science Letters*, *139*(1), 147–163. https://doi.org/10.1016/0012-821X(95)00238-8

Sobolev, S. V., Babeyko, A. Y., Koulakov, I., & Oncken, O. (2006). Mechanism of the Andean Orogeny: Insight from Numerical Modeling. In O. Oncken, G. Chong, G. Franz, P. Giese, H.-J. Götze, V. A. Ramos, et al. (Eds.), *The Andes: Active Subduction Orogeny* (pp. 513–535). Berlin, Heidelberg: Springer Berlin Heidelberg. https://doi.org/10.1007/978-3-540-48684-8_25

Sobolev, S.V., & Babeyko, A. Y. (2005). What drives orogeny in the Andes? *Geology*, *33*(8), 617–620. https://doi.org/10.1130/G21557AR.1

Spalletti, L., & Limarino, C. (2017). The Choiyoi magmatism in south western Gondwana: implications for the end-permian mass extinction—a review. 44, 328–338. *Andean Geol.*, *44*(3), 328–338. https://doi.org/10.5027/andgeoV44n3-a05

Spooner, C., Scheck-Wenderoth, M., Götze, H.-J., Ebbing, J., & Hetényi, G. (2019). Density distribution across the Alpine lithosphere constrained by 3-D gravity modelling and relation to seismicity and deformation. *Solid Earth*, *10*(6), 2073–2088. https://doi.org/10.5194/se-10-2073-2019

Spooner, C., Scheck-Wenderoth, M., Cacace, M., Götze, H.-J., & Luijendijk, E. (2020). The 3D thermal field across the Alpine orogen and its forelands and the relation to seismicity. *Global and Planetary Change*, *193*, 103288. https://doi.org/10.1016/j.gloplacha.2020.103288

Stadtlander, R., Mechie, J., & Schulze, A. (1999). Deep structure of the southern Ural mountains as derived from wide-angle seismic data. *Geophysical Journal International*, *137*(2), 501–515. https://doi.org/10.1046/j.1365-246X.1999.00794.x

Steinberger, B., & Calderwood, A. R. (2006). Models of large-scale viscous flow in the Earth’s mantle with constraints from mineral physics and surface observations. *Geophysical Journal International*, *167*(3), 1461–1481. https://doi.org/10.1111/j.1365-246X.2006.03131.x

Stern, C. R. (2004). Active Andean volcanism: its geologic and tectonic setting. *Revista Geológica de Chile*, *31*(2), 161–206.

Stern, C. R., & Skewes, M. A. (1995). Miocene to present magmatic evolution at the northern end of the Andean Southern Volcanic Zone, Central Chile. *Andean Geology*, *22*(2), 261–272. http://dx.doi.org/10.5027/andgeoV22n2-a09

Stern, R. J. (2002). SUBDUCTION ZONES. *Reviews of Geophysics*, *40*(4), 3–1. https://doi.org/10.1029/2001RG000108

Stixrude, L., & Lithgow-Bertelloni, Carolina. (2005). Mineralogy and elasticity of the oceanic upper mantle: Origin of the low-velocity zone. *Journal of Geophysical Research*, *110*(B3), B03204. https://doi.org/10.1029/2004JB002965

Straume, E., Gaina, C., Medvedev, S., Hochmuth, K., Gohl, K., Whittaker, J. M., et al. (2019). GlobSed: Updated total sediment thickness in the world’s oceans. *Geochemistry, Geophysics, Geosystems*, *20*(4), 1756–1772. https://doi.org/10.1029/2018GC008115

Strecker, M. R., Cerveny, P., Bloom, A. L., & Malizia, D. (1989). Late Cenozoic tectonism and landscape development in the foreland of the Andes: Northern Sierras Pampeanas (26°–28°S), Argentina. *Tectonics*, *8*(3), 517–534. https://doi.org/10.1029/TC008i003p00517

Stüwe, K. (2007). *Geodynamics of the Lithosphere*. Berlin Heidelberg: Springer-Verlag Berlin Heidelberg.

Syracuse, E. M., van Keken, P. E., & Abers, G. A. (2010). The global range of subduction zone thermal models. *Special Issue on Deep Slab and Mantle Dynamics*, *183*(1), 73–90. https://doi.org/10.1016/j.pepi.2010.02.004

Tape, C., Liu, Q., Maggi, A., & Tromp, J. (2010). Seismic tomography of the southern California crust based on spectral-element and adjoint methods. *Geophysical Journal International*, *180*(1), 433–462. https://doi.org/10.1111/j.1365-246X.2009.04429.x

Tapia, F., Farías, M., Naipauer, M., & Puratich, J. (2015). Late Cenozoic contractional evolution of the current arc-volcanic region along the southern Central Andes (35°20′S). *Journal of Geodynamics*, *88*, 36–51. https://doi.org/10.1016/j.jog.2015.01.001

Tassara, A. (2005). Interaction between the Nazca and South American plates and formation of the Altiplano–Puna plateau: Review of a flexural analysis along the Andean margin (15°–34°S). *Tectonophysics*, *399*(1), 39–57. https://doi.org/10.1016/j.tecto.2004.12.014

Tassara, A. (2006). Factors controlling the crustal density structure underneath active continental margins with implications for their evolution: CONTINENTAL MARGIN CRUSTAL DENSITY. *Geochemistry, Geophysics, Geosystems*, *7*(1), n/a-n/a. https://doi.org/10.1029/2005GC001040

Tassara, A., & Echaurren, A. (2012). Anatomy of the Andean subduction zone: three-dimensional density model upgraded and compared against global-scale models: Anatomy of the Andean subduction zone. *Geophysical Journal International*, *189*(1), 161–168. https://doi.org/10.1111/j.1365-246X.2012.05397.x

Tassara, A., & Yáñez, G. (2003). Relación entre el espesor elástico de la litosfera y la segmentación tectónica del margen andino (15-47°S). *Andean Geology*, *30*(2), 159–186.

Tassara, A., Götze, H.-J., Schmidt, S., & Hackney, R. (2006). Three-dimensional density model of the Nazca plate and the Andean continental margin. *Journal of Geophysical Research*, *111*(B9), B09404. https://doi.org/10.1029/2005JB003976

Taylor, S. R. (1967). The origin and growth of continents. *Tectonophysics*, *4*(1), 17–34. https://doi.org/10.1016/0040-1951(67)90056-X

Tesauro, M., Kaban, M. K., & Cloetingh, S. A. P. L. (2009). How rigid is Europe's lithosphere? *Geophysical Research Letters*, *36*(16). https://doi.org/10.1029/2009GL039229

Tesauro, M., Audet, P., Kaban, M. K., Bürgmann, R., & Cloetingh, S. (2012). The effective elastic thickness of the continental lithosphere: Comparison between rheological and inverse approaches: *Te* OF THE CONTINENTAL LITHOSPHERE. *Geochemistry, Geophysics, Geosystems*, *13*(9). https://doi.org/10.1029/2012GC004162

Tesauro, M., Kaban, M. K., & Mooney, W. D. (2015). Variations of the lithospheric strength and elastic thickness in North America: lithospheric Strength and Te variations. *Geochemistry, Geophysics, Geosystems*, *16*(7), 2197–2220. https://doi.org/10.1002/2015GC005937

The pyrocko Developers. (2018). Pyrocko: A Versatile Seismology Toolkit for Python. (Version 2018.1.29). https://doi.org/10.5880/GFZ.2.1.2017.001

Thielmann, M., Rozel, A., Kaus, B. J. P., & Ricard, Y. (2015). Intermediate-depth earthquake generation and shear zone formation caused by grain size reduction and shear heating. *Geology*, *43*(9), 791–794. https://doi.org/10.1130/G36864.1

Thielmann, M. (2018). Grain size assisted thermal runaway as a nucleation mechanism for continental mantle earthquakes: Impact of complex rheologies. *Understanding Geological Processes through Modelling - A Memorial Volume Honouring Evgenii Burov*, *746*, 611–623. https://doi.org/10.1016/j.tecto.2017.08.038

Thompson, A. B., Schulmann, K., Jezek, J., & Tolar, V. (2001). Thermally softened continental extensional zones (arcs and rifts) as precursors to thickened orogenic belts. *Tectonophysics*, *332*(1), 115–141. https://doi.org/10.1016/S0040-1951(00)00252-3

Thrastarson, S., van Herwaarden, D.-P., Krischer, L., & Fichtner, A. (2021). LArge-scale Seismic Inversion Framework, an updated version. *EarthArXiv*. https://doi.org/10.31223/X5NC84

Tichelaar, B. W., & Ruff, L. J. (1993). Depth of seismic coupling along subduction zones. *Journal of Geophysical Research: Solid Earth*, *98*(B2), 2017–2037. https://doi.org/10.1029/92JB02045

Turcotte, D. L., & Schubert, G. (2002a). *Geodynamics*. Cambridge: Cambridge university press.

Turcotte, D. L., & Schubert, G. (2002b). *Geodynamics*. Cambridge university press.

Turner, J. C. M. (1960). Estratigrafía de la Sierra de Santa Victoria y adyacencias. *Boletín de La Academia Nacional de Ciencias de Córdoba*, *41*(2), 163–196.

Uieda, L., Oliveira Jr, V. C., & Barbosa, V. C. (2013). Modeling the earth with fatiando a terra (pp. 96–103). Presented at the Proceedings of the 12th Python in Science Conference.

Uliana, M., Biddle, K., & Cerdan, J. (1989). Mesozoic Extension and the Formation of Argentine Sedimentary Basins: Chapter 39: Analogs. *American Association of Petroleum Geologists*. https://doi.org/10.1306/M46497C39

Uyeda, S., & Watanabe, T. (1982). Terrestrial heat flow in western South America. *Tectonophysics*, *83*(1–2), 63–70. https://doi.org/10.1016/0040-1951(82)90007-5

Van Rossum, G., & Drake, F. L. (2009). *Python 3 Reference Manual*. Scotts Valley, CA: CreateSpace.

Van Rossum, G., & Drake Jr, F. L. (1995). *Python reference manual*. Centrum voor Wiskunde en Informatica Amsterdam.

Vannucchi, P., Remitti, F., & Bettelli, G. (2008). Geological record of fluid flow and seismogenesis along an erosive subducting plate boundary. *Nature*, *451*(7179), 699–703. https://doi.org/10.1038/nature06486

Vauchez, A., Tommasi, A., & Barruol, G. (1998). Rheological heterogeneity, mechanical anisotropy and deformation of the continental lithosphere. *Tectonophysics*, *296*(1), 61–86. https://doi.org/10.1016/S0040-1951(98)00137-1

Venerdini, A., Alvarado, P., Ammirati, J.-B., Podesta, M., López, L., Fuentes, F., et al. (2020). Crustal seismicity in the Andean Precordillera of Argentina using seismic broadband data. *Tectonophysics*, *786*, 228450. https://doi.org/10.1016/j.tecto.2020.228450

Vergani, G. D., Tankard, A. J., Belotti, H. J., & Welsink, H. J. (1995). Tectonic Evolution and Paleogeography of the Neuquén Basin, Argentina. In *M 62: Petroleum Basins of South America* (Vol. 62, pp. 383–402). AAPG Special Volumes.

Vilà, M., Fernández, M., & Jiménez-Munt, I. (2010). Radiogenic heat production variability of some common lithological groups and its significance to lithospheric thermal modeling. *Tectonophysics*, *490*(3–4), 152–164. https://doi.org/10.1016/j.tecto.2010.05.003

Virtanen, P., Gommers, R., Oliphant, T. E., Haberland, M., Reddy, T., Cournapeau, D., et al. (2020). SciPy 1.0: Fundamental Algorithms for Scientific Computing in Python. *Nature Methods*, *17*, 261–272. https://doi.org/10.1038/s41592-019-0686-2

Völker, D., Geersen, J., Contreras-Reyes, E., & Reichert, C. (2013). Sedimentary fill of the Chile Trench (32–46°S): volumetric distribution and causal factors. *Journal of the Geological Society*, *170*(5), 723–736. https://doi.org/10.1144/jgs2012-119

Vujovich, G. I., & Kay, S. M. (1998). A Laurentian? Grenville-age oceanic arc/back-arc terrane in the Sierra de Pie de Palo, Western Sierras Pampeanas, Argentina. *Geological Society, London, Special Publications*, *142*(1), 159–179. https://doi.org/10.1144/GSL.SP.1998.142.01.09

Wagner, L., Beck, S., Zandt, G., & Ducea, M. (2006). Depleted lithosphere, cold, trapped asthenosphere, and frozen melt puddles above the flat slab in central Chile and Argentina. *Earth and Planetary Science Letters*, *245*(1–2), 289–301. https://doi.org/10.1016/j.epsl.2006.02.014

Wagner, L. S., Beck, S., & Zandt, G. (2005). Upper mantle structure in the south central Chilean subduction zone (30° to 36°S). *Journal of Geophysical Research: Solid Earth*, *110*(B1). https://doi.org/10.1029/2004JB003238

Wagner, L.S., Caddick, M. J., Kumar, A., Beck, S. L., & Long, M. D. (2020). Effects of Oceanic Crustal Thickness on Intermediate Depth Seismicity. *Frontiers in Earth Science*, *8*, 244. https://doi.org/10.3389/feart.2020.00244

Wang, K. (2002). Unbending combined with dehydration embrittlement as a cause for double and triple seismic zones. *Geophysical Research Letters*, *29*(18), 36–1. https://doi.org/10.1029/2002GL015441

Wangen, M. (1994). The blanketing effect in sedimentary basins. *Basin Research*, *7*(4), 283–298.

Ward, K. M., Porter, R. C., Zandt, G., Beck, S. L., Wagner, L. S., Minaya, E., & Tavera, H. (2013). Ambient noise tomography across the Central Andes. *Geophysical Journal International*, *194*(3), 1559–1573. https://doi.org/10.1093/gji/ggt166

Watts, A. B., & Burov, E. B. (2003). Lithospheric strength and its relationship to the elastic and seismogenic layer thickness. *Earth and Planetary Science Letters*, *213*(1), 113–131. https://doi.org/10.1016/S0012-821X(03)00289-9

Weiss, J. R., Qiu, Q., Barbot, S., Wright, T. J., Foster, J. H., Saunders, A., et al. (2019). Illuminating subduction zone rheological properties in the wake of a giant earthquake. *Science Advances*, *5*(12), eaax6720. https://doi.org/10.1126/sciadv.aax6720

Wiemer, S., & Wyss, M. (2000). Minimum Magnitude of Completeness in Earthquake Catalogs: Examples from Alaska, the Western United States, and Japan. *Bulletin of the Seismological Society of America*, *90*(4), 859–869. https://doi.org/10.1785/0119990114

Wilks, K. R., & Carter, N. L. (1990). Rheology of some continental lower crustal rocks. *Tectonophysics*, *182*(1–2), 57–77. https://doi.org/10.1016/0040-1951(90)90342-6

Willett, S., Beaumont, C., & Fullsack, P. (1993). Mechanical model for the tectonics of doubly vergent compressional orogens. *Geology*, *21*(4), 371–374. https://doi.org/10.1130/0091-7613(1993)021<0371:MMFTTO>2.3.CO;2

Winocur, D. A., Litvak, V. D., & Ramos, V. A. (2015). Magmatic and tectonic evolution of the Oligocene Valle del Cura basin, main Andes of Argentina and Chile: evidence for generalized extension. https://doi.org/10.1144/SP399.2

Wolf, S. G., & Huismans, R. S. (2019). Mountain Building or Backarc Extension in Ocean-Continent Subduction Systems: A Function of Backarc Lithospheric Strength and Absolute Plate Velocities. *Journal of Geophysical Research: Solid Earth*, *124*(7), 7461–7482. https://doi.org/10.1029/2018JB017171

Wyllie, P. (1981). Plate tectonics and magma genesis. *Geologische Rundschau*, *70*(1), 128–153. https://doi.org/10.1007/BF01764318

Xu, Y., Shankland, T. J., Linhardt, S., Rubie, D. C., Langenhorst, F., & Klasinski, K. (2004). Thermal diffusivity and conductivity of olivine, wadsleyite and ringwoodite to 20 GPa and 1373 K. *Physics of the Earth and Planetary Interiors*, *143–144*, 321–336. https://doi.org/10.1016/j.pepi.2004.03.005

Yáñez, G.A., & Cembrano, J. (2004). Role of viscous plate coupling in the late Tertiary Andean tectonics. *Journal of Geophysical Research: Solid Earth*, *109*(B2). https://doi.org/10.1029/2003JB002494

Yáñez, G. A., Ranero, C. R., von Huene, R., & Díaz, J. (2001). Magnetic anomaly interpretation across the southern central Andes (32–34 S): The role of the Juan Fernández

Ridge in the late Tertiary evolution of the margin. *Journal of Geophysical Research: Solid Earth*, *106*(B4), 6325–6345.

Yang, X.-Z., Xia, Q.-K., Deloule, E., Dallai, L., Fan, Q.-C., & Feng, M. (2008). Water in minerals of the continental lithospheric mantle and overlying lower crust: a comparative study of peridotite and granulite xenoliths from the North China Craton. *Chemical Geology*, *256*(1–2), 33–45. https://doi.org/10.1007/s11434-013-5949-1

Zapata, S., Sobel, E. R., Del Papa, C., & Glodny, J. (2020). Upper Plate Controls on the Formation of Broken Foreland Basins in the Andean Retroarc Between 26°S and 28°S: From Cretaceous Rifting to Paleogene and Miocene Broken Foreland Basins. *Geochemistry, Geophysics, Geosystems*, *21*(7). https://doi.org/10.1029/2019GC008876